Universiteit Leiden
The Netherlands

Imperfections: using defects to program designer matter

Meeussen, A.S.

Citation
Meeussen, A. S. (2021, May 26). *Imperfections: using defects to program designer matter*. *Casimir PhD Series*. Retrieved from https://hdl.handle.net/1887/3179459

Version:	Publisher's Version
License:	Licence agreement concerning inclusion of doctoral thesis in the Institutional Repository of the University of Leiden
Downloaded from:	https://hdl.handle.net/1887/3179459

Note: To cite this publication please use the final published version (if applicable).

Cover Page

Universiteit Leiden

Leiden University Repository

The handle https://hdl.handle.net/1887/3179459 holds various files of this Leiden University dissertation.

Author: Meeussen, A.S.
Title: Imperfections: using defects to program designer matter
Issue Date: 2021-05-26

Imperfections

using defects to program designer matter

Anne S. Meeussen

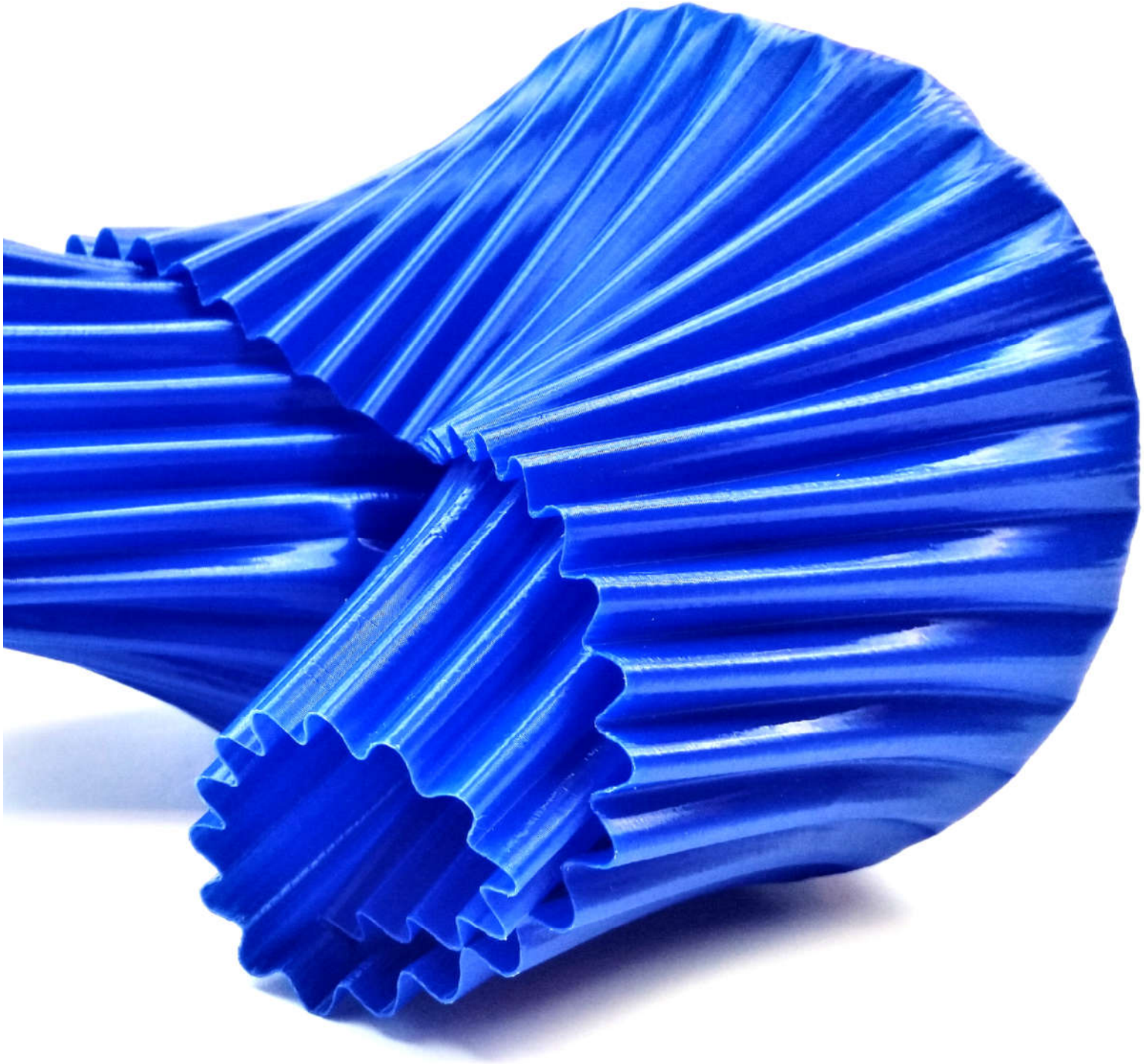

Imperfections:
using defects to program designer matter

Proefschrift

ter verkrijging van
de graad van doctor aan de Universiteit Leiden,
op gezag van rector magnificus prof.dr.ir. H. Bijl,
volgens besluit van het college voor promoties
te verdedigen op woensdag 26 mei 2021
klokke 16:15 uur

door

Anne Sophia Meeussen
geboren te Rotterdam, Nederland
in 1990

Promotor	Prof.dr. M. L. van Hecke
Co-promotor	Dr. D. J. Kraft
Promotiecommissie	Prof.dr. K. Bertoldi (Harvard University, Cambridge, USA) Prof.dr. C. Daraio (California Institute of Technology, Pasadena, USA) Prof.dr. A. Achúcarro Prof.dr. E. R. Eliel
Nederlandse titel	Imperfecties: het gebruik van defecten voor het programmeren van designer-materialen

Casimir PhD series, Delft-Leiden, 2021-03
ISBN 978-90-8593-469-1
An electronic version of this dissertation can be found at openaccess.leidenuniv.nl.

The work presented in this dissertation was conducted at AMOLF, Amsterdam, an institute of the Netherlands Organisation for Scientific Research (NWO), and at the Leiden Institute of Physics, Leiden University.

The cover shows a hand-sized groovy sheet, 3D-printed using a flexible material (courtesy of Jeroen Mesman-Vergeer), snapped into a spiralling shape.

Contents

1. Introduction **7**
1.1. The importance of imperfections . . . 7
1.2. Topological defects . . . 8
1.3. Snap-through defects . . . 10

2. A spin-ice-inspired class of complex metamaterials **15**
Abstract . . . 15
2.1. Introduction . . . 15
2.2. Triangular building blocks . . . 16
2.3. Compatible metamaterials . . . 17
2.3.1. Parity of paths of internal bonds . . . 19
2.3.2. Mapping compatible metamaterials to an antiferromagnetic Ising model on the kagome lattice . . . 21
2.3.3. Diversity of compatible metamaterial architectures . . . 22
2.3.4. Compatible metamaterials with fully antiferromagnetic block spin interactions . . . 25
2.4. Incompatible metamaterials . . . 26
2.4.1. Triangle rotations as fundamental architectural transformations . . . 27
2.4.2. A structural defect . . . 27
2.4.3. A topological defect . . . 28
2.4.4. More odd local loops . . . 29
2.5. Conclusions and outlook . . . 30
Acknowledgements . . . 30

3. Topological defects produce exotic mechanics in complex metamaterials **31**
Abstract . . . 31
3.1. Introduction . . . 31
3.2. Probing frustration: models and experiments . . . 32
3.2.1. Experimental realizations . . . 32
3.2.2. Model FH: freely hinging spring network . . . 34
3.2.3. Model TR and LTR: torsionally rigid hinges . . . 36
3.2.4. Comparing experiments and models . . . 37
3.3. Mechanical signature of defects . . . 40
3.3.1. Detection protocol: measuring the boundary . . . 41
3.3.2. Probing the entire boundary . . . 42
3.3.3. Hinge stiffness: the right value . . . 44
3.3.4. Probing a few boundary blocks . . . 44
3.3.5. Decay limits detection . . . 47
3.3.6. Error estimates . . . 48
3.4. Exotic mechanics with topological defects . . . 49
3.4.1. Mechanics and path parity . . . 50
3.4.2. Stress and deformation steering . . . 54
3.4.3. Mode splitting in the presence of topological defects . . . 57

3.5. Conclusions and outlook . . . 61
Acknowledgements . . . 61

4. Response evolution of mechanical metamaterials under architectural transformations 63
Abstract . . . 63
4.1. Introduction . . . 63
4.2. Linear mechanics: states of self stress and floppy modes . . . 65
4.3. Structurally complex mechanical metamaterials . . . 67
4.4. States of self stress in superhexagons and larger metamaterials . . . 69
4.5. Architectural defects . . . 72
4.6. Response evolution under architectural transformations . . . 74
4.6.1. Constructing the states of self stress . . . 75
4.6.2. Process I: supertriangle rotation from a compatible to an incompatible geometry . . . 78
4.6.3. Process II: supertriangle rotation from an incompatible to another incompatible geometry . . . 79
4.6.4. Mechanical interpretation and consequences . . . 82
4.7. Re-steering a stress response with architectural transformations . . . 83
4.8. Conclusions and outlook . . . 84
Acknowledgements . . . 85

5. Reshapeable groovy sheets 87
Abstract . . . 87
5.1. Introduction . . . 88
5.2. Making groovy sheets . . . 95
5.2.1. Geometry . . . 95
5.2.2. Fabrication . . . 95
5.3. Measuring groovy sheet shapes . . . 104
5.3.1. 2D photography . . . 104
5.3.2. 3D imaging . . . 104
5.4. In-plane elasticity of groovy sheets . . . 110
5.4.1. Groovy sheets are not symmetric . . . 110
5.4.2. Stiffness along the grooves . . . 111
5.4.3. Stiffness across the grooves . . . 111
5.4.4. Modelling stiffness . . . 111
5.4.5. A 3D sheet simulation . . . 116
5.5. Bistability of grooves . . . 119
5.5.1. Making single defects . . . 119
5.5.2. Sheet size dependence . . . 122
5.6. Interactions between defects . . . 128
5.6.1. Defects interact with their nearest neighbours . . . 128
5.6.2. Defects attract and repel . . . 130
5.6.3. Interactions via curvature . . . 132
5.7. Shaping groovy sheets with scar lines . . . 139
5.7.1. A single scar . . . 140
5.7.2. Combining scars . . . 146
5.7.3. Parallel scars . . . 148
5.7.4. Understanding sheet shapes: outlook . . . 157

5.8. Conclusions and outlook . . . 160
Acknowledgements . . . 161

A. Appendices **163**
A.1. Floppy motion of a triangular building block . . . 163
A.2. Constructing delocalized SS-states . . . 165
A.3. Evolution of LB-spaces under architectural transformations . . . 165
A.3.1. Process I: compatible to incompatible metamaterial . . . 168
A.3.2. Process II: incompatible to incompatible metamaterial . . . 169
A.3.3. Process III: compatible to compatible metamaterial . . . 170
A.4. Mechanical interpretation of evolving LB-states . . . 170
A.5. Derivation of stress response differences . . . 173
A.6. BoPET film properties . . . 176
A.7. Spring-back, yielding, and groove design . . . 179
A.8. Elasticity of groovy sheets: accordion model . . . 183
A.9. 3D numerical sheet model . . . 185
A.9.1. Parameters . . . 185
A.9.2. Algorithm . . . 185
A.9.3. Energy and forces . . . 186
A.10. Defect energetics in a 3D numerical sheet model . . . 188
A.11. Calculating surface curvature . . . 189
A.12. Elastic model of groovy sheets with a single scar line . . . 191

Bibliography **197**

Summary **207**

Samenvatting **211**

Publications **215**

Curriculum Vitae **217**

Thank you **219**

You are trying to solve a problem.
You're almost certainly halfway done,
maybe more.

Jane Hirshfield

1. Introduction

1.1. The importance of imperfections

Errors are everywhere. Mechanical failures are especially common: from buckled grain silos and tubes that balloon when they had better not, to cracked support columns (Fig. 1.1). These types of mechanical failure are, justly, seen as an issue to be avoided. Entire fields of study are dedicated to engineering structures and materials that can withstand extreme circumstances.

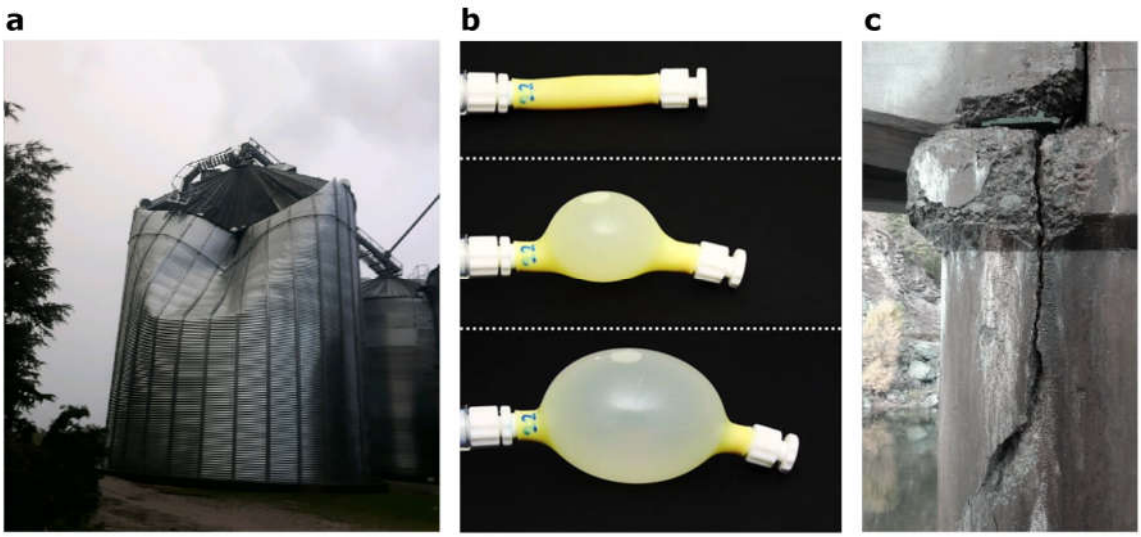

Fig. 1.1.: Imperfections to be avoided. a, Buckled grain silos in Iowa after the 2020 USA Midwest derecho (a thunder-gust event). Photo: Iowa Governor's Office, via radioiowa.com. **b,** Ballooning in an inflated cylindrical tube: a prototypical model of aneurysms. Image adapted from Ref.[1]. **c,** Cracked concrete columns supporting a bridge in Washington, 2014. Photo: Washington State Department of Transportation, via methowvalleynews.com.

Crucially, such research provides not only the means to prevent mechanical failure, but also the means to understand its sources: different flaws, errors, imperfections- each provides a distinct and unique challenge. This understanding of mechanical flaws' sources and effects allows us to expand our horizons: flaws can be *used* to design materials with unique functionalities. For example, buckling is harnessed to create structures that morph between different shapes[2] (Fig. 1.2a); carefully textured balloons inflate to soft robotic grippers, suited for manipulating fragile objects[3] (Fig. 1.2b); and crack paths can be engineered to produce controlled trajectories and edge patterns[4] (Fig. 1.2c). The special behaviour of these functional structures exists by the grace of defects.

In the work presented here, we follow the same idea: defects can be put to use. Throughout this dissertation, we use two types of imperfections to create functional

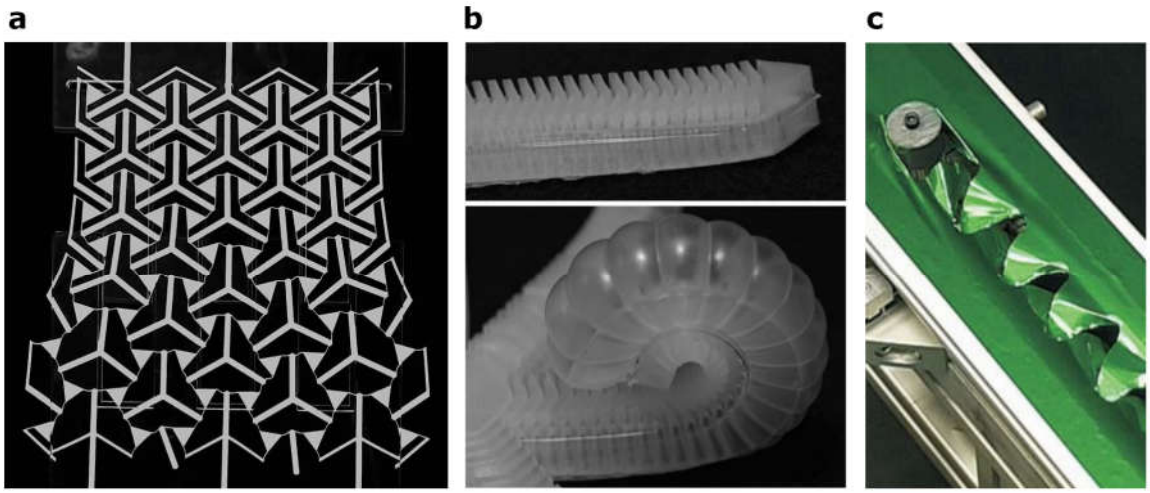

Fig. 1.2.: Useful imperfections. a, Buckling in a 2-D geometric structure produces a shape-morphing structure that can expand and contract quickly. Image adapted from Ref.[2]. **b,** Ballooning in a thin rubber structure is harnessed to make a curling soft robotic gripper. Image adapted from Ref.[3]. **c,** Tearing cracks in a thin film with a moving cylindrical rod results in a characteristic and controllable periodic cut pattern. Photo: Benoît Roman, via Ref.[4].

structures. First, we design materials that are locally stiff or soft, depending on how they are actuated, using topological imperfections: mistakes in their underlying architecture (chapters 2-4). Second, we create structures that shape-morph, because their individual elements fail, buckle, and snap- features that should be avoided otherwise (chapter 5). We briefly discuss their background and our main findings below.

1.2. Topological defects

In chapters 2-4, we harness topological defects to create materials in which deformations and stress are steered to different parts of the structure, depending on how it is actuated. Here, we discuss the basics of topology, and show the special behaviour of a material with a topological imperfection.

In essence, topology helps describe how different parts of an object, whether it is abstract or real, are interconnected. This means that topology can be used to distinguish materials with fundamentally different internal architectures. To get an intuition for how this works in different contexts, Fig. 1.3 shows three classic examples. In Fig. 1.3a, we show a thin strip of plastic that has been connected back to itself into a ring. The ring has a simple topology, with an inside and an outside surface. But when the strip is twisted once, its topology changes drastically. Imagine walking around this Möbius loop: to get back to your point of departure, you have to circle the strip twice. As a different example, a pair of topologically distinct doughnuts is shown in Fig. 1.3b. The pastries' topology is set by the number of holes: the jam doughnut has none, the regular doughnut has one. Interestingly, the number of holes can be counted locally by keeping track of the patisserie's surface curvature. We finish with an inedible case in Fig. 1.3c: liquid crystals. These are long and thin molecular rods that, under the right circumstances, align alongside each other into a simple topology. However, mismatches in alignment

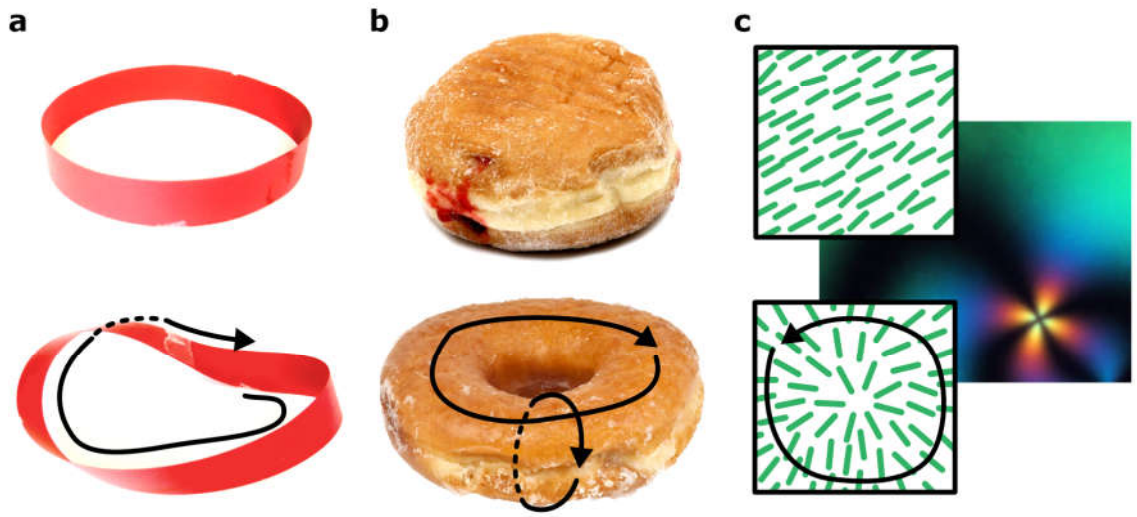

Fig. 1.3.: Topology can be used to classify objects. a, A thin plastic strip is looped back on itself into a ring (top). Twisting the strip once produces a Möbius loop with a distinct topology: traversing the Möbius loop once gets you to the opposite side (bottom, arrow). **b,** A jam doughnut (top) and a regular doughnut (bottom) are topologically distinct: one has a hole, which can be detected by tracking the doughnut's local curvature across the surface (arrows). Photos: Evan Amos. **c,** Liquid crystal rods can be aligned (top) or not (bottom): alignment disruptions produce topological defects that can be distinguished by tracking the rod orientation around a loop (arrow). A typical Schlieren texture of a defect in a liquid crystal film is shown. Image: Oleg D. Lavrentovich, Kent State University.

produce defects with a distinct topological signature. The presence of these defects can be detected by tracking the rods' orientation along a closed loop at the outer boundary of the system. In short: topology describes the internal structure and connectedness of a large spectrum of objects.

While the examples shown above appear distinct, they have one thing in common. Their topological character—whether they are twisted, have holes, or other defects—is *measurable*. And measuring topology is done by looping around the object in question. Specifically, we have to keep track of the structures' local properties while traversing closed loops around it. If there are topological defects in the system, these local properties show a characteristic signature that flags whether there is mismatch: a topological defect (chapter 2).

We use topological defects with a characteristic Möbius-like loop signature to design functional structures in chapter 3. Fig. 1.4 shows the end result of this design process. To keep things simple, we work with two-dimensional structures built up out of discrete slender rods arranged in a triangular structure, as illustrated in Fig. 1.4a. The material shown there has a simple topology, analogous to a simple ring: it has no defects, topological or otherwise. As a result, compression of the structure produces a smooth, soft deformation that is even reproduced in experimental, 3D-printed samples (Fig. 1.4b). By contrast, changing the internal architecture of the structure by switching just a few rods produces a structure with a topological defect (Fig. 1.4c). Like the Möbius loop, this structure has structural mismatch that produces strange effects. When this structure is pushed (Fig. 1.4d), one half of the material deforms nicely; however, the other half is

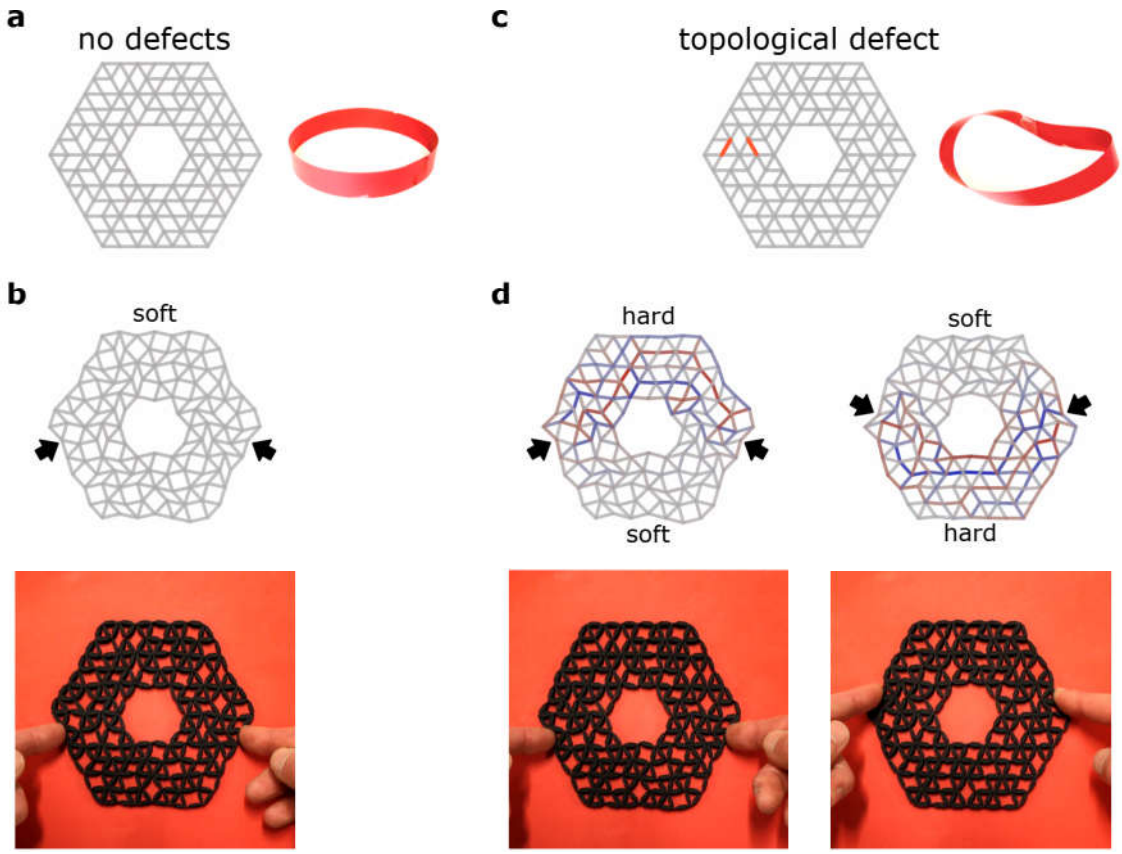

Fig. 1.4.: Topological defects steer forces and deformations. a, Top to bottom: a ring-like structure built up out of thin elastic rods (grey bars) has a simple topology, analogous to a ring (inset). **b,** Under compression (arrows), the structure deforms smoothly and easily by hinging at the bars' connecting points. Experimental realizations reproduce this behaviour (bottom). **c,** Modifying the structure by switching a few bars (red highlights) produces a topological defect, similar to twisting a strip to produce a Möbius loop. **d,** When the structure is compressed at two points, one half deforms easily, while stress (colours) builds up in the other half (left). This stress-steering response can be switched around by choosing different loading points (right). Real samples show the same effect (bottom).

stiff, does not deform, and builds up stresses. While this behaviour is unusual, build-up of stresses is not unique in the presence of mechanical defects (chapter 4). However, due to the unique topology of the material, this stress-steering response can be flipped in space: by changing where we compress the structure, stresses and deformations are steered to opposite sides of the system.

Our work thus demonstrates that topological defects can be harnessed to design functional materials, in which external actuation controllably steers stresses and deformations to different parts of the system.

1.3. Snap-through defects

Besides topological defects, we harness snap-through instabilities in chapter 5 to design shape-morphing structures. These materials switch quickly and reversibly between multiple stable states. We discuss the basic idea behind snapping and shape-morphing here,

and illustrate the shape-shifting qualities of our material.

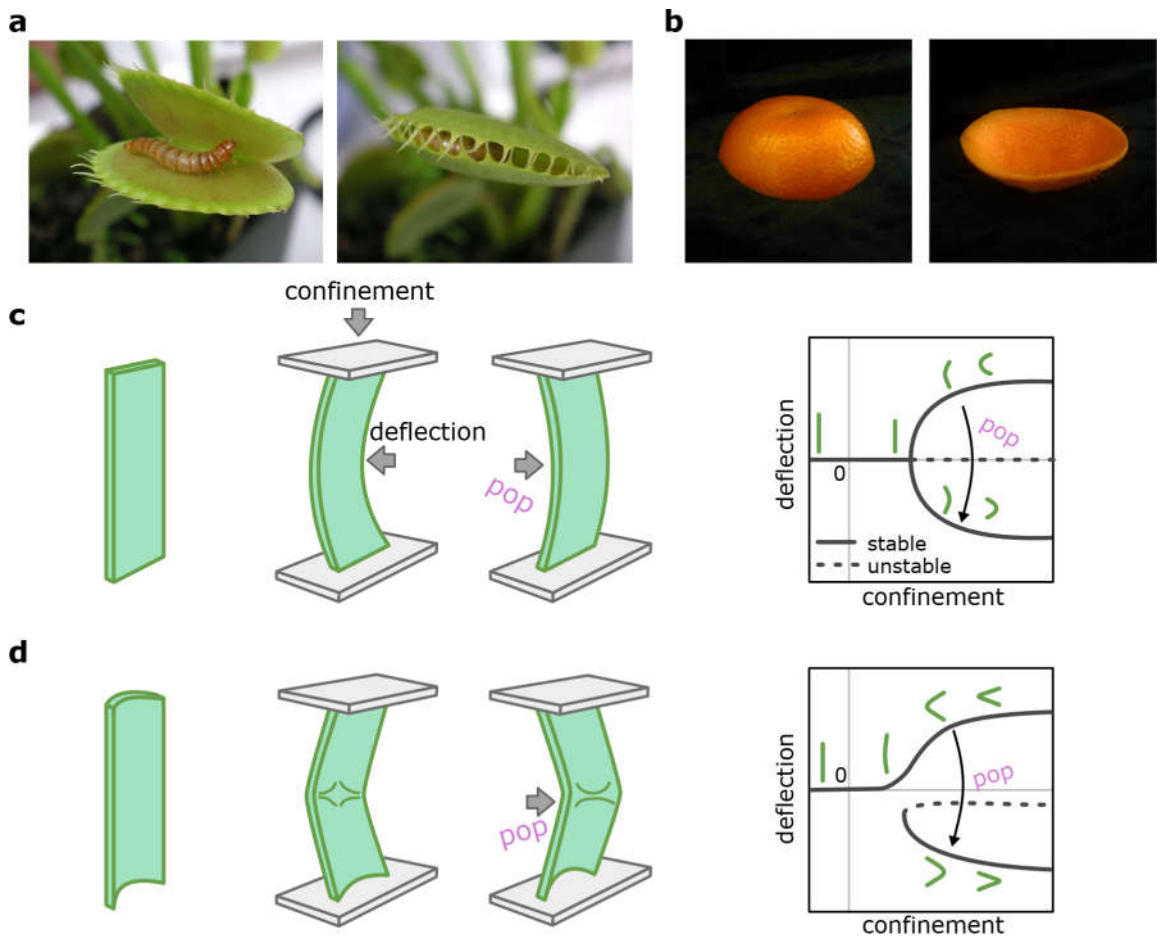

Fig. 1.5.: Snap-through instabilities allow shape-morphing. a, Venus flytrap leaves are shaped like shallow caps. The leaves invert through swelling to a closed configuration. Photos: Beatrice Murch (CC BY-SA 2.0). **b,** Snapping through geometric frustration: a convex cap cut from a tangerine (left), pops into a stable inverted shape (right). **c,** Prototypical snapping model. Left: a thin strip is confined between two plates. The strip buckles, as measured by its deflection. Right: phase diagram showing the strip's stable states. After buckling, a pitchfork bifurcation produces two stable states: left-and right-buckled. A snap-through instability, triggered by external probing, switches the state and pops the strip from left to right. **d,** Snapping with asymmetry. Left: a pre-curved groove can buckle and pop. The left- and right-buckled state are not the same. Right: the phase diagram shows a typical imperfect pitchfork bifurcation. The groove buckles left under confinement, but can be popped through into the right-buckled state.

Generally, snap-through instabilities occur in structures that have multiple stable states. The two states are separated by an energy barrier, which can be traversed if the structure is actuated with a large enough force. Snapping instabilities are common: Fig. 1.5 illustrates two instances from the natural world. For example, the leaves of a Venus flytrap (Fig. 1.5a) can snap shut to trap prey: the leaves are shaped like shallow shells, that can snap through to an inverted shape. This transition appears to be activated by differential swelling in each leaf [5]. The role of swelling can be taken up by simple mechanical action as well, as illustrated in Fig. 1.5b. There, we show a shallow spherical cap, cut from the peel of a tangerine. Though the cap is naturally convex,

it can be popped through to a concave shape by pushing the top. The energy barrier that separates these two states is mostly elastic, and arises from the tangerine's spherical shape and the slenderness of its peel. To create a shape-shifting structure, we will likewise make use of elastic, geometry-induced snapping in thin structures.

Fig. 1.5c shows a prototypical model for geometric snapping in thin sheets. The narrow elastic strip shown there does not snap spontaneously; but confining the strip between two plates forces it to buckle through. Due to the strip's symmetry, it can buckle either left or right. Thus, the confined sheet has two stable states—left- or right-buckled—and can snap between these two, reversibly, by applying an external deflection. This idea is illustrated in the state diagram (Fig. 1.5c, right) which shows the typical pitchfork bifurcation that this system undergoes: at small confinement, the sheet stays straight; after a critical confinement, the sheet buckles, and can snap back and forth between its two buckled states.

Now contrast the behaviour of a straight strip with that of a pre-curved groove, illustrated schematically in Fig. 1.5d. The groove shown is not symmetric: under external confinement, it snaps through preferentially toward its convex side (reminiscent of a tape spring). However, the groove can be popped toward its concave side under external deflection into what we call its *defect state*. Crucially, when several grooves are tiled together into a *groovy sheet* (Fig. 1.6a), the groove's defect state is stable even without external confinement. Thus, groovy sheets can snap reversibly between resting and defect configurations, due to their geometry.

We harness the reshaping capacities of groovy sheets to create shape-shifting materials. This concept is illustrated in Fig. 1.6. Fig. 1.6a shows the base material: a thin sheet, made with multiple adjacent grooves. Each groove can be popped into a defect state, in which a localized disruption curves the underlying structure into a bent shape. Fig. 1.6b shows groovy sheets with one, two, and four grooves in their defect state; crossed polarisers highlight the defect loci in colour, resulting from the plastic sheets' intrinsic birefringence. Even sheets with only a few grooves can switch to a shape that is quite drastically different from the initial flat configuration. Increasing the number of grooves allows for the creation of a wide array of defect patterns, and produces an even wider spectrum of sheet shapes: selected examples are shown in Fig. 1.6c. Curled, twisting, spiralling, and disordered shapes are observed.

Importantly, our work shows that defect patterns can be created mechanically with relative ease. Under the right conditions, defects do not produce permanent deformations in the underlying material, and one sheet can thus snap reversibly into many different shapes, one after the other. Thus, this work provides a platform that harnesses geometry-induced snap-through instabilities to create shape-morphing structures.

The work presented in this dissertation thus harnesses imperfections for functional design. We show how topological defects steer stresses and deformations inside mechanical structures, and how geometry-induced snap-through defects produce shape-morphing materials. We hope that our findings can contribute to the ever-expanding field of functional design of mechanical structures[1,2,6–12].

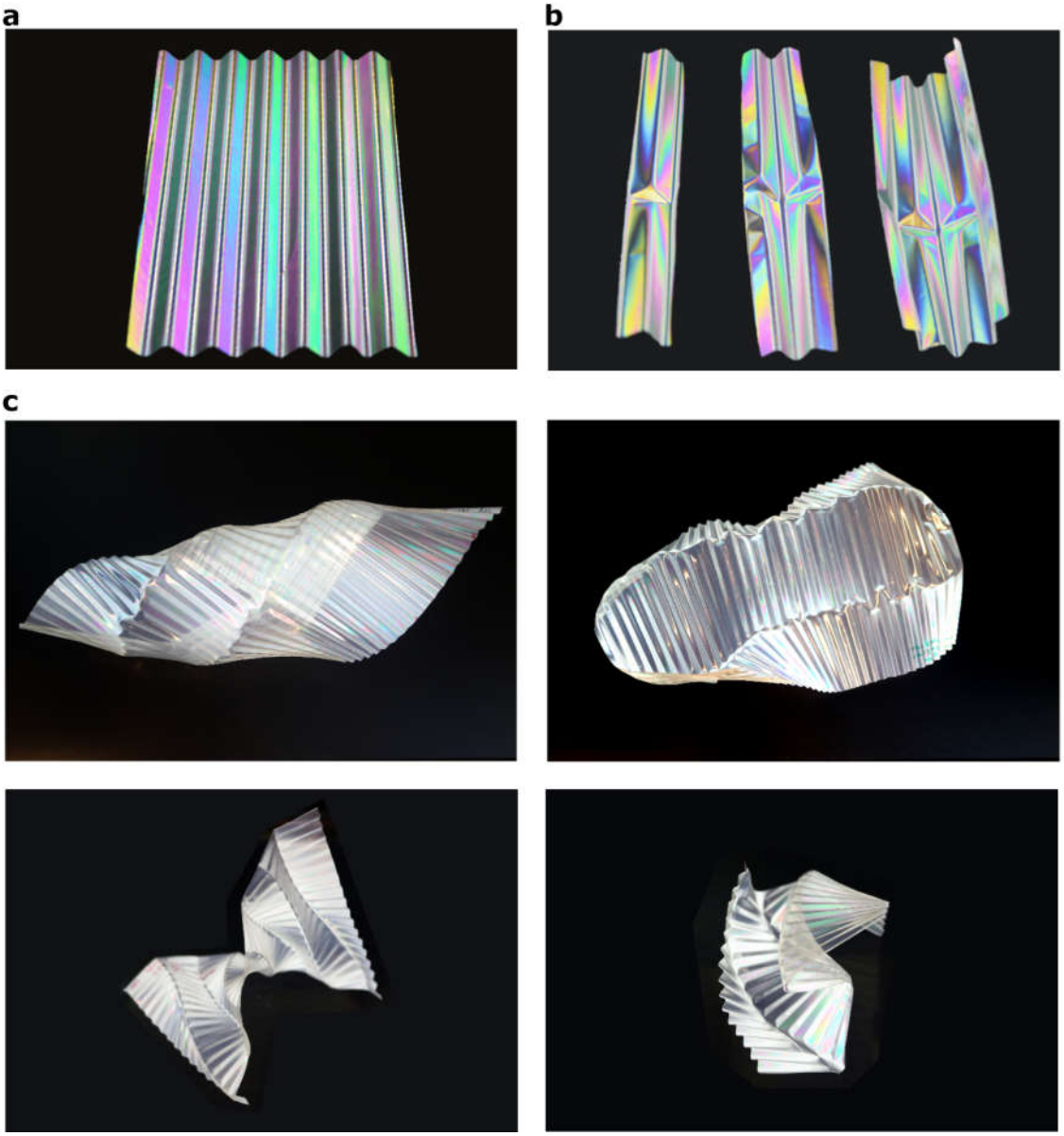

Fig. 1.6.: Undulating groovy sheets snap reversibly into complex shapes. a, A groovy sheet: thin plastic, tens of microns thick, with undulations on the centimetre scale. Colours arise from viewing between crossed polarizers. **b,** Undulations of a groovy sheet support snap-through defects. Examples of one, two, and four undulations are shown. **c,** Larger sheets snap between complex spiralling and curving three-dimensional shapes, from ordered to disordered. The sheets' shape varies depending on the location of snap-through defects in its grooves.

2. A spin-ice-inspired class of complex metamaterials[1]

Abstract

The basic tenet of metamaterials is that architecture controls the physics[7–10,15–22]. So far, mainly defect-free architectures have been considered. However, defects, and particularly topological defects, play a crucial role in natural materials[23–27]. Here we provide a systematic strategy to introduce such defects in mechanical metamaterials. We first present metamaterials that are a mechanical analogue of spin systems with tunable ferromagnetic and antiferromagnetic interactions; then design an exponential number of frustration-free metamaterials; show how we can introduce local defects by rotating specific building blocks; and finally introduce topological defects by rotating a string of building blocks in these metamaterials. Our work presents a new avenue to systematically include spatial complexity, frustration, and topology in mechanical metamaterials.

2.1. Introduction

Mechanical metamaterials are structured forms of matter with unprecedented properties, including negative response parameters[15], shape-morphing[7,8], topological mechanics[16–19], and self-folding[9]. While the focus has been on frustration-free compatible architectures, where all unit cells deform in harmony, frustration causes more complex, higher-energy deformations, leading to advanced functionalities, such as multistability and programmability[10,20–22], and may open up opportunities to probe controlled frustration in man-made systems[23–25]. We note that deformations of unit cells in compatible metamaterials often alternate, leading to horizontal and vertical ellipses[15], rigid elements that rotate left or right[10,28,29], or edges of unit cells that move in or out[7,22]: we refer to this as *antiferromagnetic order*. Hence, a promising route to introduce targeted frustration is to use fundamental building blocks that favour either antiferromagnetic order or ferromagnetic, non-alternating order, and use the freedom supplied by additive manufacturing to stack these at will. Paths connecting pairs of such building blocks carry a *parity*, given by the parity of the number of antiferromagnetic interactions along the path. In compatible architectures, all paths connecting any pair of building blocks must have the same parity, and we anticipate that we can solve the combinatorial constraints that govern such designs[7,30]. In contrast, generic configurations tend to violate such constraints, leading to frustration and defects.

We start our investigation in section 2.2 by describing simple, 2D triangular building blocks that can be stacked together to interact either ferro- or antiferromagnetically, and that form the basis of our mechanical networks. In section 2.3, we discuss a technique[30] to stack these building blocks into compatible, frustration-free architectures with controllable isotropy and periodicity. A simple design rule to ensure compatibility is formulated,

[1] The work presented in this chapter is based on Refs.[13] and [14].

based on a mapping between the mechanical network and an antiferromagnetic Ising spin-ice. As we show in section 2.4, this simple design rule naturally suggests a protocol to violate compatibility by creating controlled local and topological defects in the network. Finally, we present an outlook and suggestions for further research in section 2.5.

2.2. Triangular building blocks

To implement our design strategy, we now introduce anisotropic, triangular building blocks that set the ferromagnetic or antiferromagnetic nature of their interactions depending on their mutual orientations.

We work with a specific type of mechanical elements consisting of freely hinging nodes connected by bonds modelled as rigid bars. Compatibility in such networks means that there is a single, global mode of motion, called a *floppy motion*, such that the network deforms at zero energy cost- that is, none of the rigid bars change their length during this deformation. In a compatible network consisting of smaller building blocks, it is necessary that each of the individual building blocks is compatible as well, and has what we call a *local floppy mode*.

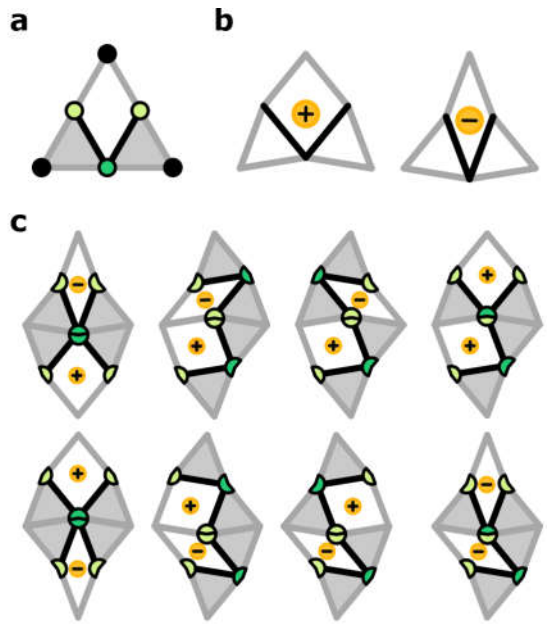

Fig. 2.1.: Stackable building block. **a**, Anisotropic building blocks consisting of edge bonds (grey), internal bonds (black), corner nodes (black), majority edge-nodes (light green), and a minority edge-node (dark green). **b**, Deformed building block in fat (+) and skinny (-) states. **c**, Adjacent building blocks may be stacked together in four distinct configurations (columns). Each configuration can be deformed in two ways (top and bottom rows). Adjacent building blocks interact antiferromagnetically (ferromagnetically) when their shared edge features an even (odd) number of minority nodes, so that their minority nodes are connected by an even (odd) number of internal bonds.

We use the triangular building block shown in Fig. 2.1a. Each block consists of six nodes in a triangle configuration in the (x, y)-plane. The six nodes are positioned at integer multiples of two triangular basis vectors $\boldsymbol{a}_1 = l(1, 0)$ and $\boldsymbol{a}_2 = l(1/2, \sqrt{3}/2)$, where the lattice parameter l may be chosen freely. We distinguish three *corner nodes* at the triangle's corners, and three *edge nodes* (of which two are *majority edge-nodes* and one a *minority edge-node*) halfway the triangle's edges. The nodes are connected by eight bonds: six *edge bonds* around the triangle's perimeter, and two *internal bonds* connecting the majority nodes to the minority node, so that all bonds have length l. This leaves the two minority nodes unconnected to each other, and results in an anisotropic building block.

The triangular building block features a floppy "hinging" motion, illustrated in Fig. 2.1b (see Appendix A.1 for details), which allows the block to deform at zero energy cost as

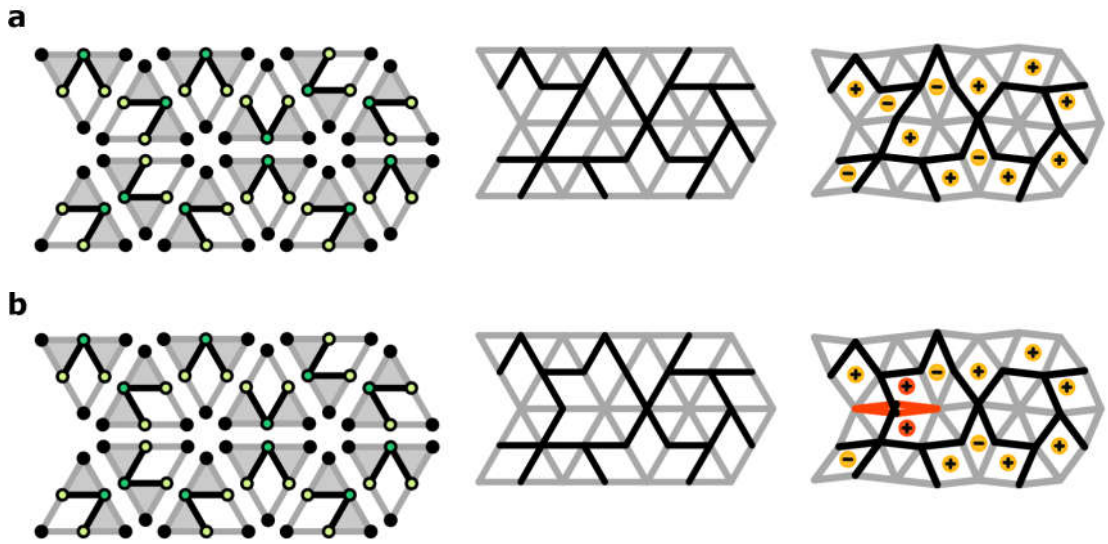

Fig. 2.2.: Randomly stacking building blocks produces floppy or frustrated networks. **a**, Stacking building blocks with various orientations on a triangular lattice (left) produces a metamaterial consisting of rigid bars connected by freely hinging joints (middle). The particular example shown exhibits a floppy mode: the blocks undergo a collective deformation and fit together like puzzle pieces (right). **b**, A slightly different random stacking is frustrated, as indicated by the red block spins and edge bonds: there is no collective deformation of the building blocks so that all deformed blocks fit together.

all bond lengths remain constant. Accordingly deformed building blocks can take on two shapes—fat and skinny—which we assign a positive or negative *block spin* variable.

When two building blocks are stacked together, they exhibit a collective floppy deformation: the two blocks deform together, each becoming either fat (positive block spin) or skinny (negative block spin). There are four unique ways to stack a block pair (Fig. 2.1c), and the relative floppy deformation of the two blocks depends on how they are stacked together. When their shared edge contains one minority node, the building blocks interact *ferromagnetically*: the zero-energy deformation then features two building blocks with the same block spin. In contrast, when their shared edge possesses either zero or two minority nodes, the interaction is said to be *antiferromagnetic*, and the deformations have opposite block spins.

2.3. Compatible metamaterials

To create metamaterials consisting of many building blocks, we stack blocks on a triangular lattice with varying orientations (Fig. 2.2). This stacking method allows us to design structures with a wide range of structurally complex geometries. Such stacked metamaterials can be either compatible, so that the stack can deform at zero energy cost (Fig. 2.2a), or frustrated (Fig. 2.2b). Stacks with randomly oriented building blocks are usually frustrated. To obtain *targeted* frustration, we start in this section by first designing compatible, frustration-free configurations, before introducing controlled frustration. That is, we formulate design rules for metamaterials where all building blocks deform simultaneously according to their local floppy mode, so that the deformed building blocks

fit as in a jigsaw puzzle.

In section 2.3.1, we first show that frustration-free configurations require that in each hexagon of six adjacent building blocks, the number of connected antiferromagnetic interactions, corresponding to the smallest possible closed *local loop* of internal bonds, is even. This finding implies that compatibility is equivalent to requiring that all local loops are of even length (Fig. 1d,e; see methods) while odd local loops generate frustration[31].

A vast number of structurally complex configurations satisfy the above compatibility condition. Counting and designing these geometries requires solving combinatorial problems. In section section 2.3.2), we explore their solutions. Since all compatible architectures feature a floppy mode where all building blocks have two edge nodes moving "in" and one minority edge-node moving "out" (or vice versa), we can map these deformations to ground states of an antiferromagnetic Ising model on the kagome lattice (*AFIK model*). Each ground state of this AFIK model generates a distinct compatible metamaterial, up to a global spin flip. The extensive ground-state entropy of that model[32,33] yields an asymptotically exact result for the exponential number of compatible architectures as a function of the system size[30]. We show in section 2.3.3 that this rich design space allows us to create structures with a wide range of secondary properties, such as (an)isotropy and periodicity.

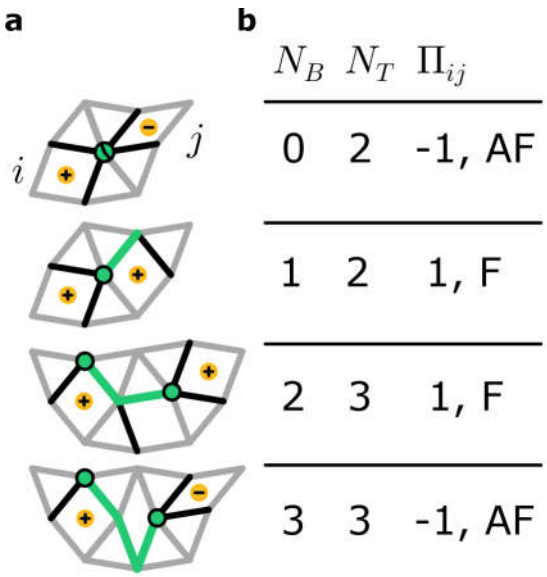

Fig. 2.3.: Path parity. **a**, Four stacks where pairs i, j of building blocks are interconnected. When blocks i, j undergo a floppy deformation, they either extend (+) or contract (-). **b**, The relative sign of the blocks' deformations depends on the length N_B of the connecting path of internal bonds (green lines), which runs from the minority node of block i to that of block j (green circles), and the number of connecting blocks N_T. A path parity $\Pi = (-1)^{N_b - N_T - 1}$ may be defined so that the block deformations of i and j are identical (different) if $\Pi = 1$ ($\Pi = -1$), corresponding to a ferromagnetic, 'F' (antiferromagnetic, 'AF') interaction between i and j.

Finally, in section 2.3.4, we discuss an important example of a frustration-free geometry: an ordered metamaterial where all interactions between block spins are antiferromagnetic. Its zero-energy deformation mode has all up-facing (down-facing) building blocks in their fat (skinny) state, or vice-versa, which corresponds to alternating positive and negative block spins. We note that this geometry is equivalent to the rotating square mechanism that underlies the design of a wide range of metamaterials[9,15,20,28,29,34]. More generally, geometries with fully antiferromagnetic block spins can be mapped to diamond tilings, where each diamond represents two building blocks with two minority nodes on their shared edge. We show that the number of possible fully antiferromagnetic designs grows exponentially with system size.

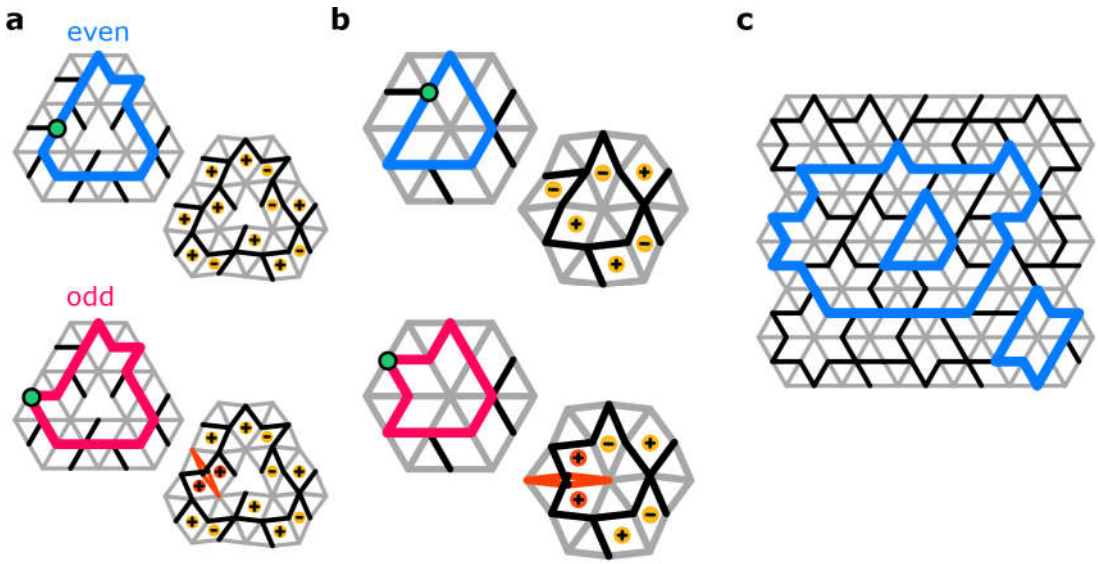

Fig. 2.4.: Compatible structures satisfy a parity rule for closed paths. **a**, A building block (minority node highlighted in dark green) is connected to itself on a triangular lattice via an even number of neighbours. Top: a loop of an even number of internal bonds (bold blue lines) runs around the cluster, ensuring that the building block interacts ferromagnetically with itself. The cluster has a floppy mode. Bottom: an odd loop (bold red lines) produces an antiferromagnetic self-interaction and leads to frustration (red edge bonds). There is no floppy mode. **b**, *Local loops* within a superhexagon of six blocks form the smallest possible closed paths of internal bonds. An even (odd) local loop produces a compatible (incompatible) hexagonal structure. **c**, If all local loops in a metamaterial are even, all larger loops are, too. Thus, evenness of each local loop ensures compatibility.

2.3.1. Parity of paths of internal bonds

As discussed above, in a compatible metamaterial, all building blocks can simultaneously deform according to their local floppy mode. We conceive of the joint floppy deformation of any pair i, j of blocks, connected by a larger cluster of building blocks, as an interaction. Examples are shown in Fig. 2.3a. For a *ferromagnetic* interaction, the blocks have the same block spin and simultaneously expand or simultaneously contract, whereas for an *antiferromagnetic* interaction the blocks' spins are opposite: one block contracts while the other expands. We show here that the internal bonds connecting blocks i, j determine their interaction type, and we formulate a design rule for the internal bonds to ensure that all blocks in a metamaterial can deform simultaneously.

We define a *path* of N_b internal bonds running from the minority node of block i to the minority node of block j through their connecting cluster of building blocks, and define N_T as the number of triangular building blocks traversed by the path (including blocks i and j). The *path parity*

$$\Pi = (-1)^{N_b - N_T - 1} \tag{2.1}$$

is then positive (negative) when the interaction between i and j is ferromagnetic (antiferromagnetic), as illustrated in Fig. 2.3b.

This path parity rule leads to a self-consistency requirement for closed paths, or *loops* of internal bonds, running from any block i to itself. After all, the block must interact

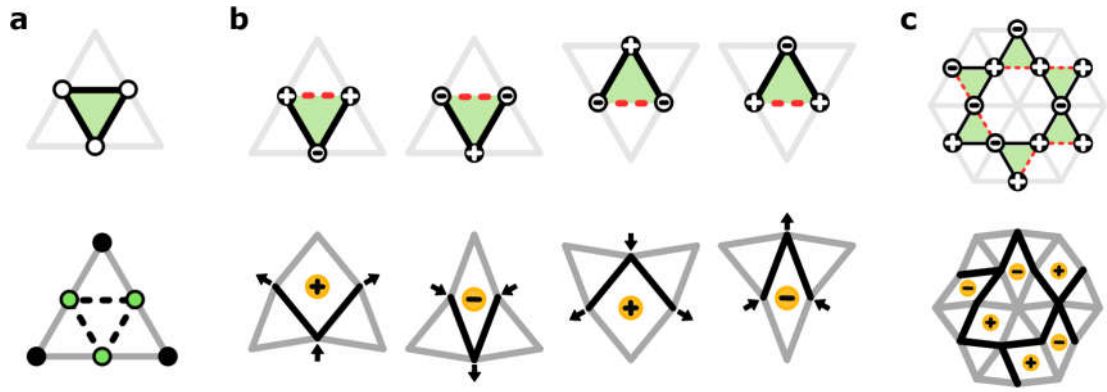

Fig. 2.5.: Compatible structures can be designed with a spin mapping. **a**, Top: a unit cell (light grey outline) of an Ising model on a kagome lattice (green triangle). Edge spin sites (open circles) are connected by antiferromagnetic interactions (black bars). Bottom: the spin cell maps to a mechanical building block with three corner nodes (black circles), six edge bonds (dark grey bars), and three possible internal bonds (dashed black lines) that connect the three edge nodes (green circles). **b**, Ground states of the spin cell (top) map to a mechanical building block with a prescribed floppy mode (bottom). Satisfied antiferromagnetic interactions correspond to internal bonds; the unsatisfied spin interaction (red dashed line) signifies an absence of bonds. Positive (negative) edge spins map to outward (inward) edge node deflections of the upward- (downward-)pointing mechanical blocks. **c**, Top: a spin ground state of a hexagonal section of the kagome lattice. Bottom: corresponding hexagonal mechanical metamaterial, which possesses a floppy mode obtained directly from the spin ground state.

ferromagnetically with itself in order to deform compatibly. Equivalently, the path parity of a loop containing the block must be positive. We can re-formulate this path parity condition, using the fact that any closed path on a triangular lattice traverses an even number of triangles. Hence, to ensure that a building block interacts ferromagnetically with itself, we must ensure that the parity of the number of internal bonds in the loop must be even; equivalently, that the number of minority nodes on shared edges is even; and that the number of (anti)ferromagnetic interactions between adjacent blocks in the path is even.

In a compatible network, all closed paths must therefore contain an even number of internal bonds. Conversely, loops with an odd number of internal bonds imply incompatibility. Fig. 2.4a shows an example of a compatible closed path with even length, and a frustrated closed path with odd length. Due to the structure of our building blocks, each lattice point—where the blocks' corner nodes meet—is circumscribed by a *local loop* within a hexagon of six adjacent blocks, which we will refer to as a *superhexagon*; two examples are shown in Fig. 2.4b. Such local loops are the smallest closed paths of internal bonds in our networks, and must all satisfy the self-consistency requirement to ensure compatibility. Conveniently, when all local loops in a metamaterial satisfy the compatibility requirement, larger loops are guaranteed to contain an even number of internal bonds as well (Fig. 2.4c). In summary, if and only if a network is compatible, then all loops of internal bonds—-from the smallest local loops around each lattice point to the largest loops around the network boundary—have an even number of bonds in their perimeter.

2.3.2. Mapping compatible metamaterials to an antiferromagnetic Ising model on the kagome lattice

The above parity rule helps us identify which structures are compatible. However, this parity rule does not help us design compatible structures from scratch. We address this issue here.

To obtain a design strategy for compatible metamaterials, we map the local FM of a building block to the ground state of an Ising spin model with antiferromagnetic interactions on the kagome lattice (AFIK model)[13] as illustrated in Fig. 2.5a. We associate a positive (negative) binary edge spin variable to an extensile (contractile) edge node deflection for a downward-pointing building block, and vice versa for upward-pointing blocks (Fig. 2.5b). In the AFIK model, the three spin sites inside a building block are connected by three antiferromagnetic interactions. These three interactions cannot be simultaneously satisfied: the lowest-energy spin configuration satisfies only two of the antiferromagnetic interactions, and violates one. The building block's mechanical FM corresponds to such a minimal-energy spin configuration that satisfies two out of the three antiferromagnetic interactions. Specifically, the building block's two internal bonds connect edge spin sites in opposite states, while the edge nodes not connected by an internal bond both move inward (or both outward), representing a frustrated antiferromagnetic interaction. Hence, the lowest-energy AFIK configuration corresponds to the local floppy mode of a single building block.

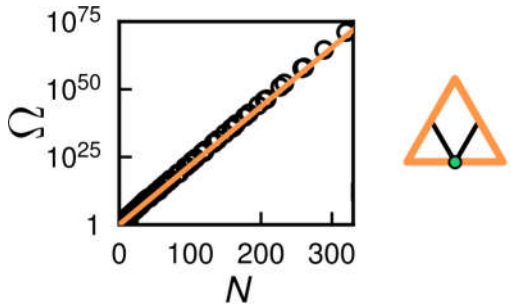

Fig. 2.6.: Counting compatible designs. The numerically obtained number of compatible designs Ω is shown as a function of the number of edge nodes N and compared to asymptotic predictions based on an Ising-spin mapping. An exact count of the number of compatible parallellogram-shaped designs[30](circles), created by combining building blocks (top right, orange triangle) in various orientations, closely matches the ground-state degeneracy of the corresponding Ising model (orange line)[32].

Adjacent blocks deform compatibly when their shared edge spins match. Thus, in compatible architectures, the edge spins form a kagome lattice where each triangular plaquette features one positive and two negative edge spins, or vice versa (Fig. 2.5c). Such collective edge spin states are precisely the degenerate ground states of the AFIK model, so that each ground-state configuration generates a distinct compatible metamaterial (up to a global spin flip).

We note here that this mapping to an Ising model with binary states is complete only for compatible metamaterials which possess a FM in which displacements alternate in direction and all have the same magnitude. As we show in the following chapter, in incompatible structures, the magnitude of the displacements varies continuously with position. In that case, the mapping to the Ising model serves only to demonstrate whether there exists a global compatible deformation.

From the AFIK mapping, we obtain an asymptotic expression for Ω_0, the number of compatible architectures, via the residual entropy $S_0 \approx 0.502N$ of the degenerate ground state of the AFIK model[32,33]

$$\Omega_0 \sim e^{0.502N} = e^{0.753T} \approx 2.1^T < 3^T = \Omega_{tot}, \tag{2.2}$$

where N denotes the number of edge spins, T the number of blocks, $N = 3T/2$ the number of edge spins in the thermodynamic limit, and Ω_{tot} the total number of architectures. The asymptotic expression agrees well with the exact number of compatible, parallelogram-shaped architectures as determined by computer algorithms[30], even for small systems (Fig. 2.6).

2.3.3. Diversity of compatible metamaterial architectures

With the AFIK mapping described above, we find that an exponential number of compatible designs can be constructed as a function of the design's size. While this implies that we can find compatible architectures with a wide range of secondary properties that arise from symmetries (such as isotropy and periodicity), the structures do share a special feature: their total area decreases under actuation of their floppy mode. Here, we discuss these two design aspects—symmetry and shrinking—briefly.

First, stacking building blocks with varying degrees of disorder produces metamaterials with more or less symmetry. Two order parameters that help describe symmetries are isotropy and periodicity. Isotropic materials are rotationally symmetric, and have the same properties in all radial directions. Conversely, periodic structures have translational symmetries, and are invariant under some discrete translations. While a prescriptive approach to constructing metamaterials with specific symmetries is outside the scope of this work, the framework used here, where we treat metamaterials as stacks of simple building blocks, invites intuitive design. That is, structures with more or less order can be found by stacking and rotating the building blocks heuristically. Some products of this approach are shown in Fig. 2.7, where four structures of varying (an)isotropy and (a)periodicity are shown.

Secondly, during floppy deformation of any compatible stack, about half of the building blocks will expand, while the other half contracts. Contraction of a building block produces a larger area change than extension, as we show below, and as a result, the total area of the metamaterial tends to decrease.

We can understand this shrinking behaviour using our knowledge of the net ground state magnetization of the AFIK model[35], and the geometry of the building blocks during deformation. We use the fact that a compatible stack of building blocks can also be seen as a stack of even local loops on a triangular mesh background, as discussed in section 2.3.1. We illustrate this concept in Fig. 2.8: Fig. 2.8a shows the eight possible shapes that even local loops inside a superhexagon of six adjacent building blocks can take, barring rotations and reflections. The local loop determines whether some of the building blocks it traverses expand or contract, as illustrated in Fig. 2.8b. Specifically, when a building block's deforming quadrangle lies inside the local loop, its deformation with respect to its loop-mates is fixed. In this way, the shape of the local loop sets the deformation of 0, 2, 4, or 6 building blocks. Inspection shows that each even local loop enforces an equal

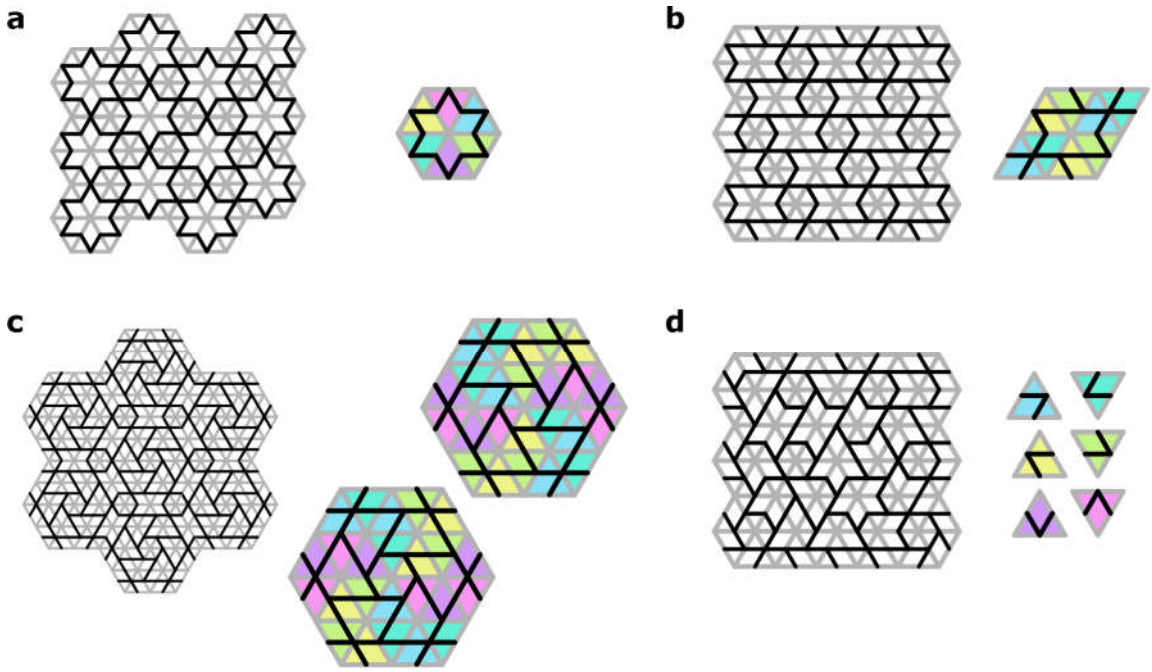

Fig. 2.7.: Compatible designs come in a wide array of (dis)order. **a**, An isotropic and periodic design (left) is highly ordered. Isotropic unit cells (right), which feature an equal number of building blocks in each of the six possible orientations (colours), create this architecture. **b**, An anisotropic yet periodic design (left) is created by stacking anisotropic unit cells (right), which contain an unequal number of building blocks in the six block orientations. **c**, An isotropic and aperiodic design (left) is made by stacking together isotropic unit cells (right). Periodicity is avoided here by stacking mirrored copies of the unit cells in a random arrangement. **d**, A disordered design (left) which is anisotropic and aperiodic. It is constructed by randomly stacking building blocks in different orientations, while respecting compatibility (right).

number of expanding and contracting building blocks. Thus, the number of expanding and contracting building blocks in a stack of even loops is equal. In a corresponding stack of triangular building blocks, this equality can only be violated at the system's boundary: there is a local design freedom to introduce more expanding or more contracting building blocks at the material's edges. An example is shown in Fig. 2.8c. In the limit of large system sizes however, the boundary contributes an eventually vanishing fraction to the total number of building blocks. As a result, half of the blocks contract and half expand during an infinitely large compatible stack's floppy deformation.

As a corollary, the area of a compatible stack decreases on average during deformation away from its initial shape. This follows from some trigonometry. Consider a building block with an opening angle $\theta_0 + \Delta\theta$ between its two internal bonds, where θ_0 is the rest opening angle and $\Delta\theta$ the deviation from the resting value during its floppy deformation (Fig. 2.9a). The area A spanned by the building block's quadrangle—the only portion that changes shape—is then given by

$$A = l^2 \sin(\theta_0 + \Delta\theta) \ , \tag{2.3}$$

where l is the bond length (Fig. 2.9b). During deformation of a compatible stack, $|\Delta\theta|$ is the deformation's control parameter: it is equal for all building blocks due to geometric

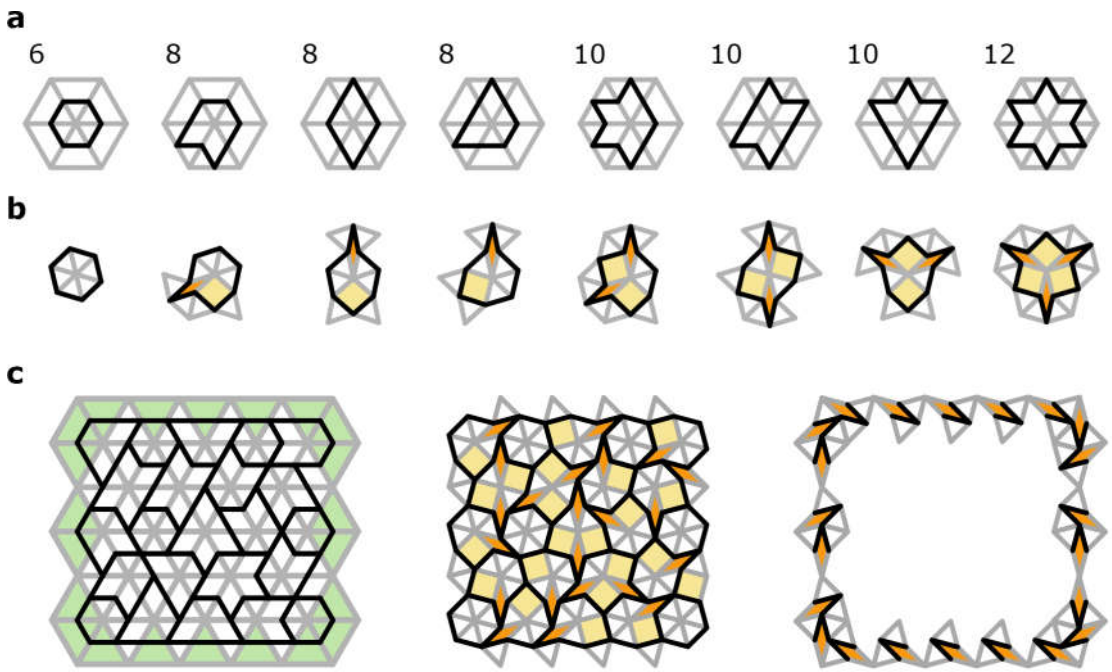

Fig. 2.8.: Compatible designs feature an approximately equal number of contracting and extending building blocks. **a**, The bulk of a compatible architecture can be created by stacking together even local loops (black bars), each contained in a hexagonal backing structure (grey bars). The eight unique even local loops are pictured and the number of internal bonds indicated. **b**, The shape of the local loop governs its deformation as shown. Each local loop sets the extension (yellow) and contraction (orange) of an equal number of triangular building blocks: 0, 1, 2, or 3. **c**, Compatible stacks can be given an unequal number of contracting and extending building blocks by exploiting the boundary. Left: an example is shown of a compatible bulk structure consisting of stacked even loops, with an open boundary (green). Middle: the structure's bulk deformation is fully determined. Right: the edge is freely decorated with arbitrary numbers of extending and contracting building blocks. Here, all boundary blocks contract.

constraints (Fig. 2.9c). Therefore, half of the building blocks increase in area, and half decrease. The area per building block, averaged over the entire stack, is then found to be

$$\langle A \rangle = l^2 \sin(\theta_0) \cos(\Delta\theta). \tag{2.4}$$

Evidently, the average area is maximal in the initial state, when all building blocks have the same shape (Fig. 2.9d). Deforming the material always decreases its area.

As a consequence, to create structures whose floppy deformation produces a net area increase, a different building block is needed. Such a building block should allow for the construction of stacks in which large clusters of neighbours can interact ferromagnetically. The construction of these specialized building blocks is outside the scope of this work. However, with our existing triangular blocks, it is possible to design compatible stacks with locally ordered patterns of expanding and contracting blocks. We discuss an important example in the following section.

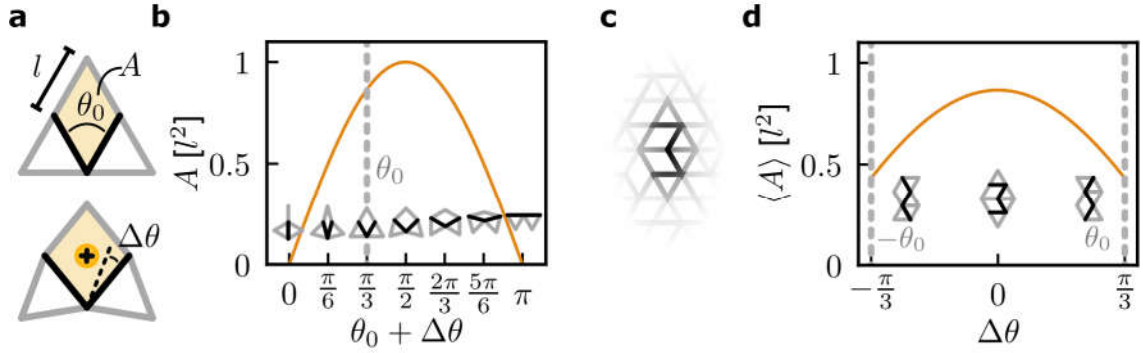

Fig. 2.9.: The area of a compatible architectures decreases under deformation. **a** A single building block with bond length l has a deforming quadrangle of area A (yellow). The deformed shape is set by the rest angle θ_0 between the internal bonds (black bars) and its deviation $\Delta\theta$. **b** Area of the deforming quadrangle as a function of $\theta_0 + \Delta\theta$. Insets show the deformed block shape at indicated angles. **c** In an infinitely large stack, an equal number of building blocks contract and extend. Two antiferromagnetically interacting blocks are shown as an example. **d** The complete stack's average area per block during deformation is shown as a function of angular deviation. The average area per block always decreases away from the rest state at $\Delta\theta = 0$.

2.3.4. Compatible metamaterials with fully antiferromagnetic block spin interactions

Our metamaterial design strategy generates many different network architectures, including the widely-studied rotating square mechanism[9,15,20,28,29,34] illustrated in Fig. 2.10a-b. This is an example of an antiferromagnetic architecture, where all neighbouring building block spins interact antiferromagnetically. Here, we map the design of general antiferromagnetic architectures to the tiling of diamonds and count the resulting number of compatible antiferromagnetic stacks.

Since only building blocks that share zero or two minority nodes interact antiferromagnetically, each building block needs to be oriented so that its minority node is paired with the minority node of one of its neighbours. Identifying such pairs of building blocks as a diamond-shaped tile (Fig. 2.10c), each antiferromagnetic architecture maps to a unique tiling of diamonds. Counting the number of antiferromagnetic architectures thus corresponds to counting diamond tilings, a partition problem of considerable interest in statistical and condensed matter physics[36].

Solutions to this problem yield the number of antiferromagnetic architectures, Ω_{AF}, as a function of the number of edge nodes N. The number of *hexagonal* diamond tilings Ω_{AF} with n diamonds along each hexagon side (e.g. Fig. 2.10c for $n = 2$) can be calculated exactly[37] to be

$$\Omega_{AF} = 2\prod_{i=1}^{n}\prod_{j=1}^{n}\prod_{k=1}^{n}\frac{i+j+k-1}{i+j+k-2}, \tag{2.5}$$

which approaches an exponential function in the thermodynamic limit[38] (Fig. 2.10d):

$$\Omega_{AF} \sim e^{\log(3^{1/2}/2^{2/3})N} \approx e^{0.087N} = e^{0.131T} \approx 1.1^{T}\ , \tag{2.6}$$

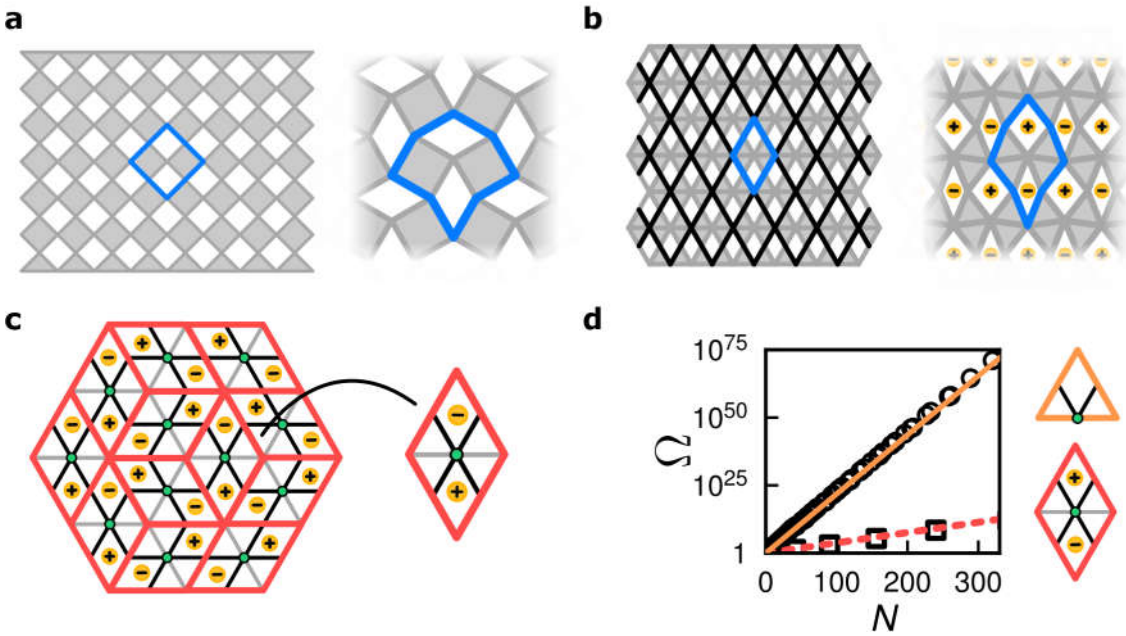

Fig. 2.10.: Counting antiferromagnetic compatible architectures. **a** The rotating square mechanism of rigid squares connected by freely pivoting hinges at rest (left) and deformed (right). The unit cell is highlighted (blue). **a**, Left: the rotating square mechanism is emulated by an ordered compatible stack. Rigid squares are marked in grey. Right: the deformed structure (internal bonds not highlighted). Each building block interacts antiferromagnetically with its neighbours: they have opposite block spin (yellow markers). **c**, All antiferromagnetic designs can be regarded as tilings of diamond-shaped elements (right, red outline) containing two building blocks. The block's minority nodes (green) sit on their shared edge. The blocks deform antiferromagnetically and have opposite block spin. Tiling these diamonds produces hexagonal antiferromagnetic compatible stacks (left). **d**, The number of antiferromagnetic designs Ω (open squares, red dashed line) corresponds to the number of ways diamonds tile a hexagon. It can be counted exactly in the limit of large systems with many edge nodes N (Eq. 2.6). For comparison, the total number of compatible designs (open circles, orange line) is shown.

where $N = 3n(3n+1)$ is the number of edge nodes, and T is the number of building blocks such that $N = 3T/2$ in the thermodynamic limit.

We now compare the number of antiferromagnetic compatible designs Ω_{AF} to the total number of compatible designs, Ω_0. While Ω_{AF} counts hexagonal systems and Ω_0 parallelogram systems, we expect boundary effects due to the material's shape to be negligible in the limit of large system sizes. We may therefore compare the two cardinalities directly at large N. From Eqs. 2.2 and 2.6, we find that $\Omega_0 \ll \Omega_{AF}$, so that in the thermodynamic limit a vanishing fraction of all compatible architectures has a purely antiferromagnetic interaction pattern (Fig. 2.10d).

2.4. Incompatible metamaterials

As compatible networks require that all local loops of internal bonds are of even length (Fig. 2.4b, top), frustration can be induced by violating this condition. Simply put, we may introduce local loops with an odd number of internal bonds, or *odd local loops*

to design targeted frustration (Fig. 2.4b, bottom). Thus, while we can make a large variety of compatible metamaterials, an even larger amount of frustrated designs exist that cannot deform harmoniously due to the presence of one or more odd local loops. The mechanical frustration induced by such defects generally produces undesired effects when their presence is not controlled, such as decay of a desired FM[29,39], or structural failure when frustration-induced bond stresses exceed the bond buckling threshold[40]. However, when frustration is introduced in a controlled and well-understood manner, it may be harnessed to design desirable or unusual physical properties, such as localized buckling zones[13,18,22], or geometric frustration in spin-ices[41–43]. In this section, we show how to introduce frustration in a targeted manner by discrete rotations of the building blocks, which changes the parity of local loops (section 2.4.1). We demonstrate that we can introduce two particular types of frustration, in the form of local, *structural* defects (section 2.4.2) and as global, *topological* defects (section 2.4.3).

2.4.1. Triangle rotations as fundamental architectural transformations

Different architectures are made by stacking together building blocks with different orientations. Therefore, a particular metamaterial design can be transformed into any other architecture by rotating a suitable sequence of building blocks. Supertriangle rotations, illustrated in Fig. 2.11, thus form the minimal architectural transformations that we employ to convert one metamaterial design to another.

Selecting and rotating a particular building block in the material's bulk affects local path parities. Effectively, the rotation removes one of the building block's internal bonds—bond r—from the network and replaces it with a newly added internal bond p (Fig. 2.11a). The bond r is part of up to two local loops: two in the bulk, and one or zero at the material's boundary, as shown in Fig. 2.11b-c. Therefore, exchanging bond r for bond p changes the parity of at most two local loops. This transformation method thus changes local bond connectivity, but preserves other network characteristics, such as the number of nodes and bonds, the node positions, and the bond constraint type.

Starting from a compatible structure containing only even local loops, we can thus obtain metamaterial architectures with isolated, frustrated odd local loops via a suitable sequence of building block rotations. We show below how to implement this strategy to obtain local, *structural* defects, as well as global *topological* defects.

2.4.2. A structural defect

We now show how to locally control frustration in our mechanical metamaterials by rotating a single building block in an initially compatible network.

Fig. 2.12a shows a compatible structure with no defects, where all superhexagons have even local loops (black lines). As discussed in section 2.3.1, all larger paths in a compatible structure enclosing multiple local loops are also even (Fig. 2.4c).

As discussed above, rotating a single building block effectively switches the position of one internal bond, changing the parity of two adjacent even local loops to create two adjacent odd local loops (Fig. 2b), as illustrated in Fig. 2.12a-b. All larger loops circumscribing the two odd local loops are unchanged and are thus still of even length. While

the odd local loops frustrate the metamaterial's floppy mode, larger loops around the network perimeter are still even, indicating only a local breakdown of compatibility.

We therefore call two adjacent odd local loops a *structural defect*: while the odd local loops frustrate the material's floppy mode, the defect can be removed by a single local transformation of the network- that is, rotating the block back.

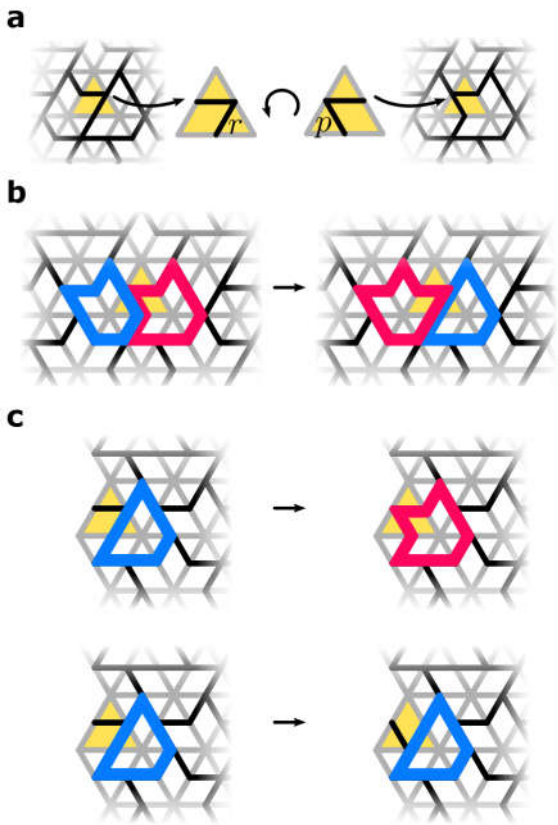

Fig. 2.11.: Supertriangle rotations transform one design to any other. **a**, Selecting and rotating a single building block in an architecture modifies its structure. Effectively, the rotation replaces internal bond r by internal bond p at a previously unoccupied location. **b**, Rotating a bulk building block changes local loop parities. The building block's internal bond r is part of exactly two local loops. Replacing bond r by p changes both loops' length by one, changing their parity from even to odd and vice versa. **c**, Rotating a boundary building block changes the parity of at most one local loop. Internal bonds of building blocks at the boundary of a stack contribute to either one or no local loops (top and bottom). Removing the internal bond by rotating a boundary block then changes the parity of one or no loops, respectively.

2.4.3. A topological defect

Evidently, we can induce *local* frustration in an initially compatible stack by rotating a single building block, generating a structural defect that consists of two adjacent odd local loops. However, we show now that controlled *global* frustration may also be obtained, by constructing metamaterials containing a single odd local loop.

We generate these globally frustrated metamaterials from an initially compatible system via a sequence of building block rotations running in a chain between the desired odd local loop locus and the system's boundary. Specifically, we rotate a building block at the edge of a structural defect, ensuring that the internal bond that is removed during the building block rotation contributes to one odd and one even local loop (Fig. 2.12b-c). As before, the rotation changes the parity of the two local loops. Consequently, the two odd local loops of the original structural defect are no longer adjacent after the transformation: they are now separated by a single even local loop (Fig. 2.12c). This defect configuration, consisting of two incompatible superhexagons separated by one or more compatible ones, can no longer be removed by a single, local building block rotation. To finally obtain a single odd local loop, we repeat the above procedure to displace one of the two odd local loops closer and closer to the system's boundary. Finally, we select a boundary building block that contributes to

exactly one odd local loop, so that its rotation causes that odd loop's parity to become even (Fig. 2.12d). One of the two odd local loops is thus 'annealed' out of the network via the boundary via a series of building block rotations—as an aside, it is therefore not possible to create single odd local loops in networks under periodic boundary conditions.

The procedure shown in Fig. 2.12a-d leaves us with an isolated odd local loop in the system's bulk, that can only be removed by an extensive number of building block rotations that involve the network boundary. In addition, all loops of internal bonds that circumscribe the isolated odd local loop are now of odd length. Thus, the parity of loops around the system's perimeter fundamentally differs in the presence of a single odd local loop. We therefore refer to the odd local loop as a *topological defect*[26,27] which affects the metamaterial at the global scale.

We note that, in contrast to defects occurring in metamaterials where the nontrivial topology results from a nonzero winding number in momentum space[17,18,44], here the topological character of defects is governed by the parity of real-space local loops.

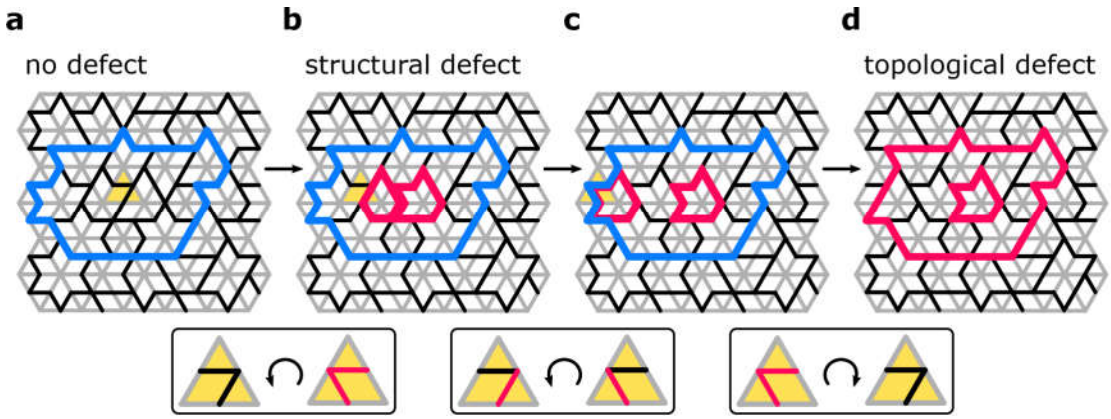

Fig. 2.12.: Generating frustration with a local or a global character. **a**, A compatible network design where all loops of internal bonds, such as the highlighted blue circuit, are of even length. **b**, Rotating a single building block (yellow triangle, inset) generates two adjacent odd local loops (red lines). These form a structural defect that frustrates the compatible motion of the material. Larger loops around the system boundary remain of even length. **c**, The adjacent odd local loops are moved apart by selecting and rotating another building block (yellow triangle, inset). The transformation generates two isolated odd local loops, separated by an even local loop. System boundary loops remain even. **d**, A final rotation removes one of the odd local loops from the material. A single topological defect remains. Its global character is felt at the system boundary: loops of internal bonds around the network edge now have odd length, signifying global frustration.

2.4.4. More odd local loops

Complex sequences of block rotations can produce more than only one or two odd local loops. Higher numbers of odd local loops can be classified to have a local or global character: in a network with an even number of odd local loops, internal bond loops around the system perimeter are of even length, showing a breakdown of compatibility that is locally confined to the material's bulk. Conversely, an odd number of odd local loops produces odd loops around the system perimeter, signifying global frustration that involves the system's edge. The parity of the number of odd local loops is therefore an

order parameter that signifies the local or global character of frustration in the network, as measured around the system's boundary.

2.5. Conclusions and outlook

Our work shows how sufficiently complex building blocks can be combined into an extensive number of compatible metamaterial designs. Such compatible metamaterials contain only closed loops of internal bonds with even length, which ensures the presence of a floppy, zero-energy deformation mode.

We include targeted, discretely controlled frustration and nontrivial topology in our metamaterials by introducing odd loops of internal bonds. Such odd loops signify frustration of the material's floppy mode: two adjacent odd local loops constitute a structural defect with a local character, while an isolated odd local loop constitutes a topological defect with a global character.

More generally, our strategy opens up a new avenue for studying topological, spatially complex states in artificial materials that are experimentally accessible[45]. In the following chapters, we accordingly study the mechanics of our complex mechanical metamaterials, focusing on the distinct mechanical signatures of structural and topological defects.

Acknowledgements

This work was performed in close collaboration with Martin van Hecke, Erdal Oğuz, and Yair Shokef. We thank Roni Ilan, Edan Lerner, Bela Mulder, Ben Pisanty, Eial Teomy and Ewold Verhagen for fruitful discussions, and Rivka Zandbergen for supplying the exact counting data in Fig. 2.6 and Fig. 2.10. This research was supported in part by the Israel Science Foundation Grant No. 968/16.

3. Topological defects produce exotic mechanics in complex metamaterials[1]

Abstract

We uncover the distinct mechanical signature of topological defects, introduced in chapter 2 via experiments and simulations, and leverage this to design complex metamaterials in which we can steer deformations and stresses towards different locations.

3.1. Introduction

Metamaterials' unusual mechanical properties arise from the geometry of their unit cells[7–10,15–22]. Many strategies exist to create metamaterials, on a spectrum of formality: from traditional and intuitive design[46] to computerized machine-learning strategies[47], topology optimization[48] and genetic algorithms[49]. While such automated techniques are valuable, a skilled operator is still needed to ensure that a suitable design can and will be found within a reasonable time. This is a classic bottleneck: reinventing the wheel (or a skyscraper) with modern techniques takes time and effort, and there are plenty of good design templates ready to go. In other words, innovative design is hard, and metamaterials are no exception.

There is therefore a need for conceptual work that helps formalize metamaterial design using simple, understandable design rules. Ideally, such design rules function as a guidebook, for example by prescribing how architectural elements should be combined to obtain desired stiffness or reconfigurability; or more indirectly, which mathematical rules the modelled system should obey[21,50]. Most seminal and ground-breaking work in this community has managed to do this by considering analogies between classical mechanics, and optical, acoustic or electronic systems[24,44,51].

In this chapter, we design metamaterials that harness mechanical frustration, analogously to geometric frustration in spin-ices. In the previous chapter, we discussed how to create stacked, compatible networks, and how to make these incompatible via local or topological defects. Evidently, defects frustrate the mechanical deformation of our metamaterials. We now explore the effect of these defects on the mechanical response of our metamaterials. We first present simple constitutive models and experimental realizations of in section 3.2. We then discuss the physical manifestations of (in)compatibility due to the presence of defects in section 3.3 and use this understanding to formulate a protocol to mechanically distinguish structural and topological defects. Finally, we harness the distinct mechanical response of topological defects to design localized deformation fields in larger networks in section 3.4. We discuss the impact of our work in section 3.5.

[1] The work presented in this chapter is based on Refs.[13] and [14].

3.2. Probing frustration: models and experiments

Studying the mechanics of our networks requires experiments and models. In this section, we discuss the construction of both.

Experimental realizations of our complex metamaterials are produced via selective laser sintering (section 3.2.1). In these experimental samples, stiff bars connected via soft living hinges (that is, thin and flexible filaments made of the same material as the bars) correspond to the bonds and nodes of the initial design. This design method produces macroscopic, malleable structures that can be actuated by hand. In order to gain a deeper understanding of our experimental results, we describe two minimal models that relate forces and displacements, which work on the network's connecting nodes, to elongations and tensions of its bonds. We first treat a mechanical model consisting of Hookean springs connected by freely hinging nodes (model FH, section 3.2.2), and then decorate this model with a torsional hinge stiffness (models TR and LTR, section 3.2.3), as illustrated schematically in Fig. 3.3a. We expect this latter model to correspond more closely to the actual behaviour of our experimental samples, whose living hinges have a finite stiffness. We compare the experimental and modelled sample's behaviours in section 3.2.4.

3.2.1. Experimental realizations

3D-printed versions of our complex mechanical metamaterials realize the network's bonds by thick elastic beams and its hinges by thin joints. We discuss their fabrication and probing strategy, as well as error estimates during deformation measurements, below.

Printing process

As illustrated in Fig. 3.1, experimental realizations of our complex metamaterials are produced using a Sinterit Lisa 3D printer with thermoplastic polyurethane powder Sinterit Flexa Black, processed at a sintering layer height of 0.1 mm at the "softer" setting[52,53]. The reported Young's modulus of the base material printed at these specifications is 4 ± 0.5 MPa, and the final printed networks have a height of 5 ± 0.2 mm. The individual bars of the network are realized as thick beams, connected by thin beams—functioning as living hinges—at each joining node, which is marked in contrasting white (Fig. 3.1a,b).

The final printed networks have a height of 5 ± 0.2 mm, a length of 107 ± 2 mm. Each bar has a length of 10 ± 0.2 mm, and the narrowest part of the connecting hinges has a length 0.5 ± 0.2 mm and width 0.7 ± 0.2 mm. An impression of the printed samples, including overall dimensions and sizes of the constituent parts, is shown in Fig. 3.1c-d.

Sample deformation measurements

To quantify the deformation of our experimental samples, we track the positions of their nodes. High-resolution images of the sample under various external probing conditions are obtained using a Canon EOS 750D camera, by placing the network on a horizontal surface at a constant position of approximately 30 mm from the camera body. The 6000-by-4000-pixel images are analysed using a custom program created using the Python 3

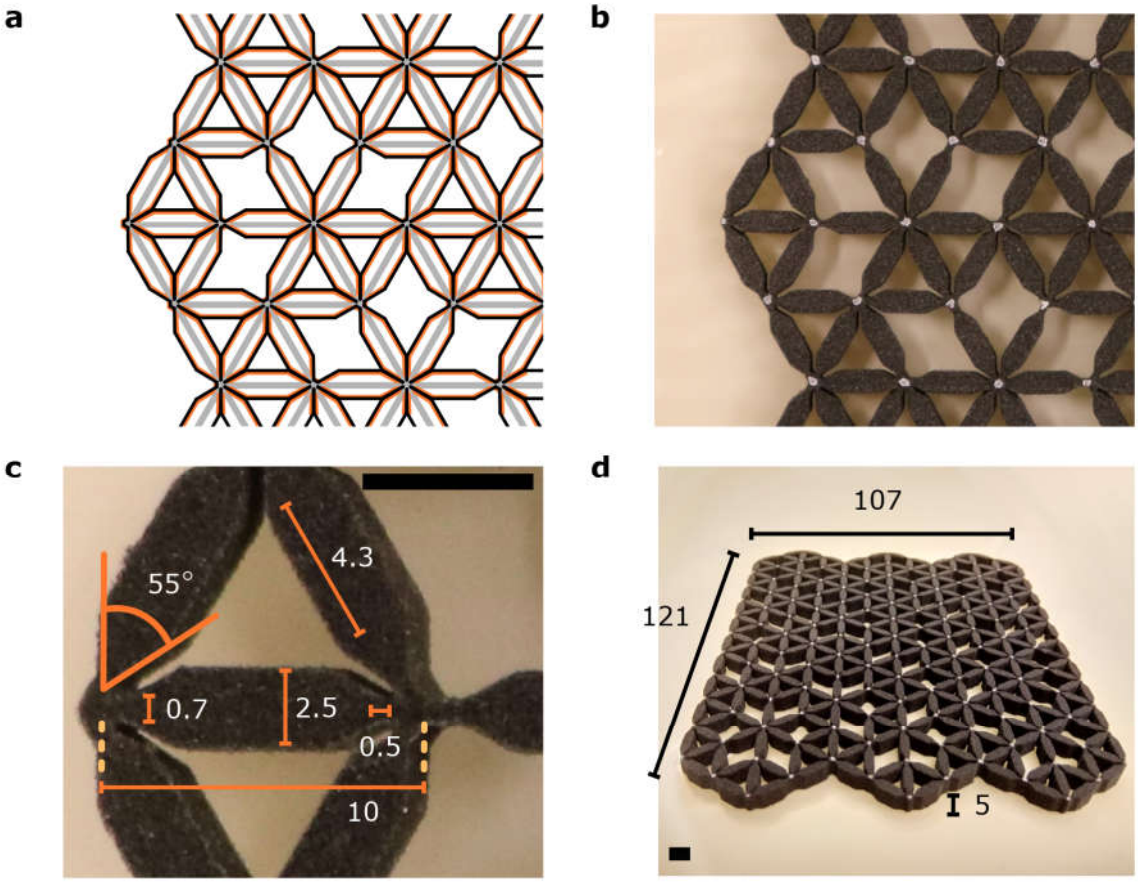

Fig. 3.1.: Fabrication of experimental samples. a, A section of the original network design is shown (grey lines). The network design is converted to an outline (black lines) suitable for fabrication with a Sinterit LISA 3D printer. The final printed sample has smaller dimensions (approximated by orange lines) due to resolution limitations. **b,** A section of the printed specimen, created by laser-sintering powdered thermoplastic polyurethane FlexaBlack, is shown. The network's bonds are realized as thick bars tapering to thin hinges that meet at a node. Nodes are manually marked with white dots after printing. Scale bar: 5mm. **c,** Dimensions of the sample's constituent parts are indicated in millimetres unless noted otherwise. An error of 0.2mm and 5° is estimated for lengths and angles respectively. **d,** A rectangular sample of 6 rows and 11 columns of building blocks and its overall dimensions in mm. Scale bar: 5mm.

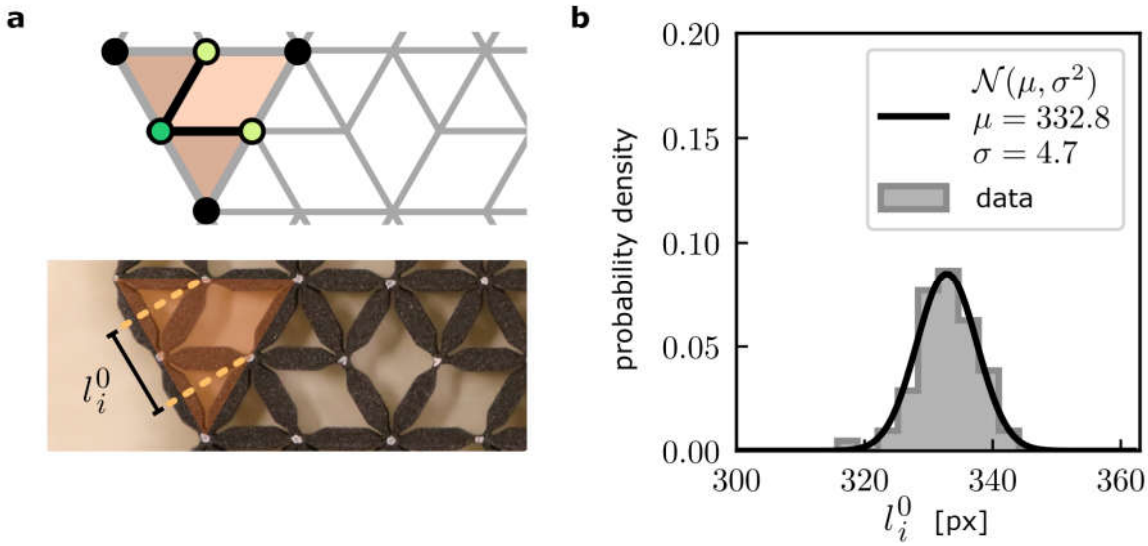

Fig. 3.2.: Deformation measurement error estimates. a) A section of a metamaterial design and its corresponded printed sample. The network's building blocks (one highlighted in orange) are characterized by a block rest length l_i^0, corresponding to the separation distance of the blocks' majority edge-nodes (top, light green circles). **b** The initial block rest lengths l_i^0 in the sample, measured in pixels by imaging and tracking the network's nodes, are normally distributed (grey area) with a mean μ and standard deviation σ (black line). Assuming the distribution's mean corresponds to the designed bar length of 10 mm, an imaging resolution of 33.3 px/mm and a standard deviation 0.15 mm on length measurements are obtained.

scripting language. Since the material's nodes are marked in a contrasting colour, the node positions of the network at rest and under various deformation conditions may be obtained from the images, and subsequently used to calculate node displacements and changes in node separation distance.

Error estimates

Length measurements in images of the samples are sensitive to errors, which we estimate as follows. Fig. 3.2a illustrates how initial block lengths l_i^0, or separation distance of each network block's majority edge-nodes, may be measured. Fig. 3.2b shows a typical distribution of initial block lengths l_i^0 in units of image pixels. The data shown were obtained for a representative sample of the size shown in Fig. 3.1d. The probability density estimate of initial block lengths is normal to good approximation, $\mathcal{N}(\mu, \sigma^2)$, with a mean $\mu = 332.8$ px and standard deviation $\sigma = 4.7$ px. We take the distribution's mean value to be equal to the designed node spacing of 10 mm to obtain an image resolution of 33 px/mm and a corresponding standard deviation $\Delta l = 0.15$mm, or approximately 5 image pixels. For simplicity, we assume that all errors are uncorrelated, which may lead to an underestimation of the measurement uncertainty.

3.2.2. Model FH: freely hinging spring network

To model the mechanical response of a complex network of stiff bonds and soft hinges, we may to treat its bonds as Hookean springs connected by freely hinging nodes. As

discussed by Pellegrino[54], the network's response to manipulation in the linear regime of small displacements can then be calculated straightforwardly. We describe the calculation method below, obtaining two sets of matrix equations that relate a network's nodal displacements and forces to its bond elongations and tensions.

In *model FH*, we capture the linear response of our systems based on networks of Hookean springs connected by freely hinging nodes[55], such that each bond contributes a potential stretching energy $\epsilon_s = \frac{k_s}{2}e^2$, where k_s is the bond's stiffness and e the elongation from its equilibrium length.

As shown in Fig. 3.3b, each node i supplies two degrees of freedom via spatial displacements $u_{x,i}$ and $u_{y,i}$, while a bond of length l^0 between two nodes at locations $\mathbf{r}_i$ and $\mathbf{r}_j$ constrains these motions by resisting linearized bond elongation $e_{ij} = \frac{\mathbf{r}_i - \mathbf{r}_j}{|\mathbf{r}_i - \mathbf{r}_j|} \cdot (\mathbf{u}_i - \mathbf{u}_j)$. For a large network, the vector of bond elongations $\mathbf{e} = (...e_{ij}...)$ is related to the vector of nodal displacements $\mathbf{u} = (...u_{x,i}, u_{y,i}...u_{x,j}, u_{y,j}...)$ via a compatibility matrix $\mathbf{R}$ so that $\mathbf{e} = \mathbf{R}\mathbf{u}$. Each row of $\mathbf{R}$ relates the displacements of two nodes to the elongation of their connecting bond. Bond elongations result in bond tensions τ_{ij}, which we will also refer to as *stresses*, via a constitutive equation: $\tau = \mathbf{K}\mathbf{e}$, where $\mathbf{K}$ is a diagonal matrix of bond stiffnesses that we set equal to the identity. Tensions are in turn converted to nodal loads $\boldsymbol{f} = (...f_i^x, f_i^y...f_j^x, f_j^y...)$ via $\mathbf{f} = \mathbf{R}^T\tau$. The collective displacements, elongations, tensions and forces fully characterize the network's mechanics.

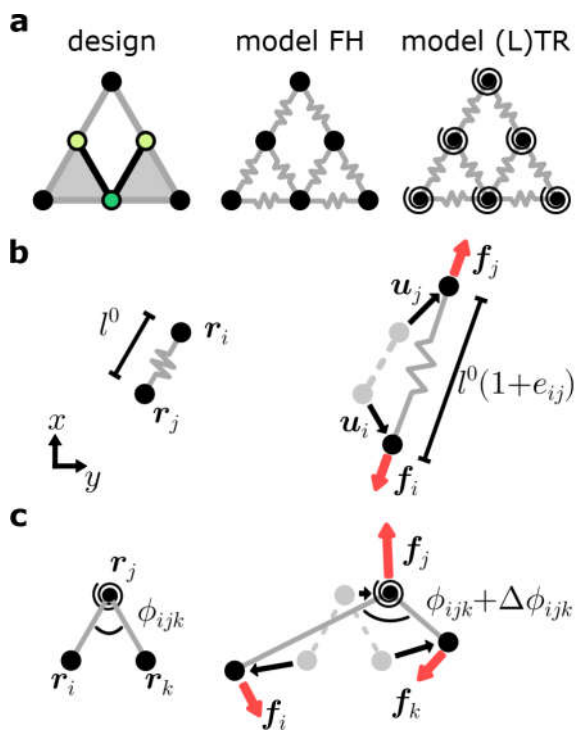

Fig. 3.3.: Modelling triangular building blocks. a, The building block design (left) corresponds to a network of freely hinging Hookean springs in model FH (middle) and is augmented with harmonic torsional hinges in models TR and LTR (right). **b,** Hookean spring mechanics. Left: two freely hinging nodes i, j, at initial positions $\boldsymbol{r}_i, \boldsymbol{r}_j$, and their connecting Hookean spring with rest length l^0 are shown in the x, y-plane. Right: the nodes undergo displacements $\boldsymbol{u}_i, \boldsymbol{u}_j$ as their degrees of freedom, elongating the spring by a dimensionless strain e_{ij} and producing a tension in the bond. The nodes undergo external loads $\boldsymbol{f}_i, \boldsymbol{f}_j$. **c,** Torsional hinge mechanics. Left: three nodes i, j, k and their connecting torsional hinge at node j with rest angle ϕ_{ijk} are shown. Right: displacing the nodes produces an angular strain $\Delta\phi_{ijk}$ and results in a torque on the hinge. The nodes undergo external loads $\boldsymbol{f}_i, \boldsymbol{f}_j, \boldsymbol{f}_k$ in response.

To actuate the network, we generally displace selected nodes by small amounts, while the remaining nodes are free to move. To calculate the resulting mechanical response, we use the following three-step approach. First, we calculate node forces $\mathbf{f}$ resulting from imposing an initial displacement $\mathbf{u} = \sum_i \mathbf{u}_i$, where $\mathbf{u}_i = (0...u_i^x, u_i^y, ...0)$ are desired individual node displacements. Second, we determine how the network relaxes

to mechanical equilibrium so that node forces vanish except along the forcing directions: an appropriate compensating force is obtained via $\mathbf{f}_p = \mathbf{f} - \mathbf{N}_p\mathbf{N}_p^T\mathbf{f}$, where $\mathbf{N}_p$ is the matrix with forcing directions $\hat{\mathbf{n}}_i = (0...n_i^x, n_i^y, ...0)$ as its columns. The corresponding relaxation displacement $\mathbf{u}_p$ is then calculated from the compensating force $\mathbf{f}_p$ and the reduced compatibility matrix $\mathbf{R}_p = \mathbf{R} - \mathbf{R}\mathbf{N}_p\mathbf{N}_p^T$. Lastly, the final displacement state of the network is given by $\mathbf{u}_{\text{full}} = \mathbf{u} + \mathbf{u}_p$, and the matching bond elongations, tensions and node forces can be obtained from this displacement state. The resulting network response, valid in the regime of small deformations, is compatible with both the imposed node displacement and the conditions of mechanical equilibrium.

Note that the compatibility matrix is not generally invertible. Therefore, calculating the network's response to imposed forces as above needs to be done via a well-defined procedure[54] using the singular value decomposition and pseudoinverse of $\mathbf{R}^T = \mathbf{U}\mathbf{D}\mathbf{W}^{\mathbf{T}}$. Here, $\mathbf{U}$ and $\mathbf{W}$ are orthonormal matrices with the respective left and right singular vectors of $\mathbf{R}^T$ as their columns,while $\mathbf{D}$ contains the singular values of $\mathbf{R}^T$ on the diagonal. Partitioning $\mathbf{U} = [\mathbf{U_r}\ \mathbf{U_{ZM}}]$ into the vectors spanning the column space and ZM of $\mathbf{R}^T$, and $\mathbf{W} = [\mathbf{W_r}\ \mathbf{W_{SS}}]$ into the vectors spanning the row space and SSS, and partitioning $\mathbf{D} = \left[\begin{smallmatrix} \mathbf{D_r} & \mathbb{O} \\ \mathbb{O} & \mathbb{O} \end{smallmatrix}\right]$ so that $\mathbf{D_r}$ is a square diagonal matrix of ordered (from big to small) nonzero singular values, we can write:

$$\begin{aligned} \boldsymbol{\tau} &= \mathbf{W_r}{\mathbf{D_r}}^{-1}{\mathbf{U_r}}^T\boldsymbol{f} \\ \boldsymbol{e} &= \mathbf{K}^{-1}\boldsymbol{\tau} \\ \boldsymbol{u} &= \mathbf{U_r}{\mathbf{D_r}}^{-1}{\mathbf{W_r}}^T + \mathbf{U_{ZM}}\boldsymbol{y} \end{aligned} \quad , \tag{3.1}$$

where the last term indicates that zero-energy node displacements—or floppy modes—that may be added freely to the displacement, proportional to the indeterminate vector $\boldsymbol{y}$. There are two additional constraints that need to be satisfied: first, we must ensure that the imposed load leads to a determinate response and so does not overlap with any ZM via the requirement ${\mathbf{U_{ZM}}}^T\boldsymbol{f} = \mathbf{0}$. In addition, the bond elongations must be compatible with the network's geometry, requiring ${\mathbf{W_{SS}}}^T\boldsymbol{e} = \mathbf{0}$. Together, once the compatibility and stiffness matrices $\mathbf{R}$ and $\mathbf{K}$ are known, the equations in Eq. 3.1 allow us to calculate the network's linear response under imposed forces.

3.2.3. Model TR and LTR: torsionally rigid hinges

In our experimental metamaterials, constituent beams act as Hookean springs with fair accuracy, but hinges do cost energy to deform. We capture this hinging cost in *model TR*, in which bonds are modelled by Hookean springs as in model FH, but an energy contribution $\epsilon_h = \frac{k_h}{2}\Delta\phi^2$ is added. Here, k_h is a torsional hinge rigidity and $\Delta\phi$ is the deviation of the angle between two neighbouring bonds from its equilibrium value. Hence, the total potential energy of a modelled network is $\epsilon = \sum_b \epsilon_s + \sum_\alpha \epsilon_h$, where the first sum runs over all bonds, and the second sum over all angles between neighbouring pairs of bonds. In this model, the dimensionless stiffness ratio $\tilde{k} = k_s(l^0)^2/k_h$ thus sets the relative resistance of bond stretching versus hinge opening.

To obtain a network's configuration under actuation, we use a standard simulated annealing algorithm, to minimize its total potential energy by probabilistically updating the spatial coordinates of a randomly chosen node at each step, with Metropolis dynamics

and a dimensionless pseudotemperature decreasing gradually to zero over $50 \cdot 10^6$ steps. Model TR and simulations were devised and executed by Erdal C. Oğuz.

Model TR allows us to simulate nonlinear displacements of the metamaterial's nodes, but is computationally costly. As a less intensive alternative, the linear response of a mechanical network of Hookean springs connected by harmonic torsional hinges, which we shall call *model LTR*, can be modelled analogously to model FH.

The additional torsional constraints are included as shown in Fig. 3.3c. In the metamaterial, we consider each clockwise-ordered triplet of nodes i, j, k at locations $\mathbf{r}_i, \mathbf{r}_j, \mathbf{r}_k$. Two bonds connect nodes i and k to central node j; a harmonic torsional spring at the central node resists changes in the initial rest angle. Each node i supplies two degrees of freedom via spatial displacements $u_{x,i}$ and $u_{y,i}$, while a torsional spring between the three nodes constrains these motions by resisting linearized rest angle deviation, or angular strain, $\Delta\phi_{ijk} = (\frac{\mathbf{r}_i - \mathbf{r}_j}{|\mathbf{r}_i - \mathbf{r}_j|^2} \times (\mathbf{u}_j - \mathbf{u}_i) + \frac{\mathbf{r}_k - \mathbf{r}_j}{|\mathbf{r}_k - \mathbf{r}_j|^2} \times (\mathbf{u}_j - \mathbf{u}_k)) \cdot \hat{\boldsymbol{z}}$ with a torsional hinge rigidity k_h. Angular changes thus result in torsional tensions τ_{ijk} via a constitutive equation $\tau_{ij} = k_h \Delta\phi_{ijk}$.

The compatibility matrix $\mathbf{R}$ of the network is then constructed as for model FH, described in section 3.2.2, but the matrix is augmented with an additional row for each torsional spring. Each extra row relates the displacements of a node triplet to the angular change between their two connecting bonds. Similarly, a suitable stiffness matrix $\mathbf{K}$ for the entire network is found as for model FH. We create a diagonal matrix $\mathbf{K} = \begin{bmatrix} \mathbb{1} & \mathbb{O} \\ \mathbb{O} & \mathbf{k_h/k_s} \end{bmatrix}$, where the first block of diagonal entries correspond to axial stiffnesses which we set to unity as before, and the second block of diagonal entries correspond to relative torsional stiffnesses k_h/k_s. The stiffness matrix thus encodes the relative importance of the bonds' axial stiffness and the hinges' torsional stiffness.

The compatibility and stiffness matrices govern the mechanical behaviour of the network. Analogously to the strategies outlined in section 3.2.2, we can then calculate the collective displacements, elongations and angular changes, (angular) tensions, and forces in the network.

3.2.4. Comparing experiments and models

The 3D-printing process described in section 3.2.1 produces soft networks that are easily manipulated. How well these samples mimic the idealized mechanics of our simple geometric networks depends, among other things, on how well the floppy mode of the initial design (see chapter 2) is mimicked. A simple assessment shows that our samples reproduce the designed floppy modes qualitatively well, as we discuss here.

Our initial compatible network design and its floppy mode are shown in Fig. 3.4a-c. We investigate how well the printed network (Fig. 3.4d) reproduces the floppy mode by compressing it uniaxially (Fig. 3.4d). In this compression experiment, the network is placed between two parallel rigid blocks on its left and right sides and subsequently compressed by 3 mm, starting from a lateral dimension of 121 ± 2mm. By inspection, Fig. 3.4e-f show that the designed floppy mode is mimicked with reasonable accuracy.

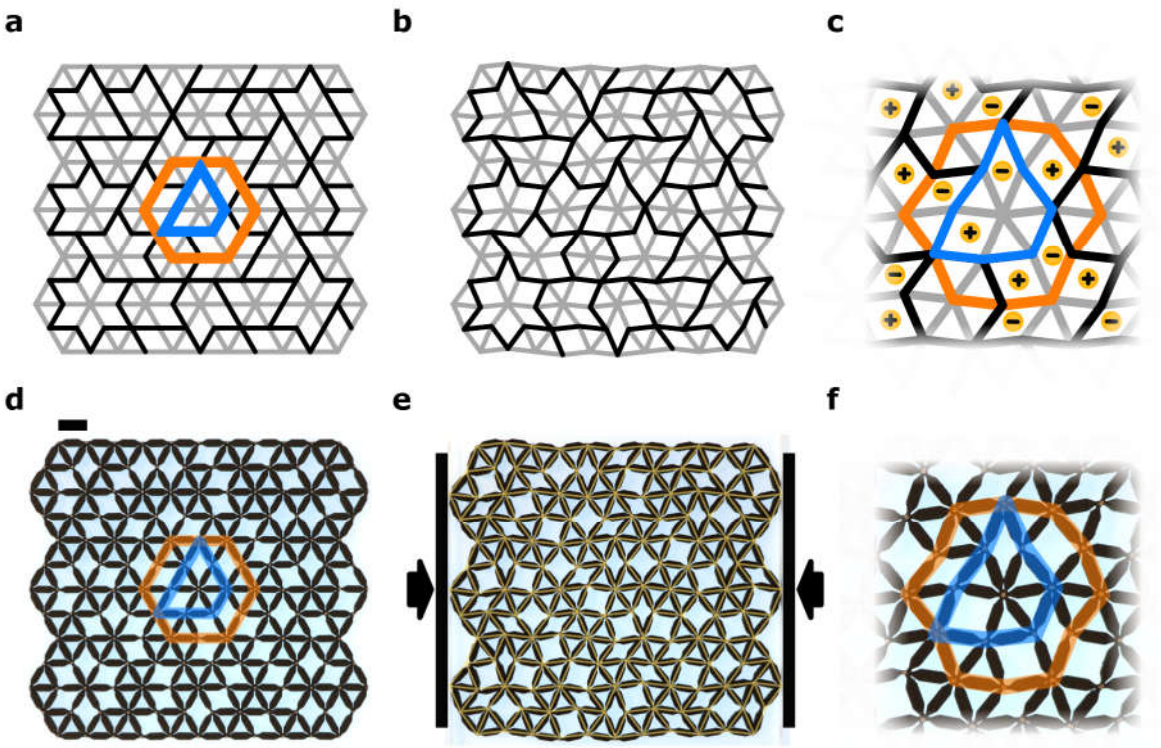

Fig. 3.4.: How printed samples deform compared to the designed floppy mode. **a,** An initial compatible network design is shown (edge and internal bonds shown as grey and black lines). A central hexagon (orange) and its even local loop (blue) are highlighted. **b,** The floppy mode of the network is visualized: this deformation mode does not change the length of any bonds. **c,** Zoom-in on the deformed central hexagon and its local loop. Positive and negative block spins corresponding to extension and contraction of the building blocks are indicated (yellow markers). **d,** Experimental realization of the design, 3D-printed as shown in Fig. 3.1. Scale bar: 10mm. **e,** The network is uniformly compressed by 3mm at its left and right edges (arrows). The network's designed floppy mode is superimposed (yellow lines). **f,** Zoom-in on the printed structure's central hexagon and local loop. Visual inspection shows a close match between the sample's deformation and the designed floppy mode.

The finite stiffness of the printed sample's hinges contributes to deviations from the designed floppy mode. This hinge stiffness, k_h, is included in models TR and LTR (see section 3.2.3), which crucially depend on the dimensionless *stiffness ratio*

$$\tilde{k} = k_s (l^0)^2 / k_h \ . \tag{3.2}$$

To accurately model our experimental findings, we estimate the order of magnitude of $\tilde{k}$ in our 3D printed networks by assuming all torsional and stretching deformations take place in the hinges, which have thickness t, length l, and width w and are made of a material with Poisson's ratio ν and Young's modulus E. To linear order, the bending and stretching stiffnesses of such a hinge are given by[56] $k_h = Et^3 w/[12(1-\nu^2)l]$ and $k_s = Etw/l$, resulting in a stiffness ratio $\tilde{k} = 12(1-\nu^2)l^{0\,2}/t^2$. Using the experimental values $l^0 = 10 \pm 0.2$ mm, $t = 0.7 \pm 0.2$ mm, and an experimentally estimated Poisson's ratio of $\nu = 0.43 \pm 0.03$ (see section 3.2.4 below), we estimate $\tilde{k} \approx 2000$ as our starting point. We refine this estimate later, in section 3.3.3, by matching the samples' experimentally measured and modelled properties directly.

Poisson ratio of flexible material

Experimental measurements of the FlexaBlack 3D-printed material's Poisson ratio were performed. The data were measured using an Instron 3336 series universal testing machine (UTM) managed with a Bluehill 2 software suite, outfitted with an Instron 2530-427 static load cell rated at 100N.

Three samples were printed according to the ISO-37 standard[57] for dumb-bell samples of type 1A. The gauge region of the samples was marked with contrasting white bars and measured to have a thickness 2.3 ± 0.05 mm, width $w = 5.3 \pm 0.05$ mm, and length $l = 20 \pm 0.3$ mm. Each sample was mounted in Instron 2710-series clamps and ensured to be at neutral load prior to testing. The sample was cycled four times from the neutral load position between -0.5 mm and 2.5 mm extension at a speed of 0.2 mm/s, while images of the sample at 3840 by 2748 pixels were recorded using a Basler acA3800 camera and lens of 75mm focal length. The camera was linked to the trigger output of the Instron UTM at a frequency of 1.33 Hz with custom-built recording software, to ensure that the recorded load data, extension data, and images were synchronized.

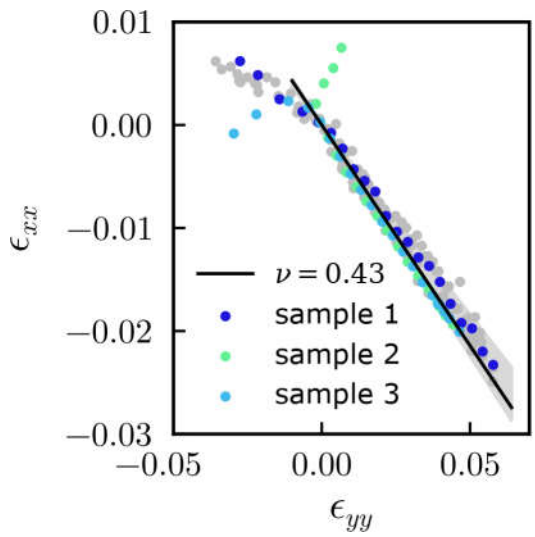

Fig. 3.5.: Poisson ratio of FlexaBlack 3D-printed material. Measurements of lateral and axial strain ϵ_{xx} and ϵ_{yy} of small samples of FlexaBlack material under a controlled extension applied by an Instron UTM. Three dumb-bell shaped samples compliant with ISO-37 type 1A (legend) were tested by extending and contracting them at least three times at a fixed speed; see text for details. The sample-averaged Poisson ratio $\nu = 0.43 \pm 0.03$ is indicated (black line). Additional measurements of sample 1 at lower and higher speeds were performed (grey circles). The minimal and maximal fitted Poisson ratios are indicated (grey area).

A custom Python program was used to extract the gauge section's length and width from the digital photographs using image thresholding. Data were averaged over the last three cycles. From these quantities, the engineering strain in lateral and axial directions were calculated via $\epsilon_{yy}(u) = l(u)/l(0)$, $\epsilon_{xx}(u) = w(u)/w(0)$ as a function of extension u. The measurement results are shown in Fig. 3.5.

An average Poisson ratio was obtained by fitting the relation between positive axial strain and lateral strain with a linear function for all three samples and averaging over the three measurements, as indicated in Fig. 3.5. The average Poisson ratio was found to be $\nu = 0.43 \pm 0.03$. Strain data for sample 1 were obtained additionally at testing speeds of $0.03, 0.02, 0.05, 0.1, 0.2$ and 0.5 mm/s and are indicated in grey in Fig. 3.5. The range of fitted Poisson ratios across all measurements are indicated by a light grey area.

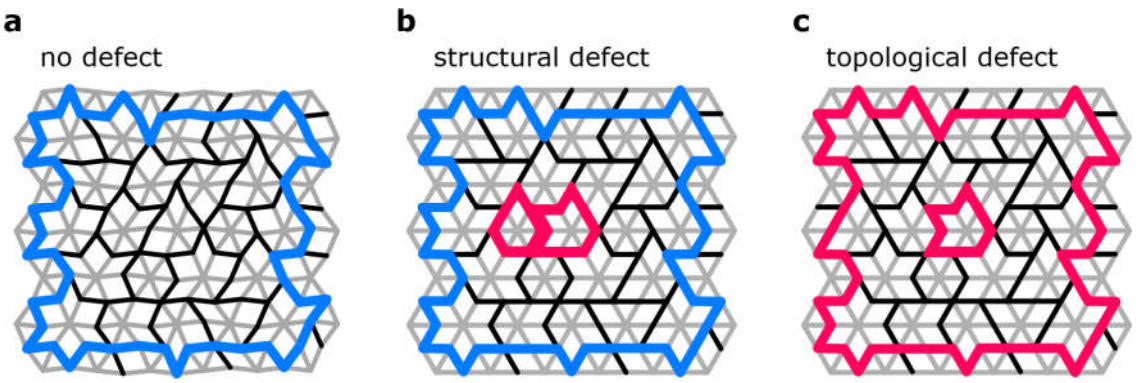

Fig. 3.6.: Networks with no defect, a structural defect, and a topological defect are structurally distinct. **a,** Compatible network design with no defect. Edge and internal bonds (grey and black lines) are shown. The network deforms according to its floppy mode as visualized. Internal bond loops around the system's boundary are of even length (blue lines). **b,** Frustrated network design with a structural defect, which blocks the floppy mode. Two local loops are of odd length (red lines). Loops around the system boundary remain of even length. **c,** Frustrated network design with a topological defect. One odd local loop is present. Loops around the system boundary are odd in length.

3.3. Mechanical signature of defects

We now turn our attention to the distinct mechanical response of metamaterials with structural, topological, or no defects. Our aim is to devise a mechanical measurement protocol that successfully distinguishes the presence of a defect as well as its character (structural or topological).

In chapter 2, we showed that the three network types have distinct architectures. There are two particular properties in which they differ. First of all, a compatible network has a system-spanning zero mode (Fig. 3.6a) that is absent in the presence of defects (Fig. 3.6b). Secondly, a topological defect is hallmarked by the fact that all loops around it contain an odd number of internal bonds, while loops around structural defects and compatible structures have an even perimeter (Fig. 3.6c). A testing protocol to distinguish the three network types should therefore measure the presence of a zero-energy deformation, as well as the parity of the loop of internal bonds running through blocks at the system's boundary.

We note that a mechanical implementation with infinitely rigid bars and perfectly flexible hinges has only zero and infinite energy deformations. This leads to a true floppy mode in the absence of defects, and a blocked system otherwise. In that case, structural and topological defects cannot be distinguished. However, once elastic deformations are allowed, such as in the experimental samples and models described in section 3.2, the mechanics becomes much richer and requires solving for mechanical equilibrium or performing direct measurements. It is precisely this mechanical richness that allows us to distinguish structural and topological defects.

In section 3.3.1, we introduce a testing protocol that uniquely distinguishes networks with a topological defect from those with no defect or a structural one, by merely probing the system's boundary. The results of this detection method are discussed in sections 3.3.2

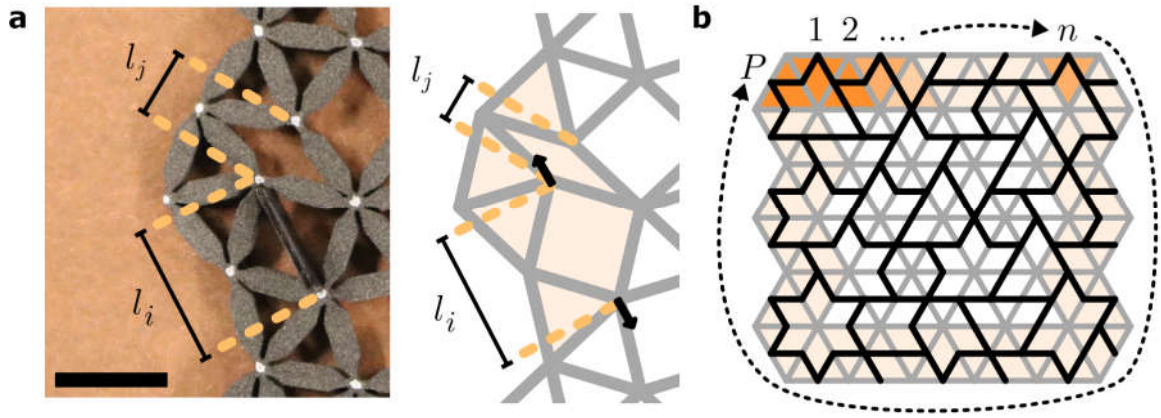

Fig. 3.7.: Probing the perimeter of a metamaterial. a, Left: a building block is extended experimentally by inserting a wedge, displacing its majority edge-nodes to a spacing l_i. The deformation of neighbouring block j is measured by the majority edge-node spacing l_j. Scale bar: 1 cm. Right: modelled extension is achieved by displacing the block's majority edge-nodes (arrows). **b,** For each pair of adjacent building blocks around the network's perimeter (dashed arrow), the extension of block j in response to the extension of block i is recorded consecutively. This results in pairwise measurements of block deformations l_i, l_j for all P block pairs $(1,2), ..., (n, n+1), ..., (P, 1)$.

and 3.3.4, where we demonstrate that the unique bulk character of a network is identifiable in experimental samples as well as computational models via simple mechanical experiments. Our results show that there is a binary order parameter, or *topological probe*, measured at the system's edge, which is negative if and only if a topological defect is present. The two bulk material phases—with and without a topological defect—thus exhibit a unique bulk-boundary correspondence and are topologically distinct.

3.3.1. Detection protocol: measuring the boundary

Metamaterials with structural, topological, or no defects have distinct architectures and concomitant mechanical signatures. We detect (topological) defects in elastic metamaterials by considering pairs of building blocks at the system's boundary, deforming one building block and tracking the deformation of the other.

The basic idea is illustrated in 3.7a. Specifically, we extend a block i by forcing its majority nodes from a rest separation l^0 to a distance $l^0(1+\delta_i)$, measure the resulting deformation δ_j of neighbouring block j, and define a deformation *transfer factor*

$$q_{ij} = \delta_j / \delta_i \tag{3.3}$$

In a compatible metamaterial of freely hinging springs, $q_{ij} = \pm 1$, while incompatibilities or bending interactions cause $|q_{ij}| < 1$ due to elastic decay. Crucially, the sign of q_{ij} reflects the nature of the interactions between neighbouring blocks i and j, being antiferromagnetic (ferromagnetic) if $q_{ij} < 0$ ($q_{ij} > 0$). We separately measure the transfer factors between all neighbouring pairs of the P blocks around the network's perimeter;

define a *cumulative transfer product*

$$q_n := \prod_{i=1}^{n} q_{i,i+1} \tag{3.4}$$

that relates block 1 to block $n+1$; and introduce a normalized *topological probe*

$$Q := sign(q_P) \cdot |q_P|^{1/P} \tag{3.5}$$

that characterizes the full perimeter.

By definition, the magnitude and sign of the topological probe Q distinguish metamaterials with structural, topological, or no defects. In particular, the sign of Q precisely measures the parity of the closed loop of internal bonds around the boundary, being positive for a structural defect and negative for a topological defect. Note here that networks with an odd (even) number of odd local loops yield a negative (positive) Q. For a compatible system, deformations follow the global floppy mode, all building blocks deform with nearly equal magnitude and, since any loop around the system boundary is even, $Q \lessapprox 1$. An incompatible network has no global floppy mode, hence deformations decay more strongly away from the actuation point so that $|q_{ij}| < 1$ and $|Q| < 1$; crucially, the sign of Q should not be sensitive to this decay. A single structural and a single topological defect may thus be distinguished by the sign of Q, which gives the net topological charge enclosed by the system boundary.

3.3.2. Probing the entire boundary

We demonstrate the efficacy of our topological detection protocol in this section. We perform the detection protocol outlined above on three network designs, one compatible, one with a local defect, and one with a topological defect, using the design shown in Fig. 3.6a-c. The protocol is executed on experimental samples, as well as in models FH and (L)TR. An overview of the detection results is shown in Fig. 3.8, which figure we discuss below.

Fig. 3.8a indicates all edge blocks that are probed (orange triangles) from 1 to P. In the experimental samples, we actuate each edge block i by inserting a stiff wedge between its majority edge-nodes (recall Fig. 3.7a), separating them from an initial distance of 10 ± 0.2mm to 13.4 ± 0.2mm to obtain a block strain $\delta_i = 0.34 \pm 0.03$. In model TR, edge blocks are actuated by forcing their majority edge-nodes to separate to a block strain $\delta_i = 0.23$. A stiffness ratio $\tilde{k} = 3200$ is used to match experimental and modelled results (see section 3.3.3). For the topological detection scheme in the linear models FH and LTR, the results are independent of the imposed block strain to leading order. The node positions of the deformed sample in experiments as well as models are used to calculate the displacement of each node, after subtracting rigid-body translations and rotations. From this data we extract the initial and final lengths $l_{i,0}$ and l_i of the distances between the majority edge-nodes of each building block to determine the block strains $\delta_i = l_i/l_{i,0} - 1$. The resulting output block strains δ_j, transfer factors q_{ij}, cumulative transfer product q_n, and topological probe $Q(P)$ are calculated following Eqs. 3.3- 3.5.

Fig. 3.8b shows the cumulative transfer product, q_n, as a function of the number of

probed edge blocks n. Data are shown for networks with no defect (ND, top); a structural defect (SD, middle); and a topological defect (TD, bottom). Markers distinguish experimental and modelled results (legend). The numerical hinge model (L)TR and the experimental results show an overall excellent agreement, indicating that the behaviour of our networks is successfully captured by a simple network model of interconnected Hookean and torsional springs.

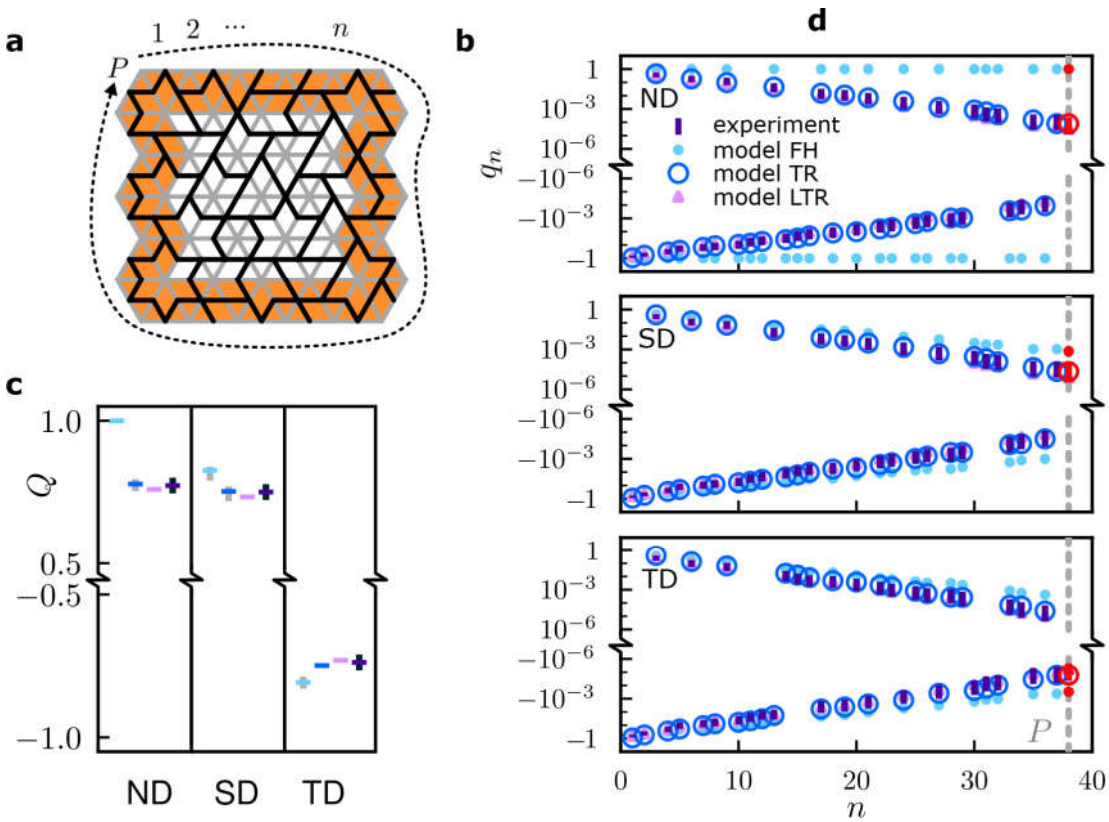

Fig. 3.8.: Defects are successfully distinguished by probing in a loop around the boundary. a, All boundary blocks (orange triangles) of a metamaterial are actuated consecutively (dashed arrow). With the protocol shown in Fig. 3.7, we track the response of each building block to actuation of its neighbour. **b,** The cumulative response of building block pairs around the system boundary is captured in the cumulative transfer factor q_n (Eq. 3.4). q_n is shown for structures with no defect (ND, top), a structural defect (SD, middle), and a topological defect (TD, bottom). Experimental and numerical data for identical network designs of each type are shown (legend). While the sign of q_n fluctuates rapidly in experiments, these trends are reproduced correctly in all models. The magnitude of q_n is successfully captured by models TR and LTR. The experimental data appear linear on a log-linear scale, implying an exponential decay of the deformation field across the material's building blocks under local actuation. **c,** The overall response of the network is summarized by the topological probe Q (Eq. 3.5), which is shown for the three network types (ND, SD, TD) in both experiments and models (legend). While the magnitude of Q depends on the details of each model, the sign of Q is negative if and only if a topological defect is present.

For all three network types, q_n shows an exponential decay with the exception of the compatible structure simulated with model FH. Recall that model FH corresponds to an idealized metamaterial in the small-displacement regime, consisting of Hookean springs connected by freely hinging nodes. For a system with no defect, deformations in model

FH thus follow the structure's global floppy mode, all building blocks deform with equal magnitude and, since any loop around the system boundary is even, $|q_n| = 1$. y contrast, since the experimental samples and model (L)TR have a nonzero hinge stiffness, they do not have a zero-energy floppy mode: even for a compatible network design, the sample's deformations decay away from the point of actuation. Thus, $|q_n| < 1$ due to elastic decay that stems from finite torsional resistance of the hinges[29]. Note that an incompatible network, which has either a structural or topological defect, has no global floppy mode. Hence, deformations decay away from the actuation point so that $|q_n| < 1$ for all incompatible structures, regardless of their experimental or modelled details.

Crucially, the sign of q_n is not sensitive to such details. The data show that the sign of q_n can vary wildly with $n < P$, reflecting the mixed antiferromagnetic and ferromagnetic interactions in our designs (see section 2.3.1). However, the sign of q_n at $n = P$ precisely measures the parity of the closed loop of internal bonds around the boundary, being positive for a structural defect and negative for a topological defect (Fig. 3.8b, red markers). A single structural and a single topological defect can thus be distinguished by the sign of q_P, which gives the net topological charge enclosed by the system boundary.

Finally, Fig. 3.8c shows the collected experimental and numerical results for the topological probe Q. The topological probes calculated for experimental samples and models (L)TR are similar in magnitude and smaller than unity, which results from their inclusion of a finite hinge stiffness. By comparison, the values of Q for model FH are consistently larger in magnitude. These results indicate that elastic decay—whether from a finite hinging stiffness or the presence of defects—blurs the distinction between defect-free metamaterials and those with a single structural defect, as both have $0 < Q < 1$. Nevertheless, our method allows us to unambiguously detect topological defects, for which the topological probe is exclusively negative: $Q < 0$.

3.3.3. Hinge stiffness: the right value

Here, we refine our estimate of section 3.2.4 for the stiffness ratio $\tilde{k} \approx 2000$, which describes the stiffness ratio between hinge bending and bond stretching. We compute the topological probe Q for model TR at various values of $\tilde{k}$ for networks corresponding to the experimental sample designs and compare the resulting values of Q to their experimental counterparts. Fig. 3.9 shows that the best match is found at $\tilde{k} \approx 3200$, of the same order of magnitude as the initial estimate, and the updated stiffness ratio is therefore used for model TR in all results presented in this chapter.

3.3.4. Probing a few boundary blocks

The detection scheme of section 3.3.2, while robust, requires a multitude of measurements proportional to the length of the material's perimeter. This becomes prohibitive for large systems. We now show that the topological character of a metamaterial can also be detected by considering a much smaller number of edge block pairs.

Specifically, we choose a subset of B roughly equally-spaced boundary blocks, actuating each block by extending it to a block deformation of δ_i, and calculate the transfer factor

$q_{ij} = \delta_j/\delta_i$ for each block pair. In analogy to the full cumulative transfer product q_n and topological probe Q, we define a diluted cumulative transfer product

$$q_n^B := \prod_{i,j}^{n} q_{ij} \ , \tag{3.6}$$

and a diluted topological probe

$$Q(B) = sign(q_P^B) \cdot |q_B^P|^{1/P} \ . \tag{3.7}$$

We calculate these diluted measures for networks of all three bulk types, using experiments and models. The resulting data are shown in Fig. 3.10.

First, Fig. 3.10a shows an example where $B = 7$ boundary building blocks (blue triangles) are probed.

The corresponding cumulative transfer product q_n^B is shown in Fig. 3.10b. Three sets of data, corresponding to $B = 38, 7$, and $B = 4$ are shown (colours). Experiments and models are indicated with different markers (legend). The three network types are again represented: a material with no defect (ND, top), a structural defect (SD, middle), and one with a topological defect (TD, bottom) are indicated. Even though the data are more sparsely spaced when fewer building blocks are probed, the general trends of the cumulative product- fluctuations in sign as well as decay- reproduce well across all measurements. These findings again suggest an exponential decay of the deformation field across the material's building blocks under local actuation.

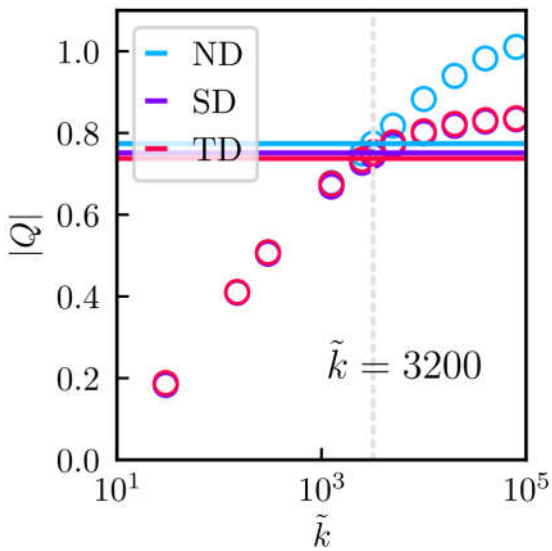

Fig. 3.9.: Comparing experiments and model TR, we select the right value for the modelled stiffness ratio $\tilde{k}$. The network response predicted by model TR yields a topological probe Q (see Eq. 3.5) that varies with the stiffness ratio $\tilde{k}$ between the bonds' axial stiffness and the nodes' hinging stiffness. Comparison of results from model TR (circles) and experiments (solid line) indicate that stiffness ratio $\tilde{k} \approx 3200$ (dashed line) yields the best match between experiment and model for networks with no defect (ND), and a good match for networks with a structural (SD) or topological (TD) defect.

Finally, in Fig. 3.10c, we show the diluted topological probe $Q(B)$ as a function of the fraction of boundary blocks that are probed, B/P. We find that the diluted topological probe $Q(B)$ has a sign that is independent, and a magnitude that is nearly independent, of the number of probed edge blocks, demonstrating the effectiveness of the diluted detection scheme for both experimental and model data. Hence, topological defects can practically and effectively be detected by probing a small fraction of the metamaterial's edge.

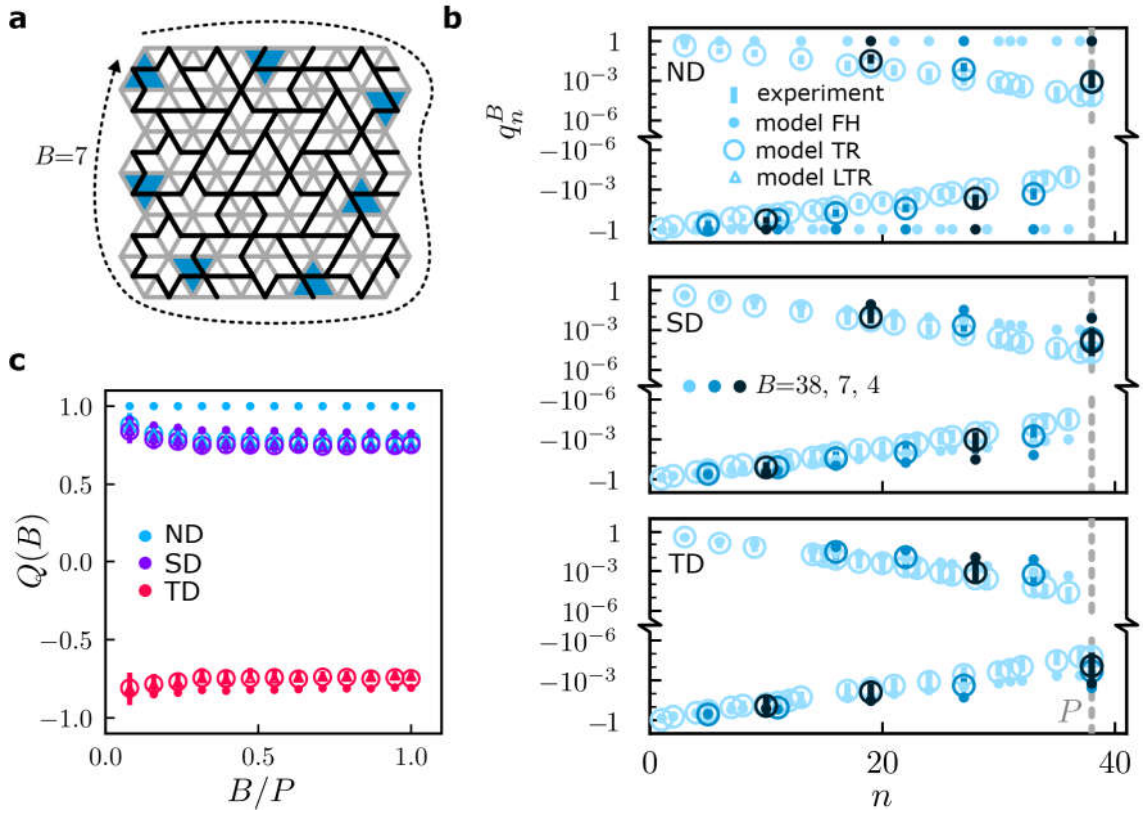

Fig. 3.10.: Defects are successfully distinguished, even with only a few measurements. a, B out of all P boundary blocks (blue triangles) of a metamaterial are actuated consecutively (dashed arrow). **b,** The cumulative response of building block pairs around the system boundary is captured by the diluted cumulative transfer factor q_n^B (Eq. 3.6). Structures with no defect (ND, top), a structural defect (SD, middle), and a topological defect (TD, bottom) were measured. Experimental and numerical data for identical network designs of each type are shown for various numbers of edge blocks B (legends). Experimental and modelled data show good agreement. The overlapping data for different values of B imply an exponential decay of the materials' deformation fields away from the probing point. **c,** The overall response of the network is summarized by the topological probe $Q(B)$ (Eq. 3.7), shown for the three network types (colours) in both experiments and models (legend). While the magnitude of Q depends weakly on the details of each model as well as the fraction of probed edge blocks B/P, the sign of Q is negative if and only if a topological defect is present.

3.3.5. Decay limits detection

The results in sections 3.3.2 and 3.3.4 show that the bulk character of a metamaterial can be detected robustly by probing the material's boundary. However, the detection results are affected by elastic decay.

Here, we explore how such decay influences the detection of defects. We show that the detection protocol is robust, as long as the elastic decay length for material deformations is larger than the spacing between the probed boundary blocks. The decay length is influenced by the stiffness ratio between hinge bending and bar stretching, as well as system size; however, the decay length stays above the unit cell spacing at all system sizes and at most stiffness ratios. These findings indicate that our detection protocol is robust across a broad range of metamaterial designs.

First, we note that the deformation field inside our metamaterials under local actuation appears to decay exponentially along the boundary. This finding is supported by the (diluted) cumulative transfer factors shown in Figs. 3.8b and 3.10b. There, q_n shows the ratio of block deformations away from the actuation point as a function of n, which corresponds roughly to the decay of material deformations as a function of distance. Using block strain as a measure of deformation, this means that a building block j at a distance d_{ij} from an actuated block i undergoes a block strain $\delta_j \approx \delta_i e^{-d_{ij}/d_Q}$, where δ_i is the strain on the actuated block and d_Q is the elastic decay length in units of the metamaterial's bond lengths, l^0. With this assumption for exponential decay, we find the following expression that relates the topological probe Q to the decay length:

$$d_Q \approx -\ln |Q|^{-1} \tag{3.8}$$

To check this expression, we note that the diluted topological probe $Q(B)^P \approx \pm e^{-\langle d_{ij}\rangle/d_Q}$ should decay exponentially with increasing average spacing between the probing points, $\langle d_{ij}\rangle$. Fig. 3.11a shows $Q(B)^P$ calculated for various values of the average block spacing $\langle d_{ij}\rangle$, the average distance between the geometric centres of consecutively actuated building blocks. Data shown were obtained for the three network types of Fig. 3.6 from experiments, model FH, and models (L)TR. The exponential relation $\pm e^{-\langle d_{ij}\rangle/d_Q}$ is overlaid on top of the measured data. The data suggest that d_Q is constant to fair approximation, supporting our assumption for exponential decay.

The exponential decay length d_Q is affected by two parameters: the stiffness ratio $\tilde{k}$ and the system size, which we explore now.

Fig. 3.11b shows the decay length d_Q as a function of the stiffness ratio $\tilde{k}$, where increasing $\tilde{k}$ corresponds to softer hinges and stiffer bars. The data shown were modelled using models TR and LTR for the three network types of Fig. 3.6. The data show three notable features. First, as $\tilde{k}$ increases and the hinges become softer, the decay length d_Q diverges in the absence of defects and saturates to a constant value when a defect (structural or topological) is present. The divergence of d_Q is due to the non-decaying floppy mode of compatible metamaterials with freely-hinging nodes, while the saturation of d_Q reflects a base level of geometric frustration in the presence of a defect. Secondly, there is a crossover stiffness ratio around $\tilde{k} \approx 1000$ at which the decay lengths for all three material types reach the same value. At this point, compatible and incompatible materials can no longer be distinguished by probing the boundary. This yields a practical

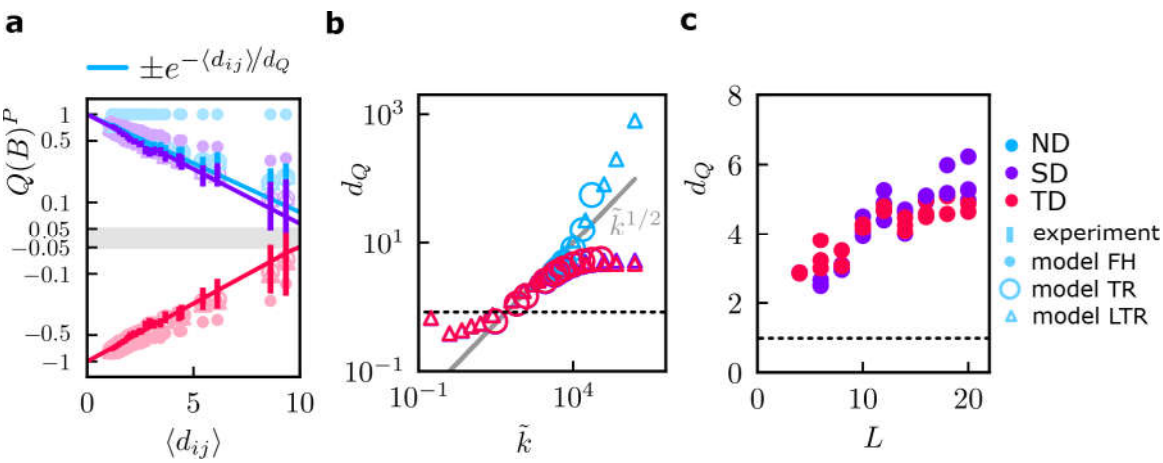

Fig. 3.11.: Elastic decay due to hinge stiffness and system size affects the topological probe Q. a, $Q(B)^P$ as a function of average block spacing $\langle d_{ij}\rangle$ for experiments, model FH, and model (L)TR (legend). The exponential trend $e^{-\langle d_{ij}\rangle/d_Q}$ confirms that d_Q (Eq. 3.8) is a fair measure of the elastic decay length of deformations around an actuated block. Data for one networks of each bulk type (ND, no defect; SD, structural defect; and TD, topological defect) are shown. **b,** Decay length d_Q varies with $\tilde{k}$, the stiffness ratio between spring and hinging stiffness. A low hinge stiffness, when $\tilde{k}$ is large, d_Q diverges for in the absence of defects: compatible and incompatible networks are easier to distinguish there. $\tilde{k}^{1/2}$ shown for reference[29]. **c,** d_Q increases with system size L. Results are shown for model FH, where $\tilde{k} \to \infty$.

rule of thumb for metamaterial design where defects should play a significant mechanical role: the stiffness ratio must then be larger than 1000. In our experimental samples, this corresponds to a maximal hinge thickness of approximately 1 mm (see section 3.2.4). Lastly, the decay length becomes smaller than the typical building block size, $d_Q < 1$, at a stiffness ratio of $\tilde{k} \approx 100$. At this point, the deformation field may decay so quickly that it is no longer possible to measure the deformation response of a building block when its neighbour is actuated. As a ballpark estimate, this crossover takes place in our experimental samples when the living hinges are made thicker than the connecting bars themselves. In that case, the three bulk architectures (with no defect, with a structural defect, and with a topological defect) cannot be distinguished from one another. In conclusion, for our defect detection protocol to be effective, the material's hinges must be sufficiently soft.

While the size of a metamaterials affects its decay length, the detection protocol works for both small and large networks. Fig. 3.11c shows d_Q as a function of network size L in units of bond length l^0, measured along the material's width. The data shown were modelled using model FH, with freely hinging nodes. The decay length shows a weak dependence on system size, increasing in magnitude for larger systems. The decay length does not dip below unity: $d_Q > 1$ for all system sizes. This suggests that our boundary detection protocol can distinguish metamaterial types regardless of size.

3.3.6. Error estimates

Using standard uncertainty propagation methods, we estimate the variance on quantities derived from the experimentally measured lengths l_i (see section 3.2.1 for an estimate of

the standard error Δl). These quantities are the transfer factor q_{ij}, cumulative transfer product q_n, and topological probe Q, defined as follows:

$$\begin{aligned} q_{ij} &= \frac{\delta_j}{\delta_i} = \frac{l_j/l_j^0 - 1}{l_i/l_i^0 - 1} \\ q_n &= \prod_{ij}^{n} q_{ij} \\ Q &= q_P^{1/P} \ . \end{aligned} \tag{3.9}$$

The following variance estimates are calculated for these quantities:

$$\begin{aligned} \Delta q_{ij}^2 &\approx \Delta l^2 q_{ij}^2 A_{ij} \ , \text{ where } A_{ij} = \left(\frac{(l_j/l_j^0)^2 + 1}{(l_j - l_j^0)^2} + \frac{(l_i/l_i^0)^2 + 1}{(l_i - l_i^0)^2} \right) \\ \Delta \log(q_n)^2 &= \Delta l^2 \sum_{ij}^{n} A_{ij} \\ \Delta Q^2 &\approx Q^2 \frac{\Delta l^2}{n^2} \sum_{ij}^{n} A_{ij} \ . \end{aligned} \tag{3.10}$$

The above estimates are used to calculate standard errors for the experimental data presented in this chapter.

3.4. Exotic mechanics with topological defects

The identification of distinct topological mechanical phases in our network designs opens up new vistas for practical design rules for structures with desirable mechanical properties. We discuss such design rules here.

In the previous sections, we showed that metamaterials with and without topological defects have fundamentally distinct architectures. This difference manifests mechanically via *geometric frustration*: defects generate strain when the material is actuated. We now show that geometric frustration is, at its heart, governed by *path parity*. We argue that controlling path parity allows us to design where stresses and deformations localize inside our metamaterials.

In section 3.4.1, we explain our design strategy from the bottom up. We study a pair of building blocks connected by one or more paths of internal bonds, corresponding to smaller and larger metamaterials. Under actuation of the two building blocks, the structure may deform freely or store energy. We show that the connecting paths' parity controls how deformations and stress distribute throughout the material. Section 3.4.1 demonstrates how to use path parity to design metamaterials with a directed, localized stress and deformation response under simultaneous actuation of two building blocks. We show that the presence of a topological defect produces a characteristic antisymmetric mechanical response, while the response of topologically trivial networks is symmetric. Finally, in section 3.4.3, we present the *mode splitting* phenomenon that underlies the asymmetric response in the presence of topological defects.

3.4.1. Mechanics and path parity

Here, we investigate the mechanical response of our metamaterials by exploring the behaviour of a single building block; a strip of stacked building blocks; and finally, a full 2D stacked metamaterial design.

Recall that a single building block has a local floppy mode, which can be activated by displacing the block's majority edge-nodes (Fig. 3.12a). The block responds by contracting or expanding, depending on the sign of the imposed displacements. This motion does not elongate any of the bonds, and does not produce geometric frustration.

Multiple building blocks can be chained into a single, one-dimensional strip. Consider the strip shown in Fig. 3.12b, top: its two end blocks (yellow triangles) are connected together by a single path of internal bonds (blue line). Recalling Eq. 2.1 in section 2.3.1, the parity of the path is positive, which corresponds to a ferromagnetic interaction between the two end blocks. When both end blocks are forced to extend (Fig. 3.12b, bottom, yellow markers), they are forced into a ferromagnetic state: their block spins are identical. This forcing matches the positive path parity, and as a consequence, the strip's floppy mode is actuated. Conversely, the strip shown in Fig. 3.12c consists of two end blocks connected by a negative-parity path (red line). Extending one end block and contracting the other imposes antiferromagnetic block spins, matching the path's parity and activating the strip's floppy mode. All blocks deform harmoniously.

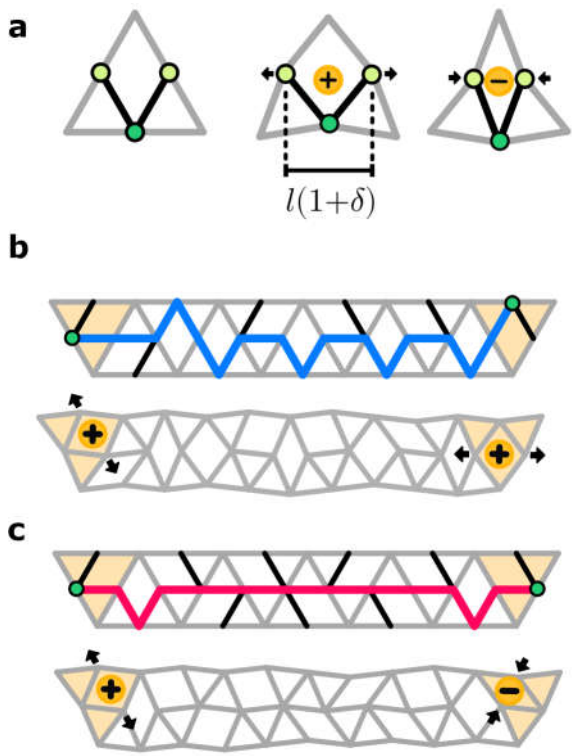

Fig. 3.12.: Understanding network mechanics with path parity. a, A single building block's floppy mode is actuated by displacing its majority edge-nodes (light green circles) to a positive or negative block spin (yellow markers), quantified by the block strain δ. **b,** How connected building blocks deform depends on the parity of their connecting path (section 2.3.1) Top: two blocks (yellow triangles) are connected by a ferromagnetic path (blue line). Bottom: the blocks' spins have the same sign (yellow markers) under actuation of the strip's floppy mode. **c,** Alternatively, two blocks are connected by an antiferromagnetic path (red line). The blocks' spins are opposite when the floppy mode is activated.

In other words: blocks are connected by paths. These paths have a positive or negative parity. If we impose block spins that match the paths' parity, the structure deforms easily. Equal block spins match positive paths, while opposite block spins match negative paths.

By contrast, imposing block spins that do not match the path parity produces geometric frustration, which we illustrate and quantify in Fig. 3.13. To ensure that we study geometric rather than elastic frustration due to finite hinge bending stiffness, we use model FH (see section 3.2.2) to simulate the network mechanics. In Fig. 3.13a, we

present a metamaterial strip of N_T building blocks, stacked along the x-direction in the plane. A path of positive parity connects the strip's end blocks. Enforcing opposite block spins by imposing a local block strain $\pm\delta_i$ (yellow markers) thus generates frustration, which manifests mechanically: first, building block deformations decay away from the actuated blocks, and second, bond lengths change. We measure changes in bond length using the bond strain δ_b (colours), and we measure block deformations using the block strain δ_j.

In Fig. 3.13b, we explore how bond and block strain are affected by the strip's length. We probe metamaterial strips of varying numbers of triangles N_T under incompatible forcing of magnitude $|\delta_i|$, and record the resulting bond and block strains δ_b and $|\delta_j|$ at a distance x along the strip's length. Note that all lengths have units of bond length l^0. In order to compare the results for various values of N_T, we divide the x-positions by the distance between the probed end blocks, $(N_T - 1)$.

At the top of Fig. 3.13b, we show the relative magnitude of output to input block strain, $|\delta_j|/|\delta_i|$, for each building block, sorted by normalized position. Block strains in the strip of Fig. 3.13a are indicated (black line), as well as results for various values of N_T (colours). The data collapses for all values of N_T. The block strains decay linearly to (near) zero in the middle of the strip: deformation of the building blocks is prohibited there. At the bottom of Fig. 3.13b, we show the bond strain $\delta_b(N_T - 1)/|\delta_i|$, normalized by the input block strain and the strip's total length. Here, too, the data collapses across strip lengths. Two features stand out: first, the bond strain is constant throughout the strip and shows no decay. Second, the bond strains take on discrete values, which we suggest to be a consequence of the six-fold symmetry of the bond's orientations.

The fact that block strains decay linearly while bond strains remain constant along the strip's length is reminiscent of Hookean elastic behaviour. Consider a piece of material with Young's modulus E, length L, and area A. The energy stored in this material when its length increases by ΔL is given by $\mathcal{E} = AE\Delta L^2/L$. Evidently, the stored energy scales inversely with the material's length. For comparison, Fig. 3.13c shows the elastic energy $\mathcal{E}$ stored in a metamaterial strip with an effective length $N_T - 1$ between its two actuated ends. The data are shown on a double logarithmic scale. Comparison between the data and a reciprocal scaling (black line, inset) shows that in our metamaterials, the stored energy scales inversely with length. Effectively, our metamaterial thus behaves like a regular, Hookean solid: work must be performed and energy is stored in the network when the strip is geometrically frustrated.

Parity helps us understand frustration in larger networks as well. Fig. 3.14 shows three different network architectures: with no defect, with a structural defect, and with a topological defect. We show that the localization of frustration in these networks, under actuation of a pair of building blocks, correlates with the parity of the block pair's connecting paths.

Fig. 3.14a shows a compatible, defect-free network. A pair of building blocks (yellow triangles) is connected by a large number of paths that run throughout the material. Since all closed paths in the system are of positive parity—a requirement for compatibility, recall section 2.3—all paths between the block pair have the same parity. In this example, all paths are positive (e.g. blue lines). Actuating the blocks by extending

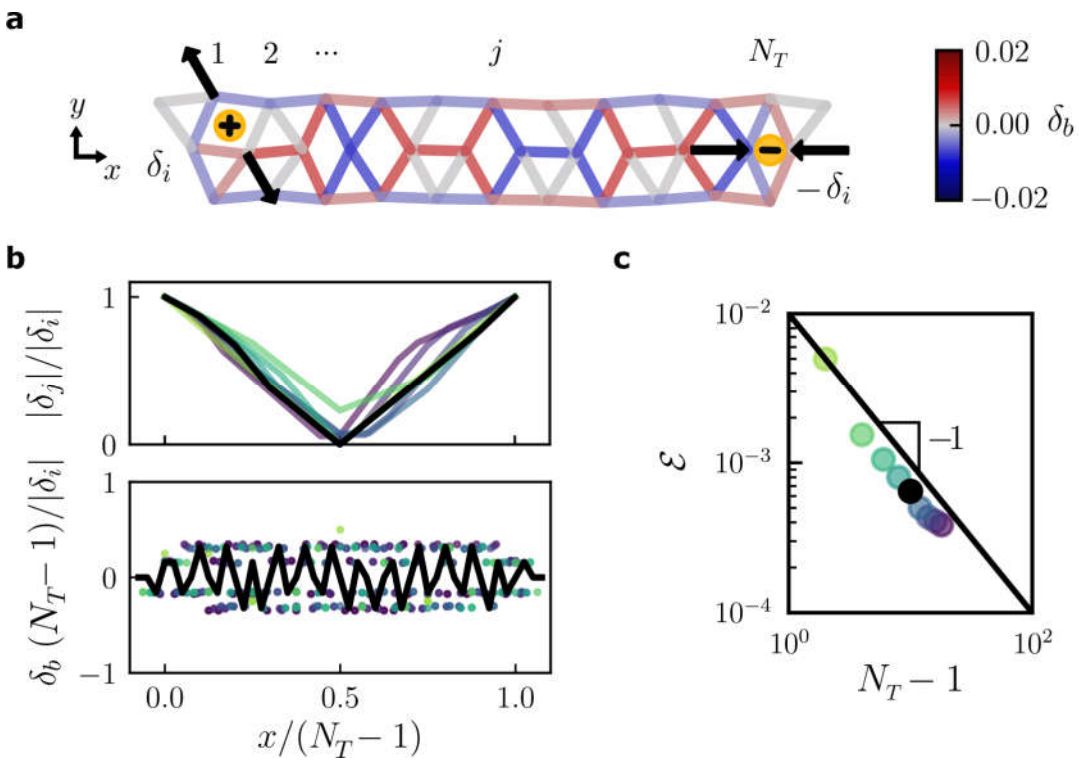

Fig. 3.13.: Geometric frustration manifests mechanically. **a,** Two building blocks connected by a ferromagnetic path of N_T building blocks (Fig. 3.12b) are given opposite block spins $\pm\delta_i$ (yellow markers) by displacing their majority edge-nodes (black arrows). Geometric frustration leads to energy being stored in deformed bars, producing a bond strain δ_b (colours). **b,** Blocks deform and bonds are strained under incompatible forcing. Normalized block strain (top) and bond strain (bottom) are shown as a function of normalized position $x/(N_T-1)$ along the strip. Colours correspond to strips of varying size N_T; black lines correspond to the structure shown in **a.** Top: relative block strain magnitude $|\delta_j|/|\delta_i|$ of the j-th building block. Frustration leads to a linear decay of block strain magnitudes. Bottom: local bond strain δ_b, normalized by the structure's length N_T-1 and input block strain δ_i, does not decay along the strip. Discrete bond strain values arise from the triangular architecture. **c,** Total elastic energy $\mathcal{E}$ stored in a strip as a function of its length N_T-1 under equal values of δ_i. $\mathcal{E}$ is inversely proportional to length (black line), consistent with normal elasticity (see text).

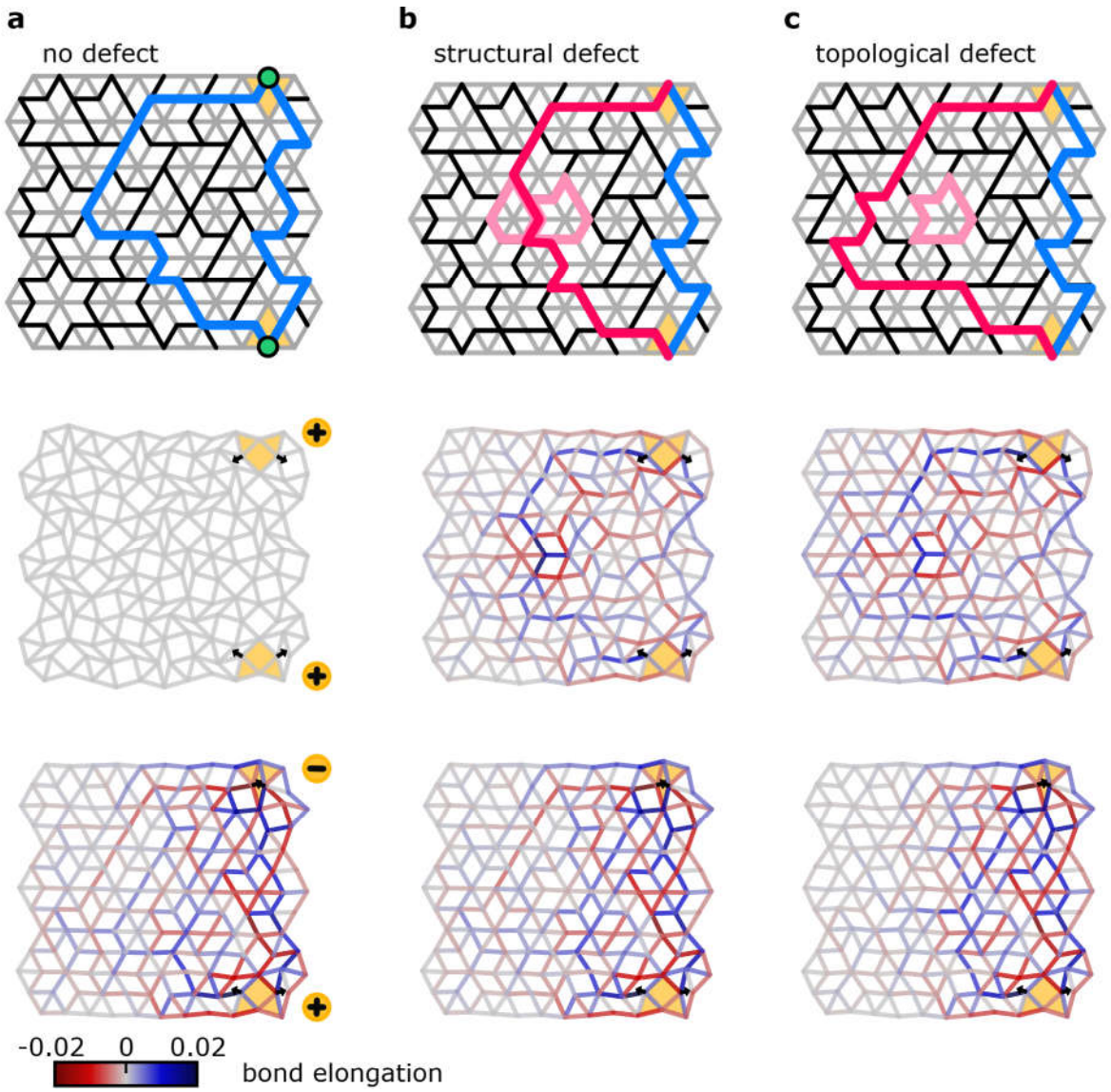

Fig. 3.14.: Path parity predicts frustration. a, Defect-free network (top) under compatible (middle) and incompatible forcing (bottom). Top: ferromagnetic paths (blue lines, e.g.) connect the minority nodes (green circles) of two building blocks (yellow triangles). Middle: enforcing compatible, ferromagnetic block spins (yellow markers, black arrows) activates the floppy mode. Bottom: enforcing antiferromagnetic block spins produces bond elongation along all ferromagnetic paths (colours). **b,** Top: a network with a structural defect (pink local loops) contains a single antiferromagnetic path (red line). Middle, bottom: ferromagnetic (antiferromagnetic) block spins produce bond elongation along the antiferromagnetic (ferromagnetic) path. **c,** Top: a network with a topological defect (pink local loop) contains both ferro- and antiferromagnetic paths that run along either side of the defect (blue and red lines, e.g.). Middle, bottom: ferromagnetic block spins produce geometric frustration along paths of antiferromagnetic parity, and vice versa.

them to the same block spin (3.14a, middle, yellow markers) thus matches the parity of all their connecting paths: there is no geometric frustration, and the structure deforms easily. Conversely, forcing the blocks to have opposite block spin (3.14a, bottom) is inconsistent with the parities of all their connecting paths. As a consequence, all paths are geometrically frustrated, and bonds throughout the system are elongated (colours). Since the density of frustrated paths is highest near the actuated blocks, bond elongations are larger there. In short: the mechanical response of a compatible network can be understood by considering the path parity between actuated blocks.

The mechanical response of a network with a structural defect may be understood in the same terms. When a structural defect is present in the network (Fig. 3.14b), most paths between our pair of building blocks (yellow triangles) have identical, positive parity (blue line, e.g.). However, any paths that run in between the two odd local loops that constitute the structural defect must have opposite, negative parity (Fig. 3.14b, red line, e.g.). As a result, when the building block pair is actuated to equal block spins, their deformation is consistent with the positive-parity paths and inconsistent with the negative-parity paths. The latter paths generate geometric frustration, and bonds along them will elongate. Since the density of negative-parity paths is highest at the structural defect, bonds in those areas experience the largest elongation (Fig. 3.14b, middle). Conversely, when the blocks are given opposite block spins, all positive-parity paths that go around the structural defect are frustrated and experience stress. Since no frustrated paths run between the defect's two odd local loops, bonds do not elongate much there (Fig. 3.14b, bottom). Evidently, frustration can be concentrated either inside or outside the area surrounding the structural defect, depending on the actuation parity.

Finally, the frustration situation changes once more for topological defects. Consider the network shown in Fig. 3.14c. Connecting paths running between our block pair (yellow triangles) have negative parity on the left side of the defect (e.g., red line), and positive on the right (blue line). This is a consequence of the fact that all closed paths in the system now have negative parity (see section 2.4). When the blocks are both dilated to a positive block spin (Fig. 3.14c, middle), all negative-parity paths are frustrated. Thus, the density of frustrated paths is largest on the left side of the system. Bond elongations are concentrated, correspondingly, on the left side of the topological defect. This situation is reversed when the blocks are forced to have unequal block spin (Fig. 3.14c, bottom): frustration is concentrated on the right side of the defect. In summary, in a network containing a topological defect, frustration may be concentrated on opposite sides of the defect under actuation of a pair of building blocks.

3.4.2. Stress and deformation steering

The previous section explores how the mechanical response of a network can be understood in terms of its connecting paths' parities. In particular, the mechanical responses of networks that have no defects, a structural defect, or a topological one have a very distinct spatial signature: frustration and deformation concentrate in different ways inside the networks' bulk. Here, we design metamaterials in which we exploit parity to steer deformations and stresses by actuating a small number of building blocks.

Consider a strip of metamaterial connecting two building blocks; depending on the con-

necting path's parity— positive or negative— extending both blocks respectively leads to a low energy deformation, or a highly frustrated response. Now define two pairs of blocks, i, j and i, j'. In the topologically trivial case, all paths connecting i and j have the same parity — and similarly for i and j'. Now consider a metamaterial with a centre hole, where the blocks are thus connected by two different strips (Fig. 3.15a). Designing i, j (i, j') to interact ferromagnetically (antiferromagnetically), expanding the former pair leads predominantly to deformations, while expanding the latter leads to a stressed, frustrated state. Fig. 3.15b shows the deformation and bond elongation fields for model FH, experiments, and model TR. In the experiments, two building blocks are simultaneously actuated by inserting wedges of 12.5 ± 0.2 mm width, inducing an majority edge-node separation from 10 ± 0.2 mm to 13.5 ± 0.4 mm. The modelled results were obtained by extending virtual building blocks to a strain of $\delta = \pm 0.35$. With these parameters, model TR matches experimental results with good accuracy: comparing the experimental and modelled deformation fields $\boldsymbol{u}_{\mathsf{exp}}$ and $\boldsymbol{u}_{\mathsf{TR}}$ via their cosine similarity $\hat{\boldsymbol{u}}_{\mathsf{exp}} \cdot \hat{\boldsymbol{u}}_{\mathsf{TR}}$, we find a match of 70 to 98 per cent. Fig. 3.15b shows that deformations and stresses (quantified by bond elongations) are distributed in the structures as expected.

In contrast, consider a non-trivial configuration with a topological defect in its excised centre, implying that the parities of the two strips are opposite (Fig. 3.15c). Expanding blocks i and j produces deformations in the positive-parity strip and stresses in the other, thus steering deformations and stresses to distinct parts of the sample; expanding blocks i and j' reverses the character of the upper and lower paths and the concomitant deformations and stresses (Fig. 3.15d). We note that actuating a single pair of blocks with the same or opposite parity (i.e., extending one and contracting the other) steers stresses and deformations similarly [13]. Crucially, actuating a *single* block simply leads to a smeared-out stress field, similar to what happens when an ordinary structural defect is present; only the combination of a topological defect and multi-site actuation leads to the stress steering shown in Fig. 3.15d.

With the above strategy, we actuate two distinct building block pairs inside a metamaterial to harness the antisymmetric signature of topological defects. A conceptually simpler method, which is experimentally slightly more complex but produces similar results, is achieved as follows. Consider a single block pair i, j. The two blocks may be actuated antiferromagnetically by expanding one and contracting the other, or ferromagnetically by expanding both. In the topologically trivial architecture shown in Fig. 3.15, a particular block pair i, j is connected by two positive-parity strips. Under ferromagnetic actuation, the entire structure deforms; under antiferromagnetic actuation, the structure is frustrated. Conversely, two blocks in the nontrivial metamaterial are connected by one ferromagnetic, positive-parity and one antiferromagnetic, negative-parity strip. Thus, (anti)ferromagnetic block actuation produces deformations in the (anti)ferromagnetic strip, and stresses in the other. We therefore observe a similar capacity for steering stress and deformation by actuating a single pair of building blocks in the metamaterial.

Hence, (excised) topological defects combined with targeted actuation at multiple sites allows for precisely designed, spatially steered mechanical responses.

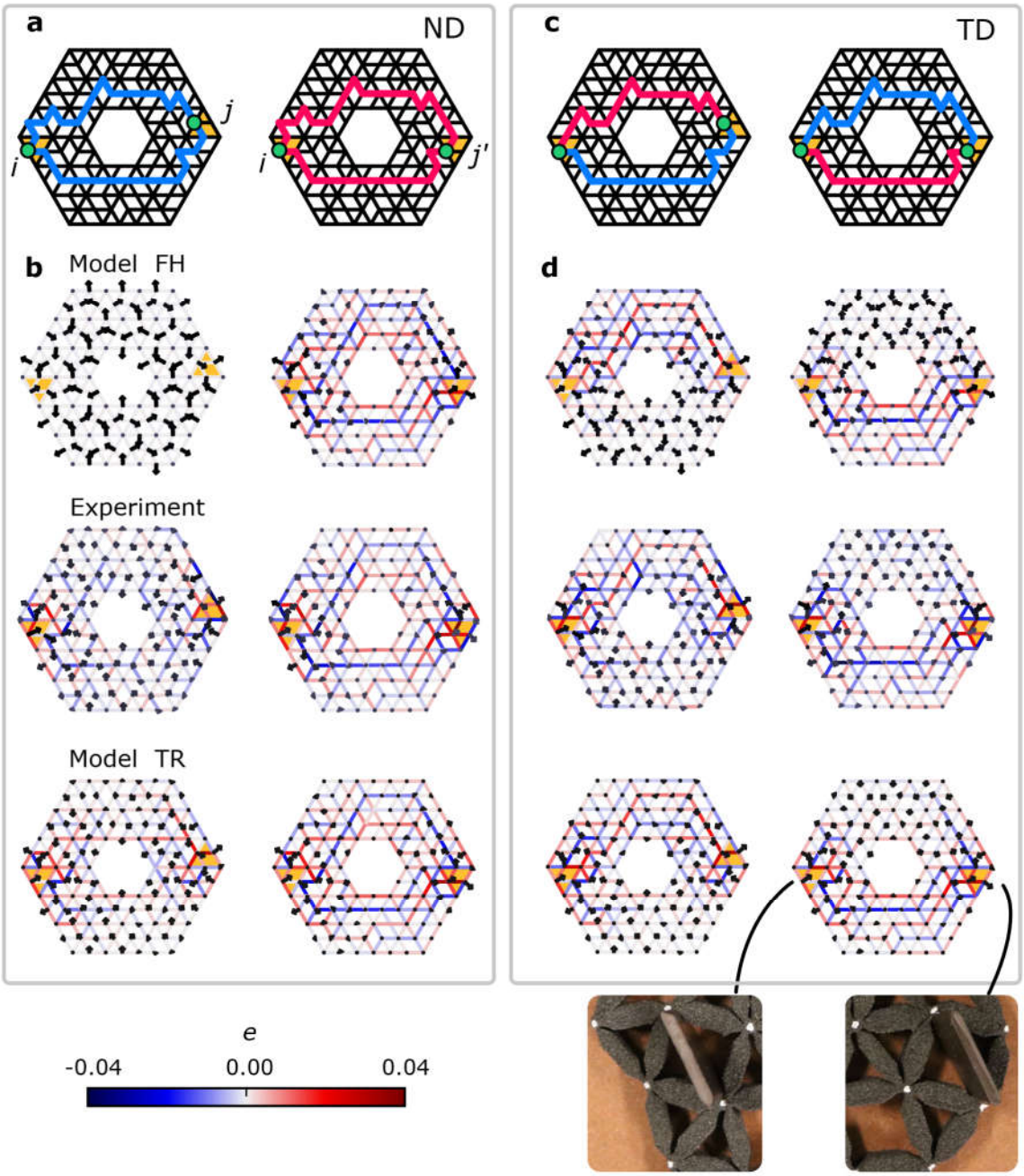

Fig. 3.15.: Stiffness steering. **a,** Compatible architecture (ND) with centre removed; blue and red indicate positive- and negative-parity paths between the actuation sites i, j and j' (yellow markers). **b,** Expanding blocks i and j mainly leads to displacements (left); arrows indicate deformation and are tripled in length for clarity, while bond colours indicate bond elongation e (colour bar). Expanding blocks i and j' mainly lead to bond stretching (right). **c,** Non-trivial architecture with a topological defect (TD) in the excised centre. **d,** Under simultaneous extension of the blocks i, j, bond stretching localizes in the upper portion of the sample, while node deformations localize in the lower part (middle); under actuation of blocks i, j', stretching localizes in the lower and deformations in the upper part (bottom). Stiffness steering is observed in modelled as well as experimental results, with model TR in quantitative agreement with experiments.

3.4.3. Mode splitting in the presence of topological defects

Topological defects produce unusual mechanics due to their architecture. Here, we explore the connection between architecture and mechanics from a different point of view: that of the structure's *normal modes*.

We first show that low-energy normal modes of a mechanical metamaterial, which are similar in nature to acoustic plane waves, dominate the structure's response to external probing. Secondly, we demonstrate that topologically trivial materials possess a single, symmetric, lowest-energy mode, which splits into two antisymmetric low-energy modes in the presence of topological defects. These antisymmetric modes underlie the exotic mechanics of topological defects.

Normal modes in metamaterials

We first consider the normal modes of a mechanical structure. Physically, normal modes are similar to stationary acoustic plane waves, where nodes are periodically displaced from their resting position across the metamaterial. Waves at higher spatial frequencies correspond to normal modes with proportionally larger energies.

In order to tease apart the effects of geometry and elasticity, we consider our metamaterials as freely hinging nodes connected by linear springs, as in model FH. In the linear regime of small displacements, normal modes of such a metamaterial are then configurations of node forces $\boldsymbol{f}_m$ that map to proportional node displacements $\boldsymbol{u}_m = c_m \boldsymbol{f}_m$.

To find a structure's normal modes, we use the following strategy. In section 3.2.2, node displacements and forces were shown to be related via a compatibility matrix $\mathbf{R}$, such that $\boldsymbol{f} = \mathbf{R}^T\mathbf{K}\mathbf{R}\boldsymbol{u}$. Here, $\mathbf{K}$ is a matrix of bond stiffnesses that we have set equal to unity. Mathematically, the normal modes are thus the right eigenvectors of the matrix $\mathbf{R}^T\mathbf{R}$. Since the transpose of the compatibility matrix can be written in terms of a unique singular value decomposition $\mathbf{R}^T = \mathbf{U}\mathbf{D}\mathbf{W}^T$, we may write $\mathbf{R}^T\mathbf{R} = \mathbf{U}\mathbf{D}\mathbf{D}\mathbf{U}^T$, where $\mathbf{U}$ and $\mathbf{W}$ are orthonormal matrices with the respective left and right singular vectors of $\mathbf{R}^T$ as their columns, while $\mathbf{D}$ contains the singular values of $\mathbf{R}^T$ on the diagonal. Thus, for each left singular vectors $\boldsymbol{u}_m$, there is a corresponding proportional force $\boldsymbol{f}_m = d_m^2 \boldsymbol{u}_m$. Therefore, the deformation vectors $\boldsymbol{u}_m$ are the normal modes of the system, with a corresponding eigenvalue d_m^2. The energy of such a mode, obtained by dotting $\hat{\boldsymbol{u}}_m$ with its resulting force, is $\mathcal{E}_m = \frac{1}{2} d_m^2$.

Note that each displacement field in the metamaterial can be written as a combination of normal modes: $\boldsymbol{u} = \sum_m (\boldsymbol{u} \cdot \hat{\boldsymbol{u}}_m)\hat{\boldsymbol{u}}_m = \sum_m c_m \hat{\boldsymbol{u}}_m$. The corresponding force is $\boldsymbol{f} = \sum_m d_m^2 c_m \hat{\boldsymbol{u}}_m$, resulting in an elastic energy $\frac{1}{2}\sum_m (d_m c_m)^2$. The magnitude of the force and energy scale quadratically with the singular values d_m.

We now consider the metamaterial's response under actuation of a single building block, and show that the resulting displacement field is a very particular linear combination of normal modes. The localized force needed to expand our building block can be written as a linear combination of load normal modes. This is reminiscent of a two-dimensional Dirac delta function around a point $\boldsymbol{r}_0$ (that is, a localized force), which can be expressed as a superposition of plane waves (or normal modes). We might expect the localized force

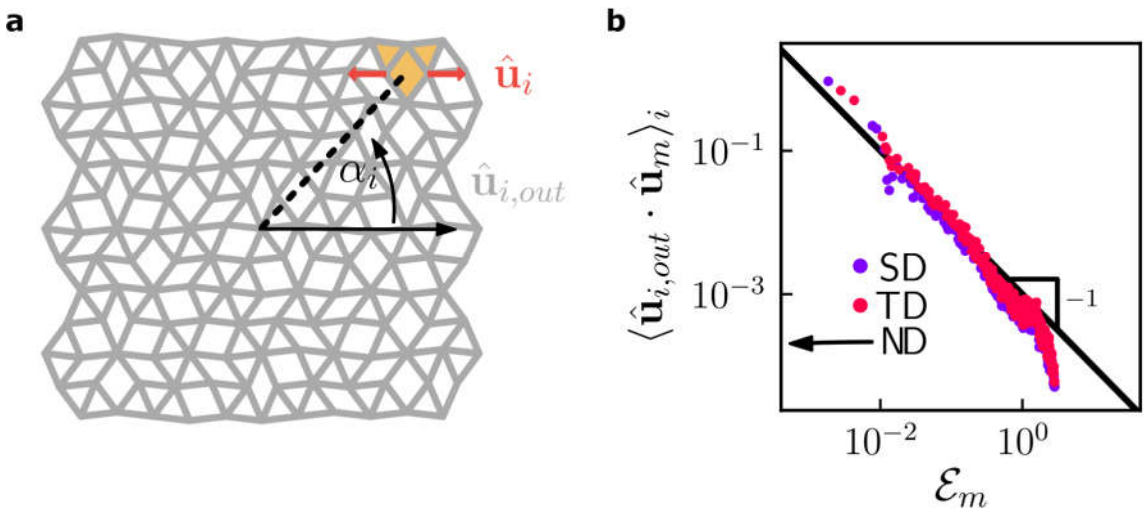

Fig. 3.16.: Displacement of a metamaterial under local probing in terms of normal modes. a, A metamaterial is actuated at a single boundary building block i (yellow triangle) at polar angle α_i with respect to the structure's centre. The input displacement field $\hat{\boldsymbol{u}}_i$ (red arrows) results in an output displacement field $\hat{\boldsymbol{u}}_{i,out}$ as shown. **b,** The relative contribution to $\hat{\boldsymbol{u}}_{i,out}$ of each of the structure's normal modes $\hat{\boldsymbol{u}}_m$ is plotted against the normal mode energy $\mathcal{E}_m$. Relative contributions are averaged over all building blocks i along the structure's boundary. Results for metamaterials with a structural (SD) and a topological defect (TD) are shown (colours). Metamaterials without a defect (ND) are dominated by a normal mode at $\mathcal{E}_m = 0$ (not shown). Displacement field contributions scale inversely proportional to the energy (black line).

to be a superposition of normal modes, in which the mode coefficients scale similarly to the coefficients of a Dirac delta function's discrete Fourier transform:

$$\delta(\boldsymbol{r} - \boldsymbol{r}_0) = \frac{1}{(2\pi)^2} \sum_{n=-\infty}^{\infty} \sum_{m=-\infty}^{\infty} e^{-in(x-x_0)\pi/L_x} e^{-im(y-y_0)\pi/L_y} \tag{3.11}$$

Evidently, the Dirac delta function's Fourier coefficients are equal to unity. Thus, we may expect the different load normal modes that make up our localized force to be represented at similar magnitudes: $\boldsymbol{f} \propto \sum_m \hat{\boldsymbol{f}}_m$. Mapping the load normal modes back to the displacement normal modes, we then hypothesize that the metamaterial's displacement field can be written as $\boldsymbol{u} \propto \sum_m 1/d_m^2 \hat{\boldsymbol{u}}_m$. Thus, under localized forcing, the displacement normal modes should be represented in the output deformation field with a magnitude that is inversely proportional to their corresponding energy $\mathcal{E}_m = \frac{1}{2} d_m^2$.

We confirm this hypothesis in our metamaterials as follows. Inside a metamaterial (Fig. 3.16a) we actuate each boundary building block i (yellow triangle, e.g.) at a polar angle α_i from the structure's centre. A displacement $\hat{\boldsymbol{u}}_i$ (red arrows) is imposed, and the resulting modelled deformation field $\hat{\boldsymbol{u}}_{i,out}$ is recorded. The relative contribution of each normal mode to the deformation field, $\hat{\boldsymbol{u}}_{i,out} \cdot \hat{\boldsymbol{u}}_m$, is identified. The relative contributions are then averaged over the material's boundary to reduce the impact of local architecture. Fig. 3.16b shows the resulting average contribution of each normal mode as a function of mode energy $\mathcal{E}_m$. The response of metamaterials with no defect (ND), a structural defect (SD), and a topological defect (TD) were investigated. Note that defect-free structures have a dominant floppy mode at $\mathcal{E}_m = 0$, which lies outside the domain of Fig. 3.16b. The data support that, to good approximation, each

normal mode is represented with a magnitude that is inversely proportional to its energy.

To summarize: under local actuation of a metamaterial, low-energy modes are strongly represented, while high-energy modes are not. Low-energy modes dominate the mechanical response.

Mode splitting

We now argue that the low-energy normal modes in metamaterials with and without a topological defect are fundamentally different.

Fig. 3.17a shows normal mode energy spectra for three metamaterials with distinct bulk characters: defect-free, with a structural defect, and with a topological defect. The first two structures are topologically trivial. They share a common feature: an energetic gap separates one low-energy mode from the rest. By contrast, the topologically nontrivial metamaterial exhibits two normal modes at low energy, separated by an energy gap from the remainder.

Fig. 3.17b illustrates the first two normal modes for each structure. The lowest-energy mode of the defect-free network (that is, the floppy mode) extends evenly throughout the network. In the presence of a structural defect, the lowest-energy mode is somewhat attenuated around the defect, but remains diffuse throughout the material. Conversely, networks with a topological defect have two low-energy normal modes (Fig. 3.17b, right), spatially localized to opposite sides of the system. These modes are *antisymmetric*: they cannot be combined to produce an evenly distributed deformation field. Any linear combination of the two modes results in a deformation field that is concentrated in one half of the system, in a phenomenon we call *mode splitting*.

Finally, we confirm that modes below the energetic gap dominate the mechanical response in our metamaterials. We calculate the deformation field $\hat{\boldsymbol{u}}_{i,out}$ in each structure, due to actuation of a single boundary building block at polar angle α_i (see Fig. 3.16a). Fig. 3.17c shows the overlap of each mode $\hat{\boldsymbol{u}}_m$ with the deformation field as a function of α_i. The data show that the lowest-energy modes (one for topologically trivial structures, and two for the nontrivial material) are represented at a much larger magnitude than higher-energy modes. In addition, the two antisymmetric normal modes in the presence of a topological defect dominate at opposite sides of the system (Fig. 3.17c, right).

As an aside, mode splitting gives rise to an interesting effect: when a topological metamaterial is periodically driven by squeezing and expanding two building blocks out-of-phase, the structure can support a polar wave that travels around the system. Conversely, topologically trivial structures can only exhibit planar waves that travel back and forth between the actuation points.

In short: the behaviour of a topological metamaterial is governed by two antisymmetric low-energy modes. Their antisymmetry gives rise to the stress-steering behaviour shown in section 3.4.2: deformations cannot be distributed evenly, but must be concentrated in one half of the metamaterial. Choosing the right actuation points gives control over which half.

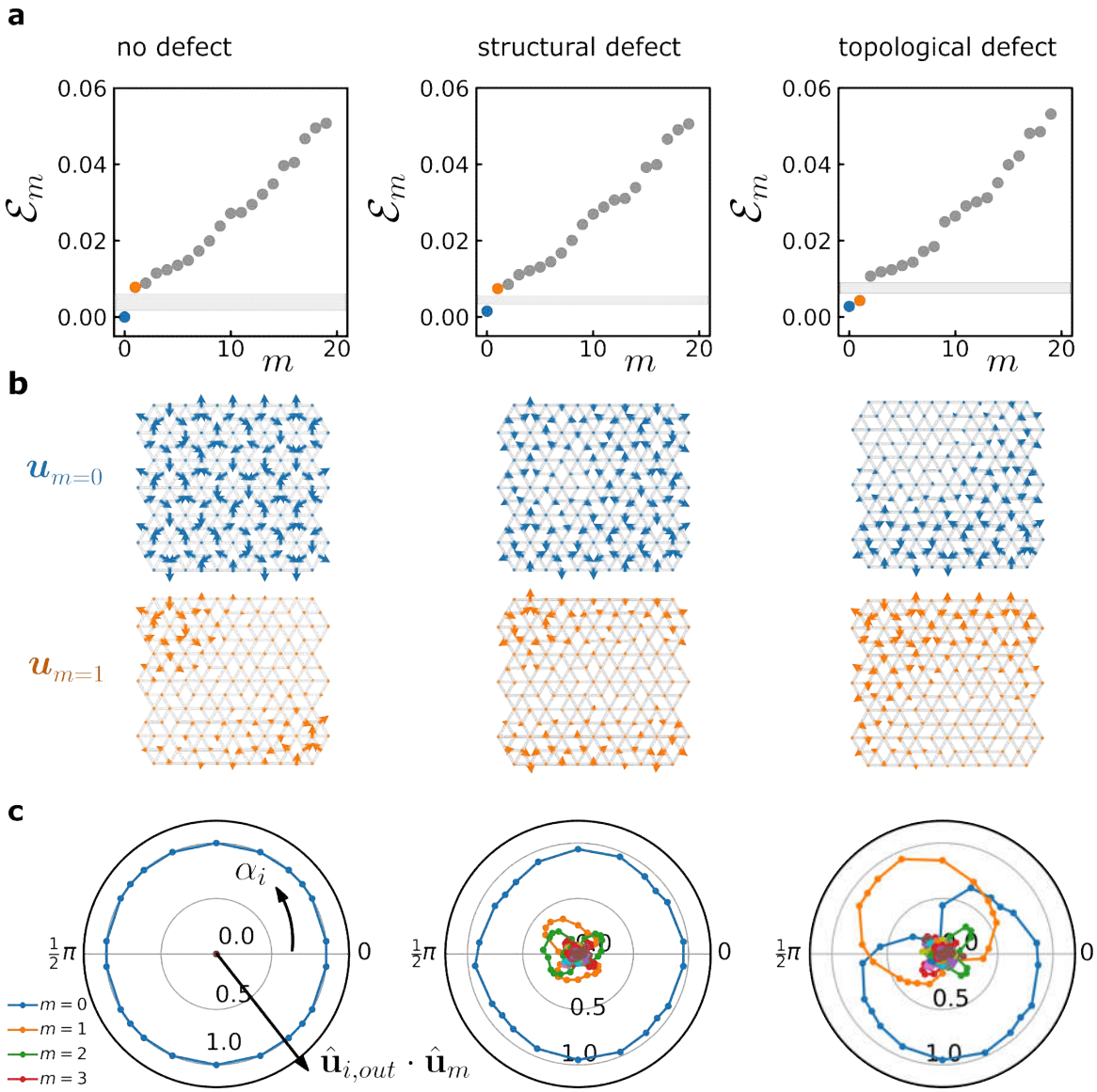

Fig. 3.17.: Topological defects produce antisymmetric normal modes. **a,** Energy spectrum $\mathcal{E}_m$ of the m-th normal mode of three representative metamaterials (no defect; structural defect; and topological defect) in model FH. Energy gaps are observed above the first or second mode (light grey areas). **b,** Displacement fields $\hat{\boldsymbol{u}}_m$ of to the two lowest-energy normal modes. Only structures with a topological defect exhibit two antisymmetric normal modes at similar energies. **c,** (A)symmetry of the materials' normal modes. Polar plots show the overlap of the normal modes (legend) with the structure's deformation field $\hat{\boldsymbol{u}}_{i,out}$, under extension of a single boundary block at polar angle α_i from the structure's centre (Fig. 3.16a). For structures without defects or with a structural defect (left, middle) the symmetric lowest-energy mode $m = 0$ (blue line) dominates the response. In the presence of a topological defect, the two antisymmetric modes $m = 0, 1$ contribute equally at opposite orientations (blue, orange lines).

3.5. Conclusions and outlook

In this chapter, we studied the mechanical response of the metamaterials introduced in chapter 2. We explored the mechanics of defects and determined that topological defects have a distinct signature that can be detected at the boundary of our metamaterials. We showed that this topological signature can be understood in terms of path parities between the metamaterials' building blocks, and harnessed this understanding to design metamaterials with characteristic symmetric and antisymmetric responses under two-point probing, showing how to use topological defects to steer stress and deformation fields inside our metamaterials. Finally, we argued that antisymmetric, low-energy mode splitting in the presence of topological defects underlies their stress-steering behaviour.

Previous work on mechanical metamaterials has been focused on studying compatible materials with one or several pre-programmed floppy modes[7,11,58,59]. However, designing the energy landscape of metamaterials at higher energies may help us create multifunctional materials that can perform more complex mechanical actions. Here, we have shown how topological defects may be used to engineer a directed finite-energy response. Our approach is based on an analogy to geometric frustration in spin-ices, which allows us to understand the mechanical response of metamaterials by considering interactions between different parts of the system via path parities. Our work thus presents an avenue into the design of metamaterial energy landscapes by harnessing controlled mechanical frustration.

This strategy to generate controlled and directed frustration may be extended to the design of novel classes of frustrated metamaterials, including origami, kirigami and 3D metamaterials[7,21,60], provided the deformations of the building blocks can be characterized by discrete, spin-like variables. The resulting complex metamaterials may impact future technologies concerning sensing, actuation, and soft robotics[61–63].

Acknowledgements

We thank Roni Ilan, Edan Lerner, Bela Mulder, Ben Pisanty, Eial Teomy and Ewold Verhagen for fruitful discussions, Jayson Paulose for co-developing code for the numerical model FH, and Dion Ursem for technical support. This research was supported in part by the Israel Science Foundation Grant No. 968/16.

4. Response evolution of mechanical metamaterials under architectural transformations[1]

Abstract

Architectural transformations play a key role in the evolution of complex systems, from design algorithms for metamaterials to flow and plasticity of disordered media. Here, we develop a general framework for the evolution of the linear mechanical response of network structures under discrete architectural transformations via sequential bond swapping: the removal and addition of elastic elements. We focus on a class of spatially complex metamaterials, consisting of triangular building blocks. Rotations of these building blocks, corresponding to removing and adding elastic elements, introduce (topological) architectural defects. We show that the metamaterials' states of self stress play a crucial role in the mechanical response, and that the mutually exclusive self stress states between two different network architectures span the difference in their mechanical response. For our class of metamaterials, we identify a localized representation of these states of self stress, which allows us to capture the evolving response. We use our insights to understand the unusual stress-steering behaviour of topological defects.

4.1. Introduction

The unique properties of mechanical metamaterials emerge from the assembly of simple structural unit cells connected by local interactions. Targeted design of such assemblies has aided the creation of metamaterials with a broad range of responses and potential functionalities[8,18,22,50,64–67]. So far, most metamaterial design has been focused on the creation of metamaterials with compatible or *floppy* motions: low-energy deformations, which dominate the material's response to external probing, and lead to unusual properties such as negative Poisson ratio or vanishing shear modulus[68,69]. However, incompatibility or frustration offers a new avenue for designing material responses at higher energies, for example to produce materials with tunable stiffness[29]. Such frustration in mechanical metamaterials is closely related to other artificial frustrated systems, such as artificial spin ice[23,24], colloidal ice[42,70] and colloidal antiferromagnets[71–73].

Recently, we presented a systematic strategy to introduce defects, and in particular topological defects, in a novel class of mechanical metamaterials[13]. These consist of 2D triangular building blocks, and are a mechanical analogue of spin systems with tunable ferromagnetic and antiferromagnetic interactions, where the nature of the interaction is set by the orientation of the building blocks. We showed how to design a large number of compatible structures in this class—including the well-known rotating square mechanism[13,15,74]. We subsequently introduced (topological) defects in our metamaterials by rotating one or more building blocks. These architectural transformations affect the mechanical response and allow us to direct the stress concentration in these structures[13].

[1] The work presented in this chapter is based on Refs.[13] and [14].

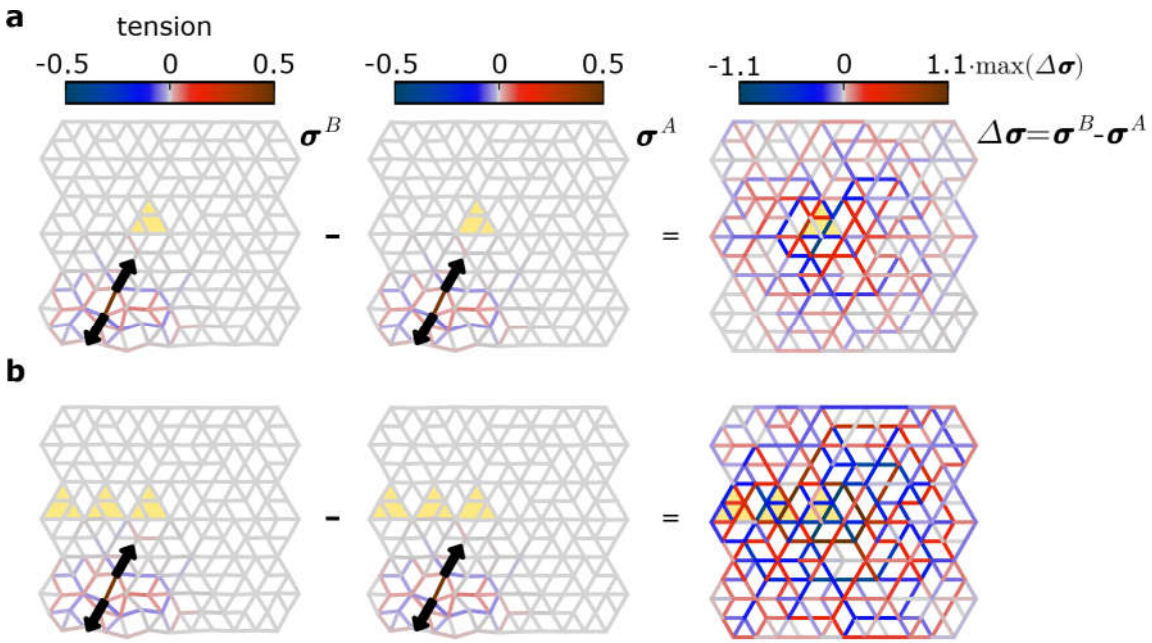

Fig. 4.1.: **a**, Under the same applied load (black arrows), two mechanical networks differing by a small number of bonds, highlighted by the yellow triangles (left vs. centre) differ in their stress response (colour bar). Depending on the material's changing internal architecture, the stress difference ($\Delta\boldsymbol{\sigma}$, right) can be either quasilocalized when an ordinary defect is introduced (**a**) or diffuse if a *topological* defect is created (**b**). The same physical principles underlie both cases: the stress difference is governed by the networks' states of self stress.

Similarly, bond cutting strategies have recently been used to modify the elastic moduli of disordered networks[75–77], and spatial deformations in allosteric networks[78]. More widely, discrete changes in contact networks of flowing disordered media similarly lead to the evolution of mechanical properties[79–82]. A formalism for calculating the changes in linear response under bond cutting has been worked out recently[78,80]. Here we extend this formalism to bond swapping, which involves the sequential cutting and adding of bonds. We focus on rotations of building blocks for a particular class of mechanical metamaterials[13], in which the resulting mechanical consequences are tractable.

To motivate our work, consider two examples of the response evolution under architectural transformations, illustrated in Fig. 4.1. The examples show two architectural transformations that produce an ordinary (Fig. 4.1a) and a topological defect (Fig. 4.1b) respectively. For each case, we show the stress response under an applied load before and after transformation, and focus on the stress difference as a measure of the evolution of the response. In the former case, where a single triangular building block is rotated, the stress difference is localized around the rotated block (Fig. 4.1a). In the latter case, the stress difference spreads throughout the system (Fig. 4.1b).

Our goal is to understand what controls these distinct stress differences. To do so, we study the linear response of spring networks under architectural transformations. The possible stress fields inside such a network form the *stress space*, which is composed of load-bearing states (*LB-states*), accessible via external loading, and states of self-stress (*SS-states*), which are stress configurations with zero net force on all nodes. Under-

standing the evolution of the mechanical response entails describing the evolution of these spaces. For the overconstrained system at hand, the states of self-stress can be obtained in closed form, and we show how to use this information to completely capture the response evolution. Specifically, we find that the stress field difference between two networks as shown in Fig. 4.1, is spanned by their small number of mutually exclusive SS-states. The presence of closed form SS-states in our metamaterials therefore enables us to determine a priori how small modifications in network architecture affect the mechanical response.

In the following sections, we discuss the linear mechanical formalism underlying our findings, which states that stress distributions inside mechanical networks under external loading are spanned by LB-states, while SS-states—which produce zero net forces—are inaccessible stress states of the network. We conclude that the stress response difference between networks with related architectures must be spanned by their mutually exclusive SS-states (Sec. 4.2). We then present our non-periodic compatible mechanical metamaterials, consisting of stacked anisotropic unit cells that can deform in harmony[13] (Sec. 4.3), and in which the SS-space can be represented as a set of localized states (Sec. 4.4). We demonstrate how sequential building-block rotations produce architectural changes that introduce controlled frustration, producing varying configurations of (topological) defects (Sec. 4.5). In spite of the presence of such frustration, all SS-states can still be constructed straightforwardly (Sec. 4.6.1). As a consequence, SS-states that are not shared between any two architecturally-related networks are easily identified, and are confirmed to span the stress response difference under identical loads (Sec. 4.6.2–4.6.4). Lastly, we use our knowledge of the SS-states to understand how topological defects steer stresses into different parts of a metamaterial, illustrating that our findings may be useful for designing metamaterials with targeted stress responses (Sec. 4.7).

4.2. Linear mechanics: states of self stress and floppy modes

In order to understand the comparative response of mechanical networks with closely related architectures, we recall the linear-elastic material model described in section 3.2.2 that underlies our findings[54,55] We discuss how a mechanical metamaterial's floppy modes (FM), load-bearing stresses (LB-states), and states of self stress (SS-states) naturally arise from this model, and show that knowledge of the SS-states suffices to understand the difference in mechanical response of two architecturally related materials.

We model our networks as freely hinging nodes connected by Hookean springs. The network's mechanics are described by three linear-algebraic matrix equations that relate forces exerted by each bond—which we refer to as stresses—to the net forces on and displacements of each node. First, node forces $\boldsymbol{f}$ are related to bond stresses (or tensions), $\boldsymbol{\sigma}$ via a kinematic matrix, $\boldsymbol{R}^T$, which is constructed using the network's architectural layout, such that $\boldsymbol{f} = \boldsymbol{R}^T\boldsymbol{\sigma}$. Similarly, node displacements $\boldsymbol{u}$ map to bond elongations $\boldsymbol{e}$ via the transpose of the kinematic matrix, known as the rigidity matrix $\boldsymbol{R}$, so that $\boldsymbol{e} = \boldsymbol{R}\boldsymbol{u}$. Finally, bond elongations and bond stresses are related by a Hookean constitutive law, $\boldsymbol{\sigma} = \boldsymbol{K}\boldsymbol{e}$, where $\boldsymbol{K}$ is a diagonal matrix of spring constants, which we will set to unity in what follows. The three matrix equations above relate all possible node forces, bond stresses, bond elongations, and node displacements of the network, and thus govern the material's linear mechanical response.

In practice, we construct a material's kinematic matrix as follows. Consider two nodes i, j in a 2D plane, connected by a bond ij. Their linearized elongation under planar displacements of the nodes $\boldsymbol{u} = (u_{ix}, u_{iy}, u_{jx}, u_{jy})$ is then given by $e_{ij} = [-n_x, -n_y, n_x, n_y]\boldsymbol{u}$, where $\hat{\boldsymbol{n}}$ is the unit vector along the bond running from i to j. The 4×1 kinematic matrix is then given by $\boldsymbol{R}^T = [-n_x, -n_y, n_x, n_y]^T$, and maps the bond's stress due to bond elongation, $s_{ij} = Ke_{ij}$, to node forces $\boldsymbol{f} = (f_{ix}, f_{iy}, f_{jx}, f_{jy}) = \boldsymbol{R}^T s_{ij}$. Extending this 2D network to include N_n nodes and N_b bonds produces a $2N_n \times N_b$ kinematic matrix, where each of the columns corresponds to a particular bond's connection between two end nodes, as above. Therefore, the domain of the kinematic matrix is an N_b-dimensional space of stress vectors, in which each vector component corresponds to a bond.

The vector subspaces of the kinematic matrix—its kernel and row space, which form the domain, and its cokernel and column space, which form the codomain—have a particular insightful physical interpretation[55]. First, the row space is spanned by the LB-states, symbolized by $\hat{\boldsymbol{\sigma}}$, or stress eigenvectors that produce finite node forces. Secondly, if the system is overconstrained[83], the kinematic matrix's kernel is nontrivial and spanned by a finite number of zero eigenvectors, or bond stress configurations that lead to zero net node forces. These are the network's SS-states, symbolized by $\hat{\boldsymbol{\tau}}$. Similarly, if the network is underconstrained, the cokernel consists of *floppy modes* (FM), node displacement vectors that produce no bond elongations and thus cost no elastic energy. In two dimensions, these FM include a total of three rigid-body motions, a rotation and two translations. Lastly, the column space contains all displacement vectors that produce finite bond elongations: this column space corresponds one-to-one to the LB-states of the row space. Thus, the SS-space and LB-space together span the entire space of possible bond stress configurations—the former being inaccessible states, and the latter supported states—and they therefore govern the network's response to external loading.

While the subspaces' bases are often not simple to determine, their dimensions follow directly from the rank-nullity theorem that relates the subspace dimensions of the network's kinematic matrix[54,84–87]. The rank-nullity theorem states that the sum of the number of independent FM (N_{FM}) and the number of independent LB-states is equal to $2N_n$, while the sum of the number of independent SS-states (N_{SSS}) and LB-states must be equal to N_b. Therefore, the difference between the number of SS-states and FM has a consistent expression for all 2D materials:

$$\nu = N_{FM} - N_{SSS} - 3 = 2N_n - N_b - 3, \tag{4.1}$$

where the final term of -3 represents the three trivial rigid-body motions in 2D, so that N_{FM} includes only internal floppy deformations of the structure.

The above linear-elastic model helps understand the difference in stress response between two networks with closely related architectures that differ by a small number of bonds, but have the same number and spatial configuration of nodes. In either network, the SS-space and LB-space together span the entire space of possible bond stress configurations. Some SS-states and LB-states are shared between the two materials, while others are unique to either of the pair. Any SS-state unique to one network must be an LB-state—up to stresses on the networks' distinct bonds—in the other structure. Since the stress response of any network is a linear combination of its LB-states, the stress

response difference between the two networks must therefore lie in the space spanned by their unique, non-shared SS-states. In other words, *with knowledge of the mutually exclusive SS-states of two mechanical networks, we can a priori determine how their stress response differs under arbitrary external loading.*

We note here that our analysis concerns the material's response under an applied *supported* load: external forces that actuate a floppy motion of the material lead to an indeterminate response[54], which we do not consider here.

4.3. Structurally complex mechanical metamaterials

We now demonstrate the efficacy of predicting the stress response difference using SS-states—an approach valid for *any* mechanical network architecture—in the particular class of structurally complex mechanical metamaterials[13] introduced in chapter 2. The specific architecture of these metamaterials allows us to easily enumerate and construct a basis of SS-space consisting of highly spatially localized states, and we show later that this complete description of SS-space produces a direct prediction of the stress response difference between two networks of differing designs under identical, external, supported loads.

Our complex mechanical metamaterials are assembled by stacking together copies of an anisotropic triangular building block[13] (Fig. 4.2a, first introduced in chapter 2.2) that we will refer to in the remainder of this chapter as a *supertriangle.*

The smallest nontrivial structure, made with six supertriangles, is a hexagonal stack or *superhexagon* (Fig. 4.2c). Such stacks are called *compatible* when there is a collective FM, such that all individual supertriangles can deform according to their local FM simultaneously; otherwise, the stack is *incompatible* or frustrated. Evidently, even though the number of nodes and bonds of compatible and incompatible superhexagons are identical ($N_n = 19$ and $N_b = 8$), they show distinct mechanical behaviour. Using Eq. (4.1), we find that incompatible superhexagons have no FM and a single SS-state, while compatible superhexagons have a single FM and two SS-states.

We map the local FM of a supertriangle to the ground state of an Ising model with antiferromagnetic interactions[13]. Specifically, each internal node corresponds to a spin site, while each internal bond represents an antiferromagnetic interaction. Spins may be in an 'out' state or an 'in' state; mechanically, this corresponds to an outward or inward motion of the internal nodes with respect to the centre for upward-pointing supertriangles (and vice versa for downward-pointing supertriangles) indicated by the red and blue arrows in Fig. 4.2b. The supertriangle's mechanical FM then corresponds uniquely to a spin configuration that satisfies both antiferromagnetic interactions: the internal bonds connect spin sites at two internal nodes in opposite states, while nodes not connected by an internal bond both move inward (or both outward), representing two ferromagnetically interacting spins.

For a compatible superhexagon, the spin orientations of all adjacent supertriangles have to match up exactly.This requirement is only met if the local loop contains an even number of interactions. Hence, a superhexagon is only compatible if the local loop con-

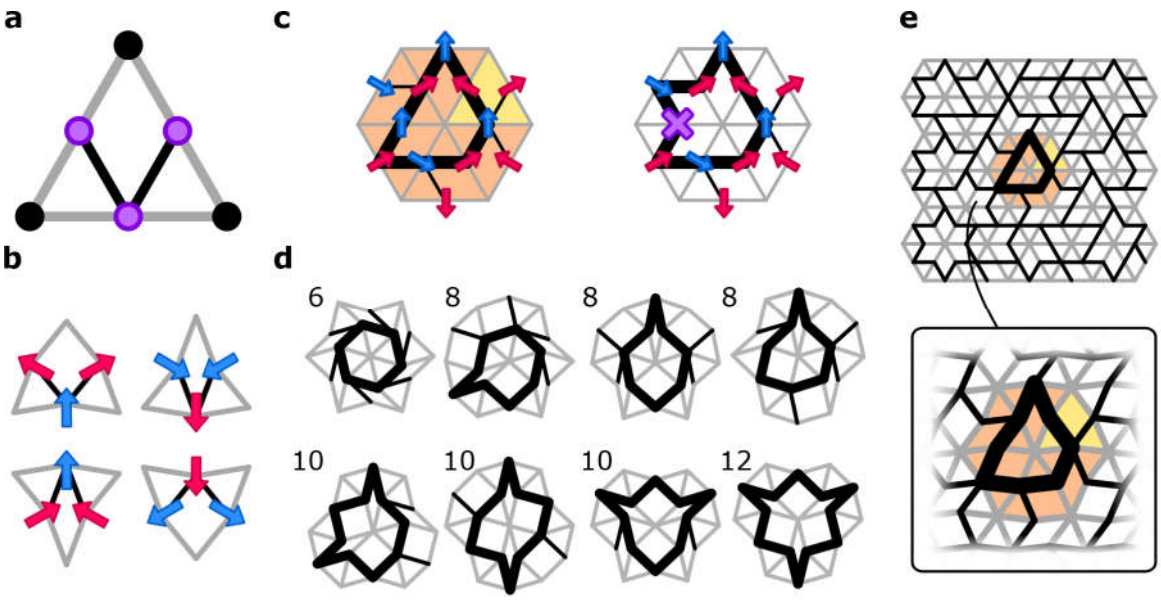

Fig. 4.2.: **a**, Our mechanical building block, or supertriangle, consists of three corner nodes (black circles) and three edge nodes (purple), connected by a perimeter of edge bonds (grey lines). The edge nodes are connected by two internal bonds (black). **b**, Internal node motions and internal bonds map to Ising spins and antiferromagnetic interactions. Compatible deformations of the supertriangle correspond to ground states of this Ising model. The correspondence between spin states ('in' and 'out', indicated with blue and red arrows) and motion of the edge nodes is opposite for upward- and downward-pointing building blocks. **c**, Supertriangles (yellow triangle) are stacked together to create a superhexagon. Superhexagons contain a closed *local loop* of internal bonds (bold black lines). The metamaterial deforms harmoniously only when a spin ground states exists that satisfies all antiferromagnetic constraints simultaneously. Local loops with an even number of bonds satisfy this requirement (left): the superhexagon is compatible. Incompatible superhexagons have loops containing an odd number of bonds (right) that frustrate at least one antiferromagnetic interaction (purple cross). The odd local loop represents a *defect* in the system. **d**, The eight possible even local loop shapes (number of bonds indicated) in a compatible superhexagon are shown (bold black lines). Internal bonds outside the local loop were chosen arbitrarily, and the corresponding floppy modes are illustrated as deformations of the superhexagons. **e**, A large compatible metamaterial is created by stacking building blocks, ensuring that the local loops inside each superhexagon (orange hexagon) contain an even number of bonds. The compatible metamaterial deforms harmoniously (zoom-in).

tains an even number of internal bonds (Fig. 4.2c, left).

By contrast, when the local loop has an odd number of internal bonds, the superhexagon is geometrically frustrated and incompatible[41,88]. In the Ising model language, there is then always an antiferromagnetic interaction that cannot be satisfied (Fig. 4.2c, right), so that the odd local loop represents a defect in the mechanical system.

In Fig. 4.2d, we show the FM in compatible superhexagons for each of the eight possible even local loop shapes (with six, eight, ten or twelve bonds, bold black lines); the FM is present independently of the choice of internal bonds outside the local loop (thin black lines).

Metamaterials consisting of large stacks containing many supertriangles (Fig. 4.2e) typically contain many superhexagons, each sporting a local loop of internal bonds. Designing the material so that there are only even local loops in the system ensures that all superhexagons are compatible, the material has a single global FM, and can deform harmoniously. Conversely, odd local loops generate geometric frustration and incompatibility, resulting in the absence of a global FM. As discussed in section 2.3.2, there is an extensive number of metamaterial designs made of these supertriangular building blocks. Moreover, we can design a wide array of geometries with varying isotropy, auxeticity, and periodicity. Here, we explore the evolving mechanical response under architectural changes in this class of spatially complex metamaterials, and our findings thus hold for metamaterials with a wide range of mechanical properties.

4.4. States of self stress in superhexagons and larger metamaterials

We now show how to identify the dimension and shape of the SS-space in our complex metamaterials, which governs the differential response of architecturally related networks. Our compatible metamaterials have one global FM by construction, while frustrated ones have none. Hence, to obtain the number of independent SS-states from Eq. (4.1), it suffices to calculate the index ν. We show below that ν follows directly from the number H of superhexagons contained inside our metamaterial, and that each compatible (incompatible) superhexagon contains two (one) localized SS-states that can be explicitly and straightforwardly constructed.

To count the number of superhexagons in a metamaterial, we first focus on the structure's scaffold that consists of corner nodes connected by a triangular lattice (Fig. 4.3a). If such a scaffold contains T triangles and a perimeter of P bonds, it contains

$$H = \frac{T - P}{2} + 1 \tag{4.2}$$

full hexagons of six triangles, each surrounding a distinct bulk corner node (orange hexagon and bold black dots in Fig. 4.3a). This expression is derived as follows: a single triangle has $T = 1$, a perimeter of $P = 3$ and $H = 0$ hexagons. Adding a triangle to an existing system increases the number of triangles by one ($T \to T+1$), and either increases the perimeter by two bonds and produces no new hexagon ($P \to P + 2, H \to H$), or increases the perimeter by one bond and produces a new hexagon ($P \to P+1, H \to H+1$). By induction, Eq. (4.2) then holds for all lattices.

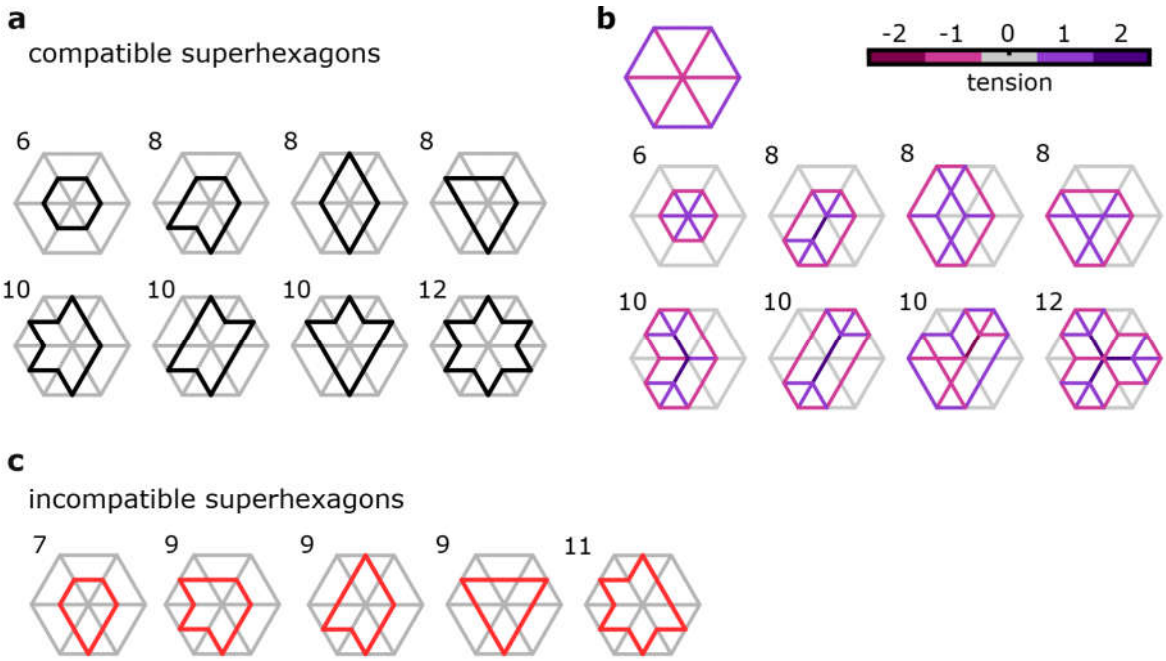

Fig. 4.4.: States of self stress (SS-states) are localized in superhexagons. **a**, The eight possible even local loop shapes in a compatible superhexagon are shown (black lines). The number of bonds in each loop is indicated. Some internal bonds outside the local loop may be chosen freely (not shown here for clarity), while the triangular scaffold (grey solid lines) is always present. **b**, The compatible superhexagons contain two non-orthonormal SS-states (colours): a *radial SS-state* localized on the triangular scaffold (top), and a *loop SS-state* fully localized on internal bonds in the local loop and the triangular scaffold. **c**, Incompatible superhexagons contain odd local loops that come in five distinct shapes (red lines). These structures each support only the radial SS-state.

We now use this information to determine a general expression for ν in our metamaterials. Adding two internal bonds and three edge nodes to every triangle in the scaffold—thus creating a stack of T supertriangles—generates a metamaterial (Fig. 4.3b). Since the triangular scaffold contains a total of $N_b = \frac{3T+P}{2}$ bonds, the metamaterial will contain $3T + P$ edge bonds and an additional two internal bonds per triangle, yielding a total of $N_b = 5T + P$ edge and internal bonds. In addition, the scaffold contains $N_n = \frac{T+P}{2} + 1$ corner nodes; the metamaterial has an additional three edge nodes that are shared between two triangles, unless they lie on the structure's perimeter. This yields a total of $N_n = 2T + P + 1$ corner and edge nodes in the metamaterial (Fig. 4.3c). The metamaterial's index ν is thus equal to

$$\nu = 1 - 2H. \tag{4.3}$$

From Eq. (4.1), and using the fact that the number of FM in a metamaterial is either one or zero, we obtain an exact expression for the dimension of SS-space in our metamaterials: $N_{SSS} = 2H$ in compatible systems, and $N_{SSS} = 2H - 1$ in incompatible ones. This expression is consistent with our finding in Sec. 4.3 that a compatible superhexagon contains two SS-states, while an incompatible superhexagon has one SS-state. Thus, in a compatible metamaterial with H hexagons, we can identify $2H$ independent SS-states

localized within each of the metamaterial's superhexagons; these SS-states exactly span the $2H$-dimensional SS-space. Therefore, *all independent SS-states of a compatible metamaterial can be constructed as localized states within each of the larger metamaterial's superhexagons.*

We illustrate the compact, superhexagon-localized representation of all independent SS-states in Fig. 4.4. Consider a metamaterial consisting of a single, compatible superhexagon. Its local loop contains an even number of internal bonds; the structure has a single FM, and two SS-states. Figure 4.4a enumerates the eight possible even local loop shapes (up to rotations and reflections); internal bonds outside of the local loop do not carry stress in any of the SS-states, and are not shown for clarity. Due to the network's highly regular geometry, the SS-states are found by inspection to have a simple structure: one *radial SS-state* is independent of the superhexagon's internal bonds and is purely supported on edge bonds, while the other *loop SS-state* involves the internal bonds of the local loop (Fig. 4.4b). The location of internal bonds that are not part of the local loop are irrelevant for both the radial and loop SS-states. Bond stresses of both radial and loop SS-states are integer multiples due to the underlying building blocks' six-fold rotational symmetry. By contrast, a single, incompatible superhexagon containing an odd local loop has no FM and only one SS-state; the local loop has five possible shapes (Fig. 4.4c), and the superhexagon supports only the single radial SS-state (Fig. 4.4b, left).

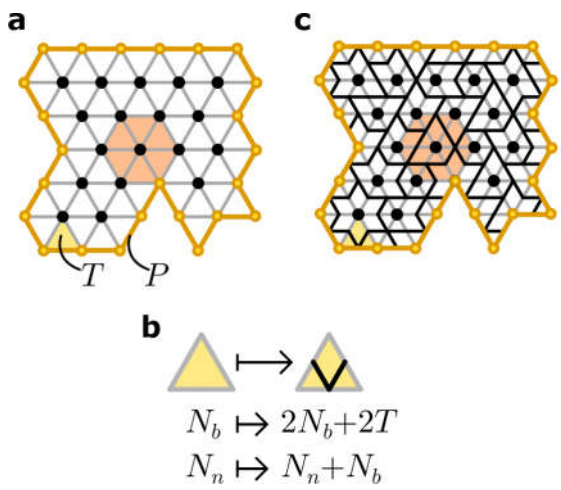

Fig. 4.3.: The number of nodes and bonds in a metamaterial can be counted exactly. **a**, Starting from a network of T adjacent triangular cells (yellow triangle) with a perimeter of P bonds and P nodes (orange lines and circles), the number of nodes and bonds N_n and N_b can be counted exactly. Each internal lattice point (black circles) is surrounded by a hexagon of six triangular blocks (orange hexagon). **b**, Each block is decorated with two internal bonds and three edge nodes, producing a supertriangle. **c**, This decoration produces a metamaterial. The number of nodes and bonds increases to $N_n + N_b$ and $2N_b + 2T$.

In compatible metamaterials consisting of H compatible superhexagons, the $2H$ -dimensional SS-space is therefore spanned by H radial and H loop SS-states, each of which is localized to a single superhexagon. Similarly, in a metamaterial with a single incompatible superhexagon, the $(2H-1)$-dimensional SS-space consists of the H radial SS-states, and the $H-1$ loop SS-states in the remaining compatible superhexagons. For larger numbers $H_o > 1$ of incompatible superhexagons, H radial and $H - H_o$ loop SS-states are present in the network, with the remaining $H_o - 1$ SS-states not localized to a single superhexagon.

4.5. Architectural defects

While we can make a large variety of compatible metamaterials (a number that grows exponentially with the number of supertriangles in the structure, see section 2.3.2), an even larger amount of frustrated designs exist that cannot deform harmoniously due to the presence of one or more odd local loops. The mechanical frustration induced by such defects generally produces undesired effects when their presence is not controlled, such as decay of a desired FM[29,39], or structural failure when frustration-induced bond stresses exceed the bond buckling threshold[40]. However, when frustration is introduced in a controlled and well-understood manner, it may be harnessed to design desirable or unusual physical properties, such as localized buckling zones[13,18,22], or geometric frustration in spin-ices[41–43].

We now show how to redirect frustration in our mechanical metamaterials by rotating select supertriangles in an initially compatible network. Figure 4.5a shows a compatible structure with no defects (A), where all superhexagons have even local loops (black lines). Selecting and rotating a particular supertriangle in the material's bulk (Fig. 4.5a, inset) effectively removes one of the supertriangle's internal bonds—bond r—from the network and replaces it with a newly added internal bond p. The bond r is part of exactly two local loops. In general, exchanging bond r for bond p changes the parity of these two local loops. Here, since we start from a compatible structure, rotating a supertriangle creates two adjacent odd local loops (Fig. 4.5b). We will refer to such a pair of adjacent odd local loops as a *structural defect* (network B), since the odd loops may be removed by locally rotating a single supertriangle[13].

Metamaterials containing a single incompatible superhexagon can also be constructed, and have been shown in previous work to have a topological signature[13]. Such *topological defects* (network C) can be generated from an initially compatible system via a sequence of supertriangle rotations running in a chain between the defect locus and the system's boundary. Specifically, we rotate a supertriangle at the edge of a structural defect, ensuring that this supertriangle contributes an internal bond to one odd and one even local loop (Fig. 4.5b). As before, the rotation changes the parity of the two local loops it contributes to. Consequently, the two odd local loops are no longer adjacent after the transformation: they are now separated by a single even local loop. This defect configuration, consisting of two incompatible superhexagons separated by one or more compatible ones, is a complex of two *topological defects* (network C): the odd local loops can no longer be removed by a single, local supertriangle rotation. To finally obtain a single topological defect, we repeat the above procedure to displace one of the odd local loops closer and closer to the system's boundary. Finally, we select a boundary supertriangle that contributes to exactly one odd local loop, so that its rotation causes the odd loop's parity to become even (Fig. 4.5c). This transformation leaves us with an isolated incompatible superhexagon in the system's bulk, that can only be removed by an extensive number of supertriangle rotations, and that we therefore refer to as a topological defect (Fig. 4.5d).

Supertriangle rotations thus form the minimal architectural transformations that allow us to convert one metamaterial design to any other. By a series of sequential supertriangle rotations, we can thus obtain metamaterial architectures with any desired number of frustrated odd local loops, starting from a compatible structure containing only even

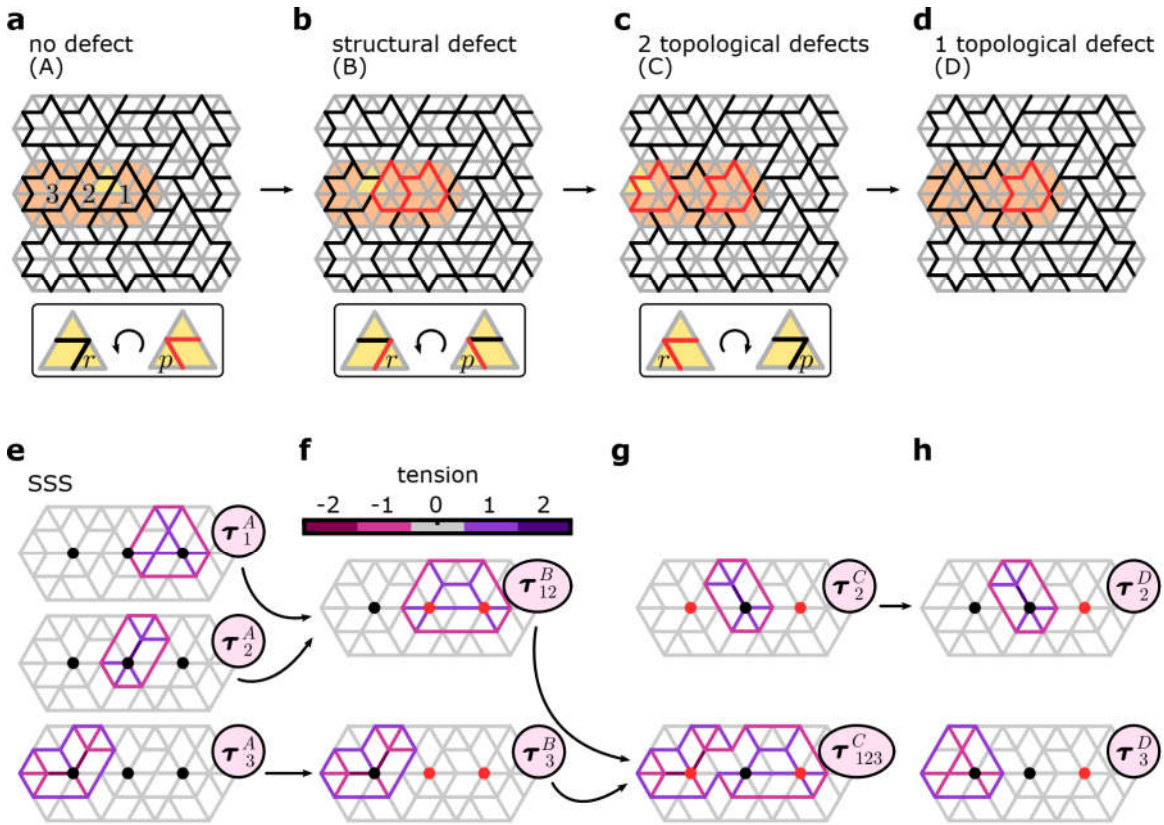

Fig. 4.5.: **a**, A compatible metamaterial (no defect, A) contains only even local loops (internal bonds highlighted in black). Three superhexagons $(1, 2, 3$; orange) that change parity under consecutive transformations are highlighted. Rotating a single bulk supertriangle shared by superhexagons 1 and 2 (yellow triangle, inset) removes a bond r and adds a bond p. **b**, The supertriangle rotation generates two adjacent odd local loops (red lines). These form a *structural defect* (B) that frustrates the compatible motion of the material. The adjacent odd local loops are moved apart by selecting and rotating a second supertriangle in superhexagons 2 and 3 (inset). **c**, Two *topological defects* (C), or isolated odd local loops, are created: an even local loop now separates the odd local loops. A final rotation in superhexagon 3 (inset) removes one of the odd local loops from the material. **d**, A single topological defect (D) remains. **e**, The three numbered superhexagons in the compatible metamaterial are shown, along with their central corner nodes (black circles) and their corresponding loop SS-states $\boldsymbol{\tau}_1^A$, $\boldsymbol{\tau}_2^A$ and $\boldsymbol{\tau}_3^A$ (colours). (f-h) Transforming the network to produce a structural defect, two topological defects, and a single topological defect (central corner nodes of incompatible superhexagons indicated in red) results in a sequential evolution where new SS-states are formed from linear combinations of old SS-states (arrows; see text for detailed expressions). In panels **f** and **g**, two odd local loops are present in the network, and the SS-space can no longer be represented by purely superhexagon-localized SS-states. However, a (maximally) localized representation does exist, where an SS-state runs over the superhexagons along the shortest path between the two odd local loops. In panel **h**, there is only one incompatible superhexagon; all SS-states are localized within distinct superhexagons.

local loops.

4.6. Response evolution under architectural transformations

Starting from an initially compatible metamaterial, supertriangle rotations form minimal architectural transformations that generate predictable defect configurations. Here, we investigate how the concomitant frustration manifests in the mechanical response. Clearly, a frustrated metamaterial cannot deform harmoniously, so external forcing will generate stresses and elastic deformations. We want to understand where these stresses are localized, and how they relate to the sequence of architectural transformations that generate a given network design.

In Sec. 4.2, we discussed how the mechanical response of a network is determined by its N_b-dimensional stress space, which can be decomposed into two mutually orthogonal sub-spaces: the N_{SS}-dimensional SS-space, and the N_{LB}-dimensional LB-space. To understand how architectural changes affect the stress response, we therefore need to establish how the SS-space and the complementary LB-space change under architectural modifications. Our metamaterials, with their readily constructed SS-states, are especially suitable to address such general questions.

To capture the changes of the SS- and LB-spaces due to architectural modifications, we repeatedly use a number of basic principles that we outline here. We only consider architectural changes that consist of sequences of supertriangle rotations, and break up each supertriangle rotation into a step-by-step process where we first remove a bond and then add a bond at a different location, which simplifies our calculations and generalizes easily to other network architectures.

Supertriangle rotations can mutate the compatibility of our metamaterials: there exist three different mutation processes. First of all, in process I, a compatible system A transforms into an incompatible system B (see e.g. Fig. 4.5a,b). Secondly, process II converts an incompatible system B into a distinct incompatible system C (see e.g. Fig. 4.5b,c), and lastly, process III converts a compatible system A into a compatible system A'. Process III can only occur for specific supertriangle rotations at the edge of a metamaterial, and is trivial from the perspective of the mechanical response; we do not consider it further here (see Appendix A.3 for details). In process I, we start from a compatible system A, then remove a bond labelled r to obtain the intermediate system AB, and then add bond labelled p to obtain the incompatible system B. In process II, we start from an incompatible system B, then remove a bond labelled r to obtain the intermediate system BC, and then add bond labelled p to obtain the incompatible system C.

Now that we have broken down possible structural changes into a precise sequence of removing and adding bonds, we can determine how the *dimension* of the SS- and LB-space changes in each transformation step, using constraint counting (see Sec. 4.4). First of all, in process I, step $A \to AB$ removes one SS-state, while the number of LB-states remains constant. Step $AB \to B$ leaves the SS-states unaffected, while the number of LB-states increases by one. Secondly, in process II, step $B \to BC$ removes one SS-state, while the number of LB-states remains constant. Step $BC \to C$ adds one SS-state, while

the number of LB-states remains constant.

Crucially, changes to the *dimensionality* of the SS- and LB-spaces do not capture their full reconfiguration. As an example, consider step $A \to AB$, where bond r is removed from network A: while the number of LB-states remains constant, the removal of bond r induces changes to the structure of these states. After all, LB-states may have a finite stress on bond r in network A, but LB-states of network AB must have zero stress on the nonexistent bond r.

In order to fully capture changes in the SS- and LB-spaces, we must construct appropriate bases for them, to make their evolution tractable. As the SS-states are easier to identify than the LB-states in our particular metamaterials, we construct an orthonormal basis for the SS-space of our metamaterials, such that removing a bond b will affect at most one basis vector. This basis consists of *(i)* at most one SS-state vector that has a finite stress on bond b, which is modified under removal of bond b, and *(ii)* all other basis vectors that have zero stress on bond b[89].

The two subspaces *(i)-(ii)* are mutually orthogonal; moreover, the LB-space is orthogonal and complementary to the SS-space. Hence, changes in the subspace *(i)* directly affect the LB-space. The LB-space ultimately determines the metamaterial's response under external loading. However, as we discussed at the end of Sec. 4.2, the stress response difference between two networks related by a single supertriangle rotation is determined by their mutually exclusive SS-states. Thus, the evolution of the SS-space suffices to capture the evolution of the metamaterial's response, as a detailed derivation in Appendices A.3–A.5 confirms.

In the following, we therefore first describe how to construct all SS-states in compatible and incompatible metamaterials as linear combinations of radial and loop SS-states in Sec. 4.6.1. We consider process I in Sec. 4.6.2, identifying the changes to the SS-space, and process II in Sec. 4.6.3, again determining changes to the SS-space. Ultimately, we establish that the evolution of SS-space under supertriangle rotations is limited to a small and predictable span of stress vectors. We close this section with a discussion in Sec. 4.6.4 of the mechanical consequences of these SS-space changes due to supertriangle rotations.

4.6.1. Constructing the states of self stress

As shown in Sec. 4.4, the SS-space of any compatible metamaterial is spanned by superhexagon-localized radial and loop SS-states (see Fig. 4.4b). Together, the superhexagon-localized states form a complete, non-orthogonal basis of the material's SS-space. However, a different approach is needed to identify a complete basis of the SS-space for incompatible metamaterials: as we will show below, in frustrated systems, some SS-states cannot be represented as superhexagon-localized states, but must be *delocalized*. Here, we present an iterative approach to construct a basis of SS-space for *any* metamaterial—compatible or not—and show that all delocalized SS-states can be constructed as linear combinations of radial and loop SS-states.

We illustrate our approach by constructing a basis of the SS-space in the four architecturally related networks presented in Fig. 4.5a-d, with network A containing no defect,

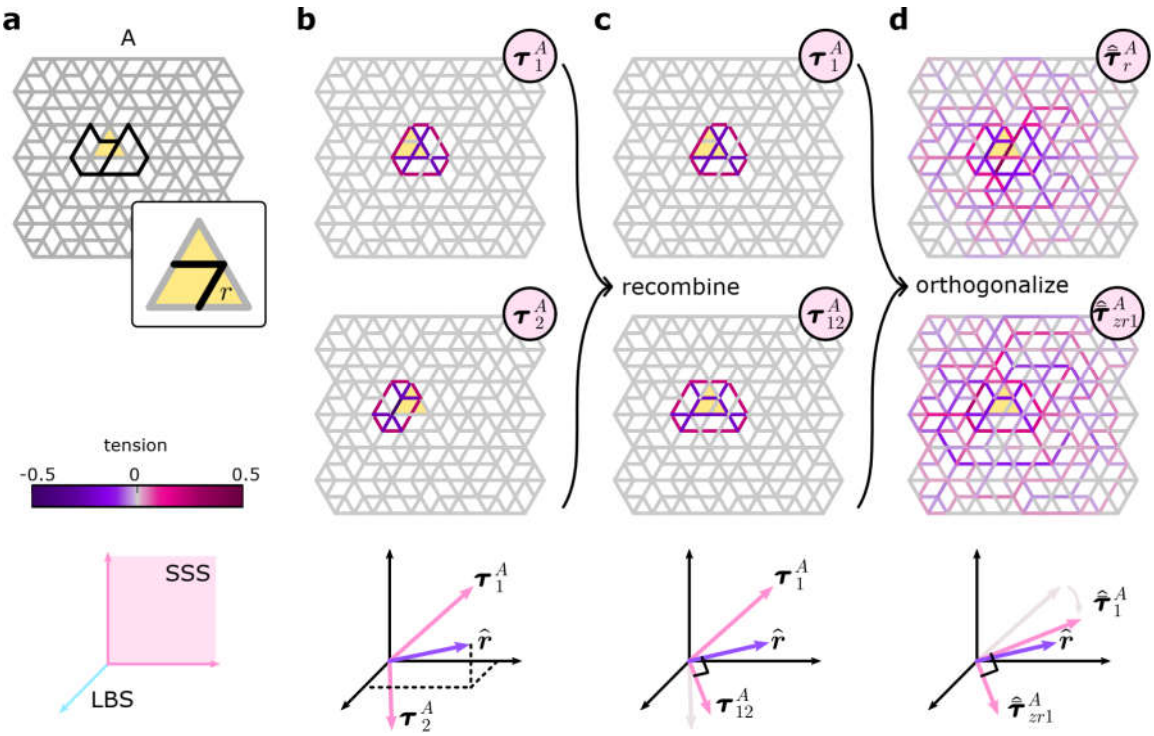

Fig. 4.6.: We identify the unique state of self stress (SS-state) $\hat{\bar{\boldsymbol{\tau}}}_r^A$ that is modified under a supertriangle rotation in an initially compatible network A. **a**, We transform the network by rotating a certain building block (yellow triangle), such that bond r (zoom-in) is removed from the network. Bottom: the N_b-dimensional space of bond stress states is schematically represented as a space consisting of LB-states (blue, represented as a one-dimensional line) and SS-states (pink). **b**, Only the two loop SS-states $\boldsymbol{\tau}_1^A$ and $\boldsymbol{\tau}_2^A$ with a nonzero stress on bond r need to be considered. Bottom: the non-orthogonal SS-states $\boldsymbol{\tau}_1^A$ and $\boldsymbol{\tau}_2^A$ lie in the SS-space plane (pink vectors), while the stress vector $\hat{\boldsymbol{r}}$ (purple vector), with nonzero stress on bond r, overlaps with both SS-space and LB-space (dashed lines). Both SS-states overlap with $\hat{\boldsymbol{r}}$. **c**, The two SS-states are recombined to yield the vectors $\boldsymbol{\tau}_1^A$ and $\boldsymbol{\tau}_{12}^A$, so that $\boldsymbol{\tau}_1^A$ is the only SS-state with nonzero stress on bond r^A. Bottom: the SS-states are recombined so that $\boldsymbol{\tau}_{12}^A$ is orthogonal to $\hat{\boldsymbol{r}}$, and only $\boldsymbol{\tau}_1^A$ overlaps with $\hat{\boldsymbol{r}}$. **d**, The two SS-states are orthogonalized with respect to all other (superhexagon-localized) SS-states via a Gram-Schmidt process. Two SS-states $\hat{\bar{\boldsymbol{\tau}}}_r^A$ and $\hat{\bar{\boldsymbol{\tau}}}_{zr1}^A$ are obtained, such that only the former has nonzero stress on bond r. Thus, $\hat{\bar{\boldsymbol{\tau}}}_r^A$ is lost after the supertriangle rotation that removes bond r. Bottom: orthogonalization produces the SS-state $\hat{\bar{\boldsymbol{\tau}}}_r^A$, orthogonal to all LB-states and the remaining SS-states, and uniquely overlapping with $\hat{\boldsymbol{r}}$.

B a structural defect, C two topological defects, and D a single topological defect, as a specific demonstration of our general strategy. Figure 4.5e shows the three highlighted compatible superhexagons, numbered 1, 2 and 3 in the compatible network A, that are modified during the network transformations. The three superhexagons support three radial SS-states (see Fig. 4.4b above), not shown here for brevity. As the network transformations considered here leave the scaffold of edge bonds intact, the H radial SS-states remain, irrespective of the number of supertriangle rotations. We focus on the loop SS-states that are localized in these three superhexagons, which we will denote $\boldsymbol{\tau}_1^A$, $\boldsymbol{\tau}_2^A$, and $\boldsymbol{\tau}_3^A$, and which are shown in Figure 4.5e. Rotating a supertriangle in network A that is part of both superhexagons 1 and 2 removes one bond, r (Fig. 4.5a,b). This rotation also lowers the number of SS-states by one. First, we note that $\boldsymbol{\tau}_3^A$ does not induce a stress on bond r, so that this SS-state is retained in network B. However, $\boldsymbol{\tau}_1^A$ and $\boldsymbol{\tau}_2^A$ do include a stress on bond r: hence, they cannot be SS-states of network B. We construct a new SS-state for network B as a linear combination of $\boldsymbol{\tau}_1^A$ and $\boldsymbol{\tau}_2^A$ that leaves bond r unstressed: $\boldsymbol{\tau}_{12}^B = \boldsymbol{\tau}_1^A + \boldsymbol{\tau}_2^A$ (see Fig. 4.5f)). Here we use the subscript 12 to indicate that this SS-state is delocalized: it is contained within the two incompatible superhexagons 1 and 2. All other SS-states in network A, similar to $\boldsymbol{\tau}_3^B = \boldsymbol{\tau}_3^A$, are retained in network B.

A second supertriangle rotation in network B produces two separated topological defects in network C (Fig. 4.5c), but does not change the number of SS-states. Since a distinct bond r is now removed during the supertriangle rotation, and both $\boldsymbol{\tau}_{12}^B$ and $\boldsymbol{\tau}_3^B$ produce a finite stress on bond r, these two SS-states cannot persist in the network. By a similar superposition as above, we obtain a new SS-state $\boldsymbol{\tau}_{123}^C = \boldsymbol{\tau}_{12}^B + \boldsymbol{\tau}_3^B$. This SS-state spans the connecting path between the two odd loops, since $\boldsymbol{\tau}_{123}^C = \boldsymbol{\tau}_1^A + \boldsymbol{\tau}_2^A + \boldsymbol{\tau}_3^B$. However, to maintain the overall number of SS-states, a new SS-state is also formed: the supertriangle rotation makes superhexagon 2 compatible, resulting in the appearance of the localized loop SS-state $\boldsymbol{\tau}_2^C$ (see Fig. 4.5f). In general, in a network denoted X, the two SS-states $\boldsymbol{\tau}_i^X$ and $\boldsymbol{\tau}_j^X$—with nonzero stress on the bond r that is removed due to a supertriangle rotation—are recombined to form a new SS-state $\boldsymbol{\tau}_{ij}^{X+1}$. This SS-state is found via the equation

$$\boldsymbol{\tau}_{ij}^{X+1} = \boldsymbol{\tau}_i^X - \frac{\boldsymbol{\tau}_i^X \cdot \hat{\boldsymbol{r}}}{\boldsymbol{\tau}_j^X \cdot \hat{\boldsymbol{r}}} \boldsymbol{\tau}_j^X, \tag{4.4}$$

where $\hat{\boldsymbol{r}}$ is a bond stress vector with unity value on bond r, and zero value on all other network bonds.

Finally, rotating a last supertriangle in network C produces network D that contains a single topological defect; the number of SS-states remains the same. The delocalized state $\boldsymbol{\tau}_{123}^C$, with its nonzero stress on the removed bond r, is no longer an SS-state; however, the loop SS-state $\boldsymbol{\tau}_2^C$ is retained, and a new loop SS-state $\boldsymbol{\tau}_3^D$ arises in the newly formed compatible superhexagon (see Fig. 4.5h). Note that the SS-states of network D, with its single incompatible superhexagon, can be identified directly. Since this network is incompatible, it has $2H - 1$ SS-states; H of these are radial SS-states that are localized in all superhexagons, and $H-1$ SS-states are localized on the $H-1$ compatible superhexagons.

In general, a complete basis of SS-space can be obtained for any H-superhexagon incompatible metamaterial with $H_o > 1$ odd loops (see Appendix A.2) by constructing the $H_o - 1$ delocalized SS-states (Sec. 4.4) via the steps shown in Fig. 4.5e-g. Thus, an independent, yet non-unique and non-orthogonal basis of SS-space can be constructed in

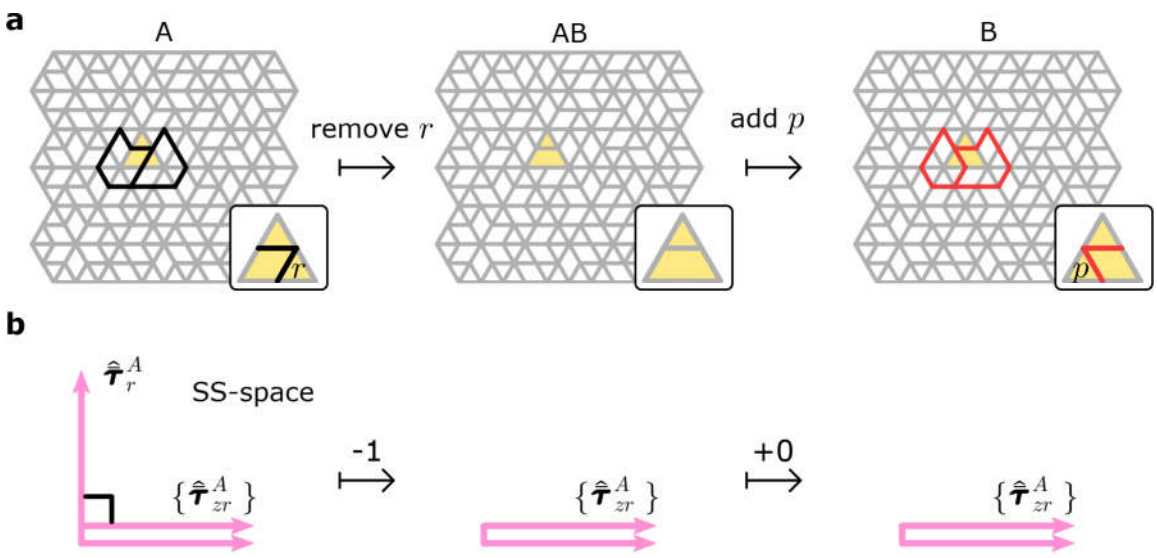

Fig. 4.7.: Evolution of the SS-space under a supertriangle rotation according to process I. **a**, A compatible network A is transformed to an incompatible network B via an intermediate network AB, by first removing bond r and then adding bond p (insets). **b**, For network A, we construct orthogonal bases for the SS-space that contain the states $\{\hat{\bar{\boldsymbol{\tau}}}_{zr}^A\}$ that have zero stress on bond r and that remain in the SS-spaces of network AB as well as B. The full basis of network A additionally contains an SS-state $\hat{\bar{\boldsymbol{\tau}}}_r^A$ that is removed during the architectural transformation (see text). Black square signifies orthogonality, and arrows with numbers indicate changes in the dimensions of the SS-space.

each of our mechanical metamaterials.

This procedure illustrates that in all cases, whether the metamaterial contains no, one, or more local odd loops, the SS-space is spanned by a complete basis consisting of radial SS-states; loop SS-states localized in compatible superhexagons; and delocalized linear combinations of loop SS-states running between incompatible superhexagons. Such extended SS-states are reminiscent of flux lines that connect pairs of defects in artificial spin-ice models[90].

4.6.2. Process I: supertriangle rotation from a compatible to an incompatible geometry

Now that we are able to construct bases of the SS-spaces of our metamaterials, we are in a position to understand how the SS-spaces change under architectural transformations, beginning with process I that converts a compatible to an incompatible metamaterial.

(i) We first construct a suitable orthogonal basis for the SS-space for a compatible network A. Our goal is to identify the unique SS-state in network A, $\bar{\boldsymbol{\tau}}_r^A$, that has a finite stress on bond r and that therefore is not present in network AB; and to construct the set of $2H-1$ orthonormal basis vectors $\{\bar{\boldsymbol{\tau}}_{zr}^A\}$ that have zero stress on bond r, are perpendicular to $\bar{\boldsymbol{\tau}}_r^A$, and remain present in network AB. Here, the symbol $\boldsymbol{\tau}$ indicates an SS-state; the superscript A indicates the network; and the subscripts r or zr indicate whether the vector has nonzero or zero stress on bond r, respectively.

We construct $\bar{\boldsymbol{\tau}}_r^A$ and $\{\bar{\boldsymbol{\tau}}_{zr}^A\}$ as follows, as shown in Fig. 4.6. First, as bond r is shared between exactly two even local loops in A (Fig. 4.6a), there are two unique loop SS-states $\boldsymbol{\tau}_1^A$ and $\boldsymbol{\tau}_2^A$ with nonzero stress on r (Fig. 4.6b), and $2H-2$ loop SS-states $\{\boldsymbol{\tau}_i^A\}_{i=3}^{2H-2}$ with zero stress on r. We construct an additional SS-state with zero stress on r by taking a linear combination of $\boldsymbol{\tau}_1^A$ and $\boldsymbol{\tau}_2^A$ (Fig. 4.6c):

$$\boldsymbol{\tau}_{12}^A = \boldsymbol{\tau}_1^A - \frac{\boldsymbol{\tau}_1^A \cdot \hat{\boldsymbol{r}}}{\boldsymbol{\tau}_2^A \cdot \hat{\boldsymbol{r}}}\, \boldsymbol{\tau}_2^A \ , \tag{4.5}$$

where $\hat{\boldsymbol{r}}$ is the unit bond stress vector with unity value on bond r, and zero stress elsewhere. The SS-state $\boldsymbol{\tau}_1^A$ is, by construction, the only state in our SS-space basis $\{\boldsymbol{\tau}_1^A, \boldsymbol{\tau}_{12}^A, \{\boldsymbol{\tau}_i^A\}_{i=3}^{2H}\}$ with nonzero stress on r. We now perform a sequential Gram-Schmidt process (GS) on the ordered set (left to right) of SS-states to orthonormalize the basis:

$$\{\{\hat{\bar{\boldsymbol{\tau}}}_{zr}^A\}, \hat{\bar{\boldsymbol{\tau}}}_r^A\} = \mathrm{GS}[\{\{\boldsymbol{\tau}_i^A\}_{i=3}^{2H}, \boldsymbol{\tau}_{12}^A, \boldsymbol{\tau}_1^A\}] \ , \tag{4.6}$$

where the bar and hat in $\hat{\bar{\boldsymbol{\tau}}}$ indicate orthogonality and normality respectively. The first two SS-states of the basis are illustrated in Fig. 4.6d. Going from network A to AB by removing bond r removes one SS-state, which must be $\hat{\bar{\boldsymbol{\tau}}}_r^A$ (Fig. 4.6d), while the remaining $\{\hat{\bar{\boldsymbol{\tau}}}_{zr}^A\}$ span the SS-space of network AB. Going from network AB to B by adding bond p leaves the SS-space unaffected.

For completeness, the evolution of the complementary LB-space is presented in Appendix A.3 via a similar strategy.

In summary, when a compatible metamaterial A is converted to an incompatible architecture B according to process I, the evolution of the SS-space is simple once an appropriate basis is constructed. The SS-spaces of architecturally related networks A and B are identical up to the SS-state $\hat{\bar{\boldsymbol{\tau}}}_r^A$, present in network A, but not in B, as illustrated schematically in Fig. 4.7.

4.6.3. Process II: supertriangle rotation from an incompatible to another incompatible geometry

We now discuss the stress space changes of process II, converting an incompatible network B to an intermediate network BC and finally to a distinct incompatible network C, as shown in Fig. 4.8a. There are two calculations necessary to understand process II, and they are shown schematically in Fig. 4.8b. With minor modifications, these calculations follow the strategy developed for process I above. We again denote the removed and added bonds by r and p, although we note that these refer to different bonds than in process I.

(i) We construct an orthogonal basis for the SS-space of the incompatible network B by identifying its unique SS-state, $\hat{\bar{\boldsymbol{\tau}}}_r^B$, that has a finite stress on bond r (and is thus not present in network BC), and constructing the remaining set of orthogonal basis vectors $\{\hat{\bar{\boldsymbol{\tau}}}_{zr}^B\}$ that have zero stress on bond r (and thus remain present in network BC). To do this, we use the same method as for process I, step *(i)* above: we first construct τ_{12}^B, create a basis $\{\boldsymbol{\tau}_1^B, \boldsymbol{\tau}_{12}^B, \{\boldsymbol{\tau}_i^B\}_{i=3}^{2H}\}$, and perform a sequential Gram-Schmidt process (Eq. (4.6))

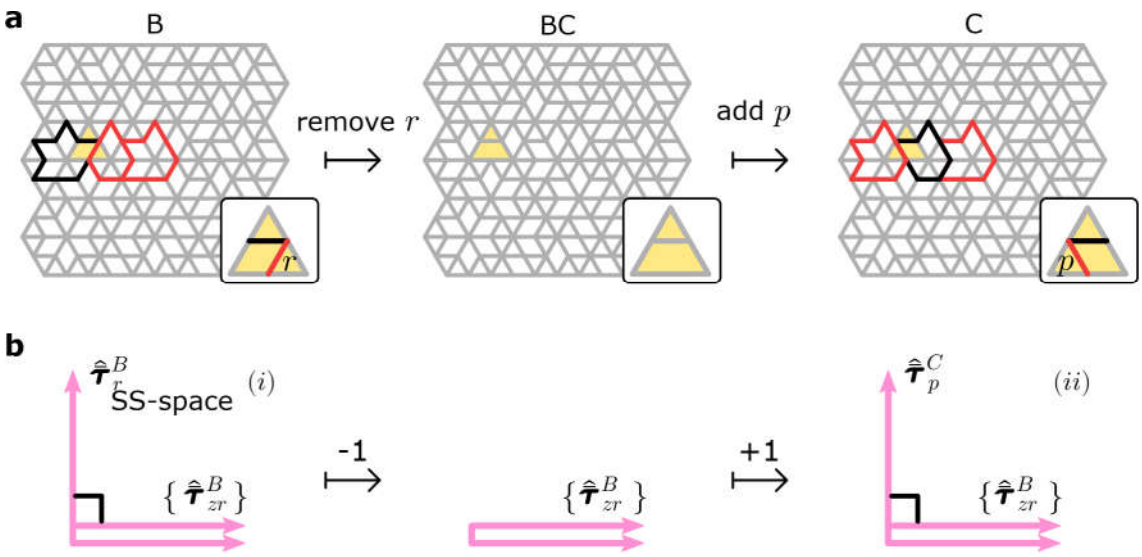

Fig. 4.8.: Evolution of the SS-space under a supertriangle rotation according to process II. **a**, An incompatible network B is transformed to an incompatible network C via an intermediate network BC, by first removing bond r and then adding bond p (insets). **b**, For network B, we construct orthogonal bases for the SS-space that contain the states $\{\hat{\bar{\tau}}^B_{zr}\}$ that remain in the SS-space of network BC as well as in that of C. The full bases of networks B and C additionally contain the respective SS-states $\hat{\bar{\tau}}^B_r$ and $\hat{\bar{\tau}}^C_r$ that are removed and added during the architectural transformation (see text). Black squares signify orthogonality, and arrows with numbers indicate changes in the dimensions of the SS-space.

to obtain the orthogonal basis $\{\{\hat{\bar{\tau}}^B_{zr}\}, \hat{\bar{\tau}}^B_r\}$. Going from network B to BC by removing bond r, the SS-state $\hat{\bar{\tau}}^B_r$ is removed from the SS-space (see Fig. 4.8b, left).

(ii) To go from network BC to network C, we add bond p, which increases the dimension of the SS-space by one. To construct a basis for the new SS-space, we use an inverse procedure and start from network C, constructing a basis suitable for removing bond p to obtain network BC. We use the same procedure as in step *(i)* above, and we readily obtain a basis $\{\{\hat{\bar{\tau}}^C_{zp}\}, \hat{\bar{\tau}}^C_p\}$. Noting that removing bond p from network C and removing bond r from network B produces the same network BC, it trivially follows that $\{\hat{\bar{\tau}}^C_{zp}\} = \{\hat{\bar{\tau}}^B_{zr}\}$. Hence, the step from network BC to C simply adds the basis vector $\hat{\bar{\tau}}^C_p$ to the SS-space (see Fig. 4.8b, right).

For completeness, the evolution of the complementary LB-space is presented in Appendix A.3 following a similar set of calculations.

Together, steps *(i)* and *(ii)* describe the evolution of the SS-space for process II, converting an incompatible network B to a second, distinct incompatible network C. The SS-spaces of architecturally related networks B and C are identical up to the SS-state $\hat{\bar{\tau}}^B_r$, present in network B, but not in C; and the SS-state $\hat{\bar{\tau}}^C_p$, present in network C, but not in B.

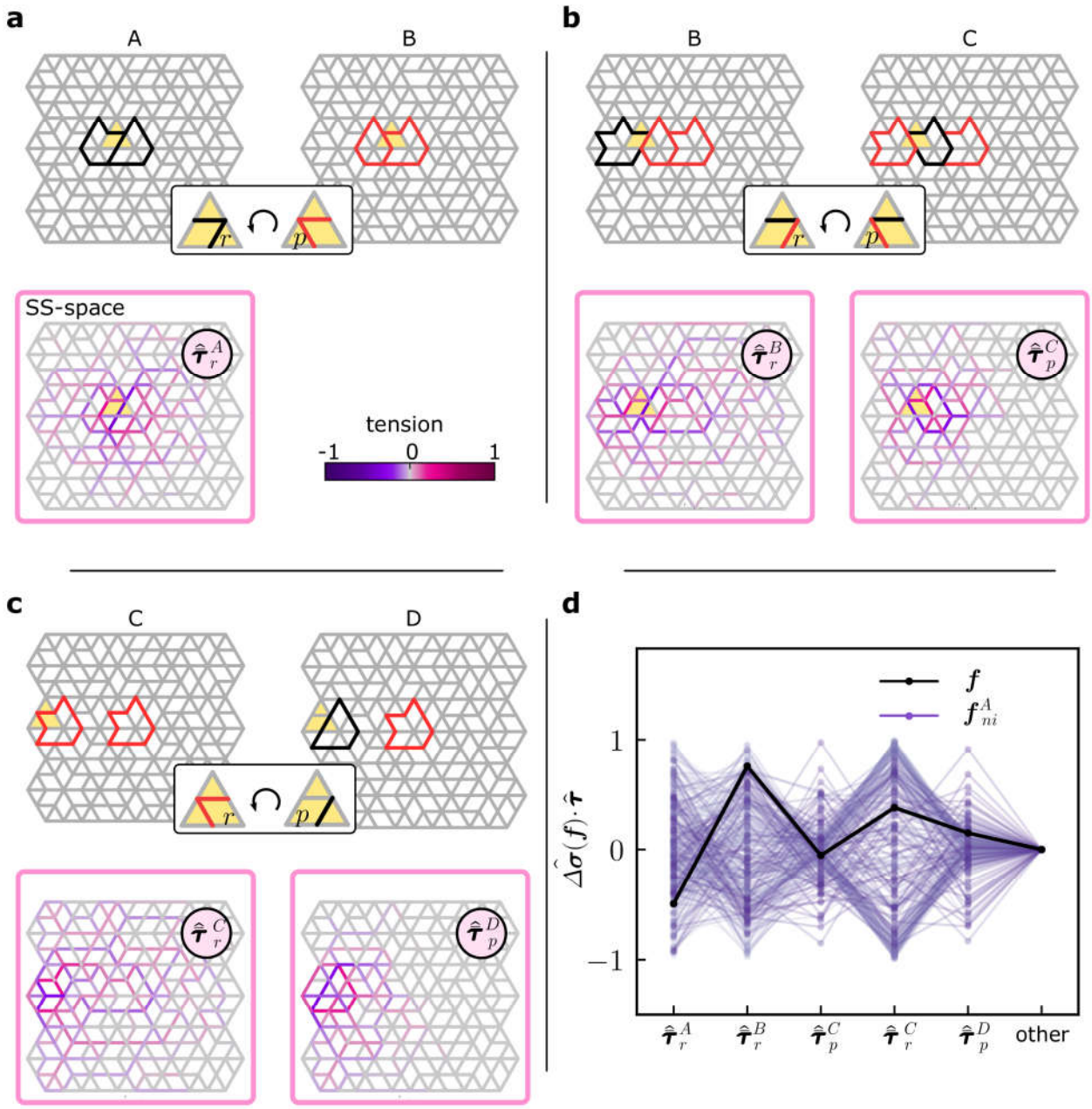

Fig. 4.9.: Examples of the reconfiguration of a metamaterial's SS-states under a sequence of supertriangle rotations, shown for network pairs A–B, B–C, and C–D. **a**, A compatible network A (left) is transformed to exhibit a structural defect in network B (right) by rotating a supertriangle, effectively removing bond r and adding bond p (inset). Local loops whose parity is modified are indicated cf. Fig. 4.4. The unique SS-state $\hat{\hat{\boldsymbol{\tau}}}_1^A$ with nonzero stress on bond r that is not an SS-state of network B is shown. **b**, Network B is transformed into network C, which contains two topological defects. The evolution of the SS-space is set by the two mutually exclusive SS-states $\hat{\hat{\boldsymbol{\tau}}}_r^B$ and $\hat{\hat{\boldsymbol{\tau}}}_p^C$. **c**, Network C is converted to network D containing a single topological defect. The SS-space is modified such that only the two SS-states $\hat{\hat{\boldsymbol{\tau}}}_r^C$ and $\hat{\hat{\boldsymbol{\tau}}}_p^D$ are not shared by the two networks. **d**, The stress response difference $\Delta\boldsymbol{\sigma}$ between networks A and D under identical loading is a linear combination of the five mutually exclusive SS-states. $\Delta\boldsymbol{\sigma}$ is calculated for all independent normal mode loads $\boldsymbol{f}_{ni}^A$ of network A (see text), as well as the load illustrated in Fig. 4.1b. The overlap of the normalized stress difference with the five SS-states is shown; it has no component outside of their span.

4.6.4. Mechanical interpretation and consequences

The above results show how the SS-space changes under a supertriangle rotation. Specifically, we constructed the mutually exclusive SS-states of two architecturally related networks. There is one such SS-state for a network pair where the dimension of the LB-space changes (process I), two such SS-states for networks where the dimension of the LB-space does not change (process II), and no such SS-states for process III.

Due to the linear-algebraic structure of our model, we have argued that the SS-space evolution between two architecturally related metamaterials governs their difference in stress response. After all, the stress response of both metamaterials must be perpendicular to their respective SS-spaces. This enables us to answer the following question: *when two metamaterials with distinct architectures are subjected to the same external nodal load $\boldsymbol{f}$, what is the difference $\Delta\boldsymbol{\sigma}$ in their stress response?*

We show an explicit example for the three network pairs $A-B$ and $B-C$ in Fig. 4.9a–b, corresponding to processes I and II respectively. The figure illustrates the SS-states that mutate under architectural transformations. When network A is transformed into network B, the only difference between the two respective SS-spaces is the SS-state $\hat{\bar{\boldsymbol{\tau}}}_r^A$ (Fig. 4.9a, bottom). Thus, the stress difference between networks A and B under identical supported loading is parallel to $\hat{\bar{\boldsymbol{\tau}}}_r^A$. To show this precisely, some linear algebra is necessary; details are shown in Appendix A.4. With this result, we can understand the localization of the stress response difference between networks A and B, introduced in Fig. 4.1a: the localization of the stress response difference is due to the localization of the SS-state $\hat{\bar{\boldsymbol{\tau}}}_r^A$ around the removed bond r.

Similarly, the stress response difference between the networks B and C, related via process II, is spanned by the changed SS-states $\hat{\bar{\boldsymbol{\tau}}}_r^B$ and $\hat{\bar{\boldsymbol{\tau}}}_p^C$ (Fig. 4.9b, bottom; see Appendix A.4 for details).

As a consequence, we can make an inductive statement about the stress response difference between a pair of networks related by multiple, consecutive block rotations, such as the network pair $A-D$ shown in Fig. 4.1b. The stress response difference between the two networks must be limited to the span of SS-states that have changed during the sequential transformations. The network with a topological defect (D) is related to the compatible network (A) by a minimal number of three architectural transformations, shown in Fig. 4.9a–c, that correspond to processes I, II, and II respectively. As a consequence, the stress response difference between networks A and D should be contained in a five-dimensional stress subspace of changed SS-states (Fig. 4.9a–c, bottom). To confirm this, we calculate the stress response difference between networks A and D under all $N_b - N_{SS}$ independent supported loads of network A. We choose the independent supported loads to be the supported normal loads $\boldsymbol{f}_{ni}^A$ (i.e. left singular vectors with nonzero singular values of the kinematic matrix of network A). The overlap of the resulting normalized stress response differences $\hat{\Delta\boldsymbol{\sigma}}$ with the five normalized SS-states is shown in Fig. 4.9d. The data demonstrate that the stress response difference is a linear combination of only the five mutually exclusive SS-states for any applied load, with zero projection on any other stress states. Results are also shown for the particular stress response difference under the loading illustrated in Fig. 4.1b (right). Thus, the stress response difference shown in Fig. 4.9d is confirmed to be a linear combination of the

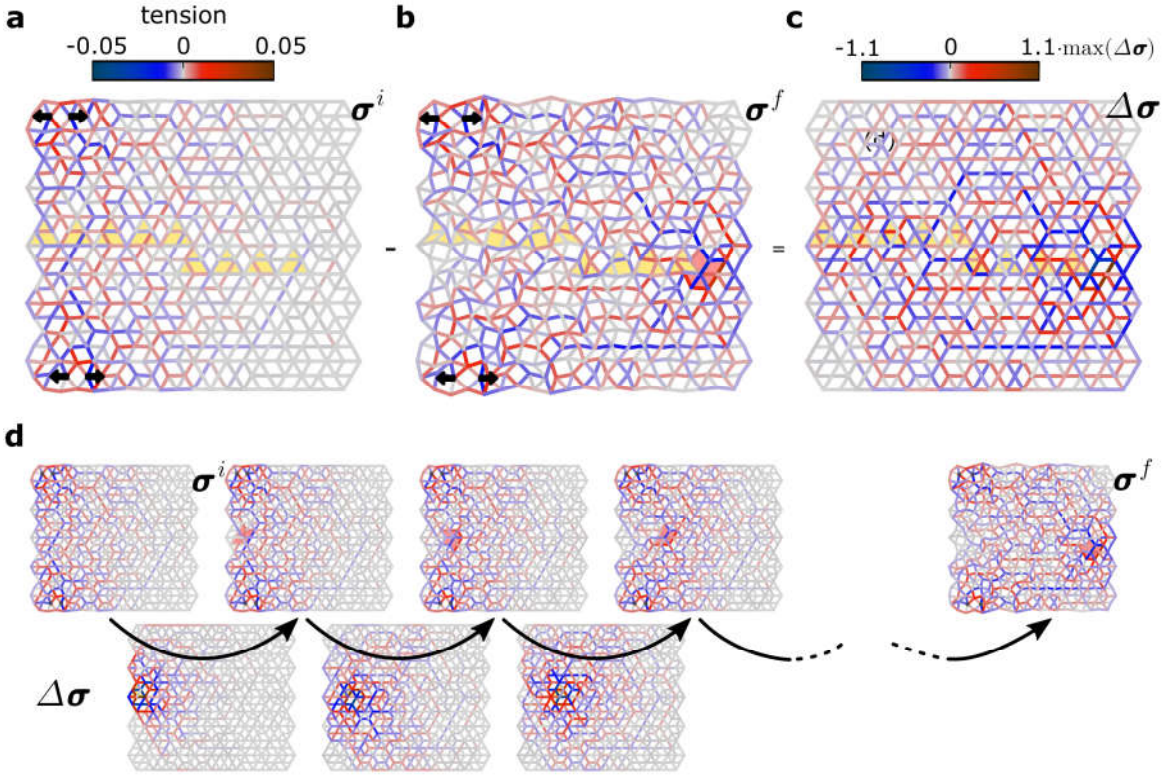

Fig. 4.10.: **a**, An initially compatible metamaterial under loading at the network's leftmost corners (arrows, length multiplied by a factor 100 for clarity) concentrates stresses $\boldsymbol{\sigma}^i$ (colours) along the shortest path between the two probing points. Nine sequential supertriangle rotations (yellow triangles) introduce a topological defect from the left boundary and guide it to the right. **b**, Once the topological defect has been moved to the right boundary, the stress field $\boldsymbol{\sigma}^f$ is diverted to run between the two probing points and along the right side of the topological defect (odd local loop highlighted with red infill). **c**, The differential stress response $\Delta\boldsymbol{\sigma}$ of the two networks is such that stresses on the left of the system are decreased, while stresses on the right increase. $\Delta\boldsymbol{\sigma}$ is a linear combination of the 17 SS-states that have changed during the nine sequential architectural transformations. **d**, The stress response and stepwise stress response difference for the first three intermediate steps is shown. Intermediate stress response difference are linear combinations of SS-states that are quasilocalized near the rotated supertriangles. The SS-states produce a typical stress re-steering that affects stress magnitudes near the moving topological defect: stresses to the left are decreased, while stresses on the right increase.

five SS-states, each of which is concentrated in a different part of the network. Since the stress response difference is a linear combination of mutated SS-states with different localizations, the total stress response difference is diffuse.

4.7. Re-steering a stress response with architectural transformations

In this section, we show that our understanding of SS-space modifications during architectural transformations allows us to explain how the inclusion of a topological defects affects the stress response field of a metamaterial.

In previous work, we have shown that metamaterials containing a single topological defect show unusual stress-localizing behaviour when compared to a compatible metama-

terial[13]. Specifically, consider a compatible network; an example of a large compatible network containing 95 superhexagons is shown in Fig. 4.10. We pick two supertriangles at the left top and bottom corners for actuation. To make sure that we have a supported load, and for simplicity, we force both supertriangles with load dipoles that actuate their local FM, but that is not compatible with the network's global FM and is therefore a supported load. Under this driving, stresses are concentrated along the leftmost sample edge, running along the shortest path between the two actuation points (Fig. 4.10a). When the metamaterial undergoes a particular sequence of supertriangle rotations to generate a topological defect that progressively moves from left to right through the system, the same loading conditions produce a stress field that runs along the rightmost edge of the network instead (Fig. 4.10b). The differential stress response is concentrated on the right side of the system (Fig. 4.10c). Based on the evolution of SS-space during each supertriangle rotation, we can understand why this unusual stress-localizing behaviour takes place.

Starting from the compatible structure, we rotate a supertriangle at the leftmost edge to locally create a topological defect. This removes a SS-state at the leftmost edge of the system (Fig. 4.10d, left). The particular removed SS-state is structured so that the stress response of the new network is reduced at the left and increased to the right of the newly created topological defect. In the next transformation step, we shift the topological defect to the right by rotating a supertriangle on the right side of the topological defect. This transformation locally modifies the SS-states, which are again configured such that the stress response is decreased to the left and increased to the right, so that stresses are steered along the right edge of the topological defect. Repeating this process leads to the path of highest stress concentration to be pushed farther and farther towards the right side of the system, ahead of the direction of 'motion' of the topological defect (Fig. 4.10d, middle). Finally, after the transformation sequence is complete, the topological defect is located at the rightmost side of the network; the stress field runs between the two actuation points around the defect along the right edge, leaving the left edge with a lowered stress response (Fig. 4.10d, right). SS-states that are modified during such transformations fully determine the difference in stress response under an equal applied load.

4.8. Conclusions and outlook

In previous work, SS-states have been used to design localized mechanical responses in materials with a topologically nontrivial band structure[16,17,44,59,91]; to investigate the mechanical response of mechanical networks[18,89,92] and jammed particle packings[79–82,87,93–97]; and to study the mechanical evolution of networks under bond removal[78,80]. In contrast, here we have worked out in detail how architectural *bond-preserving* transformations govern the *evolution* of the SS-states, LB-states, and mechanical response of a complex mechanical metamaterial[13].

In particular, we started from a linear-algebraic description of network mechanics, which dictates that the stress difference of architecturally related networks under identical loading is governed by the networks' differing SS-spaces. It should be noted here that this result holds not only for the metamaterial architectures presented in this work, but for *any* network material whose architecture is transformed by removing a bond, and

then adding a bond at another position: under identical supported loads, the response difference between the two architecturally related networks is governed by their mutually exclusive SS-states.

For the specific family of metamaterials considered here, closed-form SS-states spanning the full SS-space were constructed straightforwardly, due to the regular geometry of the metamaterial building block. We then considered rotations of a single triangular building block as the fundamental architectural transformations that can introduce (topological) defects into formerly compatible designs[13]. These rotations were shown to lead to distortions of the SS-space that we calculated explicitly. In turn, since changes in the SS-space govern the evolution of the metamaterial's stress response under externally applied loads, we were able to explicitly calculate how the response of a metamaterial evolves under architectural transformations. Finally, we demonstrated how these insights clarify how topological defects steer stress fields.

While our approach helps understand the steering of stresses in the particular case of a moving topological defect, designing a target stress response with an inverse procedure is more complex. Suppose, for example, that we aim to construct a sequence of architectural transformations to generate a given target stress response, starting from a particular metamaterial design and loading conditions. In general, this requires an in-depth analysis of the evolution of the SS-states to ensure their cumulative contribution leads to the desired stress response. Nevertheless, our approach suggests a systematic pathway to do so. Moreover, metamaterial designs may be constructed where the SS-states are a priori known or more easy to construct, simplifying the practical implementation of our approach to design the (differential) stress response of complex metamaterials.

Acknowledgements

We thank Aparna Baskaran, Roni Ilan, Edan Lerner, and Ben Pisanty for fruitful discussions. This research was supported in part by the Israel Science Foundation Grant No. 968/16, and by the Israeli Ministry of Science and Technology.

5. Reshapeable groovy sheets

Abstract

Shape-morphing materials find applications in many areas of our lives, from controlled-drag surfaces to pop-up tents. However, designing them poses a challenge. We introduce a novel platform: thin materials with parallel undulations, or *groovy sheets*. Groovy sheets snap quickly and reversibly between multiple stable shapes under external manipulation. We show that individual snap-through events in each groove produce defects that lie at the heart of the sheets' elastic shape-morphing. Adjacent defects show short-range attraction which favours their alignment into chains, or scars, of defects. Scar lines have the ability to change the sheet's equilibrium shape; we show that these shapes fall into distinct categories, depending on the internal configuration of scar lines. Finally, we show that scarred sheets can be modelled as ruled surfaces, whose elastic behaviour can be captured by simple mean-field models. Our work provides the groundwork for using corrugated sheets to design and model shape-morphing materials.

5.1. Introduction

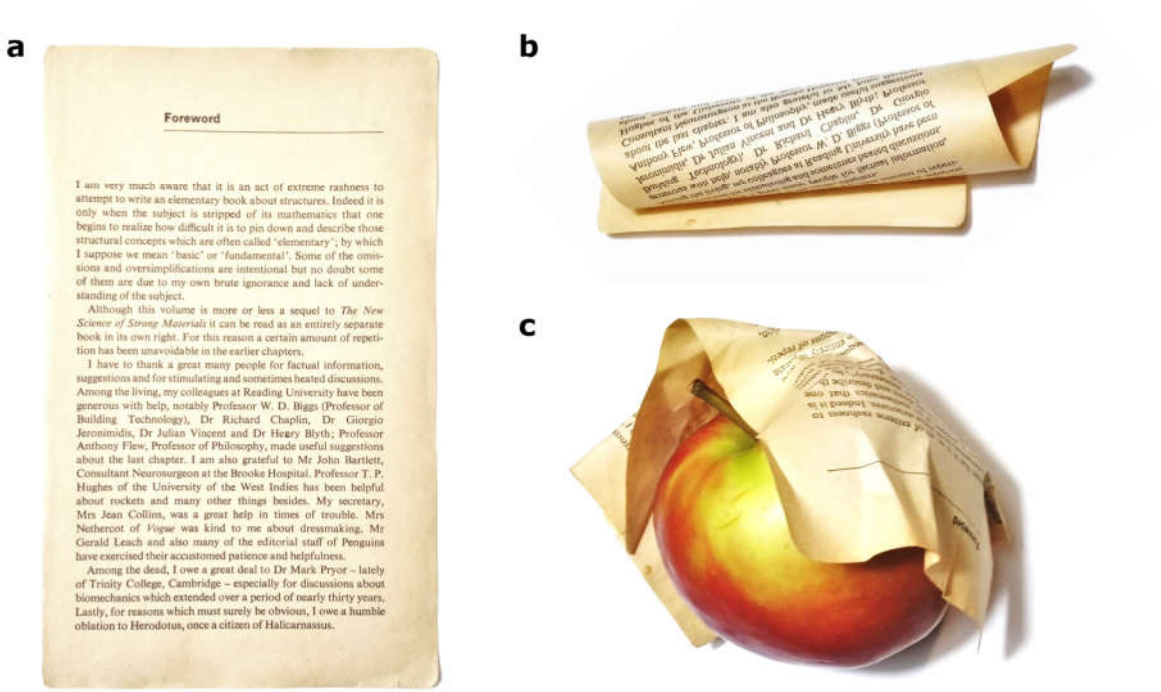

Fig. 5.1.: Thin structures reshape easily. a, A typical thin sheet: a book page, around the thickness of a human hair. **b,** The page bends and rolls smoothly, at low energy cost. **c,** Under the wrong conditions, the sheet crumples: there is no smooth way to wrap the sheet around a spherical apple. As a result, local stretching in the form of folding, dimpling and buckling takes over.

From unfurling leaves and snapping fly-traps to bendy straws and folded maps: shape-shifting materials, both natural and man-made, are useful and all around us. However, inventing, designing, and modelling reshapeable materials is challenging. In this chapter, we propose a novel approach: we make, measure, and model shape-morphing structures made from thin, corrugated, *groovy sheets*.

Why thin sheets? Because they deform easily[21]- think of crumpled paper[98–102], budding leaves[103,104], origami, and kirigami[8,46,64–66,105–107]. This makes them prime candidates to create materials that can deform from one shape to another. The reason behind a thin sheet's deformability (illustrated in Fig. 5.1a) is its dimensional contrast: it is much thinner than it is wide. This has mechanical consequences. Generally, sheets deform in two ways: they either *bend* or *stretch*[108]. Bending is easy to do, because the material's bending stiffness scales with the cube of its thickness (Fig. 5.1b). The thinner the sheet, the better it bends. On the other hand, the stretching stiffness scales linearly with how thick the material is, so stretching is hard. This is why rolling up a piece of paper is much easier than crumpling: crumples involve local stretching (focussed in patches, minimizing the energy cost) to create folds, bumps, and corners.

Thus, thin sheets do not just deform easily, but *interestingly*. Imagine wrapping a flat sheet around a sphere (Fig. 5.1c): it can't be done without crumpling. In spite of its cost, stretching is sometimes preferred over bending. Gauss' *Theorema Egregium* [108, 109] gives an intuitive explanation for this interesting behaviour. From his mathematical

point of view, the shape of a sheet can be described with two types of curvatures: mean (which measures how much a sheet bends), and Gaussian (which measures whether or not the sheet is intrinsically flat). Loosely, bending and stretching deformations correspond to changes in mean and Gaussian curvature respectively. Thus, there is a local competition between stretching and bending deformations, mediated by the sheet's curvature. Bending and stretching are geometrically coupled[110].

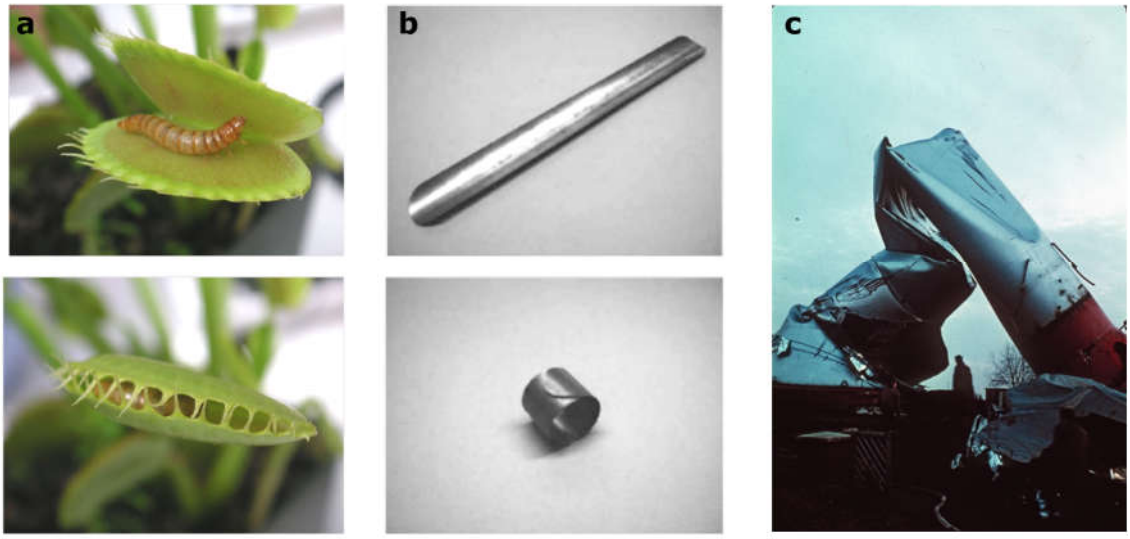

Fig. 5.2.: Thin structures can be multistable. a, Examples from the natural world: a Venus flytrap's leaves snap shut around its next meal. Image: Beatrice Murch (CC BY-SA 2.0). **b,** Man-made tape springs snap from straight to rolled. Image adapted from Ref. [111]. **c,** Unintentional bistability in a buckled water tank. Image: D. and W.D. Bushnell, shellbuckling.com (CC BY-NC-ND 3.0).

In short: thin sheets deform easily and interestingly. Both these features are hallmarks of the *geometric nonlinearity* that thin sheets naturally produce. And it is precisely such nonlinearity that allows structures to take on multiple stable shapes[112]. Consider the mechanical point of view: most structures live at rest, in a mechanical equilibrium. When left alone, they stay right where they are. Their elastic energy is at a local minimum. In order to create a shape-morphing material, the structure's energetic landscape (or, formally, its internal energy as a function of its configuration) must have multiple local minima. One way of getting multiple energetic wells is by ensuring that structural strains (deformations relative to the resting shape) depend non-linearly on the structure's internal configuration. Such geometric nonlinearity arises naturally in thin sheets[108,109], in two ways. First, they bend easily, and finite bending is nonlinear; and second, the geometry-mediated competition arises between stretching and bending leads to complex higher-order effects. In other words: thin sheets with surface patterns are good candidates for designing multistable materials[113–119], which has been recognized and researched both in natural[120–122] and man-made systems[12,65,123–128].

Unfortunately, nonlinear reshaping behaviour in thin structures is challenging to model[129–133]. Phenomena that we understand intuitively, from twisting ribbons[134–136] and poking volleyballs[137,138], to wrinkling skin[139] and fabric[140,141], are not easy to capture and predict with simple theories. Many innovations in the field of shape-morphing structures deal

with this issue by drawing inspiration from nature[4,104,142–144] (Fig. 5.2a), or focussing on easier-to-model small[111] or discrete systems, such as origami[39,105,106,145,146] (Fig. 5.2b). In addition, instabilities are traditionally seen as failure modes (a fair point for grain silos and aeroplane cabins), and engineering research is focussed on preventing[147] rather than using them (Fig. 5.2c).

In this work, we propose to harness rather than avoid the instabilities that naturally occur in thin sheets. We aim to create materials that can shape-shift in a robust, reversible, and fast way. To that end, we use thin sheets with a special corrugated geometry: *reshapeable groovy sheets*.

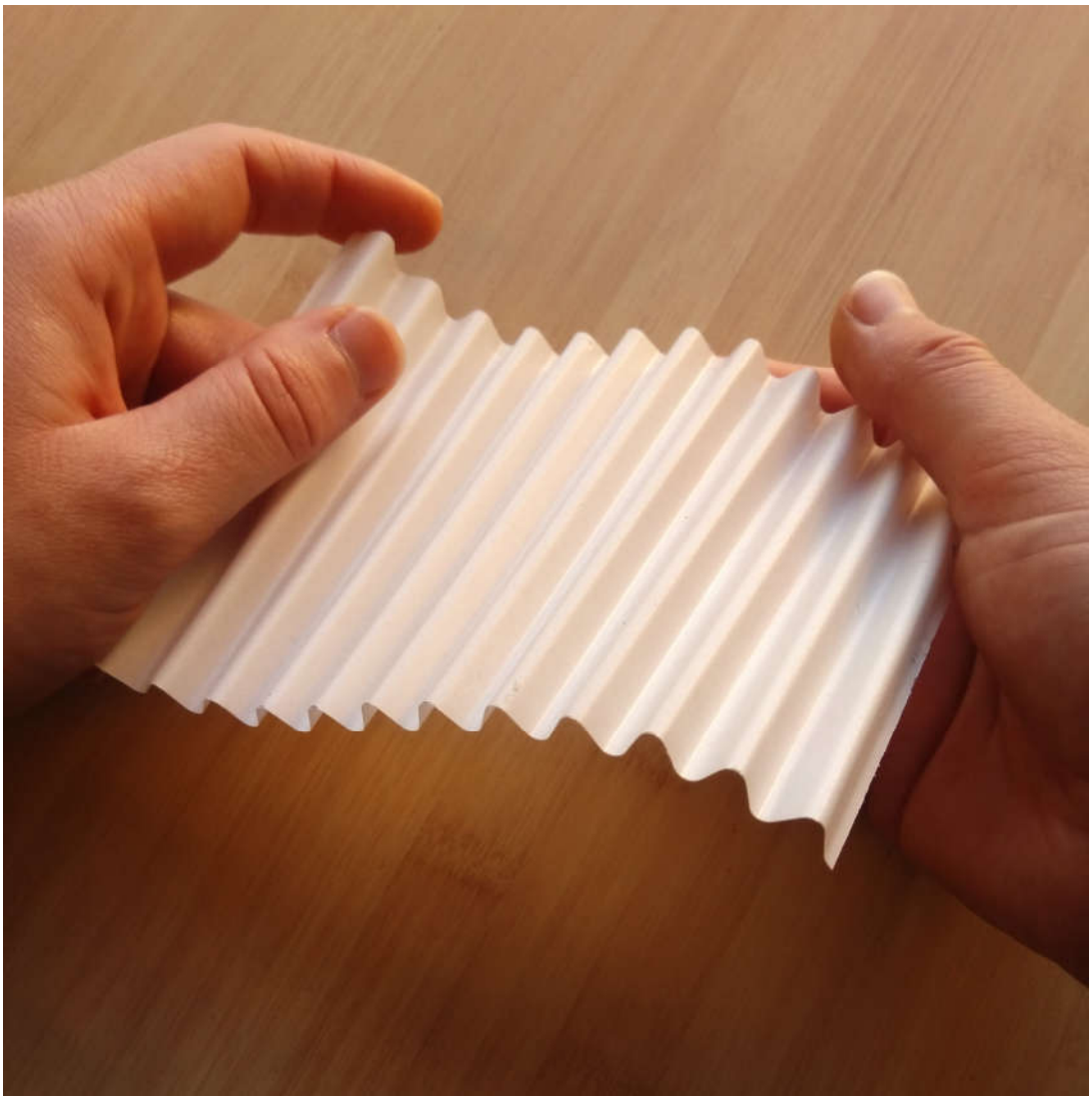

Fig. 5.3.: A groovy sheet. A thin, rubber-coated plastic sheet with thickness 0.075 mm is shown. The sheet has parallel corrugations, or grooves. The thickness is much smaller than the sheet's size and the groove wavelength.

Fig. 5.3 shows what a typical groovy sheet looks like. Its underlying material is thin and flat, much wider and longer than it is thick. Straight grooves (whose width and height are also much bigger than the thickness) run like parallel waves along one direction. While the example shown is of just the right size to be held in hand, their absolute size is not very important. As long as the material's thickness is much smaller than any other relevant lengths, we consider it a groovy sheet.

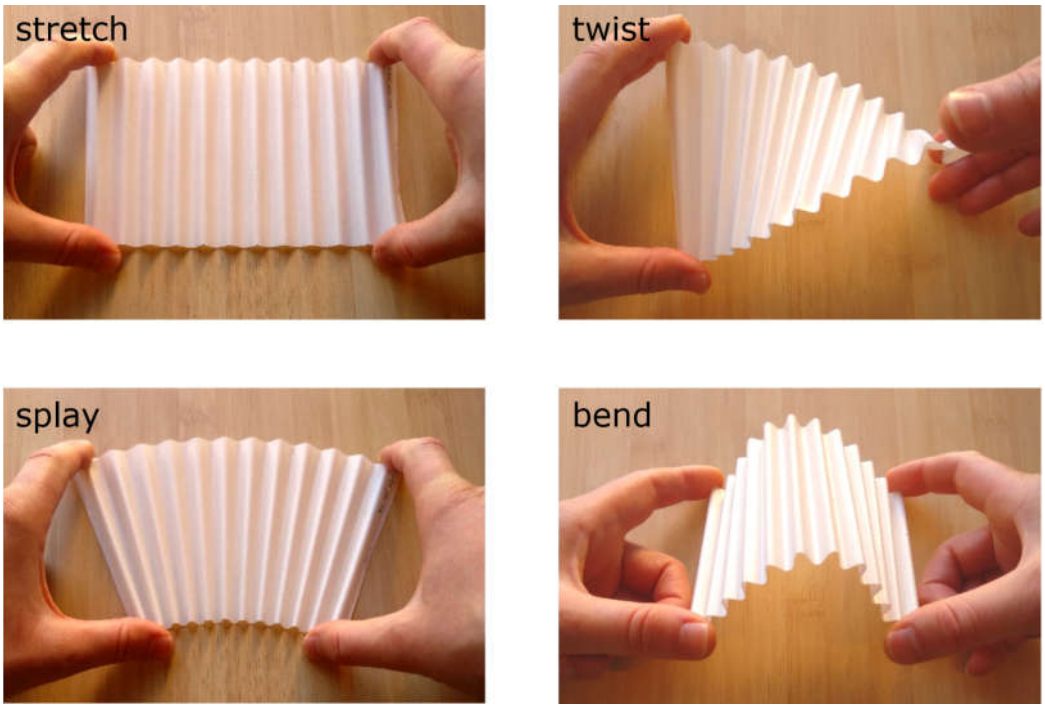

Fig. 5.4.: Groovy sheets deform easily. Left to right, top to bottom: a sheet can easily be stretched, bent, splayed, and twisted by pulling or rotating its sides uniformly. These deformations appear to dominate the sheet's mechanical behaviour.

Fig. 5.4 gives some intuition on how groovy sheets deform when they are manipulated. Stretching, twisting, splaying, and bending of the groovy sheet are easy to do. Interestingly, these deformation modes are dominated by *bending* of the underlying sheet material: overall sheet stretching does not require local material stretching.

Groovy sheets can do more than just bend and twist. Strange things happen when we apply the right boundary conditions, illustrated in Fig. 5.5. There, we pull on a groovy sheet by pinching it at two points at its edges. Initially, the sheet stretches as usual (Fig. 5.5a). But as we continue to pull, something unusual happens: the sheet's grooves *snap through* one by one, starting from the pinching points (reminiscent of the popping of a tape spring[117,148,149]). Small divots are formed in each snapped groove; we call these divots *snap-through defects* (Fig. 5.5b). As we stretch the sheet further, more and more grooves snap through, starting from the edge and into the bulk of the sheet (Fig. 5.5c). At a critical point, all remaining grooves snap through nearly simultaneously at high speed, creating a contiguous line of defects (Fig. 5.5d). Intriguingly, even when we stop pulling, the defects remain, and the sheet curves (Fig. 5.5e). Finally, when the sheet is

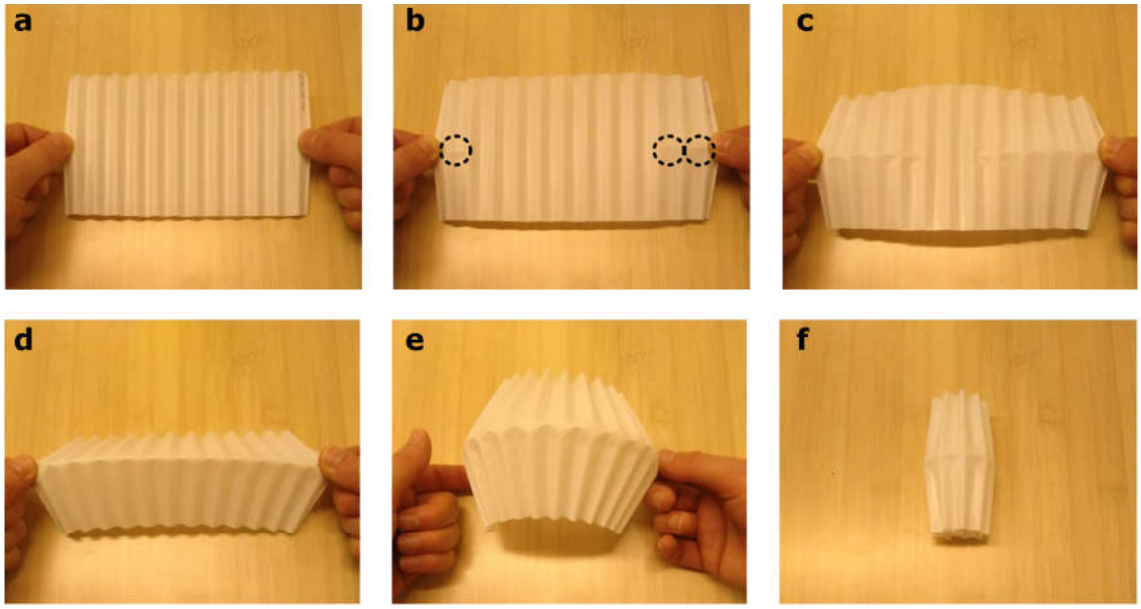

Fig. 5.5.: Groovy sheets reshape, if manipulated right. A sheet is pulled at two points (**a**). At first, the sheet stretches. Then, grooves near the pulling points pop into a new configuration with snap-through defects (**b**, circles). As the sheet is pulled farther, more defects appear slowly (**c**). At a critical point, the remaining grooves snap through rapidly, and defects form a chain (**d**). When the pulling force is released, defects remain and the sheet curves (**e**). Finally, the sheet is free and curls into a compact roll (**f**).

let go completely, it finds a new equilibrium shape: a compact roll (Fig. 5.5f). In other words: the sheet quickly snaps into a new, stable, rolled shape.

But this is not the end: groovy sheets can morph back and forth into much more complex shapes, as we show in Fig. 5.6. There, we show what happens to a groovy sheet (Fig. 5.6a) that is gently crumpled up (Fig. 5.6b,c). When the crumpling force is removed, the sheet has a disordered pattern of snap-through defects and a corresponding irregular shape (Fig. 5.6d). However, when the sheet is gently stretched (Fig. 5.6e), the defects unpop, and the sheet returns with negligible permanent deformation to its original, flat state (Fig. 5.6f). Groovy sheets morph quickly and reversibly into many different shapes, and these are exactly the kinds of features that could make them useful in real-life applications.

Morphing sheets could even find application across scales: crucially, all groovy sheets can shapeshift, whether they are big or small. Fig. 5.7 shows two extreme examples. In Fig. 5.7a, we see a commercial plastic corrugated roofing sheet of around 1 mm thick, its corrugations around 10 cm) wide. Two people, with some persistence, can pop the stiff plastic sheeting into a robust, twisted shape that withstands bumps, scrapes and drops. On the other hand, Fig. 5.7b showcases a small, twisted sheet made using a thin plastic coating that has been detached from corrugated craft paper in an acetone bath. The film is 0.015 mm thick, with grooves around 0.5 cm. Although the two sheets differ by almost a factor one hundred in size, they reshape the same way. The sheet's grooves govern shape-morphing, not its size.

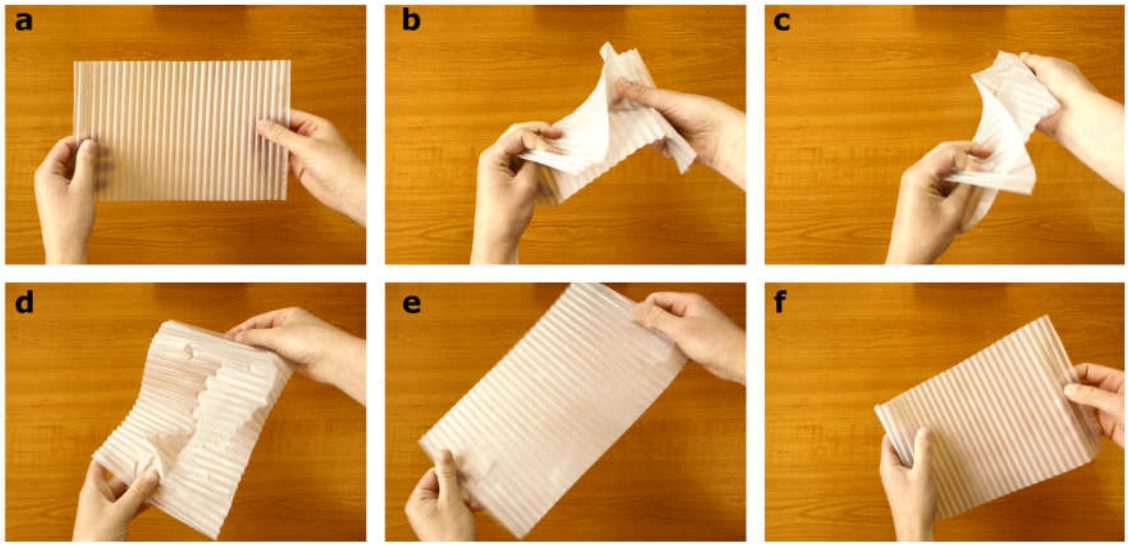

Fig. 5.6.: Groovy sheets reshape reversibly. A groovy sheet (**a**) is crumpled (**b**,**c**). Afterwards, the sheet shows a complex shape and snap-through defect pattern (**d**). Stretching the sheet unpops the defects (**e**) and reverts the sheet to its original flat state (**f**).

Over the course of four years, we have had the opportunity to present our reshaping groovy sheets to many people, both specialists and laypersons. Their response has been consistent. First, the sheet's popping behaviour proved to be evocative. Parallels were drawn to buckling in corrugated roofing, dimpling in pleated fabrics, and childhood memories of playing with packaging material. And second: there seems to be no record of using snapping groovy sheets to create shape-shifting materials.

Here, we address that gap. We explore, quantify, and model how groovy sheets reshape, and discuss prospects for geometry-controlled shape-morphing.

We first define the general shape and size of a groovy sheet in section 5.2, and discuss fabrication methods for plastic and rubber sheets on the centimetre scale. In order to quantify groovy sheet shapes, we introduce two imaging techniques in section 5.3, using both photographic projections as well as full 3D image scanning. Which shapes a groovy sheet can take on depends not only on its starting shape, but also on its (in-plane) elastic properties, which we describe both experimentally and theoretically in section 5.4. As discussed above, groovy sheets reshape due to the introduction of individual snap-through defects in their grooves. We explore the snapping of single defects in section 5.5. However, when more defects appear in the sheet, they start interacting (section 5.6): we will show that adjacent defects attract, which causes them to organize into scar lines of contiguous defects. Stable scar lines have the capacity to dramatically alter the three-dimensional shape of groovy sheets. We quantify this reshaping in the presence of scar lines in section 5.7, and present a hybrid model using both geometric and elastic models that explain groovy sheet's complex shapes. We review our findings in section 5.8, discuss the use of groovy sheets as a novel platform to create reshaping materials, and point out directions to both deepen our insight in and broaden the applications of reshapeable groovy sheets.

Fig. 5.7.: Groovy sheets of all sizes can reshape. a, A commercial plastic corrugated roofing sheet ($1\ \mathrm{mm}$ thick, with groove wavelengths around $10\ \mathrm{cm}$) is reshaped into a robust twisted configuration with the combined strength of two physicists. **b,** Plastic coating film, detached from corrugated craft paper. The film is $0.015\ \mathrm{mm}$ thick, with grooves around $0.5\ \mathrm{cm}$. Although the two sheets differ by a factor of almost one hundred in size, they reshape the same way. Modelling courtesy of Hadrien Bense.

5.2. Making groovy sheets

To study the behaviour of groovy sheets, real samples with well-defined geometric and elastic properties must be made. We present a geometric model and three experimental fabrication processes in sections 5.2.1 and 5.2.2 below, and show that thermoforming of polyethylene sheets inside a rigid mould produces suitable groovy sheets that support re-shaping behaviour.

5.2.1. Geometry

Groovy sheets can come in many shapes. Fig. 5.8 shows the parameters that govern the groove geometry. Specifically, a sheet with N grooves has an overall length L and width W. We assign a local coordinate frame that corresponds to directions orthogonal (ξ) and parallel (υ) to the grooves, and normal (ζ) to the surface (Fig. 5.8a). Zooming in on the groove geometry in Fig. 5.8b, the sheet has a uniform thickness t. The groove amplitude A, wavelength λ, and groove arc length s_λ determine the groove shape.

We assume that the grooves are well-approximated by cylindrical sections of radius of curvature R and opening angle θ, connected by flat facets of length l_{facet}. Relations between these shape parameters are given by the following equations:

$$A = 2R(1 - \cos\frac{\theta}{2}) + l_{\mathsf{facet}} \sin\frac{\theta}{2} \tag{5.1}$$

$$\lambda = 4R\sin\frac{\theta}{2} + 2l_{\mathsf{facet}}\cos\frac{\theta}{2} \tag{5.2}$$

$$s_\lambda = 2(l_{\mathsf{facet}} + \theta R) \tag{5.3}$$

$$\tan\frac{\theta}{2} = \frac{\lambda R + (A - 2R)l_{\mathsf{facet}}}{\frac{1}{2}\lambda l_{\mathsf{facet}} - 2(A - 2R)R} \tag{5.4}$$

$$l_{\mathsf{facet}} = \sqrt{A^2 - 4AR + \frac{\lambda^2}{4}}\ . \tag{5.5}$$

Note that the sheet shape is set by any three independent parameters, for example by the triplet $(R, \theta, l_{\mathsf{facet}})$.

In short, groovy sheets are thin surfaces, uniform along one material direction υ, but with alternating positive- and negative-curvature zones along the orthogonal direction ξ. Borrowing origami terminology, we refer to high- and low-curvature zones as *folds* and *facets* respectively.

5.2.2. Fabrication

To study groovy sheets, we must first make them. Below, we briefly discuss three fabrication methods and their drawbacks and benefits. We study heat-forming thin plastic films with a dynamic and a static method, and review a method to create thin rubber groovy sheets via spin-coating. We show that static heat-forming provides the best results to create reshapeable groovy sheets, and use our experimental findings to identify which groove shapes we can manufacture with this method.

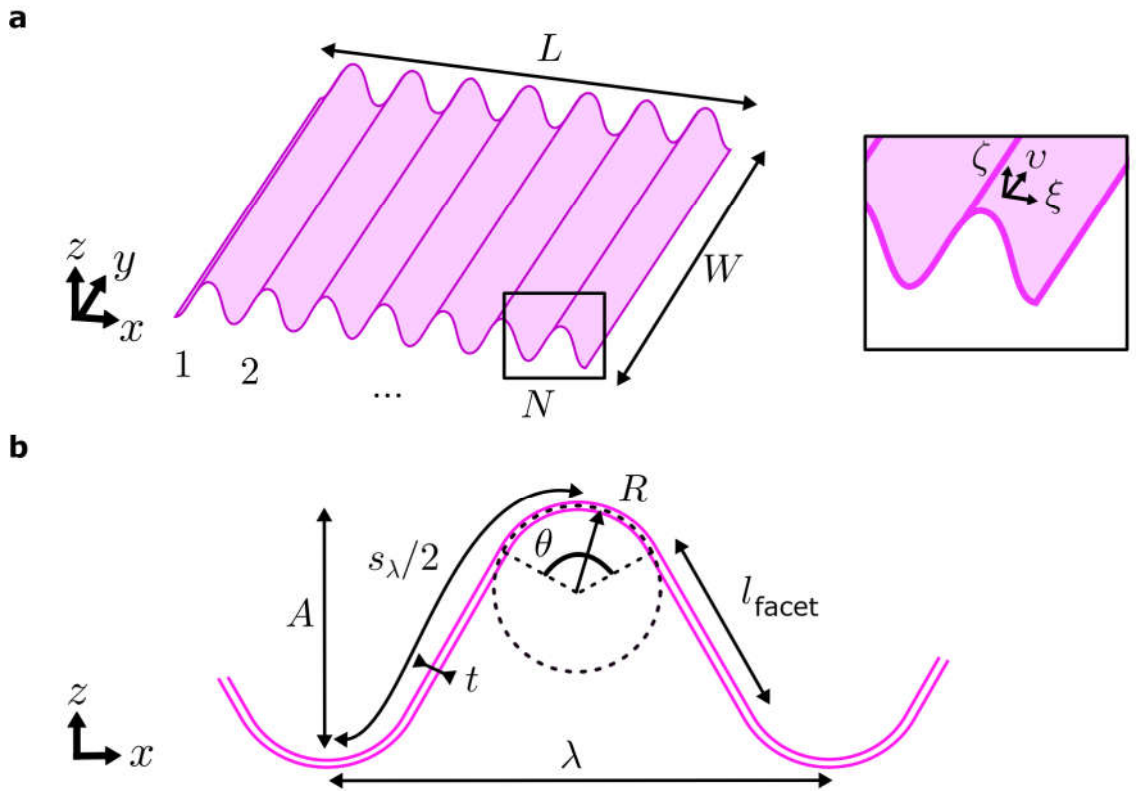

Fig. 5.8.: The shape of groovy sheets. **a**, A thin sheet of length L, width W, with N parallel grooves. Cartesian coordinates x, y, z are indicated. Inset: local sheet coordinates ξ, υ, ζ. **b**, Cross-section of a groove with thickness t, wavelength λ, amplitude A and arc length s_λ. We think of grooves as cylindrical sections with radius of curvature R and subtended angle θ, connected by flat facets of length l_{facet}.

Material choice

Making experimental groovy sheets starts with choosing a suitable material. We need a material that is easily formed into a thin sheet with grooves; that has a large range of elastic rather than plastic behaviour; and that is sufficiently stiff not to be influenced strongly by gravity. We consider biaxially-oriented polyethylene terephthalate (BoPET) film, which softens under heating and can be *thermoformed*, and polyvinyl siloxane (PVS) rubber, which can be *spin-cast* as a fluid.

Thermoforming plastic film

We discuss here how to fabricate samples by heat-forming plastic via two methods: a dynamic method, using counterrotating, heated gears; and a static method, using a compression mould and oven. We use biaxially-oriented polyethylene terephthalate (BoPET) as our base material: specifically, uncoated 'Mylar-A' films produced by Dupont Teijin[150] in a thickness range of 23 to 125 µm.

In order to create suitable groovy sheets out of BoPET film, the following material properties are important (Fig. 5.9). First, the temperature to which the material needs to be heated in order to effectively re-form the film is set by the glass transition temperature. Secondly, the importance of gravity is determined by the film's bending modulus, which is set by the structure's size, specific weight, and Young's modulus. Lastly, to what extent the film can be deformed without incurring permanent, plastic damage is set by the yield point at room temperature.

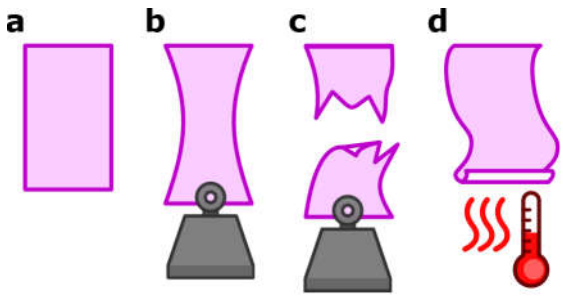

Fig. 5.9.: Important material properties for making groovy sheets. a, A piece of thermoplastic film has a stiffness (**b**), yield point (**c**), and glass transition temperature (**d**).

The reported average properties of Mylar-A BoPET[150] at 23 µm thickness suit our needs. First of all, the glass transition temperature of BoPET lies around 80 °C, while the melting temperature lies at 250 °C: the material can be formed in a conventional oven.

Second, the material's tensile modulus lies between 4.8 and 5 GPa in its two orthogonal directions. We experimentally confirm the Young's modulus, to be $E = 5 \pm 0.3$ GPa (appendix A.6). The high Young's modulus and low specific weight (1.39 gram/cm^3) of the material mean that thin sheets will be weakly affected by gravity. Consider how a sheet of length L, width W, thickness t, and density ρ deflects under gravity. When subjected to a gravitational force per unit length $f_g = tw\rho g$, where g is the gravitational constant, the sheet deforms. Euler-Bernoulli beam theory[151] tells us that the deflection has a typical length $d_g = C\frac{f_g L^4}{EI}$, where $I = \frac{Wt^3}{12}$ is the sheet's area moment of inertia. C is a numerical constant that depends on how the sheet is held, and is typically of magnitude $\mathcal{O}\left(10^{-2}\right)$ to $\mathcal{O}\left(10^{0}\right)$. We consider gravitational deflections to be small as long as $d_g \ll L$, and find a condition $\frac{C\rho g}{E} \ll \frac{t^2}{L^3}$ that must hold for gravity to have a

small influence. We define a dimensionless gravity number:

$$N_g = \frac{\rho g L^3}{E t^2} \ . \tag{5.6}$$

If N_g is much smaller than unity, gravity is negligible. An order-of-magnitude estimate for our sheets produces gravity numbers below $\mathcal{O}\left(10^{-1}\right)$ for thicknesses above 50 µm, indicating that gravity plays a minor role for sheets of sufficient thickness.

Lastly, BoPET's yield point at room temperature lies around a yield strain of 0.02 and corresponding yield stress of about 100 MPa, in line with experimental measurements of the yield strain and stress $\epsilon_y = 0.025 \pm 0.007$ and $\sigma_y = 96 \pm 5$ MPa respectively (appendix A.6). The material's yield strain is relatively low, and samples may be affected by plastic yielding. However, when the groove's radius of curvature R is much bigger than the sheet thickness t, plastic damage is expected to be minimal as long as $\frac{R}{t} \gtrsim 14$ (appendix A.7).

Thermoforming plastic sheets can be done in several ways. We first discuss a dynamic forming method using counterrotating gears, illustrated in Fig. 5.10a. The basic idea is that a PET film is guided between two counterrotating, heated gears, in order to shape it into a groovy sheet. To do this, two hollow elongated gears of around 20 cm length, machined from aluminium plate, are mounted inside a metal casing on parallel spindles with heating rods inserted in their centres. The gears, driven by an external high-torque motor, counterrotate. The heating rods are connected to a PID controller and a heat-sensitive camera, which allows the gear temperature to be controlled with an accuracy of around 5 °C. PET sheets are fed into the gear system via a slot in the casing, and emerge with a groovy shape.

To obtain a controlled groove geometry, the gears have a specific size (Fig. 5.10b): the gear diameter D lies at 23.5 mm, while the teeth have amplitude $A = 5.2$ mm, pitch $\lambda = 4.6$ mm, inner and outer radii of curvature $R_1 = 0.6$ mm and $R_2 = 1.3$ mm, and an adjustable separation distance d close to the sheet thickness, tens to hundreds of micrometers. The typical resulting groove shape is shown in Fig. 5.11. Samples are fabricated at an average feed-through speed of 1.5 ± 0.5 mm/s and a temperature of 90 ± 5 °C. While the sheets have a clearly visible groove profile, the amplitude is limited by a short forming time and a long cooling time; typical ratios of groove amplitude A to pitch λ lie around 0.3, with thicker sheets producing larger ratios. The forming time is limited by the gears' speed, which must be high enough to overcome the setup's frictional torque; and the cooling time is limited by a high gear temperature and the sheet's specific heat, which causes the grooves to sag outside the confines of the gears before hardening. Thus, while the dynamic forming method is fast, it is not suitable for making grooves with large amplitudes.

Besides the dynamic method above, static thermoforming can also be done using heated moulds as shown in Fig. 5.12a. Here, a PET film is placed on a corrugated mould of around 30 by 30 cm, machined from aluminium plate. Matching inserts are used to push the film into each corrugation, and are fastened on the mould with screws. The entire assembly is placed into a commercial oven and heated for one to two hours. After cooling for several hours, the thermoformed groovy sheet can be removed from the mould.

The mould's geometry sets the size of the grooves (Fig. 5.12b): the mould's corruga-

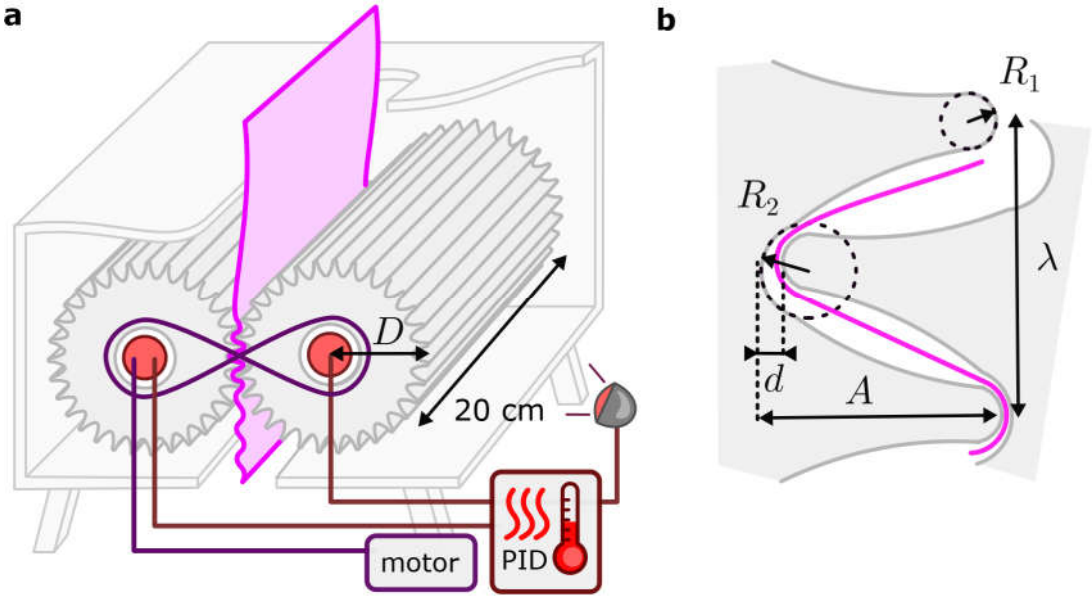

Fig. 5.10.: Dynamic thermoforming with heated gears. **a**, A schematic presentation of the setup. Two aluminium gears (grey), $20\ \mathrm{cm}$ long and with diameter D, are mounted on parallel spindles. One spindle is rotated by an external motor; a serpentine belt passively drives the second spindle. A heating rod (red) is inserted into the hollow centre of each gear. The gears are kept at temperature via a heat-sensitive camera connected to a PID controller. The gears are mounted inside a metallic casing. Flat plastic film (pink) is fed into the gears via a slot in the casing, and emerges with plastically deformed grooves. **b**, Gear geometry. Tooth amplitude A, tooth pitch λ, inner and outer radii R_1 and R_2, and gear spacing d are shown (values: see main text). The sides of each tooth are concave to ensure smooth rotation. An inserted sheet (pink line) deforms accordingly.

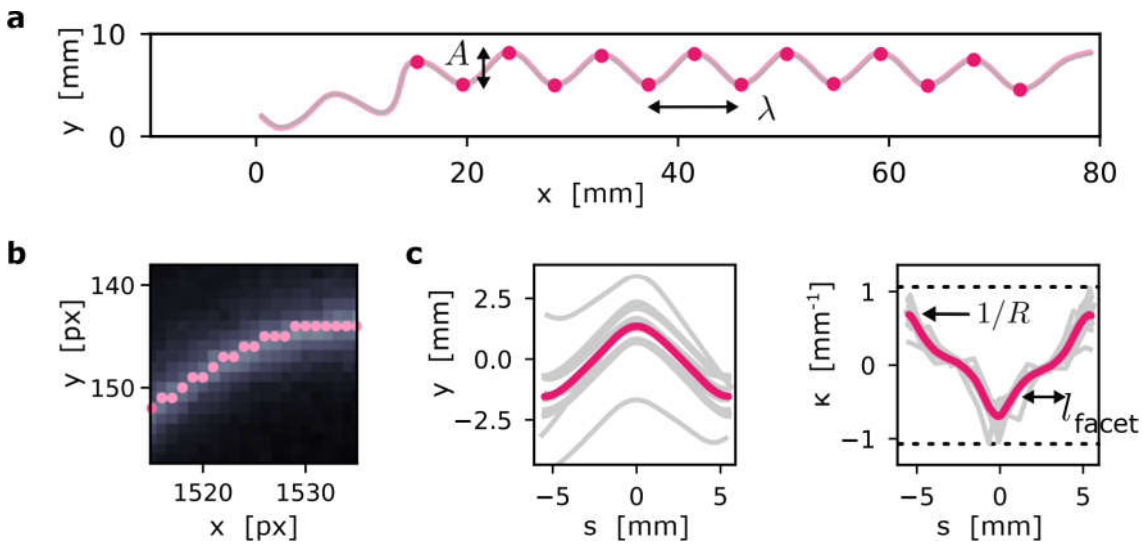

Fig. 5.11.: Typical shape of gear-thermoformed sheets. **a**, The post-forming shape of a $50\ \mu\mathrm{m}$-thick sheet (grey line), fed through the machine shown in Fig. 5.10. The location of the groove centres (pink dots) is used to calculate an average amplitude $A = 2.9 \pm 0.3$ mm and wavelength $\lambda = 8.8 \pm\ 0.3$mm. **b** Zoom-in of a CCD-camera image of the sheet's side (greyscale). The sheet profile (pink dots) is obtained from the image with a custom Python program. **c** Left: averaging over the grooves (grey lines) produces a mean groove height y (pink line) as a function of path length s, which can be used to calculate an average local curvature κ (right, pink line). The average maximum radius of curvature $R = 1.4 \pm 0.2$ mm lies near the average radius of curvature $1/2(R_1 + R_2) = 1.05$ mm of the gears' teeth (black dashed line). The curvature flattens to zero along the grooves' facets, as expected. The typical facet length lies around $R = 3$ mm.

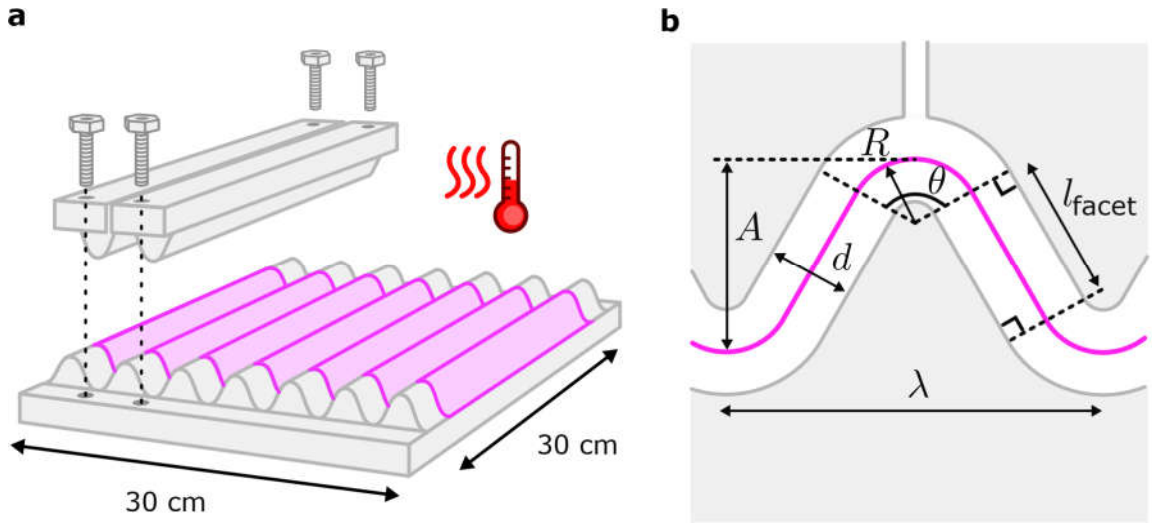

Fig. 5.12.: Static thermoforming with a heated mould. **a**, Schematic illustration of the process. Flat plastic film (pink) is placed on an aluminium mould (grey) with machined grooves. Rods with a complementary shape push the film into each groove and are fastened on the mould with screws. The effective forming surface is 30 cm in each direction. The mould is heated in a commercial oven to thermoform the confined film. **b**, Mould groove geometry. Amplitude A, wavelength λ, mean radius R, curve angle θ, facet length l_{facet} and mould spacing d to accommodate the film's finite thickness are shown. The film's mid-surface (pink line) is indicated.

tions have amplitude $A = 6.812$ mm, wavelength $\lambda = 7.437$ mm, mean radius of curvature $R = 1.5$ mm, groove angle $\theta = 160$ °, facet length $l = 4.4$ mm, and a spacing $d = 50$ µm between the mould and the inserts. We fabricate samples by thermoforming sheets in the mould for an average of 1.5 h at 120 °C and cooling for at least 2 h to allow the assembly to cool below PET's glass transition temperature at 80 °C. The typical groove shape is illustrated in Fig. 5.13. The resulting sheets have a clear groove profile, and achieve a higher ratio of groove amplitude versus pitch than the dynamic method above at a typical ratio of $A/\lambda \approx 0.5$. In addition, the statically formed sheet have less shape variation across the grooves (compare Figs. 5.11c and 5.13c). Thus, while the static forming method is slow, it produces consistently shaped grooves with large amplitudes.

Spin-coating rubber

Groovy sheets can be made by letting liquid rubber cure on a corrugated mould, as we show below. We use polyvinyl siloxane (PVS) rubber, a silicone elastomer that is formed from two liquid polymer compounds via a platinum-based addition reaction. Specifically, we use 'Elite Double' PVS rubber produced by Zhermack[152] of Shore hardness 22 to 32, corresponding to Young's moduli between 0.8 and 1.24 MPa[153].

We fabricate thin groovy sheets out of PVS by spin-coating the liquid rubber on 3D-printed moulds (Fig. 5.14a; for geometry, see Fig. 5.12). We use a simple setup, consisting of a platform mounted on a rotating motor running at (several) hundred RPM[154]. The rubber-coated mould is placed at the edge of the platform while the liquid rubber cures over a timespan of several minutes. A centrifugal force spreads the rubber across the mould's surface. This method produces groovy sheets with an average thickness of

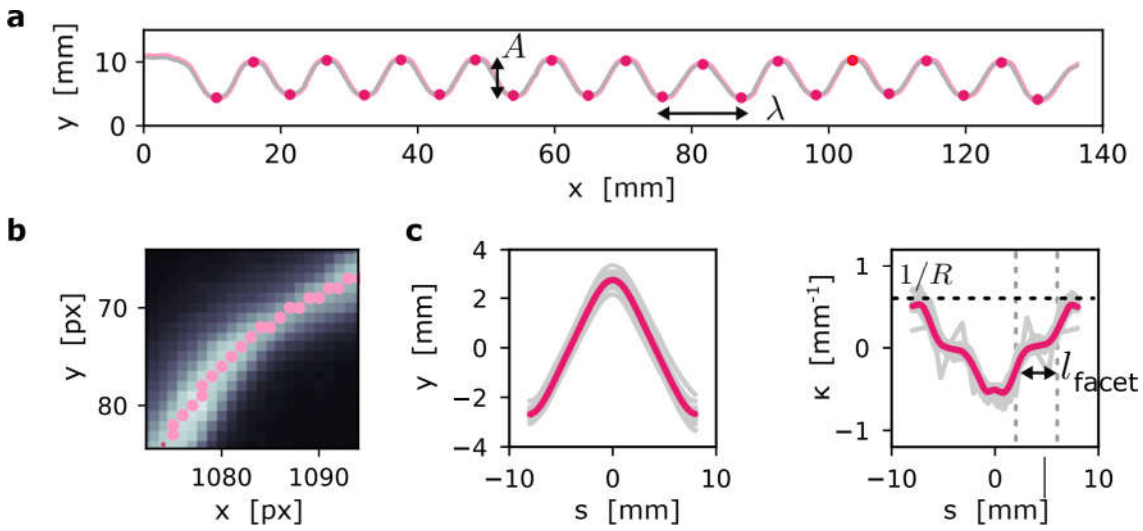

Fig. 5.13.: Typical geometry of mould-thermoformed sheets. **a**, Cross-section of a 75 µm-thick sheet after forming in the mould setup shown in Fig. 5.12a (grey line). Automatically detected groove positions (pink dots) yield an average amplitude and pitch $A = 5.4 \pm 0.3$ mm and $\lambda = 10.9 \pm 0.3$mm. **b**, Zoom-in of a CCD image (greyscale) and detected groove pixels (pink dots). **c**, The groove height as a function of arc length s along the sheet (left) is used to calculate the local curvature κ (right). The average radius of curvature of the fold, $R = 2 \pm 0.2$ mm, lies close to the mould's corrugation design (black dashed lines); the facet size l_{facet} matches well with their target length (grey dashed lines).

several hundreds of microns, with variations of tens of microns between upward- and downward-curving grooves[154].

While PVS rubber has a much larger elastic regime than plastic sheet material, its low Young's modulus compared to its specific weight (somewhat larger than that of water) makes rubber groovy sheets sensitive to gravity. For comparison, the gravity number of PVS compared to BoPET sheets (Eq. 5.6) is larger by three orders of magnitude: PVS groovy sheets must be suspended in a density-matched medium to counteract the effects of gravity.

Crucially, as Fig. 5.14b shows, rubber groovy sheets suspended in a solution of water and table salt exhibit multistability. They support defects and can be reshaped, implying that neither plasticity and residual stresses or strains nor a constant thickness are necessary to induce multistability in groovy sheets.

Conclusion

We have explored three distinct methods to fabricate groovy sheets: dynamic thermoforming of PET film; static thermoforming of PET film; and spin-coating silicone rubber.

Summarizing this section's findings, we find that thin plastic film has a high Young's modulus and small specific weight, which reduces the impact of gravity. Commercially produced film is widely available in a range of well-controlled thicknesses. While plastic has a relatively low yield point, a large ratio between groove radius of curvature and

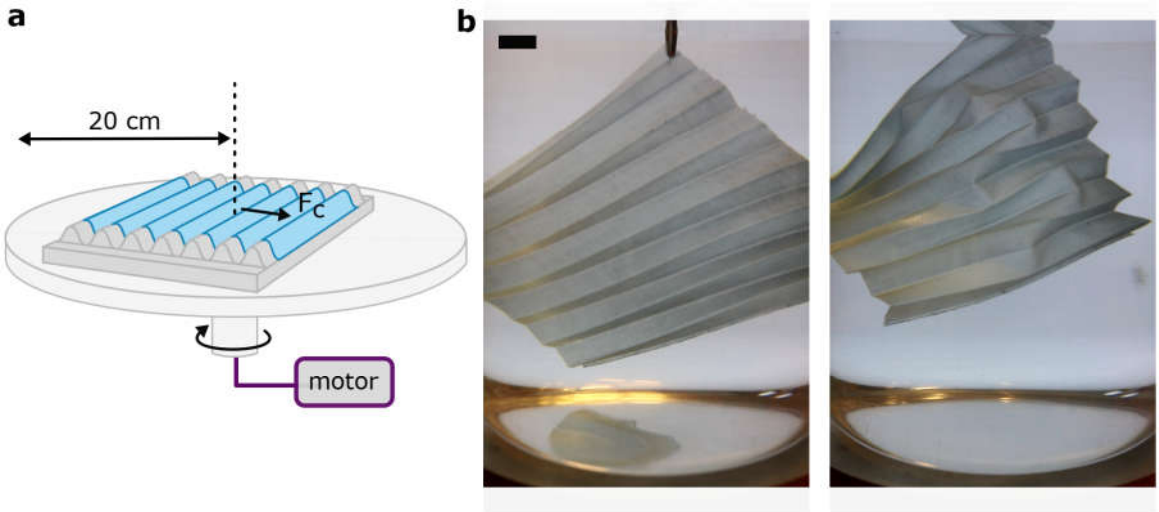

Fig. 5.14.: Spin-coating rubber groovy sheets. **a**, Schematic spin-coating setup. Liquid rubber (blue) is poured on a corrugated mould (dark grey) that is mounted on a motorized rotating platform (light grey). The rotation induces a centrifugal force F_c that spreads the liquid across the mould as it cures over several minutes. **b**, Example of a spin-coated rubber groovy sheet, suspended in an approximately density-matched solution of water and table salt (left). The sheet supports stable pop-through defects (right), suggesting that the reshaping of groovy sheets is in principle an elastic process. Scale bar: 1 cm.

sheet thickness will reduce the impact of plastic yielding. With static thermoforming, we may use temperature and forming time to vary the groove shape within a small range. In addition, bistability in groovy sheets occurs only for a range of groove geometries, as we discuss in more detail below; typically, the material's thickness must be much smaller than the groove's other length scales. The small thickness of plastic film means that the grooves, and our samples, remain of a suitable size for laboratory experiments. Static thermoforming, where a thin plastic sheet is confined in a heated metal mould, therefore meets the project's needs best.

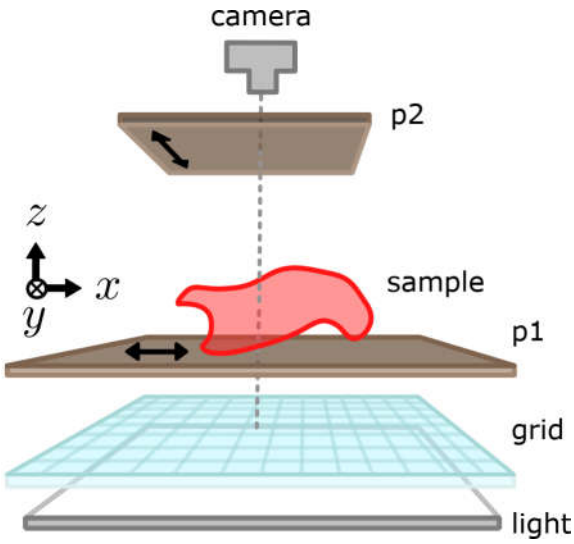

Fig. 5.15.: Photography setup for deformed groovy sheets. Images of a groovy sheet are taken by a Canon EOS 750D camera mounted over the sample. An LED light source backlights an alignment grid etched onto a transparent acrylic sheet (blue). A linearly polarising sheet (p1) is placed on the grid, and the transparent, birefringent BoPET sample is placed on top (red). A second linear polariser (p2) ensures that the light sample is contrasted by a dark background in the image recorded by the camera.

5.3. Measuring groovy sheet shapes

Groovy sheets deform in intricate ways, and their complex shapes must be quantified carefully. We use two imaging methods for shape measurements, which we discuss below. Section 5.3.1 lays out how we use photography to extract 3D shape information from a projected 2D image; and section 5.3.2 treats a 3D-scanning method, where we analyse groovy sheet shapes by projecting phase-shifted fringe patterns on them.

5.3.1. 2D photography

Groovy sheets can deform to cylindrical and helical shapes that are symmetric and regular. Their overall features can be captured by analysing 2D projections of a deformed sheet. We record such 2D images with a Canon EOS 750D camera at a resolution of 22 px/cm behind a linear polariser (see Fig. 5.15) mounted over a flat transparent surface, back-lit with LED lights and covered with a second linearly polarizing sheet. Samples are aligned manually on the surface, aided by a semi-transparent sheet with regular grid lines. Representative examples are shown in Fig 5.16; characteristic shape measures such as cylinder diameters (Fig 5.16a-b) or twisting angles (Fig 5.16c) can be extracted from these images with custom-built Python scripts as reported in section 5.7.

5.3.2. 3D imaging

In order to record the full three-dimensional shapes of our groovy sheets, we use an imaging method based on phase shifts in projected fringe pattern[155–157]. We review the 3D

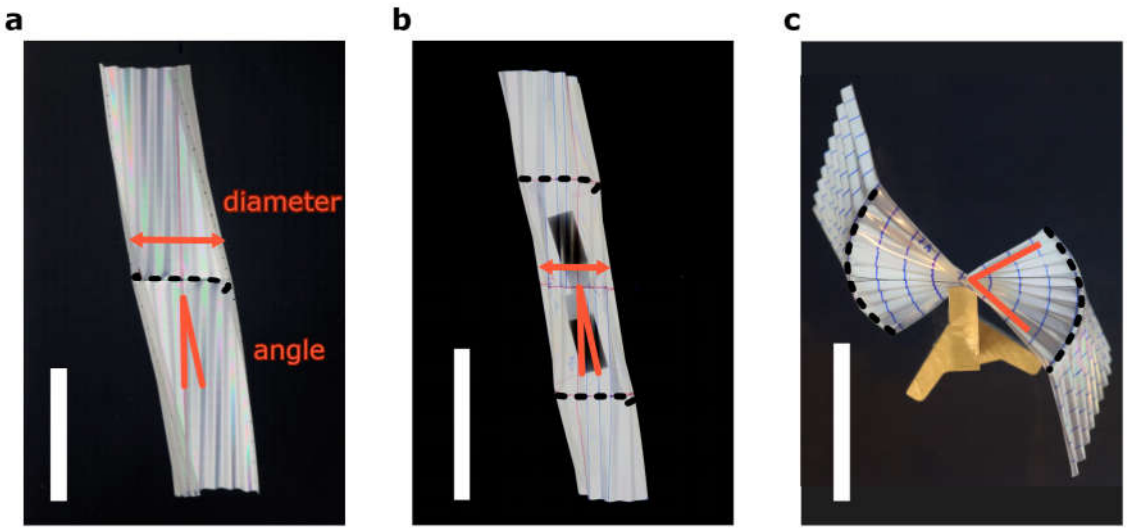

Fig. 5.16.: Typical 2D images of groovy sheets with one or two scars. a, A groovy sheet deformed into a twisted cylindrical shape (white) by the presence of a scar (dashed line) has a diameter and twist angle (red markers) that will be measured with an automated script in section 5.7. **b,** Two scars (dashed lines) on the same side of a groovy sheet produce a cylindrical, twisted shape with a measurable diameter and twist angle. **c,** Top view of a sheet with two scars on opposite sides. The helix-like surface with side lobes has a twist angle that will be measured manually in section 5.7. Scale bars: $5\ \mathrm{cm}$.

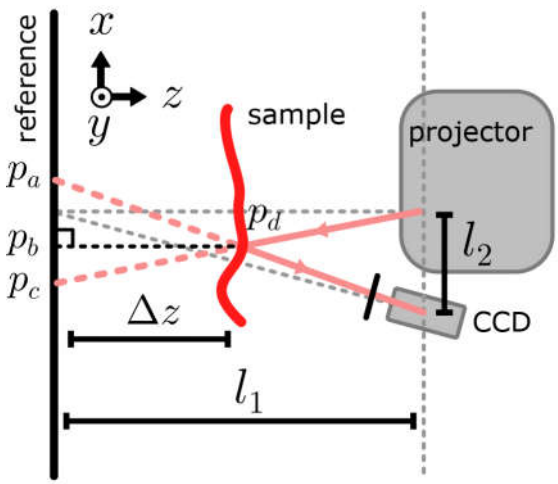

Fig. 5.17.: Schematic top view of the 3D imaging setup. A projector (top right) projects a sinusoidal fringe pattern on the reference plane (left) at a distance l_1. The projector's optical axis (grey dashed line) is orthogonal to the reference. A CCD camera (bottom right) captures the fringe pattern, after being placed at distances l_1 from the reference plane and l_2 from the projector. The camera's optical axis is indicated (grey dashed line). The imaging coordinates x, y, z are shown (top left). Placing a sample in front of the reference plane (red line) distorts the captured fringe pattern. The original and distorted pattern's phase shift between points p_a and p_d may then be used to calculate the sample's height profile $\Delta z = p_c - p_b$ (see main text) via trigonometric relations.

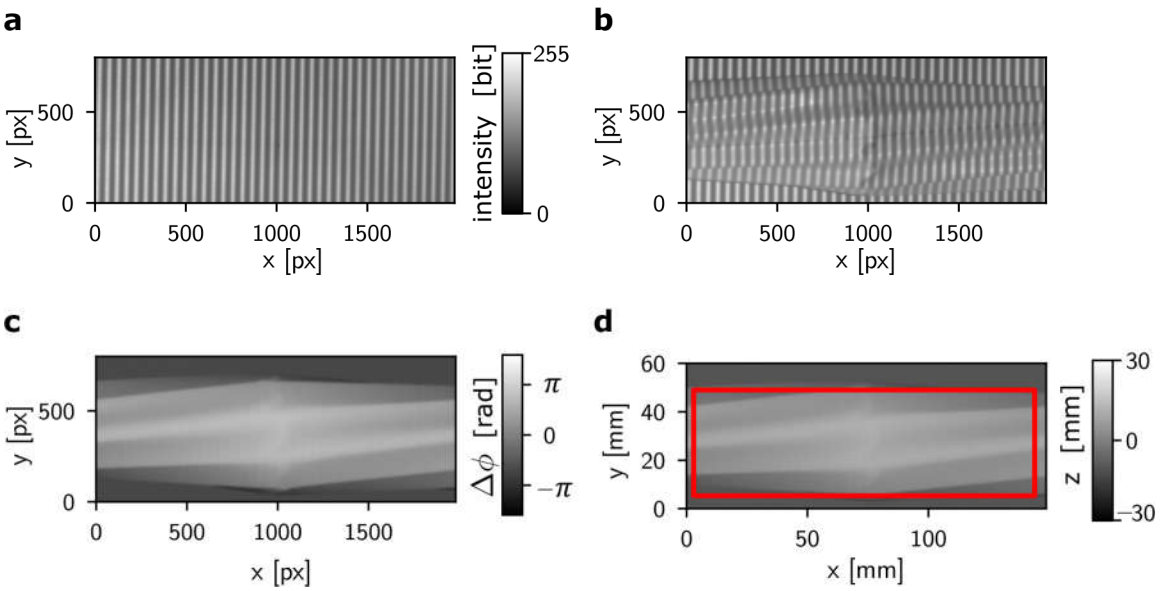

Fig. 5.18.: Image reconstruction to extract a 3D shape from a set of 2D images. a, A reference image of a projected sinusoidal intensity profile, recorded using the scanning setup of Fig. 5.18. Scale bar: light intensity (bit). **b,** Typical data image, in which the intensity profile is distorted by the presence of a groovy sheet with a central scar. Scale bar: see **a**. **c,** Phase difference $\Delta\phi$ (colour bar) of the distorted intensity profile, extracted from four doublets of reference and data images. Each doublet uses the same projected intensity profile, but is phase-shifted by $[0, \pi/4, \pi/4, \pi/4]$ respectively. **d,** Axes are rescaled to obtain width y, length x, and height z (colour bar) of the scanned surface. The approximate region of interest (red outline) is identified via a custom edge detection algorithm.

setup, image reconstruction, and typical results here.

A schematic view of the 3D imaging setup is shown in Fig. 5.17. We use an Epson EMP-X3 projector to project images of a sinusoidal fringe pattern on a blank, flat reference surface at 110 cm distance. A Basler acA2040-25gm camera, fitted with a Kowa lens of focal distance 75 cm, is positioned next to the projector at a distance of 15 cm from the projector and 110 cm from the reference surface. The fringe pattern has a wavelength of 52.7 px. The spatial resolution of the setup is 0.075 mm per pixel, which allows us to resolve the groove shape to a good degree of detail.

We now briefly describe how to obtain 3D shapes with this imaging setup, in line with the methods described in Refs. [155–157]. Basically, we project a sinusoidal fringe pattern on the reference surface and record it with a camera. The planar intensity profile of the sinusoidal pattern is given by

$$I^0_{\Delta\psi}(\boldsymbol{r}) = a_k e^{i\boldsymbol{k}\cdot(\boldsymbol{r}+\Delta\psi)} \ , \tag{5.7}$$

where $\Delta\psi$ is the pattern's phase offset. When an object is placed in front of the reference surface, the projected fringe pattern is distorted (red line in Fig. 5.17). The object creates a height offset $\Delta z(\boldsymbol{r})$. The distorted sinusoidal pattern can be described via

$$I_{\Delta\psi}(\boldsymbol{r}) = a_k e^{i\boldsymbol{k}\cdot(\boldsymbol{r}-\boldsymbol{u}(\boldsymbol{r}))+\Delta\psi} \ , \tag{5.8}$$

where $\boldsymbol{u}(\boldsymbol{r})$ is the in-plane pattern distortion (e.g. $p_d - p_a$ in Fig. 5.17). The height offset

$\Delta z(\boldsymbol{r})$ is then reconstructed from the reference and distorted fringe images by comparing their respective phase maps. To obtain difference between the two phase maps, we take four variations of the projected fringe pattern with distinct phase offsets $\Delta\psi \in [0, \pi/2, \pi, 3\pi/2]$. The phase difference $\Delta\phi$ between the recorded reference and distorted patterns can then be calculated, based on a linearisation of the intensity distortion:

$$\Delta\phi = \phi(p_d) - \phi^0(p_a) \tag{5.9}$$

where

$$\phi^0 = \arctan \frac{I^0_{3\pi/2} - I^0_{\pi/2}}{I^0_\pi - I^0_0} \tag{5.10}$$

$$\phi = \arctan \frac{I_{3\pi/2} - I_{\pi/2}}{I_\pi - I_0} \tag{5.11}$$

$$\tag{5.12}$$

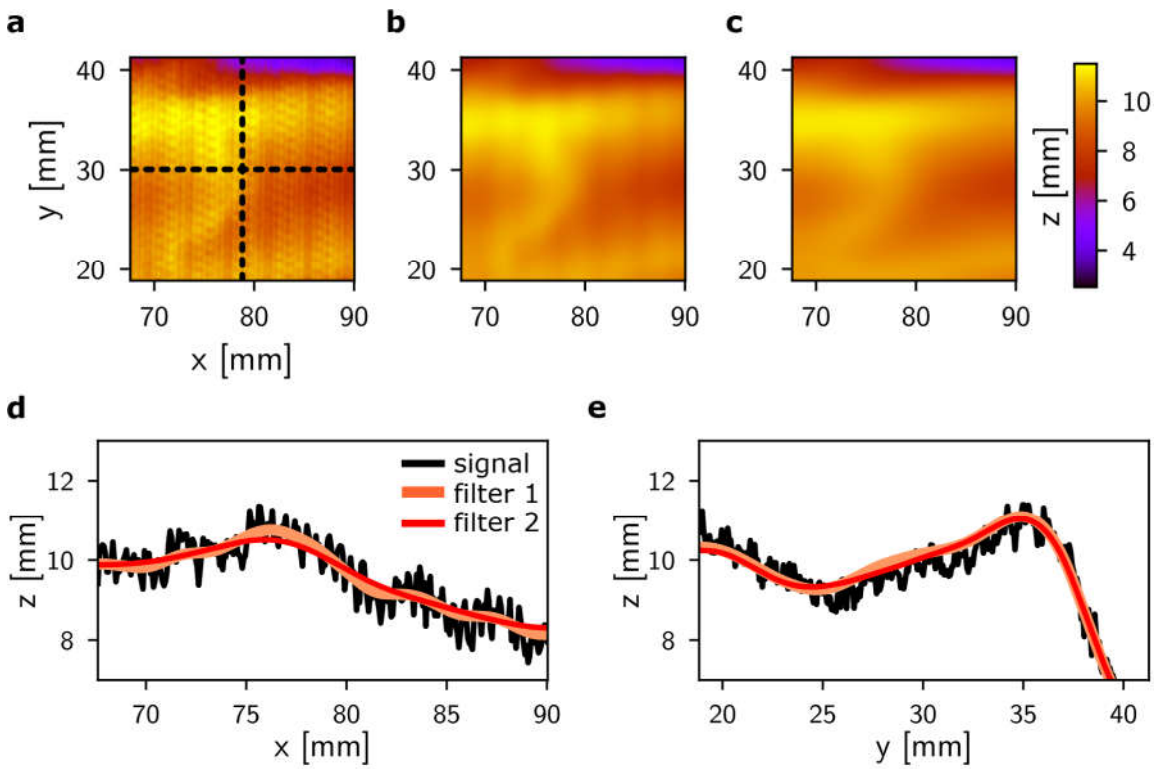

Fig. 5.19.: Noise reduction by low-pass filtering. **a,** Representative image of a noisy height profile (colour bar) of a groovy sheet near a defect. Residual noise from both the beamer's limited resolution as well as the fringe pattern's deviation from a perfect sine can be seen. **b,** Smoothing with a 2D low-pass Gaussian filter (legend: filter 1) to remove resolution noise from the signal. **c,** Sine-deviation noise is reduced with a second 1D low-pass Gaussian filter (legend: filter 2). **d,** Cross section of height profile corresponding to horizontal dashed line in **a**. Data passed through filter 1 still shows sine deviation noise, while data passed through filter 2 does not (legend). **e,** Height profile along vertical dashed line in **a**. Both filters show reduction of resolution-limited noise. Shifting of the profile is due to the two-dimensional smoothing of filter 1.

In turn, the phase difference is related to the height offset via the following geometric

relation, which assumes our setup behaves as an optically linear system:

$$p_a - p_c = \frac{\lambda}{2\pi}\Delta\phi \tag{5.13}$$

$$\Delta z(\boldsymbol{r}) = \frac{(p_a - p_c)l_1}{(p_a - p_c) + l_2}\ , \tag{5.14}$$

where p_a, p_c are shown in Fig. 5.17, and λ is the fringe spacing on the reference plane. In short: projecting phase-shifted fringe profiles on groovy sheets allows us to reconstruct their three-dimensional shape using a limited number of recorded images.

The steps of the reconstruction procedure are illustrated in Fig. 5.18, where panel 5.18a shows an example of a sinusoidal intensity profile projected on a flat reference surface. The presence of a reshaped groovy sheet sporting a central scar distorts the pattern (Fig. 5.18b). With Eqs. 5.7-5.10 above, the phase profile of the groovy sheet is found (Fig. 5.18c). Finally, the sheet's height profile is calculated via Eq. 5.10, and custom Python scripts detect the region that contains relevant data (Fig. 5.18d).

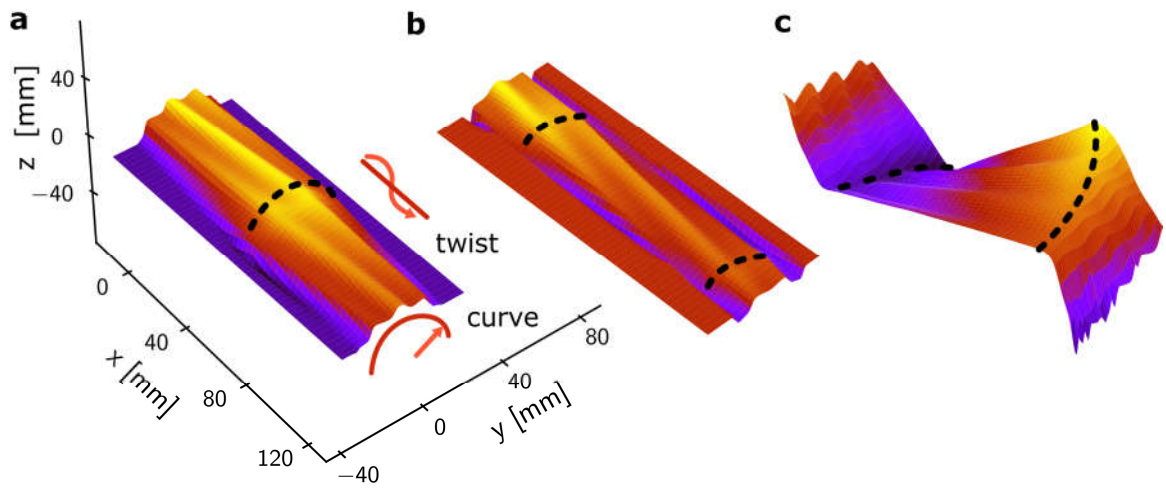

Fig. 5.20.: Typical sections of 3D-scanned groovy sheets. a, A groovy sheet deformed into a twisted cylindrical shape by the presence of a scar (dashed line). Grooves and defects can be detected, as well as the cylinder diameter and twist angle (red markers). Colours indicate height z qualitatively. **b,** Two scars (dashed lines) on the same side of a groovy sheet produce similar twisting cylinders. **c,** Top view of a sheet with two scars on opposite sides. Full details of the surface can be used to quantify the exact shape of the central, helicoidal portion.

Fig. 5.19a shows a small section of a 3D height profile; the recorded signal shows high-frequency noise, which we reduce with low-pass filtering. The high-frequency noise arises from two main sources. First, the beamer's projection resolution is limited, which shows up as high-frequency noise. We tackle this issue via Gaussian smoothing with a standard deviation of 10 pixels (corresponding to 0.75 mm on the sample) parallel to the fringes (Fig. 5.19b). Second, the projected fringe pattern is not completely sinusoidal, which induces noise orthogonal to the fringes at high frequencies. We improve this noise with Gaussian smoothing orthogonal to the fringes, with a standard deviation of half the fringe wavelength (corresponding to 2 mm on the sample, Fig. 5.19c). While low-pass filtering reduces the scanning accuracy, the typical length scales of the sheet's important

features (on the order of the groove size, 10 mm) lie above the filtered lengths and are preserved (Fig. 5.19d-e).

In short, 3D scanning allows us to measure the shape of groovy sheets. Fig. 5.20 shows representative examples of 3D scans of cylindrical and twisted shapes that sheets take on in the presence of one (Fig. 5.20a) or two scar lines (Fig. 5.20b-c); these 3D scans contain more information than the corresponding 2D projections shown in Fig. 5.16. Shape measures such as curvatures and twisting angles, but also defect positions, groove trajectories, and twisting angles can be measured in detail, as we will report in section 5.7.

5.4. In-plane elasticity of groovy sheets

5.4.1. Groovy sheets are not symmetric

Groovy sheets have an orthotropic geometry. That means the elastic response in both in-plane directions, along the grooves and across the grooves, is very different (Fig. 5.21). Along the grooves (Fig. 5.21a), the sheet is stiff: its behaviour is governed by stretching of the underlying film material, and its Young's modulus determines the stretchiness. Across the grooves (Fig. 5.21b), the response is soft with a sudden stiffening behaviour: this deformation is dominated by low-stiffness bending that flattens the grooves before the sheet's material is stretched. This type of soft-to-hard transition is typical for many biological tissues, and helps prevent instabilities (such as aneurysms in blood vessels)[158]. By contrast, in our groovy sheets, we find that this particular stress-strain behaviour creates a multistable energy landscape.

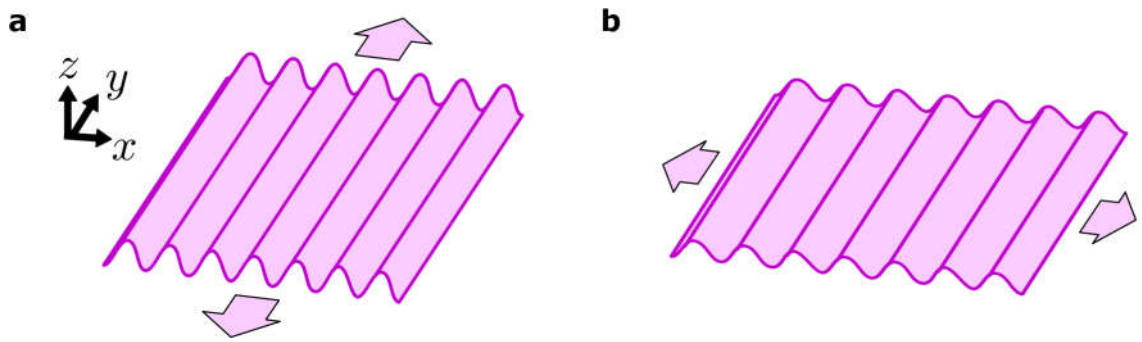

Fig. 5.21.: Groovy sheets are not symmetric under stretching. **a,** Stretching along the grooves (direction $\hat{y}$) results in elongation of the underlying material; this typically costs a lot of energy. **b,** Pulling across the grooves (direction $\hat{x}$) results in bending of the sheet and flattening of the grooves. This deformation mode requires less energy.

In the following sections, we quantify the in-plane elasticity of groovy sheets. We perform experiments and simulations to study the dependence of their response on the groove geometry. In section 5.4.2, we start by estimating the sheet stiffness parallel to the grooves, and contrast this with the experimentally measured stiffness across the grooves in section 5.4.3. Via comparison to a simple discrete model as well as numerical simulations (section 5.4.4), we find a predictive model for a sheet's stiffness. Notably, we find an *effective* stiffness, based on a simple rescaling, that predicts the response of sheets across groove geometries. Finally, we use our findings to create a simple 3D model built from discrete springs (section 5.4.5) whose geometry and stiffness mimics the elastic properties of real groovy sheets. Crucially, the 3D model also mimics the reshaping behaviour of real groovy sheets. Our findings showcase the crucial connection between geometry and energy in our groovy sheets, and show that their shape-morphing behaviour is elastic and reversible.

5.4.2. Stiffness along the grooves

When a groovy sheet is stretched by a uniform force F_y applied along the grooves (Fig. 5.21a), the underlying sheet material must stretch by an amount u_y. We estimate the stretching stiffness as follows, assuming Hookean behaviour and small strains below the material's yield point (see appendix A.6):

$$F_y = \frac{ENts_\lambda}{W} u_y \ , \tag{5.15}$$

where E is the material's Young's modulus, W the N the number of grooves, and s_λ the arc length of a groove (see Fig. 5.8). The relation above shows that the sheet stiffness along the grooves, $\frac{ENs_\lambda}{W}$, is set by the material's Young's modulus- unlike the sheet's behaviour in the orthogonal direction.

5.4.3. Stiffness across the grooves

Experimental measurements show that extending sheets across their grooves with a uniform force does not stretch the underlying material immediately; the grooves flatten our first (Fig. 5.21b). Our experimental setup is shown schematically in Fig. 5.22a: a corrugated sheet, mounted in two clamps, is extended by a displacement u while its response force F is measured (see appendix A.8). The experimental force-displacement curves shown in Fig. 5.22b-c shows the sheet's soft-to-stiff behaviour: at the onset of extension, deformations are bending-dominated and need little force (regime I). Once the sheet is fully flattened out, stretching deformations take over and the force-displacement curve rises rapidly, proportionally to the underlying material's Young's modulus (regime II).

5.4.4. Modelling stiffness

To understand the sheet's behaviour under stretching across its grooves, we present two models here: a discrete simplified one, and a continuum model. While the discrete model helps us understand the qualitative behaviour of the sheet, we will show that the continuum model allows us to predict the experimentally found sheet stiffness quantitatively; surprisingly, this prediction turns out to be largely independent of the sheet's detailed groove shape.

We first discuss a groovy sheet model made with discrete building blocks (Fig. 5.23a). The two-dimensional structure consists of $2N$ bars with rest length s^0 and Hookean stretching stiffness k_s, connected in an accordion-like pattern by torsional springs of rest angle ϕ^0 and stiffness k_t. This creates a sheet-like structure with N grooves. Deviations from the rest length and angle are penalized with a stretching energy $\mathcal{E}_s = \frac{1}{2}k_s\Delta s^2$ and a torsional energy $\mathcal{E}_t = \frac{1}{2}k_t\Delta\phi^2$. The accordion's overall rest length is given by $L = 2Ns\cos\frac{\phi}{2}$, and extensions $u = L - L^0$ of the structure are measured from the rest length $L^0 = 2Ns^0\cos\frac{\phi^0}{2}$. The force F needed to extend the accordion by a distance u can then be calculated via variation of the structure's Lagrangian $\mathcal{L}$:

$$\mathcal{L} = -2N\frac{1}{2}k_t(\phi-\phi_0)^2 - 2N\frac{1}{2}k_s(s-s^0)^2 + F\left(u - 2N(s\cos\frac{\phi}{2} - s^0\cos\frac{\phi^0}{2})\right) \ . \tag{5.16}$$

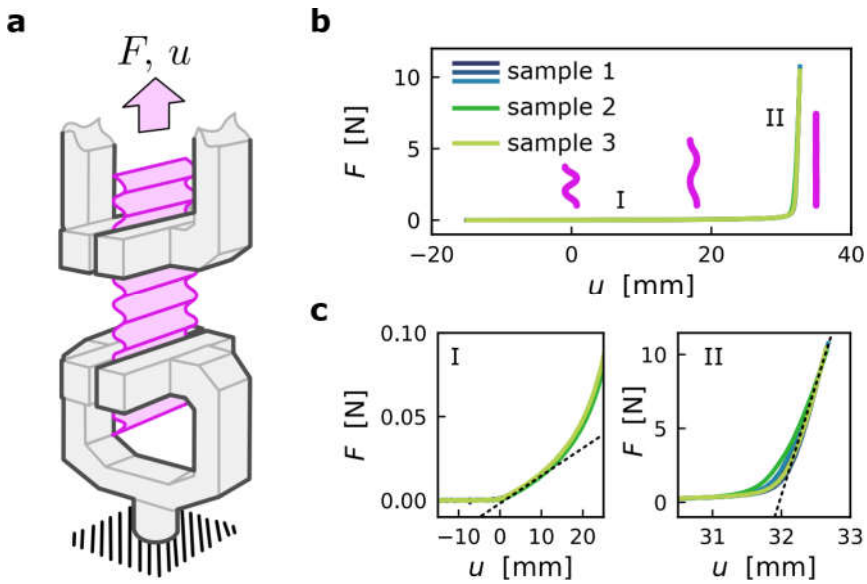

Fig. 5.22.: Experimental measurement of a groovy sheet's stiffness under tension. a, A corrugated BoPET sample with $N = 18$ grooves of thickness $t = 23$ µm, width $W = 3$ cm, total relaxed length 160.5 mm and total flattened length 192.5 mm is mounted between the clamps of an Instron universal testing machine. Displacement u of the upper clamp produces a force F that is measured by a load cell. **b,** Top: reproducible force-displacement curves of three distinct sheets (samples 1-3, see legend), stretched over 33 mm. Insets illustrate the deformed sheet (pink lines). Two regimes, I and II, can be distinguished. **c,** In regime I (left), grooves bend and flatten at low force. In regime II (right), the sheet stretches at high force. Slopes correspond to a distinct stretching stiffness in both regimes (dashed lines).

While there is no analytical expression for the force $F(u)$ for all values of u, it is possible to divide the response into three regimes: bending-dominated at small displacements, stretching-dominated at large displacements, and a mixed response in a narrow crossover regime at intermediate displacements (see appendix A.8 for details).

We briefly review the force response in the regimes of small, intermediate, and large displacements. First, at small values of u, we find

$$F = 2k_t \frac{\Delta\phi}{s^0 \sin\frac{\phi}{2}} \tag{5.17}$$

$$= -\frac{8Nk_t}{(S^0)^2 - (L^0)^2} u + \mathcal{O}\left(u^2\right) \ , \tag{5.18}$$

where $S^0 = 2Ns^0$ and $L^0 = 2Ns^0 \cos\frac{\phi^0}{2}$ are the lengths of the accordion in its flattened and rest states, respectively. Evidently, the force response in this regime depends only on the torsional hinges, and the accordion has an effective stiffness $-\frac{8Nk_t}{(S^0)^2-(L^0)^2}$ to displacements in a small linear regime. However, we can obtain a governing relation for the sheet's elastic behaviour in a much larger regime:

$$\mathcal{W} = \int_0^u F \mathrm{d}u' = -\int_{\phi^0}^{\phi} Ns^0 \sin\frac{\phi'}{2} F \mathrm{d}\phi' = \frac{1}{2}(2Nk_t)\Delta\phi^2 \ . \tag{5.19}$$

Here, $\mathcal{W}$ is the work performed on the sheet during its extension. In the bending-

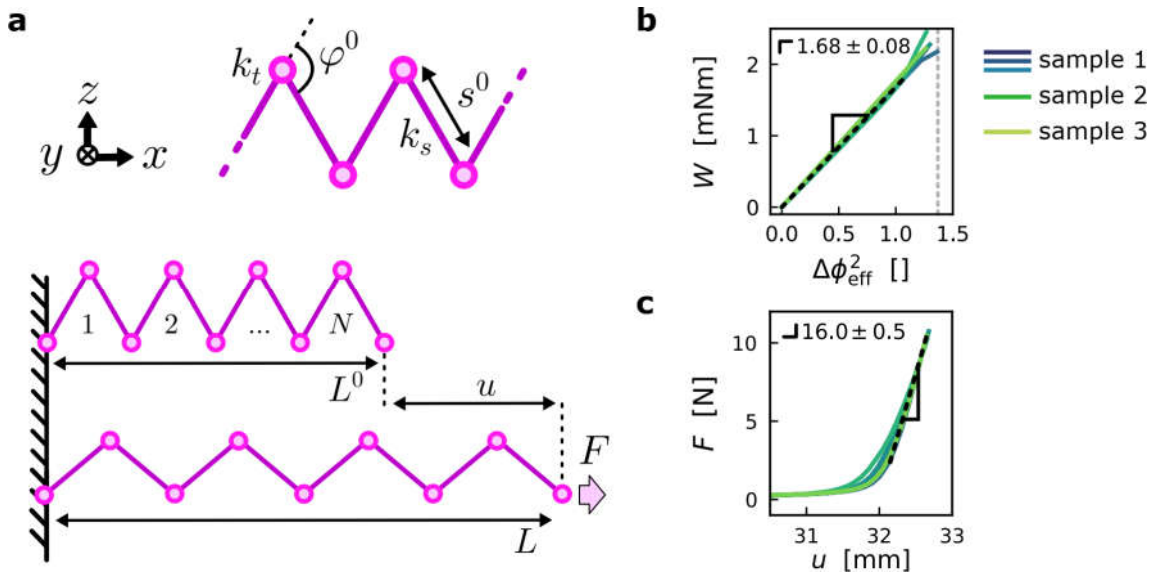

Fig. 5.23.: Discrete model for the extension of a groovy sheet. a, Top: stiff bars with length s^0 and stretching stiffness k_s (purple lines) are connected by soft torsional springs with a rest angle ϕ^0 and torsional stiffness k_t (pink circles) in an accordion pattern. Bottom: a structure with $2N$ bars and N grooves has rest length L^0. Extension by a displacement u to new length L requires a force F. **b,**

dominated regime, it has a purely quadratic dependence on the angle change $\Delta\phi$, with a corresponding stiffness of $2Nk_t$. Since the contrast between bending and stretching stiffness is large, this quadratic relation holds in a large regime of extensions. Secondly, in the crossover regime, the accordion is nearly flattened and the bars start stretching; the force is due to a mixture of hinge bending and bar stretching, and has no analytical form. Finally, when displacements are larger than $S^0 - L^0$, stretching of the bars must take place. In that case, the force reads

$$F = \frac{k_s}{2N}(u + L^0 - S^0) \ , \tag{5.20}$$

which equation shows that the accordion's stiffness $\frac{k_s}{2N}$ in the final regime comes purely from stretching of the bars. These findings match our experimental results, which also show a splitting into a soft, bending-dominated and a stiff, stretching-dominated regime.

We now investigate whether the stiffness parameters of the accordion model, k_s and k_t, can be derived from the geometry of real samples. Using the data of Fig. 5.22 and Eqs. 5.19 and 5.20, we first estimate experimental values of k_t and k_s. In Fig. 5.23b, we present the work $\mathcal{W}$ performed on the sample versus the square of the effective angular change $\Delta\phi_{\text{eff}} = \phi_{\text{eff}} - \phi^0{}_{\text{eff}}$, defined via $\phi_{\text{eff}} = 2\arccos\frac{L^0+u}{S^0}$: the relation is linear to good approximation. In Fig. 5.23c shows the force F versus extension u in the sheet-stretching regime. We find $Nk_t = 1.68 \pm 0.08$ mN m and $\frac{k_s}{2N} = 16.0 \pm 0.5$ N/mm for samples with $N = 18$ grooves, resulting in the following experimental stiffnesses:

$$k_t = 93 \pm 4 \ \mu\text{N m} \tag{5.21}$$

$$k_s = 576 \pm 18 \ \text{N/mm} \ . \tag{5.22}$$

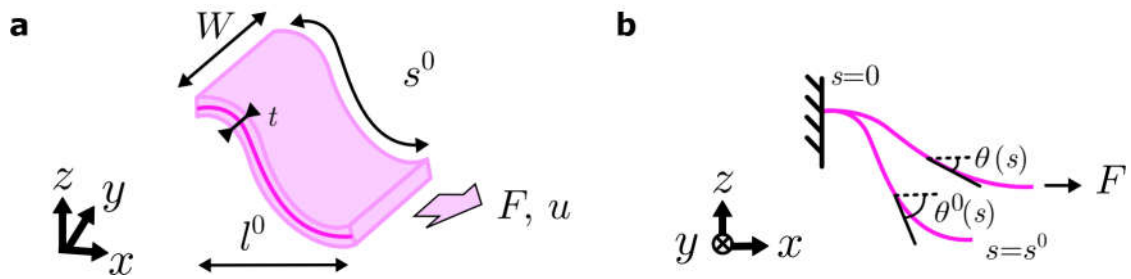

Fig. 5.24.: Elastica model of half a groove. a, The groove section has thickness t, width W, arc length s^0, and projected length l^0. **b,** The section's centroid, which determines its shape, is described by the angle θ^0 between the centroid's tangent and the $\hat{x}$-axis as a function of arc length s. Under a force F along the applied uniformly at the sheet's edge, the centroid deforms to $\theta(s)$.

The question remains how these values are related to the experimental samples' shape. We estimate the magnitude of the torsional and stretching stiffnesses of a real groovy sheet, assuming all bending takes place in the groove's fold (its curved section, see 5.2.1), while stretching takes place across the entire groove. Our experimental samples have a Young's modulus $E = 5 \pm 0.3$ GPa (see appendix A.6), width $W = 30$ mm, thickness $t = 23$ µm, flattened length $S^0 = 192.5$ mm, curved groove length $R\theta = 2 \pm 1$ mm, and number of grooves $N = 18$. We first estimate k_t of the groove fold using Winkler-Bach theory[159]. A curved sheet section of thickness t, depth W, and Young's modulus E, pre-bent to a radius of curvature R and subtending an angle θ, has a torsional stiffness

$$k_t = \frac{EWt^3}{12R\theta} \tag{5.23}$$

$$\approx 105 \pm 50 \text{ µN m} , \tag{5.24}$$

in the limit of reasonably small thickness, $\frac{t}{R\theta} < 1$. Secondly, we estimate k_t using linear elasticity. The stretching stiffness of half a flattened groove (corresponding to a single accordion bar) is, to first order,

$$k_s = \frac{EWt}{S^0/(2N)} \tag{5.25}$$

$$\approx 650 \pm 50 \text{ N/mm} . \tag{5.26}$$

While the shape-derived values for model parameters k_s and k_t match the experimentally measured values, this is mostly due to their large error margin. The accordion structure is a good toy model to understand a groovy sheet's stretching response, but it does not help us to quantitatively predict its stiffness; we need a different model for that.

We now discuss a predictive continuum model for groovy sheets. Previous work has shown that the entire groove deforms during stretching[160], and our assumption in the accordion structure above that hinging takes place near the fold may not be correct. We take this into account in a more realistic elastica model. We show below that the mechanics of these elastica grooves depends only weakly on the details of the groove's geometry.

The elastica geometry is shown in Fig. 5.24, which shows half a groove under a stretching force F and extension u. In the elastica framework, the angle profile $\theta(s)$ of the sheet

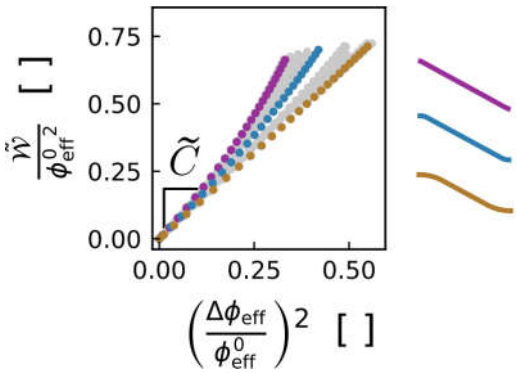

Fig. 5.25.: The mechanical response of sheets with various shapes can be rescaled to collapse on a curve. The dimensionless work $\tilde{\mathcal{W}}$ performed on a sheet section during stretching (Fig. 5.24) is shown as a function of the effective angle change $\Delta\phi_{\text{eff}} = \phi_{\text{eff}} - \phi_{\text{eff}}^0$, where $\phi_{\text{eff}} = 2\arccos\frac{l^0+u}{s^0}$. Both axes are rescaled by $(\Delta\phi_{\text{eff}}^0)^2$. The relation at small deformations is linear, with a slope $\tilde{C}$. Data for a broad range of groove shapes are shown (grey); several shape examples are highlighted in colour (see legend).

unit under an applied force F must minimize the sheet's bending-energy Lagrangian $\mathcal{L}$[108]:

$$\mathcal{L} = \frac{1}{2}D\int_0^{S^0}\left(\theta_s(s) - \theta_s^0(s)\right)^2 \mathrm{d}s - F\left[u - \int_0^{S^0}\left(\cos\theta(s) - \cos\theta^0(s)\right)\mathrm{d}s\right] , \quad (5.27)$$

where $D = \frac{Et^3W}{12(1-\nu^2)}$ is the sheet's bending stiffness and ν its Poisson ratio. Angle profiles that minimize the energy obey the elastica equation

$$\theta_{ss}(s) - \theta_{ss}^0(s) - \frac{F}{D}\sin\theta(s) = 0 \ . \quad (5.28)$$

Numerical solutions found using the Mathematica software suite[161] yield the force-displacement response for grooves of widely varying geometries (see appendix A.8). Notably, the response across geometries can be rescaled to a master curve with fair accuracy, as shown in Fig. 5.25. There, we show the relation between the adimensional work $\tilde{\mathcal{W}} = \mathcal{W}s^0/D$ performed on the groove, and the square of the effective angle change $\Delta\phi_{\text{eff}} = \phi_{\text{eff}} - \phi_{\text{eff}}^0$, where $\phi_{\text{eff}} = 2\arccos\frac{l^0+u}{s^0}$ Both quantities are rescaled by the square of the rest angle ϕ^0. The data show that the relation between the plotted quantities is linear to good approximation, especially at small angle changes. In addition, the curves for widely varying groove shapes overlap to a fair degree. Defining an effective linear slope $\tilde{C}$ so that $\tilde{\mathcal{W}} = C\Delta\phi_{\text{eff}}^2$, we find that its values lie between limiting values $1.25 < \tilde{C} < 1.5$ for *any* groove geometry (see appendix A.8). The relation between the slope $\tilde{C}$ and the experimentally measured torsional stiffness k_t is then found by combining our elastica result and Eq. 5.19:

$$\mathcal{W} = \frac{1}{2}k_t\Delta\phi_{\text{eff}}^2 \quad (5.29)$$

$$\tilde{\mathcal{W}} = \tilde{C}\Delta\phi_{\text{eff}}^2 \quad (5.30)$$

$$k_t = 2\tilde{C}\frac{EWt^3}{12(1-\nu^2)s^0} \quad (5.31)$$

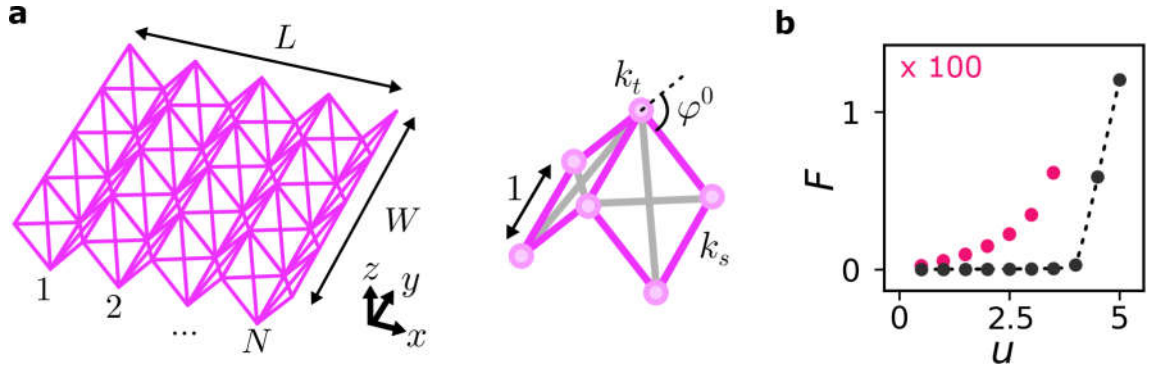

Fig. 5.26.: 3D simulation of groovy sheets. a, Left: discrete 3D model of a groovy sheet with N grooves, length L, and width W. Right: zoom-in of the model's unit cell. Springs with stiffness k_s and length 1 (purple lines) are connected in a square by torsional hinges (pink circles) of stiffness k_t and rest angles ϕ^0 along $\hat{\boldsymbol{x}}$ and 0 along $\hat{\boldsymbol{y}}$. Cross-braces springs (grey lines) of length $\sqrt{2}$ and resistance $0.1k_s$ stiffen the cell. **b,** Force F exerted by the structure under uniform extension u along $\hat{\boldsymbol{x}}$ across the grooves (compare Fig. 5.22). Data were obtained for a structure with $W = 9$, $N = 4$, $\phi^0 = 2.1$ rad, $k_s = 1$ and $k_t = 10^{-4}$ via a gradient descent algorithm. The force shows a soft hinge-dominated regime (red data points, y-scale magnified 100x) and a stiff stretch-dominated regime (black data points).

Substituting our sample's properties in Eq. 5.31, we find

$$k_t = 94 \pm 14 \ \mu\mathrm{N\,m} \ , \tag{5.32}$$

regardless of the exact groove geometry; comparing this value to our experimental measurement $k_t = 93 \pm 4$ µN m, we find an excellent agreement between our general elastica model and the real samples.

With the above models, we have explored the behaviour of groovy sheets under stretching across their grooves. Most significantly, we have shown that the sheet's initial response (that is, groove flattening) is dominated by a torsional stiffness that we can predict quantitatively within a small error margin, without needing detailed knowledge of the groove geometry.

5.4.5. A 3D sheet simulation

We now showcase a simple 3D model to simulate the reshaping behaviour of groovy sheets. In section 5.4.4, we showed that abstract models are useful tools to study the (qualitative) mechanics of groovy sheets. These models are easy to manipulate: quantities that are difficult to measure in experiments (for example, the total elastic energy contained in a deformed sheet) can be extracted straightforwardly. Here, we build on our results in the sections above to create a model mesh that mimics groovy sheet's in-plane stretching mechanics. We show that the model mesh matches the behaviour of a real groovy sheet to a good degree. Most importantly, we find that the modelled groovy sheet can sustain defects, and reshapes like a real sheet when a scar line of defects is introduced.

The 3D model mesh is shown in Fig. 5.26a, where the mesh unit cell is highlighted. Like the accordion model that we considered in Fig. 5.23, the mesh is built up out of linear springs of unit length and stretching stiffness $k_s = 1$, connected by torsional springs

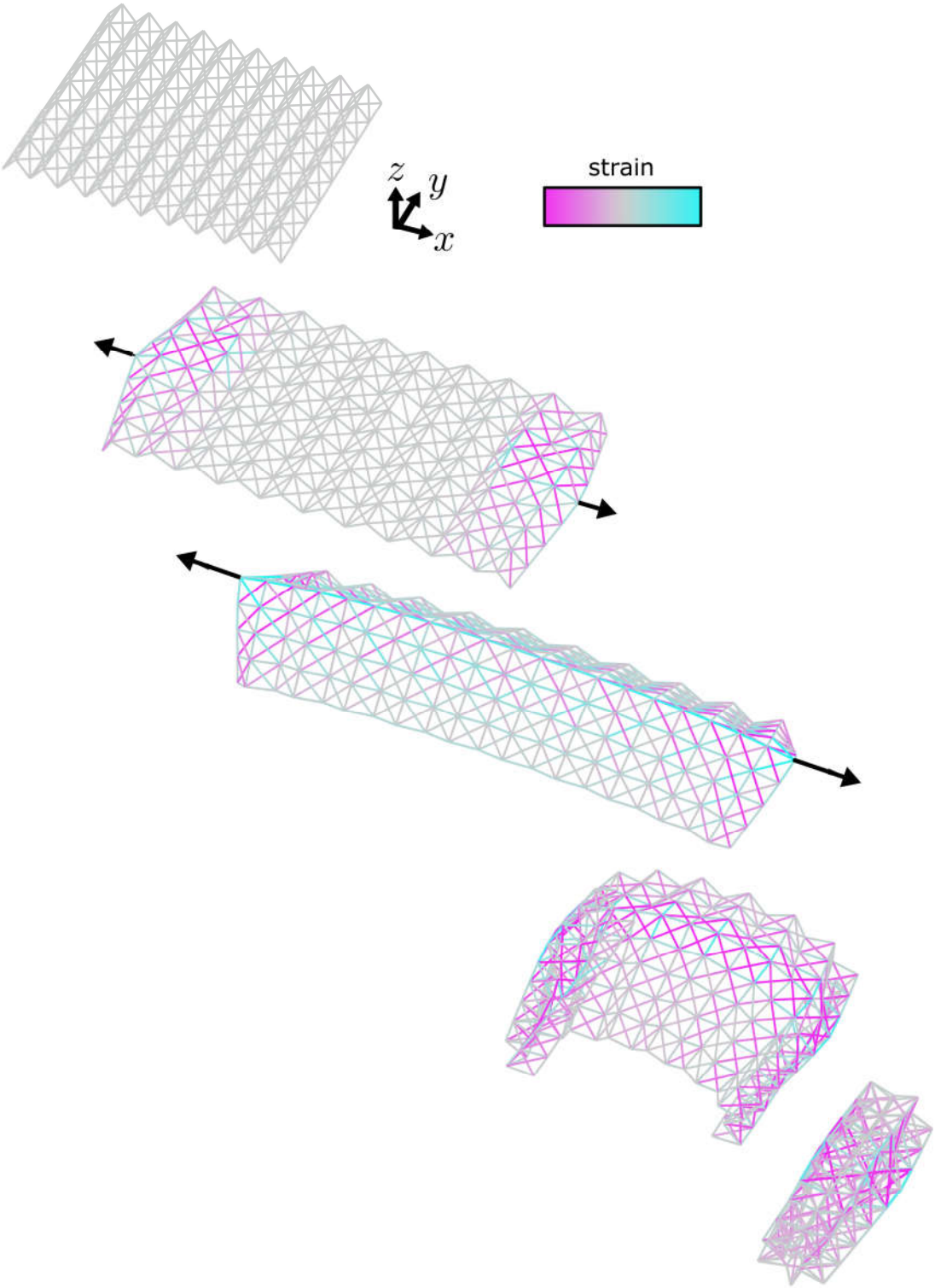

Fig. 5.27.: Simulated groovy sheets reshape via defects. Top to bottom: a modelled sheet with parameters $W = 9$, $N = 10$, $\phi^0 = 2.1$ rad, $k_s = 1$ and $k_t = 10^{-4}$ is extended by pulling at two nodes at its edges (black arrows). Defects snap through in the edge grooves and produce a local strain (colour bar). Further extension snaps the entire sheet and creates a scar line of adjacent defects. Subsequent relaxation lets the sheet curl up to a cylindrical equilibrium state with residual elastic energy.

with rest angle $\phi^0 = 2.1$ rad and hinging stiffness $k_t = 10^{-4}$ along the $\hat{\boldsymbol{x}}$-direction. Note here that we have chosen a (dimensionless) ratio between hinging and stretching stiffness $\frac{k_t}{(s^0)^2 k_s}\mathcal{O}\left(1e-4\right)$ similar to what we find in our experimental samples (see e.g. 5.21-5.22), in order to mimic real structures. Along the $\hat{\boldsymbol{y}}$-direction, neighbouring accordions are connected by additional linear springs as well as torsional springs with rest angle 0 rad. Cross-bracing springs are added with a stiffness $0.1k_s$ to mimic a real sheet's resistance to in-plane shearing (see appendix A.8). The model can be actuated by displacing its connecting nodes and letting the structure relax to equilibrium via a gradient descent method (appendix A.8).

We now show that the model's mechanics qualitatively match those of a real groovy sheet. First, Fig. 5.26b shows the force-extension curve of a mesh model under uniform stretching across its grooves. Like the experimental curves shown in Fig. 5.22, the force response shows two regimes: the first regime is dominated by hinge bending and the second by spring stretching. Secondly, Fig. 5.27 shows the mesh model's response under stretching at two point contacts on opposite sides of the sheet. The model mimics the behaviour of real sheets well (see section 5.1): initially, the entire mesh stretches out; at a critical strain, defects are formed at the sheet's edges; and finally, a scar line of aligned defects is created. When the scarred sheet is released to relax freely, it curls up into a cylindrical shape as expected.

In conclusion: our simple 3D mesh qualitatively matches the reshaping behaviour of a real groovy sheet. We will use this result to investigate energetic interactions between defects later, in section 5.6. Notably, the 3D model's success shows that groovy sheet's ability to sustain defects does not depend on pre-strain, pre-stress, or plasticity: it is a purely elastic effect.

5.5. Bistability of grooves

In section 5.1, we showed that defects pop in groovy sheets if they are stretched at two points along their two opposite edges. Here, we show that single defects can also be created by pushing down on a groove. We study their formation by experimentally popping through single grooves in their centres, and recording their force response and local shape (section 5.5.1). In section 5.5.1, we review previous research on similar structures to understand the origins of the stability of snapped-through grooves, and study the stabilizing effect of the groove's flat facets. Finally, section 5.5.2 investigates the introduction of a single defect at any position in a large groovy sheet. We show that the sheet's size influences when defects are stable, suggesting that defects do not only rely on local, but also on long-range deformations. We study these long-range effects as a function of sheet size, and show that single defects are *not* stable above a certain critical groove length, suggesting that the aspect ratio of grooves is a limiting factor in the design of shape-morphing groovy sheets.

5.5.1. Making single defects

Re-shaping a groovy sheet means snapping defects into it, for example via stretching (see section 5.1). But while snapping lots of defects at once by stretching the sheet is effective, it is also uncontrolled. Here, we show that defects can be popped through in a controlled way by indenting a groove from the top. We examine how the indentation force varies with the indentation depth, and find that the popping (and un-popping) of defects is a multi-step process that involves several snap-through events.

To study the force needed to pop a groove, we use the experimental setup shown in Fig. 5.28a. A groovy sheet is placed on two stiff support, 50 mm apart, under its central groove. The assembly is placed in an Instron 4900-series universal testing machine (UTM), modified to work horizontally. An indenter is fastened on the centre of the groovy sheet with a small ball magnet. The indenter is mounted in the UTM and attached to its translation stage and a 10 N-rated 2530-series load cell. Forces F on the indenter are measured as it moves by a displacement between $u = -0.5$ and 5 mm from the starting position at a speed of 0.1 mm/s. Moving the indenter far enough pops the groove.

Fig. 5.28b shows a typical force-displacement curve of a popping and un-popping sheet, with two distinct snap-through events (stars) in the popping stage. Data shown were obtained for a sample with $N = 5$ grooves, created with the mould-thermoforming method shown in section 5.2.2. The sheet has width $W = 100 \pm 5$ mm and thickness $t = 75$ µm. During the initial indentation (Fig. 5.28, upper curve), the force rises steeply as expected for any material, but then flattens off and becomes irregular. At a critical indentation depth, two audible snap-through events happen in short succession, and result in a popped groove with a defect. Performing the same experiment with the groovy, popped sheet reversed in the setup allows us to measure the un-popping force (Fig. 5.28b, lower curve). Comparing the popping and un-popping energies by calculating the area under the two curves, we find that popping costs 1.7mN m and un-popping 0.1mN m. In other words, the popped sheet's energy is 1.6mN m, and the barrier for reversal is more than

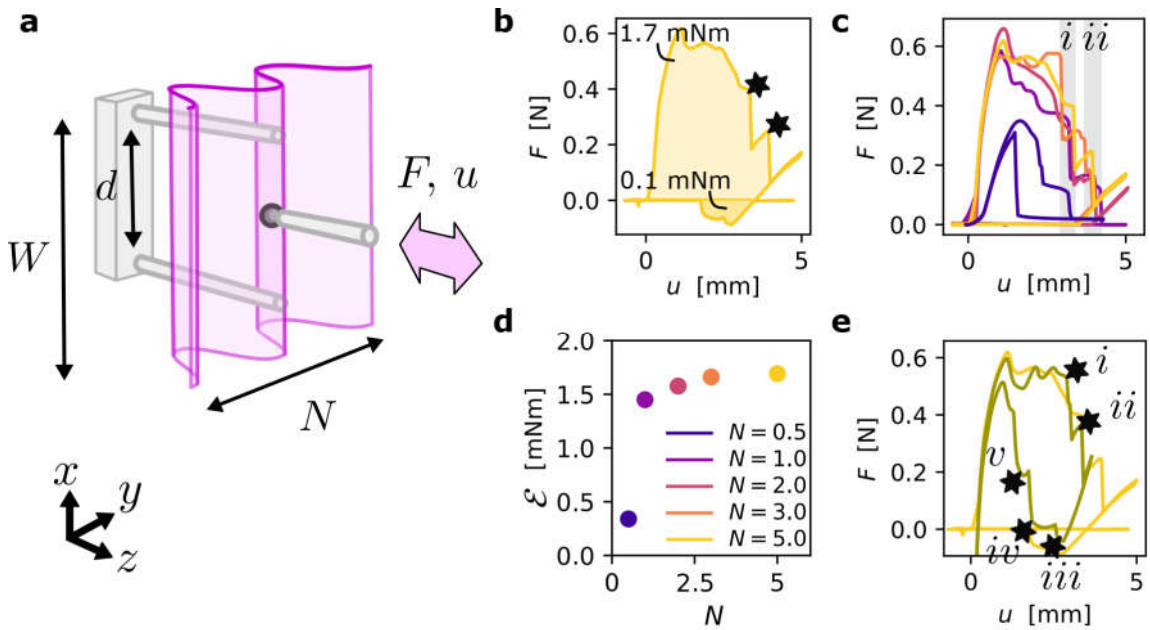

Fig. 5.28.: Popping a single defect. a, Experimental setup. An indenter (light grey) is stuck to the centre of a sheet (pink) with N grooves and width $W = 100 \pm 5\mathrm{mm}$ by a magnet (dark grey). The indented groove is held by two supports at distance $d = 50$ mm. Forces F generated by moving the indenter by a displacement u are measured by a universal testing machine. **b,** Force-displacement curve measured while popping (upper) and un-popping (lower) a sheet with $N = 5$ grooves. The onset is smooth, corresponding to slow indentation of the groove. Popping is complete after two audible snap-through events (stars) and $1.7\mathrm{mN\,m}$ of work has been done: releasing the indenter brings the force below zero. Un-popping the defect costs $0.1\mathrm{mN\,m}$. **c,** Popping of sheets with decreasing numbers of grooves: $N = 5$ to $N = 1/2$. Snap-through events i and ii (grey areas) and stable defects are seen for $N = 1$ to 5. At $N = 1/2$ (dark blue curve), the onset force is smaller, and the popped state snaps back. **d,** Work done during indentation, measured as the area under the force-displacement curves in (**c**), for $N = 5$ to $N = 1/2$. The work initially increases with N, then saturates. **e,** Force curve (green) measured when a sheet with 5 grooves is held by a magnet on each support. Forces are measured over the full range of displacements (free curve in yellow shown for comparison). Two snap-through events are seen while popping ($i - ii$), and three while un-popping ($iii - v$).

ten times as small: the bistable state lies in a fairly shallow energy well.

We investigate the importance of the number of grooves, N, in Fig. 5.28c-d. There, we show force curves for sheets of width $W = 100 \pm 5$ mm, but with different numbers of grooves: $N = 1/2$ to $N = 5$. Interestingly, there is no obvious quantitative difference between sheets with one or five grooves, or any number in between. The initial stiffness of all measured samples is similar; the curves show two snap-through events while popping, as expected (areas *i* and *ii* in Fig. 5.28c); and the final, popped state of the sheets is stable (that is, the force exerted by the indenter dips below zero). By contrast, the half-groove $N = 1/2$ is softer, needs a much smaller indentation force to snap through, and it is not stable in its popped state. These results imply that the influence of the number of grooves is only significant for very small values of N. This idea is supported by the results shown in Fig. 5.28d, where we show the work done on each sample during cyclic loading by measuring the areas under their force-displacement curves. The work done on a sample with $N = 1/2$ grooves is much smaller than the work done on samples with larger numbers of grooves. In addition, the work depends only weakly on the number of grooves, saturating to a plateau value as N grows. Thus, the behaviour of the popped central groove appears to only depend on its nearest-neighbour grooves.

To build an intuition for the snap-through events that happen inside the groove, we measure both the popping and un-popping response of a sheet with $N = 5$ grooves (Fig. 5.28c). We slightly modify the setup for these measurements: two extra magnets are used to attach the sheet to the two supports, which allows us to measure forces when the indenter pulls as well as pushes the sheet. The experimental force curve shows that indentation of the sheet produces two snap-through events (which we call *i* and *ii*) before the groove is popped through; during un-popping, pulling on the groove snaps the structure through three times (events *iii*, *iv*, and *v*).

Fig. 5.29 explores what happens to the local shape of a groove during popping and un-popping. Fig. 5.29a shows the experimental setup, while in Fig. 5.29b, we show qualitative sketches of the local mean curvature near the indenter as it is pushed and pulled. Blue and pink lines indicate positive and negative mean curvature, respectively (mountains and valleys, see legend). The sketches, based on observations, indicate that patterns of mean curvature in the groove are fairly regular and consistent across samples. Interestingly, snap-through events appear to be related to symmetry-breaking transitions in the curvature patterns. Snap-through transitions *i* and *ii*, which create a stable popped defect, both occur by annealing small regions of high negative curvature with adjacent valley grooves. Transition *iii*, which happens when the defect is un-popped, switches the defect's shape from a regular diamond to an asymmetric chevron. Finally, transitions *iv* and *v* create local regions of high negative curvature by detachment from the neighbouring valley grooves: they are the counterparts of transitions *i* and *ii*.

In short: defects in groovy sheets can be controllably popped in from the top. Our measurements show that defects do not feel much of the sheet beyond their neighbouring grooves; that they are created via multi-step snap-through events that are related to changes in the local groove curvature; and that defects live in a fairly shallow energy well, compared to their creation barrier.

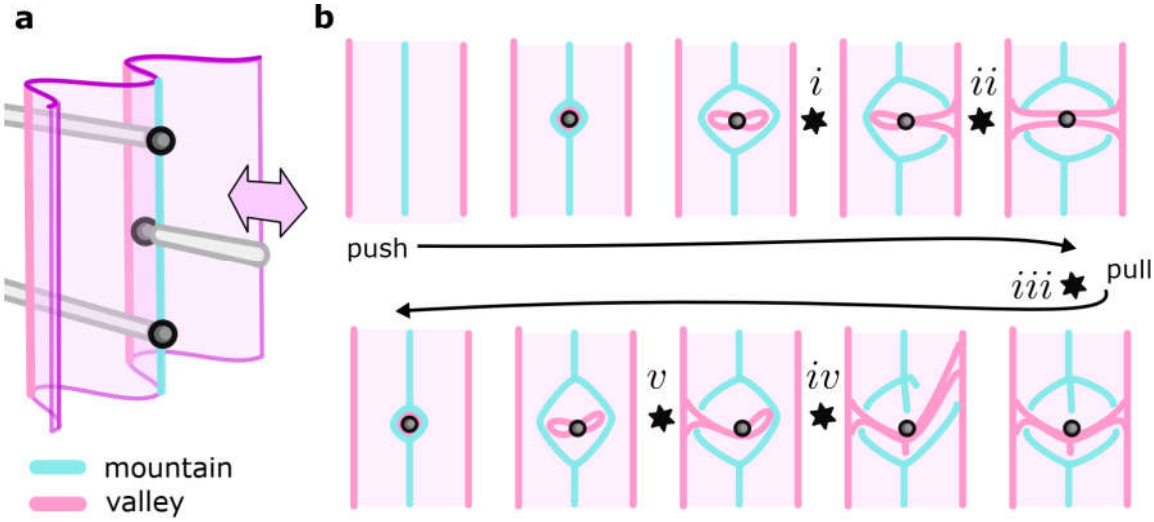

Fig. 5.29.: Local shape of a groove while snapping. **a,** Experimental setup as in Fig. 5.28, with the sheet being held by a magnet (dark grey) on each support. The indenter is pushed to pop a defect, and pulled to un-pop it. **b,** Sketches of the groove's mean curvature (blue and pink lines for mountains and valleys, see legend) during snap-through events $i - v$ shown in Fig. 5.28c. Top: pushing the groove produces a local mean curvature pattern. Regions of high mean curvature snap and disappear by annealing with a nearby valley groove (i and ii), resulting in a symmetric defect. Bottom: pulling the groove breaks the defect's symmetry (iii). Regions of high local curvature detach from neighbouring valley grooves in two snap-through steps (iv, v).

5.5.2. Sheet size dependence

In section 5.5.1 above, we showed that a defect can be popped into the centre of a sheet. For the particular sheet shape studied, we saw that this central defect is stable when the sheet has at least one groove. In addition, adding more grooves to the sheet did not significantly change the force needed to create a defect, implying that across the grooves (in the y-direction shown in Fig. 5.28a), interactions are weak: defects do not feel the neighbouring grooves much.

Here, we investigate the other direction: how do defects respond to their environment along the grooves (the x-direction in Fig. 5.28a)? We address this issue by studying the stability of single defects as a function of two variable sets, illustrated in Fig. 5.30a: the sheet size, set by the number of grooves N and the sheet width W; and the defect's position, set by its distance from the sheet's edges in terms of the number of grooves n and the edge width w.

As we show below, our findings confirm that the number of grooves does not impact defect stability much- except when defects are close to the sheet's edge. By contrast, the sheet width is very important: defects are sensitive to the length of the groove in which they live, and they are only stable if this length is neither too small, nor too large, but exactly right.

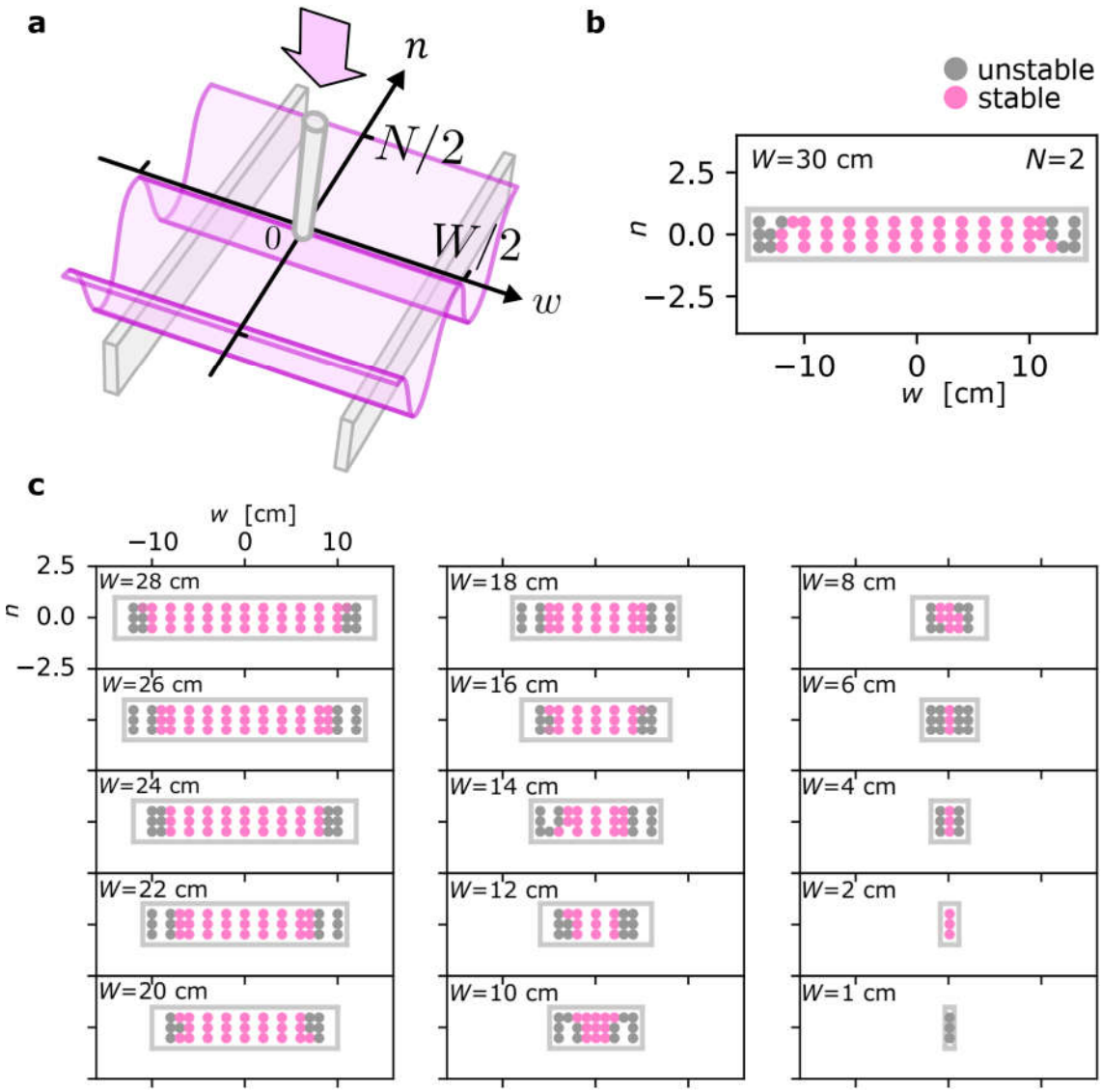

Fig. 5.30.: Probing stability of defect in a sheet. a, A sheet with N grooves, width W and thickness $t = 75\ \mu\mathrm{m}$ (pink) is placed on two supports (grey). The sheet is manually popped through with an indenter at various distances n across and w along the grooves away from the centre at $(w, n) = (0, 0)$. **b,** Stability of popped defects for a sheet with $N = 2$ and $W = 30\ \mathrm{cm}$. The sheet outline is indicated (grey box) in the (n, w)-coordinate frame. Pink and grey dots (legend) indicate where defects are stable and unstable, respectively. **c,** Stability results for $N = 2$ grooves and progressively shorter widths W are shown (scale: top left). Data were obtained by cutting to size and probing of a single sample. Only defects near the lateral edges are not stable.

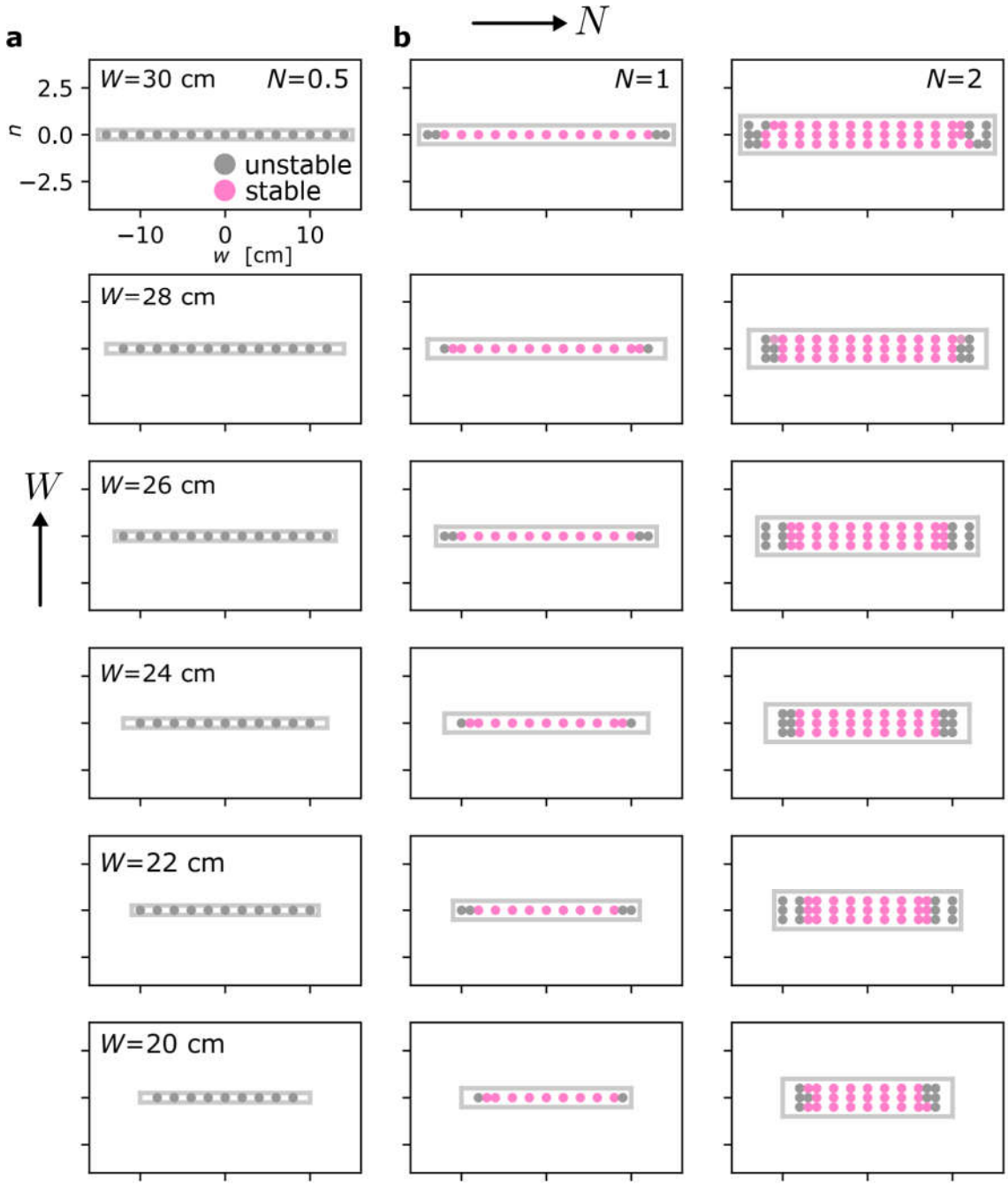

Fig. 5.31.: Defect stability depends on sheet size and location. Maps of defect stability are shown for sheets of systematically varied width W and number of grooves N. Top left: the sheet outline is indicated (grey box) in the (n, w)-coordinate frame. Pink and grey dots (legend) indicate where defects are stable and unstable, respectively. Scale is identical for each panel. Data in each column correspond to a distinct sample with $N \in [0.5, 1, 2, 3, 5, 7]$ grooves that is cut down progressively to a smaller width $W \in [30, 28, ..., 20]$ cm. **a,** Defects in narrow sheets with half a groove, $N = 0.5$, are unstable. **b,** For $N = 1, 2$, only defects near the lateral edges are unstable.

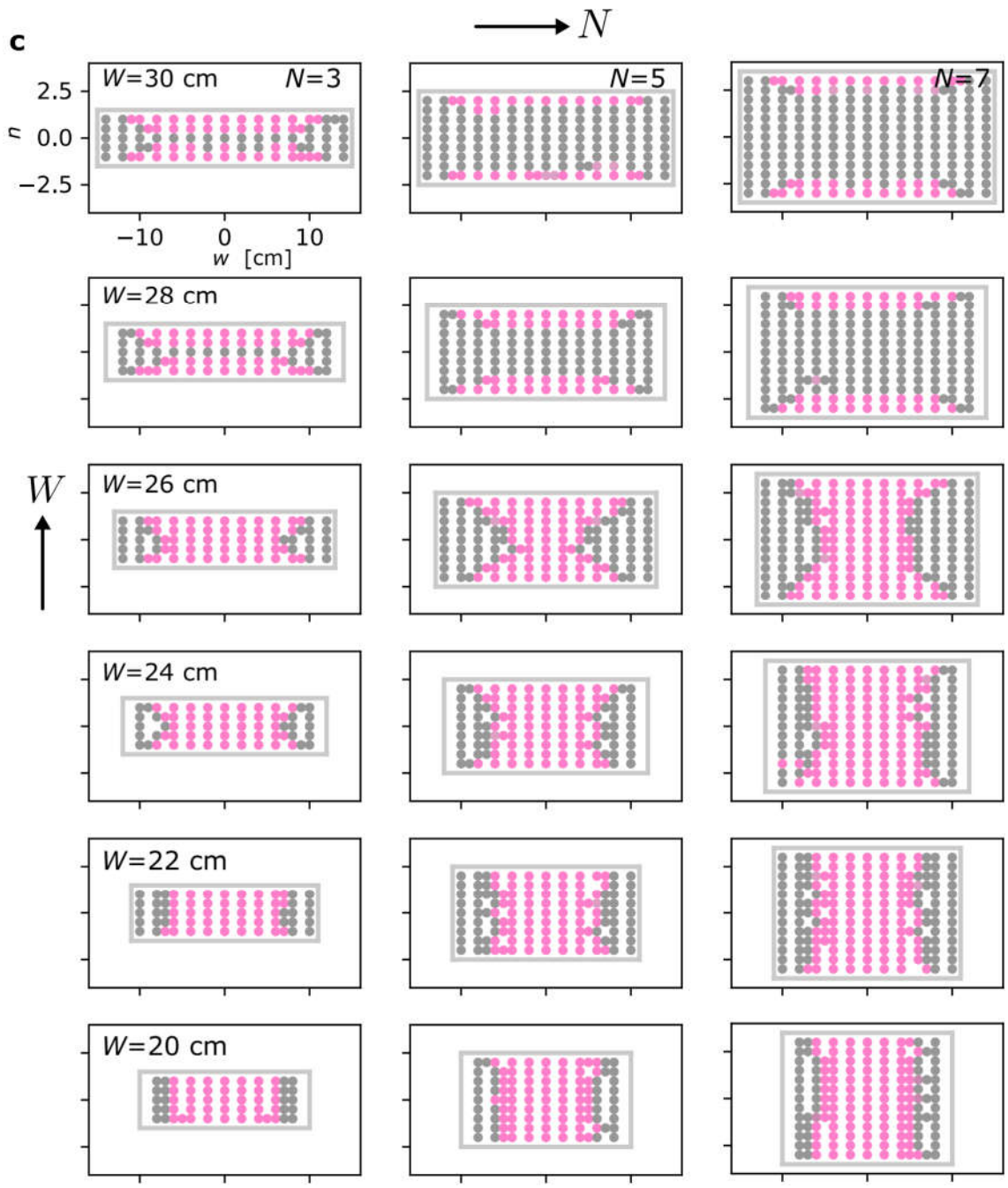

Fig. 5.31.: (continued) Defect stability depends on sheet size and location. c, For $N = 3$ and upward, defects near the lateral edges are unstable. In addition, sheets with a large width $W \geq 28$ cm show unusual behaviour: defects near the sheet centre are unstable. This difference between sheets with few and many grooves disappears, after a transition regime, at width $W \leq 22$ cm.

In Fig. 5.30a, we show our strategy to probe the stability of defects in a sheet of size N by W as a function of its position. The sheet is placed on two supports and a thin indenter is used to push the sheet down manually until no more snap-through events occur; the indenter's location is measured by distances n and w away from the sheet's centre. Fig. 5.30b shows typical stability results for a sheet of thickness $t = 75$ µm, $N = 2$ grooves, and width $W = 30$ cm. A top view of the sheet is shown, its edges indicated by

a grey outline. Dots on the sheet surface correspond to probed points: pink dots indicate that a stable defect has been created there, while grey dots indicate unstable points. Here, we take 'stable' to mean that a pop-through defect has been created successfully at this location, at least once, with a minimal lifetime of 10 seconds to account for viscous effects. Note that this definition includes points that may have been probed multiple times, producing a stable defect only once; our results may thus include false positives. Regardless, our results show a good consistency, as we show in Fig. 5.30c, where we show stability results of the sheet in Fig. 5.30b as it is gradually cut down to smaller and smaller widths W. Across the measurements shown, defects close to the lateral edges are unstable, while those near the centre are stable.

However, not every sheet supports stable defects near their centre, as we illustrate in Fig. 5.31. There, we show a grid of stability results for sheets with $N \in [0.5, 1, 2, 3, 5, 7]$ grooves (columns) that are gradually cut down to widths $W \in [30, 28, 26, 24, 22, 20]$ cm (rows). We first note that the stability results for each sheet are up-down and left-right symmetric to a good degree, consistent with our expectation that the sheet's geometry is uniform across each sample. The stability results fall into three classes, depending on the number of grooves; they are shown in panels 5.31a, b and c. First, Fig. 5.31a shows that sheets that are very narrow (only half a groove long, $N = 0.5$) do not support stable defects. While they can undergo snap-through transitions, they pop back to their starting shape, consistent with our mechanically controlled experiments in Fig. 5.28. Second, Fig. 5.31b indicates that defects in moderately narrow sheets (1 or 2 grooves long) are stable, except if they are too close to the lateral edges. Third, Fig. 5.31c illustrates that sheets with a larger number of grooves ($N = 3$, 5 and 7) show distinct behaviour. When such sheets are wide enough (above $W = 28$ cm), stable defects are only found where they are both far away from the sheet's lateral edges *and* close to the vertical edges. When the sheets are cut down to sufficiently small widths (below $W = 22$ cm), their behaviour reverts to the familiar pattern of defects that are only unstable near the lateral edges. In between these two widths, an area of stable defects near the sheet's centre appears in a typical hourglass-like shape that widens to a rectangular area at decreasing width W. Thus, the stability of defects in a sheet varies strongly with the sheet size and the defect location.

We condense the large amount of data in Fig. 5.31 in Fig. 5.32. We focus on the stability of defects at each sheet's centre (Fig. 5.32a, central cross), and on the width of the unstable regime near a sheet's lateral edges (Fig. 5.32a, arrows), which we call the unstable edge width u_w; u_w varies with the sheet's size, and with the minimal distance of a groove to the sheet's vertical edges, n_{edge}. Fig. 5.32b shows a stability diagram that shows whether or not a defect, created in the centre of a sheet with width W and number of grooves N, is stable (legend). Based on these results, we conclude that sheets can only support stable defects near their centre if they have enough grooves (here, $N > 0.5$) and are neither too narrow nor too wide ($1 < W < 28$ cm for this particular groove geometry).

Fig. 5.32c finally explores the unstable edges of our sheets: we show the unstable edge width u_w as a function of sheet width W for sheets with increasing numbers of grooves (left to right). u_w is measured for each groove of a given sheet, and colour-coded by the minimal distance of the groove to the sheet's vertical edges, n_{edge} (legend). Error bars correspond to the minimal and maximal measured values of u_w. Three features stand out: first, at small sheet widths, w_u grows proportionally to W. Second, at intermediate

sheet widths $W \approx 8$ cm, u_w plateaus to a constant value for grooves that are near the sheet's vertical edges. Finally, at large sheet widths, u_w increases with W (corresponding to the hourglass-shaped stability regimes in Fig. 5.31c); the magnitude of the increase is larger for grooves that are farther away from the sheet edge, but this trend seems to saturate beyond $n_{\text{edge}} = 2$. In essence, these results give us a design guideline for using sheets to make shape-shifting materials: sheets show *consistent* single-defect stability behaviour across their surface if they have a high enough number of grooves (here, $N > 3$) and their width lies in a goldilocks zone that is neither too small ($W \gtrsim 8$ cm), nor too large ($W \lesssim 20$ cm), but just right.

In summary: the stability of a single defect depends on the size of the surrounding groovy sheet. Specifically, the sheet width is important, more so than the number of grooves. The sheet energetics are complex, which gives rise to stable defects only in an intermediate range of sheet widths. This result has design consequences: sheets that are too big or too small may not support defects and may not be capable of shape-morphing-unless defects stabilize each other by *interacting* together.

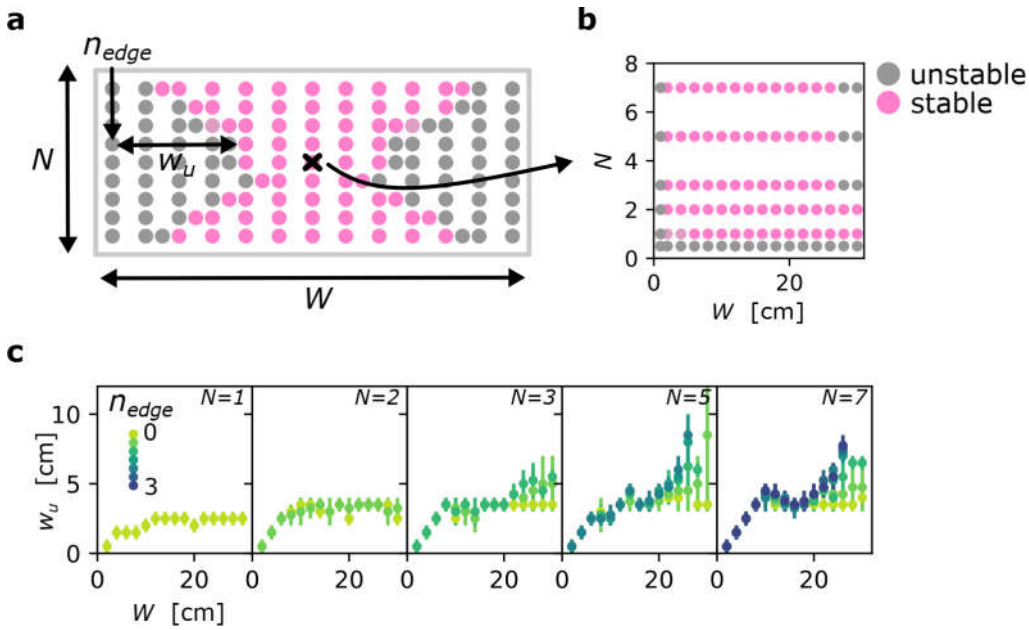

Fig. 5.32.: Stability of defects close to and far from the sheet edges. a, In a sheet of size N by W, defects are not stable if they are close to the lateral edges (legend: see **b**). We quantify an unstable edge width w_u that varies with the smallest distance to the edge along the grooves, n_{edge} (black arrows). The stability of defects at the centre (black cross) depends unambiguously on sheet size. **b,** Stability of central defects (legend) as a function of sheet size. Defects are unstable for sheets that are less than one groove long; defects are also unstable for sheets of too small or too large a width W. **c,** Unstable edge width w_u as a function of sheet width W is shown. Colours indicate the distance to the nearest edge along the grooves n_{edge} (legend). Data were obtained for sheets of various groove numbers N (left to right). The data show three effects. First, at small sheet size W, w_u increases proportionally with W. Second, w_u stabilizes to a plateau for grooves that are within 1 groove distance from the edge, $n_{\text{edge}} \leq 1$. Third, w_u increases from its plateau value for grooves farther away from the edge, $n_{\text{edge}} \geq 1.5$; the magnitude of the increase depends weakly on n_{edge}, appearing to saturate beyond $n_{\text{edge}} \approx 2$.

5.6. Interactions between defects

In this section, we explore interactions between multiple defects in a groovy sheet. Recall that in section 5.1, we observed the formation of straight *scar lines*. The fact that defects in adjacent grooves align in such scars provides strong evidence for the existence of interactions. First, scars are seen to run reasonably straight across the sheet, suggesting that defects in neighbouring grooves attract; second, the fact that scars are stable in rather large sheets, while individual defects are not (see section 5.5 above), further suggests a crucial role for interactions. We therefore probe the interaction of defect pairs, first experimentally (section 5.6.1) and then theoretically (section 5.6.2). To interpret our results, we study how defects affect a sheet's shape: interactions between defect pairs must ultimately be mediated elastically, via geometrical deformations. Based on experimental curvature measurements, we give an intuitive geometric explanation for the observed interactions and organization of defects in a groovy sheet (section 5.6.3).

5.6.1. Defects interact with their nearest neighbours

To explore the interactions between nearby defects, we first turn to qualitative experiments.

Our experiments start by creating a defect in the centre of a groovy sheet, using a small indenter. Importantly, defects are *mobile*: it may be moved along the groove at a low energy cost due to the high degree of structural symmetry along the groove direction. That is: barring edge effects, a defect produces a constant deformation (and thus strain energy) field, no matter where it is placed in the groove. Thus, in the ideal case, a defect is not prevented from moving by any *elastic* energy barrier: it is a Goldstone mode of the groovy sheet[162]. However, in practise, edge effects, dissipative losses and geometric irregularities tend to create small energetic barriers that cause defects to be pinned at certain preferred positions.

We use the central defect's mobility and pinning properties to probe defect interactions. A second defect is created in a nearby groove and allowed to glide freely to find a stable (possibly pinned) position. From this stable configuration, the second defect is moved relative to the central defect by applying a small guiding force with an indenter. When the guiding force is removed, the mobility of the second defect gives some information on how the pair interacts. We explore three scenarios for defects whose cores are close together: separated by 1/2, 1 and 2 grooves along x. (Fig. 5.33).

We start in Fig. 5.33a with two *positive* defects: they are made in the crests of two adjacent grooves, at a separation of $n = 1$ groove along $\hat{\boldsymbol{x}}$. Scar lines are made from chains of just such equal-parity defects, each separated by a single groove from its nearest neighbours. Fig. 5.33a-*i* shows the starting configuration. Two defects are made in a sheet of thickness $t = 50$ µm, width $W \approx 10$ cm and $N > 10$, fabricated with the corrugating method described in section 5.2.2. The sheet is visualized between crossed polarisers (see Fig. 5.15), which yields a colour pattern that depends on the sheet's local curvature and orientation. The defect pair is stable at a mutual distance $d \approx 0$ along $\hat{\boldsymbol{y}}$. One defect is moved to a small separation d (*ii*, black arrow), after which it spontaneously moves to an even larger stable distance d (red arrow). This repulsive motion is observed to be repeatable, though the stable distance varies somewhat. When the defects are brought

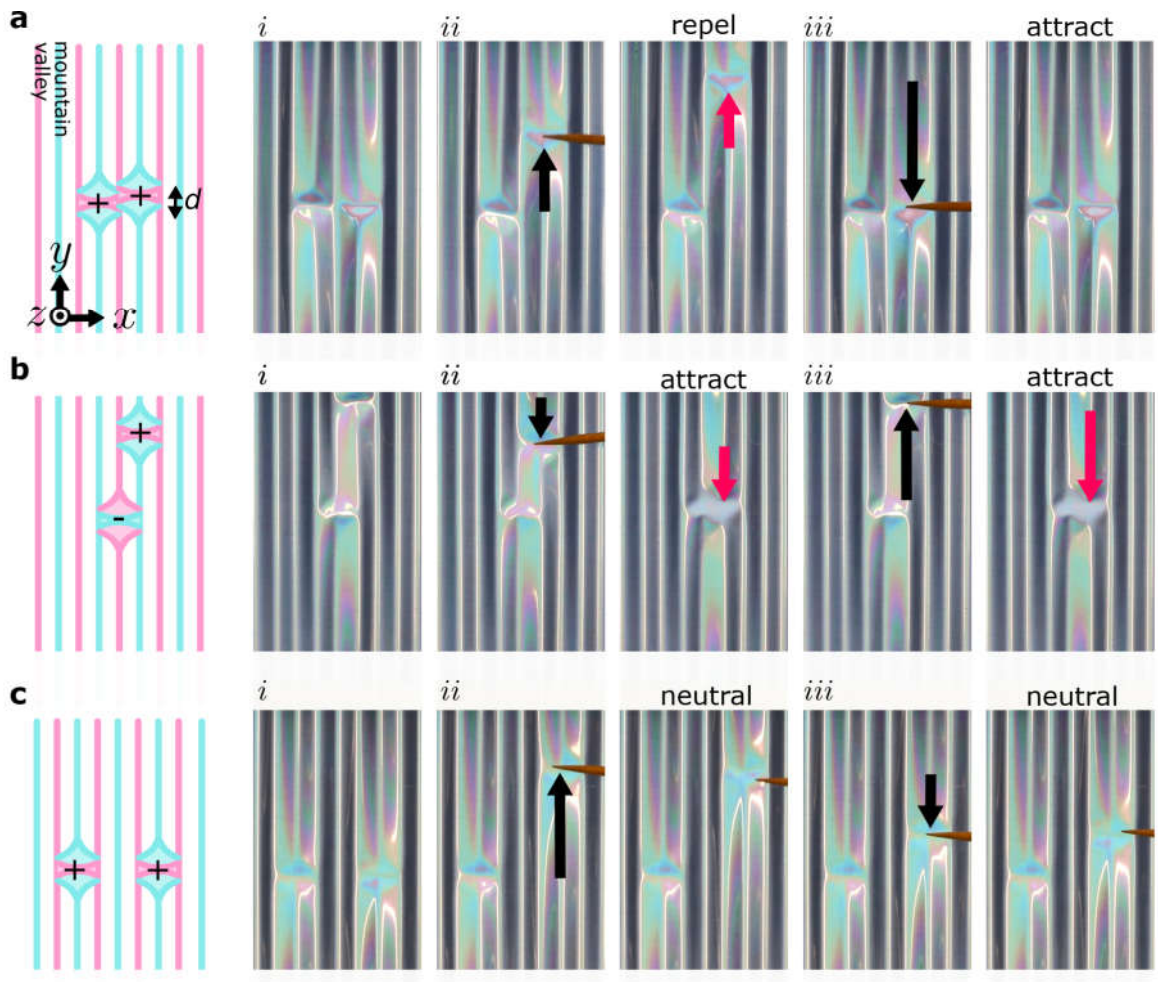

Fig. 5.33.: Defects feel their neighbours. **a,** Two positive (++) defects are introduced in the mountain folds of two neighbouring grooves (schematic, left) in a sheet with thickness $t = 50$ µm (photos, i) created with the moulding method of section 5.2.2. Moving one defect away from its neighbour with a small indenter (ii, black arrow) causes the defect to move farther spontaneously (red arrow). Joining the defects together (iii) creates a stable complex. **b,** A positive and negative (+-) defect are created in the mountain and the valley fold of one groove (i). Moving one defect toward its neighbour (ii) causes a spontaneous coalescence into a stable complex. This behaviour reproduces under repeated separation (iii). **c,** Two defects, whose cores are separated by two full grooves (i). Moving one defect does not result in spontaneous motion (ii, iii).

back together to $d \approx 0$, they remain stable (iii): there is a short-range attraction. Note that the defect's size is comparable to the groove wavelength λ (Fig. 5.8b). In terms of this typical size, the range of attraction between equal-parity defects lies below $d \approx \lambda$, while the repulsive effect is lost beyond $d \approx 4\lambda$, where defects come to rest.

Fig. 5.33b shows two defects made at a separation $n = 1/2$ along x. One *negative* defect is created in the valley of a groove, while the neighbouring crest sports a *positive* defect. Initially, the defects are stable at a distance $d \approx 4\lambda$ (i). When the positive defect is brought closer to its companion (ii), it moves spontaneously anneal into a defect complex with a separation $d \approx 0$. Forcibly separating the defects back to $d \approx 4\lambda$ does not prevent the complex from re-forming (iii), indicating that pinning effects may be responsible for the defects' initial stability in i. Thus, opposite-parity defects experience

a fairly wide range of attraction, at least up to $d \approx 4\lambda$.

Finally, we explore how defects interact when their cores are separated by two full grooves (Fig. 5.33c). A pair of equal-parity defects is created at a separation $n = 2$ along $\hat{\boldsymbol{x}}$ and a distance $d = 0$ along $\hat{\boldsymbol{y}}$ (i). Varying the defect distance does not lead to significant motion(ii, iii): there is no discernible interaction between the pair, implying that interactions between defects that are not directly adjacent are comparatively small.

The experiments in Fig. 5.33 show that defects in directly adjacent grooves interact with one another significantly. Their interaction is attractive at small distances compared to the groove wavelength. These findings are general: they reproduce across samples created with the fabrication methods shown in section 5.2.2. It is precisely this attraction between defects that allows for the creation of scar lines consisting of locked-in defect chains.

5.6.2. Defects attract and repel

The interaction between defects explored in Fig. 5.33 should be governed by defect-induced deformations of the groovy sheet, which cost work to create. While this elastic energy is challenging to measure experimentally, the simple computational model introduced in section 5.4.5 allows us to estimate the collective energy of a defect pair.

Fig. 5.34 shows our strategy. A small section of our model network is illustrated in Fig. 5.34a; a sheet with two grooves and its coordinate system are shown. The network consists of stiff Hookean springs (grey lines) with stretching stiffness $k_s = 1$, connected by soft torsional harmonic springs of stiffness $k_t = 1 \cdot 10^{-4}$ (see section 5.4.5). Lengths are measured by the model's cell spacing, l, which we set to unity. To get a sense of scale: elastic energies $\mathcal{E}$ in this system are thus measured in dimensionless units, where $\mathcal{E} = 1$ corresponds to the energy needed to stretch a single spring to twice its original length. This model allows us to estimate how much energy it costs to create defects; it is especially useful for comparing the energies of different defect configurations, such as a pair of equal-parity defects at various mutual distances.

In line with our experimental findings (recall Fig. 5.33), we study the energetics of a pair of equal-parity defects at various mutual distances (Fig. 5.34b). Starting from a sheet with $N = 2$ grooves and length $W = 20$, we introduce a defect at a position $d/2$ away from the sheet centre. The total elastic energy of the sheet, $\mathcal{E}_+$, can be calculated from the structure's deformed geometry. A second defect is then made at a distance d with respect to the first defect, ensuring that the defects are as symmetrically spaced as possible (see appendix A.10 for details). The total elastic energy of the sheet with its two positive defects, $\mathcal{E}_{++}$, is then calculated as a function of defect distance d.

The resulting energy curve is shown in Fig. 5.34c, as well as a reference curve for the energy $\sum \mathcal{E}_+$ needed to create either defect on its own. Several features stand out here, and we discuss them from large to small distances d. First, defects whose spacing is close to W are not stable, and no computational data could be obtained there. This is consistent with our experimental findings in section 5.5.2, where it was shown that defects cannot be created too close to a groove's lateral edges. Secondly, the total energy

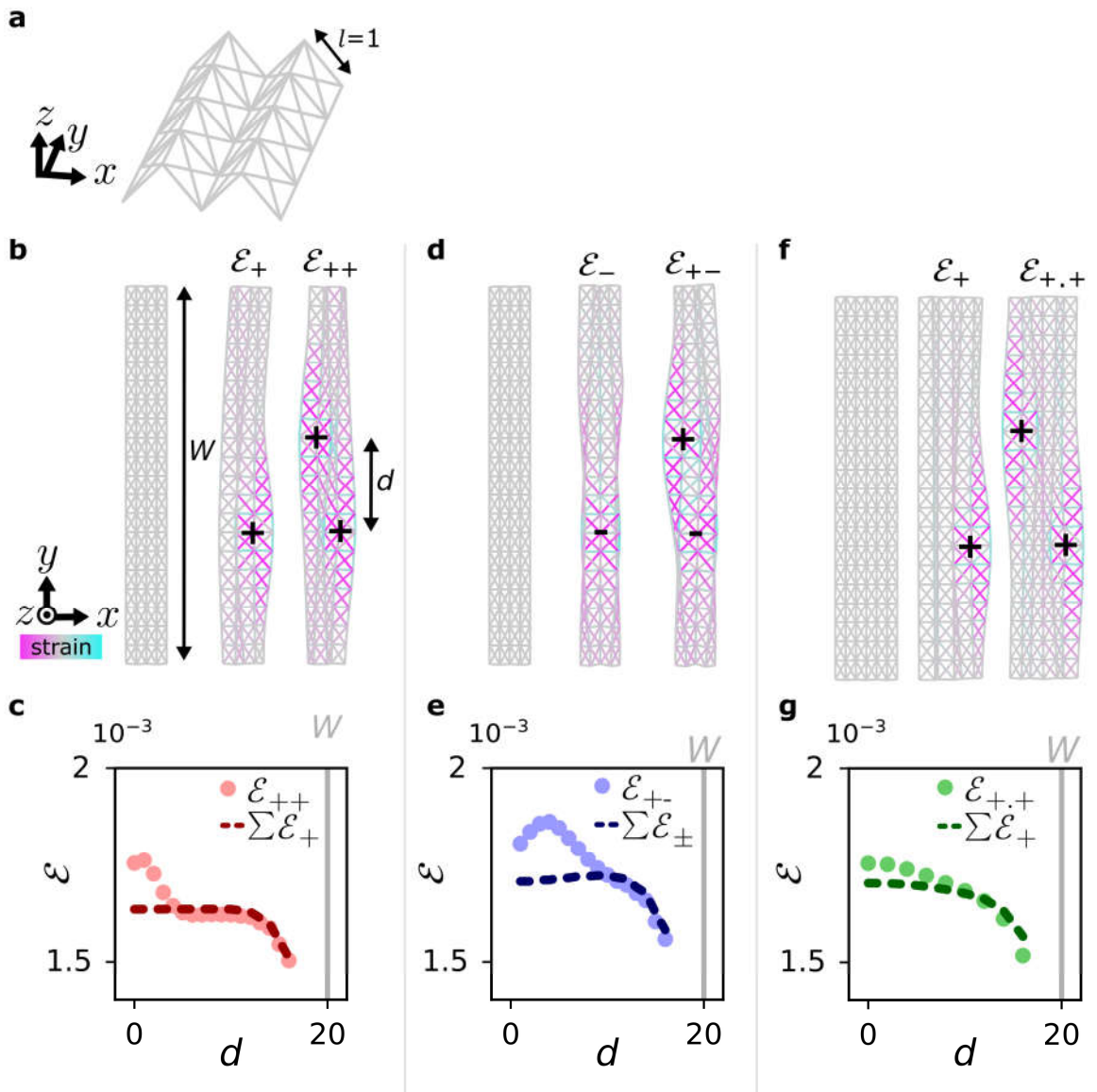

Fig. 5.34.: Defect interaction energies calculated with a computational model. **a,** Computational model of a groovy sheet, made with Hookean springs (grey bars) connected by torsional hinges. Sizes are measured in units of cell size $l = 1$. **b,** A sheet of of width $W = 20$ and $N = 2$ grooves (left) supports a positive defect (middle, marker) at distance $d/2$ from the sheet centre at an elastic energy cost $\mathcal{E}_+$. A second positive defect (right, marker) creates an equal-parity defect pair with spacing d at total energy cost $\mathcal{E}_{++}$. Strain in the network's springs is indicated for clarity (colour bar). **c,** Total energy $\mathcal{E}_{++}$ of the defect pair as a function of distance d (red circles). Baseline energy $\sum \mathcal{E}_+$ needed to create defects individually is shown for reference (red dashed line). **d,** A sheet (left) supports a negative defect in its central valley fold at energy $\mathcal{E}_-$ (middle). A positive defect in a neighbouring mountain fold at distance d increases stored energy to $\mathcal{E}_{+-}$ (right). **e,** Defect pair energy $\mathcal{E}_{+-}$ is shown, as well as the baseline $\sum \mathcal{E}_\pm$ (legend). **f,** Two positive defects separated by a groove are made in a sheet with $N = 3$ grooves (left to right) at total energy cost $\mathcal{E}_{+.+}$ **g,** Defect pair energy $\mathcal{E}_{+.+}$ and baseline $\sum \mathcal{E}_+$ (legend).

increases gradually as d shrinks, until an approximate plateau is reached at $15 \gtrsim d \gtrsim 5$. In this regime, the energy of the defect pair is nearly the same as the summed energies of the individual defects. Third, $\mathcal{E}_{++}$ increases between $5 \gtrsim d \gtrsim 1$, indicating a short-

range repulsion. Finally and crucially, the energy shows a small dip at $d \lesssim 1$. While our results are limited by the model's finite lattice spacing, these results are consistent with the experiments in section 5.6.1. That is, equal-parity defects attract at very short length scales compared to the typical groove width ($d < l$); they repel at intermediate distances($l < d < 5l$); and their interaction becomes very low after that ($d > 5l$), implying that in practise, secondary energetic effects (geometric irregularities, dissipation, and similar) may lead to defect pinning there.

We now investigate the long-range attraction of a defect pair with opposite parity with the strategy outlined above (Fig. 5.34d). The resulting energy $\mathcal{E}_{+-}$ and a reference curve $\sum \mathcal{E}_{\pm}$ as a function of defect distance d is shown in Fig. 5.34e. Interestingly, the energetic trend is similar to the positive-pair energy of Fig. 5.34c, indicating a loss of stability for defects too close to the groove's lateral edges, a lack of interaction at large distances, an intermediate-range repulsion, and short-range attraction. However, there are three differences. First, no plateau is visible, which we attribute to the finite width W of the sheet; however, the pair energy $\mathcal{E}_{+-}$ is nearly equal to the summed energy of individual defects, $\sum \mathcal{E}_{\pm}$, for $d \lesssim 12$. Second, the overall energy $\mathcal{E}_{+-}$ is higher than $\mathcal{E}_{++}$, which is due to the larger amount of (deformed) sheet material flanking the negative defect compared to the positive defects. Most importantly, consistent with the experiments in section 5.6.1, the regions of attraction and repulsion between the opposite-parity defects are much larger ($d \lesssim 4$ and $4 \lesssim d \lesssim 12$, respectively) than those between two equal-parity defects.

Finally, Fig. 5.34f-g explores how defects interact when they are separated by a full groove. A pair of equal-parity defects is created at an energy cost $\mathcal{E}_{+.+}$, which exhibits a small increase in energy at smaller values of d, indicating a repulsive effect. However, the energetic increase is significantly lower than for directly adjacent defects. Repulsive effects between spaced-out defects are thus comparatively small; here, too, secondary energetic effects can produce defect pinning in real groovy sheets.

In summary: our simple computational model shows that defects sense one another significantly only if they are separated by less than one full groove. We found that an equal-parity defect pair attracts at very small distances (compared to the typical groove size); repels at intermediate separations; and does not interact beyond that. A pair of opposite defects shows a similar interaction, but the pair senses each other over a larger range. Most importantly, both defect pairs exhibit short-range attraction. Thus, it is energetically favourable for a set of adjacent stable defects in a groovy sheet to align, which explains why defects form scar lines.

5.6.3. Interactions via curvature

Our simple computational model shows that defects interact. Given the simple ingredients of the model (elastic elements arranged in an accordion geometry), these interactions must be a product of geometrical effects that occur when defects are close together. However, the model's discreteness does not allow for an in-depth study of defect-induced deformations. Here, we turn instead to the 3D geometry of real sheets to study the geometric origins of defect interactions.

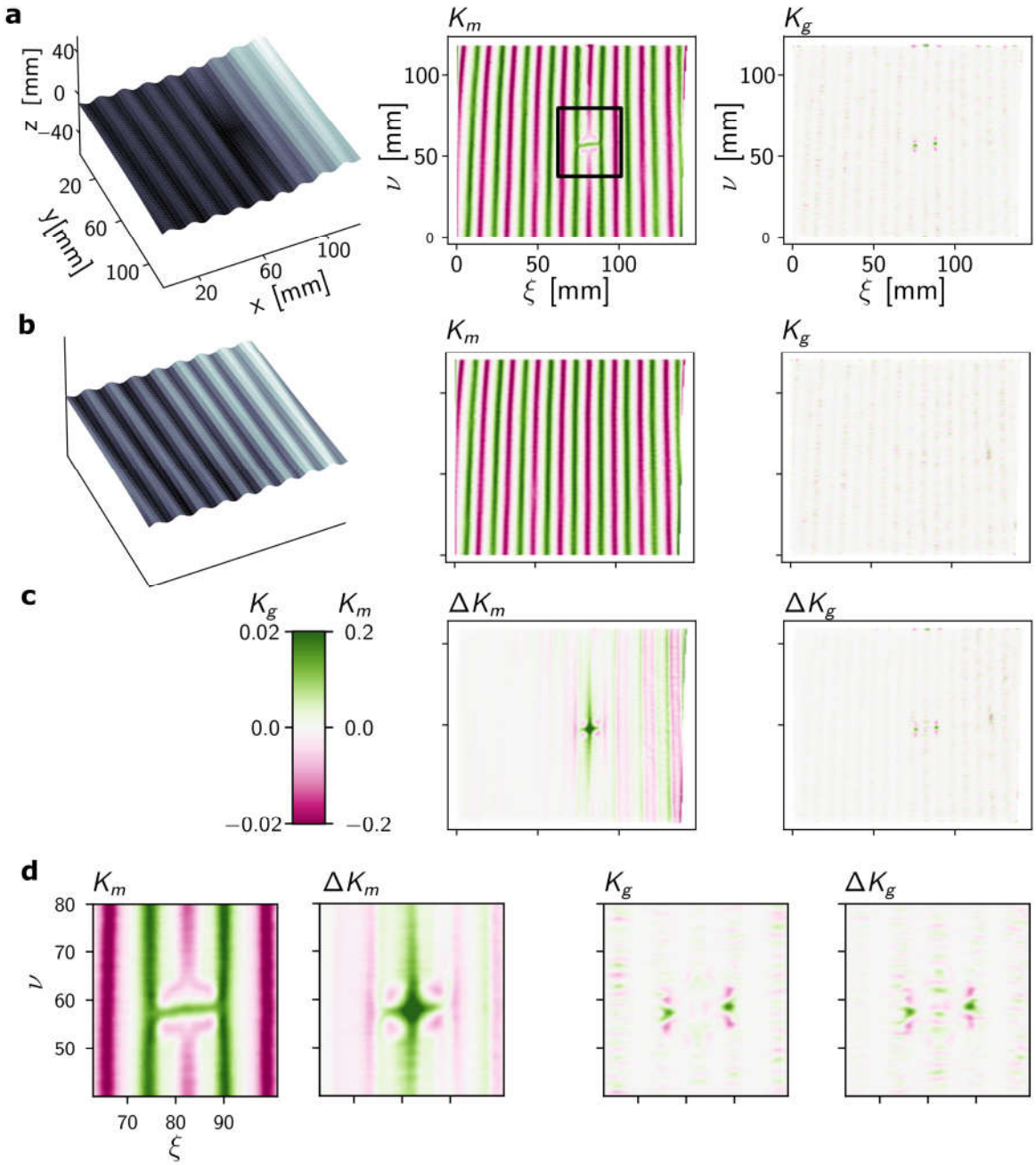

Fig. 5.35.: Defects affect both mean and Gaussian sheet curvature. a, Mean and Gaussian curvatures K_m and K_g (middle, right) in a groovy sheet with thickness $75\ \mu\mathrm{m}$, width $W = 13\ \mathrm{cm}$, and $N = 10$ grooves (left; greyscale matches height z). Curvatures, obtained by numerical differentiation of the height profile, are shown as a function of local surface coordinates ν and ξ (colour bar). **b,** Mean and Gaussian curvatures (middle, right) in a groovy sheet with no defects (left). **c,** Difference between mean and Gaussian curvatures, ΔK_m and ΔK_g, of groovy sheets with and without a defect. Long-range changes in mean curvature, as well as localized changes in Gaussian curvature are seen. **d,** Zoom-in of curvatures and curvature differences in the presence of a defect (black box in **a**).

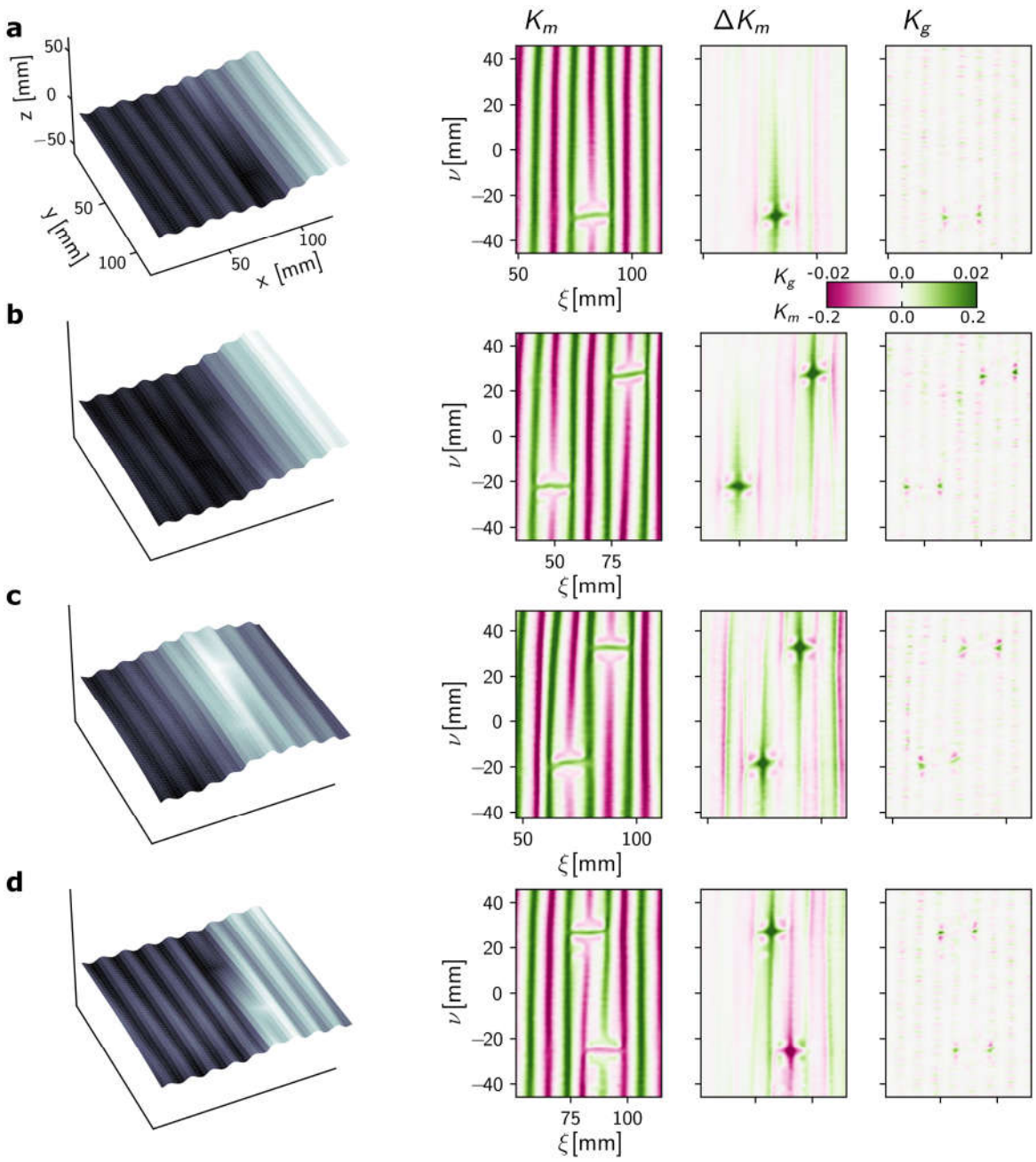

Fig. 5.36.: Defects pairs at large distances do not interact. a, Mean curvature K_m, deviation ΔK_m and Gaussian curvatures K_g and K_g (right) in a groovy sheet sporting one defect. Sheet details as in Fig. 5.35. Curvatures are shown as a function of local surface coordinates ν and ξ (colour bar). **b,** Mean and Gaussian curvatures in a groovy sheet with equal-parity defect pair at a core separation of two grooves along xi and at distance 5 cm along ν. **c,** Equal-parity defect pair at distance 5 cm and core separation of one groove. **d,** Opposite-parity defect pair at half a groove core separation and 5 cm distance. Curvature patterns for pairs do not differ from those of single-defects.

The energetics of real groovy sheets are governed by bending and stretching deformations, which we quantify as follows. Bending deformations produce a *mean curvature* $\mathbf{K}_m$. For example, a sheet rolled into a cylinder with radius a goes from zero mean curvature to $\mathbf{K}_m = a$. Thin sheets resist such deformations with a typical bending stiffness $k_{\text{bend}} = \frac{Et^3}{12(1-\nu^2)}$[108]. Contrariwise, local stretching deformations produce a *Gaussian cur-*

vature $\mathbf{K}_g$ that may be positive or negative. Typical examples of such local stretching is dimpling of a flat sheet into a spherical shell (from zero to positive Gaussian curvature) or into a saddle-shaped section (from zero to negative Gaussian curvature). Changes in Gaussian curvature are resisted by the sheet with a stiffness $k_{\text{stretch}} = \frac{Et}{12(1+\nu)}$[108]. The different thickness-dependence of the bending and stretching stiffnesses show that stretching is more energetically costly than bending for thin sheets. As a consequence, in thin sheets, stretching deformations are often much more localized than bending—crumpling in paper being a typical example—though exceptions do exist[163–166]. On a practical note: *uniform* stretching deformations do not produce either mean or Gaussian curvature; however, given the high energy cost of uniform stretching and the lack of its experimental observation in groovy sheets with defects, we do not consider it here. Together, the mean and Gaussian curvatures describe how a (groovy) sheet curves in space, and how it deforms in the presence of defects.

Thus, measuring a groovy sheet's curvature with 3-D scans (section 5.3.2) allows us to understand where defect-induced bending and stretching deformations take place. Below, we compare how these deformation distributions look for different defect pair arrangements. Our data suggest that defect pairs experience long-range interactions mediated by bending deformations, while stretching deformations play an important role at close quarters. We propose that stretching deformations are responsible for the short-range attraction between equal-parity defect pairs, explaining the formation and stability of scar lines of contiguous defects in groovy sheets.

To study the geometric interactions between defects, we first look at a reference scenario: a groovy sheet with one defect. Fig. 5.35a shows the height profile of a sheet with $N = 10$ grooves, width $W = 13$ cm and thickness $t = 75$ µm, produced using static thermoforming (section 5.2.2). A single defect has been popped into the sheet, away from its edges. The mean and Gaussian curvatures, K_m and K_g, are calculated from the scanned height profile $z(x, y)$ by calculating its discrete derivatives (section A.11). Via comparison with the curvature of a sheet with no defects (Fig. 5.35b), the differences in Gaussian and mean curvatures, ΔK_m and ΔK_g, are calculated across the sheet surface and shown in Fig. 5.35c. The following features stand out. First, the defect affects mean curvature along its groove (direction ν) over several centimetres; a larger span than across its groove (direction ξ), where differences in mean curvature become indistinguishable from noise over the span of about one groove. This limited effect of defects beyond their nearest neighbours is consistent with our experimental and computational results in the previous sections. Second, the Gaussian curvature shows a focussed peak around the defect location. While the Gaussian curvature's spatial pattern reproduces across many samples, its measured magnitude fluctuates significantly. We attribute these fluctuations to the use of squares of higher-order discrete derivatives during its calculation. Thus, we should compare its spatial distribution rather than its magnitude between different measurements. Inspecting the curvature more closely via the zoom-in in (Fig. 5.35d), we see that the defect produces a regular, reflection-symmetric change in mean and Gaussian curvature.

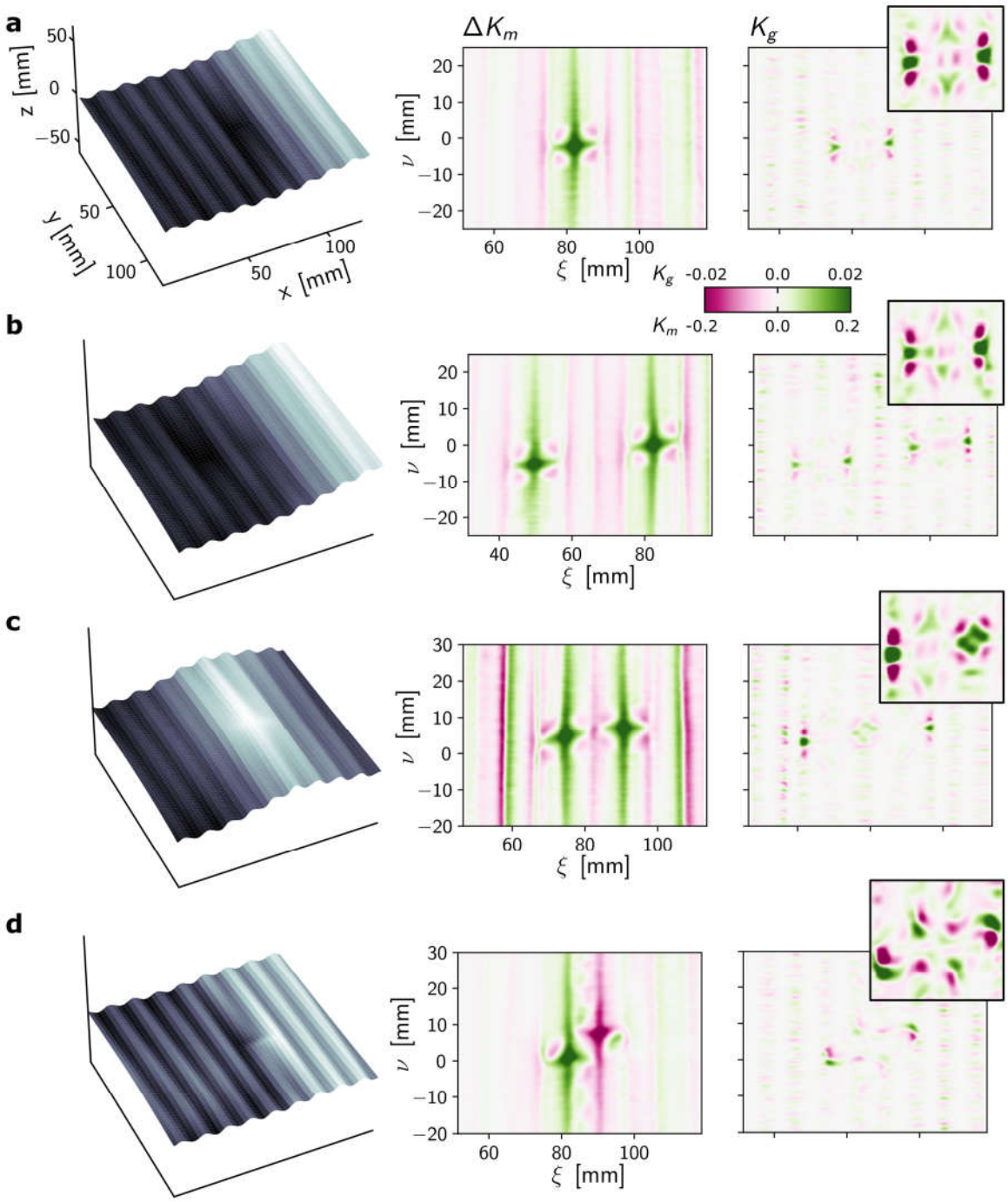

Fig. 5.37.: Defects pairs at small distances interact. **a,** Mean curvature change and Gaussian curvature, ΔK_m and K_g (middle, right), correspond to bending and stretching deformations in a groovy sheet with one defect. Sheet details as in Fig. 5.35. Inset: colour-saturated zoom-in of defect locus to highlight K_g distribution. **b,** Bending and stretching deformations for an adjacent, equal-parity defect pair at a distance of 0 cm along ν (and two grooves core separation along ξ). Deformation fields match those of isolated defects. **c,** Deformations for an adjacent equal-parity defect pair at a core separation of one groove. Bending and stretching between the pair does not match single-defect deformations. **d,** Deformations for an adjacent opposite-parity defect pair at half a groove core separation. Bending and stretching around the pair differs significantly compared to a single defect.

Most notably, differences in mean curvature are centred on the defect's core groove, while differences in Gaussian curvature show up as small, alternately positive and negative stretching patches in the grooves directly *next* to the defect. We now investigate whether these off-centre stretching deformations could be responsible for inter-defect interactions. We first look at various defect pairs at a large distances, and show that their curvature distributions look similar to those of isolated defects. By contrast, we then show that the curvature distribution for defect pairs at small distances differs significantly.

Fig. 5.36 shows curvature distributions of a sheet sporting defect pairs at a large mutual distance d along sheet direction ν. For reference, Fig. 5.36a shows a sheet with a single defect; its mean curvature K_m; its mean curvature deviation ΔK_m with respect to the undeformed sheet; and its Gaussian curvature K_g. Fig. 5.36b–d show the same curvature measures for three defect pairs. In order, we show: an equal-parity defect pair whose cores are separated by two grooves; an equal-parity defect pair at a core separation of one groove; and finally, an opposite-parity defect pair separated by half a groove. Inspection of K_g and ΔK_m shows that each defect produces a local curvature distribution that is qualitatively indistinguishable from that of a single defect, supporting our experimental and numerical observations that defects at large separations do not interact.

However, the curvature behaves differently when defects are close together, as illustrated in Fig. 5.37. Here, too, Fig. 5.37a shows a groovy sheet with a single central defect for reference; the sheet's bending and stretching deformations (ΔK_m and K_g) away from its initial state are included. Zoomed-in insets of Gaussian curvatures near the defect locus are shown; the colour map for these insets is chosen with tighter limits for larger visual contrast, highlighting the different curvature distributions. High-frequency noise is observed in the Gaussian curvature along direction ν, which we attribute to scanning errors (the noise matches the scan fringe frequency of 1.6 mm, see section 5.3.2).

Fig. 5.37b shows an equal-parity defect pair with a core separation of two grooves. Interestingly, the sheet deformations around each defect appear similar to those of isolated defects, consistent with our previous observation that such defect pairs do not interact strongly.

Fig. 5.37c also shows an equal-parity defect pair, with a smaller core separation of one groove. Here, the deformation field around the defects is different: the mean curvature of the groove right between the defect pair changes significantly, signalling local groove flattening. In addition, the defects' Gaussian curvature peaks at the central groove merge into a complex in a diamond pattern, where the amount of curvature appears to be less than for independent defects. Thus, while bending deformations appear to increase, stretching deformations may be reduced. We hypothesize that the competition between increased bending and reduced stretching in the samples studied here results in a net energetic benefit when the two defects are aligned.

Finally, we consider an opposite-parity defect pair with a core separation of half a groove in Fig. 5.37d. The defects' bending and stretching deformations show rather different distributions compared to isolated defects. Two features stand out. First, the opposing bending deformations of the two defects (quantified by ΔK_m) appear to be 'slotted' into place in a way that preserves their bending distribution symmetry. By inspection, increasing the defects' mutual distance breaks this symmetry, suggesting an

increased bending energy cost at larger distances. Second, the stretching distribution (K_g) of the two defects merges into a complex. Notably, the stretching pattern of one defect's core merges with the off-centre stretching of the other. Separating the defects thus requires the creation of more stretching patches, at an energetic penalty. Both features are consistent with the mid- and short-range attraction (mediated here via bending and stretching, respectively) that was observed experimentally and computationally.

The groovy-sheet deformation fields studied above show that interactions between defects are mediated by bending and stretching, visible as changes in mean and Gaussian curvature. Defects produce bending deformations at medium range across and along grooves, respectively (compared to the typical groove size). By contrast, stretching deformations are highly localized within half a groove from the defect's core. This means that bending-mediated interactions play a role over medium-range distances, while stretching-mediated interactions become significant if the defect pair's cores are close together. While the exact merging of defect's deformation fields at short distances may be complex, the outcome is simple: defect pairs in adjacent grooves show short-range attraction. In summary: defects attract at close range, and this interaction allows scar lines of adjacent, equal-parity defects to be formed in large sheets.

5.7. Shaping groovy sheets with scar lines

Defects in groovy sheets organize to form scar lines, as we discussed above. In the previous sections, we showed that short-range, geometrically-driven attraction between defects lies at the heart of scar line formation. Here, we explore the natural next question: *how do scar lines reshape groovy sheets?*

Figure 5.38 revisits some of the complex groovy sheet shapes first shown in section 5.1. While Fig. 5.38a–c showcase samples with intricate shapes due to their various scar line configurations—short and long, diagonal and straight—Fig. 5.38d shows our starting point: a groovy sheet with a single central scar line, orthogonal to its grooves. The resulting shape appears geometrically straightforward: the sheet is rolled up into a cylindrical shape, distended near the scar line. In other words: isolated scar lines orthogonal to the sheet's grooves lead to geometrically simple shapes.

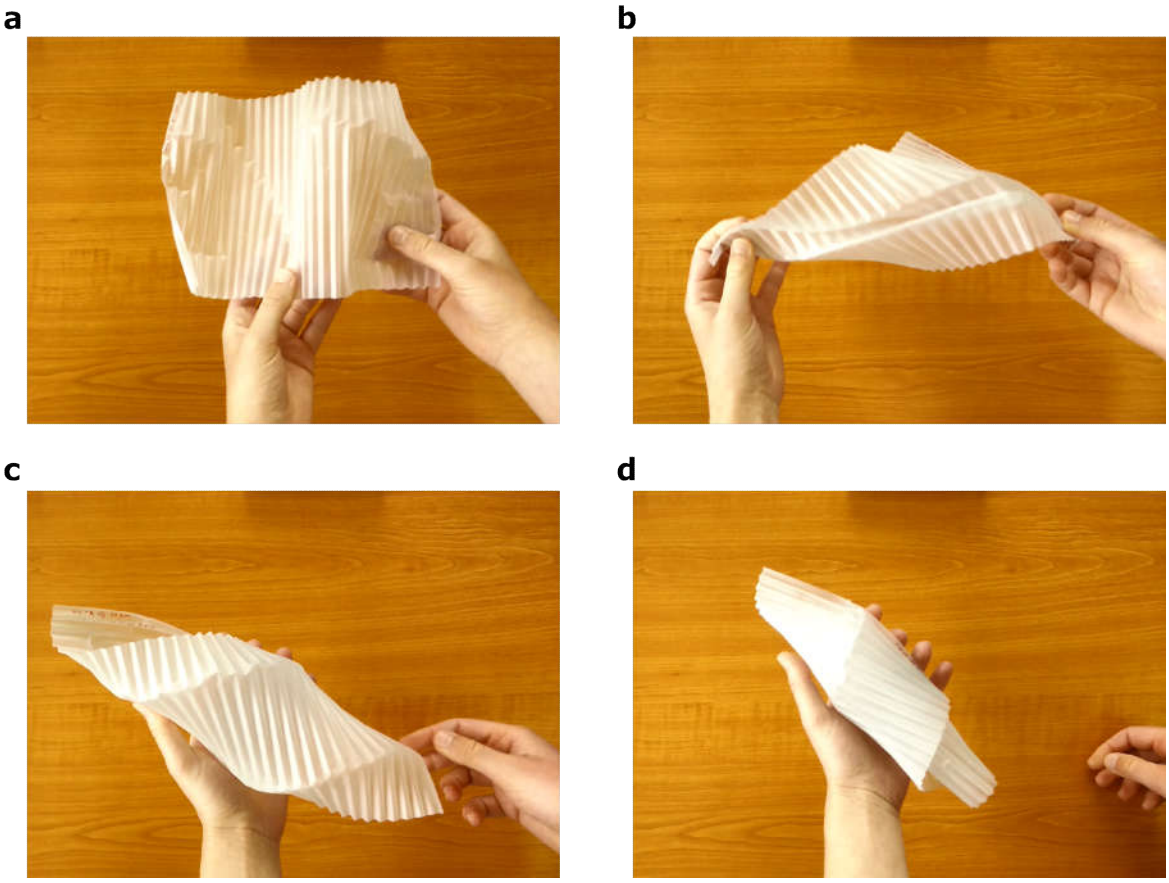

Fig. 5.38.: Scars reshape groovy sheets. Several scar configurations of a groovy sheet (100 µm thick, fabricated using the dynamic forming method described in section 5.2.2) are illustrated. **a,** A multitude of small scar lines, each spanning several grooves, produce a rough landscape with hills and dips. **b,** Three alternating scar lines create a slit surface. **c,** Spiralling shape formed via two equal-parity scar lines. **d,** A single scar line forces the sheet to roll up.

In this section, we therefore systematically study the reshaping effect of scar lines, starting with a single scar in section 5.7.1. We discuss a geometric argument that shows

why a scar line produces a rolled sheet shape, and show experimental data to support this. In addition, we show that small sheets (with a small width W) roll, while larger sheets undergo a symmetry-breaking transition that produces both a figurative and literal twist in the sheet shape. We argue in section 5.7.2 that a sheet section with a single scar line can be viewed as a puzzle piece: different configurations of scar lines can be obtained by tiling and connecting such puzzle pieces. We show that simple geometric arguments are not always sufficient to predict the resulting sheet shapes, especially when parallel scar lines are present. The shaping effect of multiple parallel scar lines is subsequently explored in section 5.7.3, where we present sheet shapes resulting from two scar lines. We show experimentally that the sheet shapes fall into two distinct categories: twisted cylinders and helicoids, whose detailed geometry is dominated mostly by the distance between scar lines. Finally, we conclude in section 5.7.4 by briefly discussing a way to model groovy sheet shapes as ruled surfaces.

5.7.1. A single scar

Here, we study the shaping effect of a single scar line. To keep things simple, we stick to scar lines placed centrally in a groovy sheet, orthogonal to its grooves. Fig. 5.38d above illustrates what happens next: the scarred sheet reshapes into a roll. To explain this behaviour, we first consider the effect that a defect has on a single groove, and then discuss how to tile defected grooves together to form a groovy sheet with a single scar line in Fig. 5.39. After this purely geometric consideration, we then measure actual rolled sheet shapes experimentally in Fig. 5.40. We will show that the rolling radius increases with the sheet's size, and present geometric arguments for this behaviour in Fig. 5.41; in addition, large sheets show twisting as well as rolling, which we capture qualitatively in a simple energetic model in Fig. 5.42. Together, our findings show that scarred sheets roll and twist; and that the amount of rolling and twisting depends on the sheet's initial geometry, as well as its elastic behaviour.

We start in Fig. 5.39 with a purely geometric model of a scarred sheet. First, Fig. 5.39a-b shows a single groove in which a defect is popped. The defect locally flattens the groove's natural curvature, and folds the groove orthogonal to the flattening direction. Thus, while the groove's footprint (the polygon spanned by its corners) is initially rectangular, the defect causes the rectangle to stretch and fold along its midline. As a result, the groove's footprint becomes a *trapezoidal fold* that consists of two isosceles trapezoids that meet at their bases at a shallow angle (Fig. 5.39b). The trapezoidal fold's geometry is set by its base length and base angle, as well as its folding angle. There is a unique way to tile our trapezoidal folds in space without distorting them, as shown in Fig. 5.39c: they can be stacked together into a rolled shape by mirroring the folds in the plane spanned by their edge points (pink dots in Fig. 5.39c). This suggest that the scarred sheet's rolling is, to first order, governed purely by geometry.

In practise, rolling of groovy sheets in the presence of a single scar line is observed consistently across a wide range of groove geometries and sheet sizes, although sheets do not support single scar lines at widths that are either too small or too large (reminiscent of our findings in section 5.5.2). Notably, we expect the precise geometry of the roll—its radius of curvature—to depend on the elastic behaviour of the sheet: after all, there is a competition between groove flattening and folding at the defect locus, and a competition

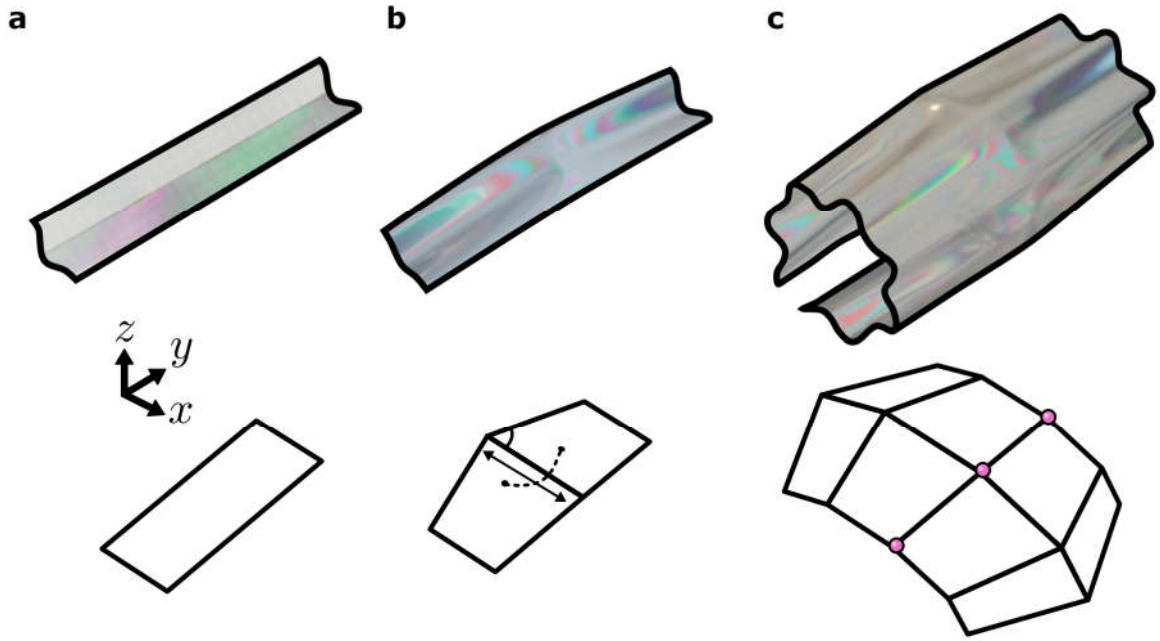

Fig. 5.39.: Geometry of a single scar line. a, A single groove (top, cropped and outlined image of a real sheet viewed between crossed polarisers) has a rectangular footprint (bottom). **b,** A defect stretches and bends the groove. Its footprint now consists of two opposing trapezoids at a mutual angle (dashed arc): a trapezoidal fold. Its geometry is set by the base length and angle of the trapezoids (arrow, solid arc). **c,** Tiling grooves with defects corresponds to tiling trapezoidal folds. There is a unique configuration, obtained by mirroring folds in the plane spanned by their edge points (pink dots), that does not distort the folds. This configuration produces a rolled structure.

between bending and twisting deformations away from the scar line. Thus, while the geometric picture is a useful qualitative tool to explain rolling, experiments are needed to quantify the exact sheet shape.

The exact rolling shape of groovy sheets can indeed be measured experimentally with photography and 3D scanning (recall sections **??**-**??**, and Figs. 5.16 and Figs. 5.20 in particular). We report our shape measurements in Fig. 5.40. Besides helping quantify sheet rolling, the data show that wide sheets twist as well as roll, as we will discuss below.

First, Fig. 5.40a illustrates the sheets' experimental parameters: thickness $t = 75$ µm, $N = 10$ grooves, and a variable total width $W \in [2, 30]$ cm. Scar lines are introduced in the centre of the sheet at a distance $W_f = W/2$ from the free edges. We explore two sheet types with deep and shallow grooves, fabricated using static and dynamic thermoforming respectively (see section 5.2.2). The deep grooves have wavelength $\lambda = 12.7 \pm 0.5$ mm, amplitude $A = 4.3 \pm 0.5$ mm, arc length $s_\lambda = 16 \pm 0.5$ mm, maximal radius of curvature $r = 2.2 \pm 0.3$ mm, and fold angle $\theta = 1.65 \pm 0.1$ rad. By contrast, the shallow grooves have wavelength $\lambda = 7.9 \pm 0.5$ mm, amplitude $A = 2.6 \pm 0.5$ mm, arc length $s_\lambda = 10 \pm 0.5$ mm, maximal radius of curvature $r = 1.4 \pm 0.1$ mm, and fold angle $\theta = 1.55 \pm 0.1$ rad.

In Fig. 5.40b, we present 3D-scanned shapes of two rolled groovy sheets with deep grooves: one narrow ($W = 6$ cm), and one wide (W=29 cm). While the short sheet shows a classical rolled shape, the longer sheet has an additional twist: the sheet forms a cylindrical roll, while its grooves twist at a small angle around the cylinder's axis. We quantify the rolling by the sheet's radius of curvature R_{scar} measured at the scar line, and the amount of twisting by the groove angle defined in Fig. 5.40b. Fig. 5.40c shows these two shape measures as a function of edge distance W_f. Two trends stand out here: first, the radius of curvature appears to be non-zero at $W_f = 0$, and increases with W_f until a plateau value is reached. The radius of curvature is of the same order of magnitude as the groove size. Second, the groove angle is negligible for a large range of edge distances W_f, until an abrupt bifurcation takes place. After this bifurcation, the groove's twisting angle jumps to a nearly constant positive (left-twisting) or negative (right-twisting) value. We have observed that the twisted roll can be flipped from right-to left-twisting by applying a small torque to the sheet's edges.

To study the effect of groove geometry, we study shallow-grooved as well as deep-grooved sheets. Typical images of a short and long sheet with shallow grooves are shown in Fig. 5.40d, similar to the 3D scans of Fig. 5.40b. The rolling radius at the scar as well as the groove angle are extracted using a custom Python script; Fig. 5.40e shows the results as a function of varying edge width W_f. Similar to the deep-grooved sheet, the radius of curvature is of the same order of magnitude as the groove size, and increases with W_f; in addition, a sudden twisting transition is seen as W_f increases beyond a critical value. We note that edge width at which the twisting transition takes place is different for the two groove shapes: shallower grooves twist at shorter widths.

Our experiments show that scarred sheets roll, and undergo a twisting bifurcation. We discuss below why these two reshaping effects take place.

First, we explore why the sheet's rolling radius varies with the sheet size in Fig. 5.41. For clarity, we again show the rolling radius of a deep-grooved sheet as a function of

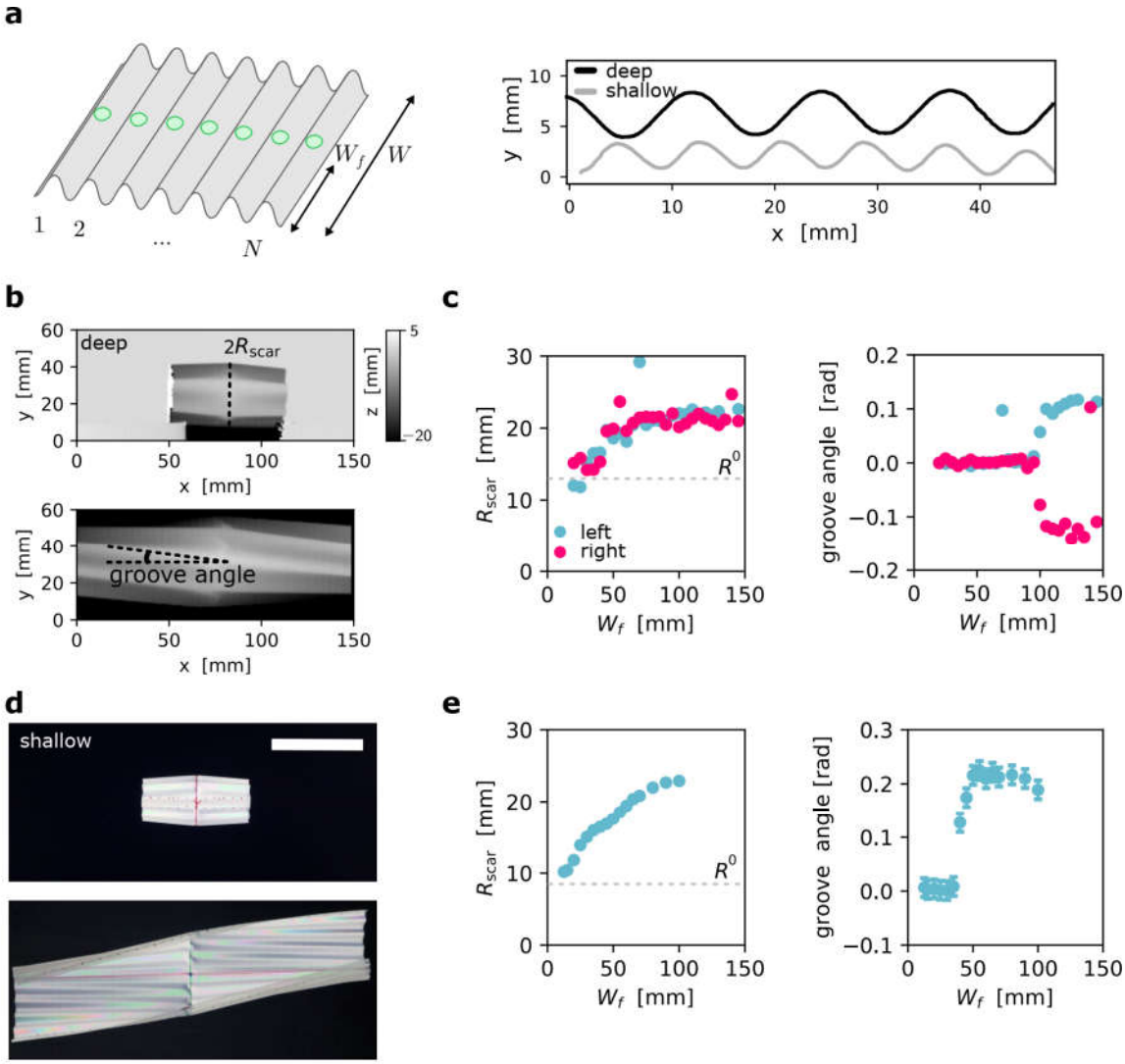

Fig. 5.40.: Detailed shaping effect of a single scar line. a, A single scar line (blue dots) is introduced in a groovy sheet of length L, N grooves, and width W. The scar line lies in the middle of the sheet, at distance W_f to both free edges. Right: experimental sheet profiles for shallow and deep grooves **b,** 3D scans of a sheet with a single scar, thickness $t = 75\ \mu\mathrm{m}$, and $N = 10$ deep grooves, fabricated with static thermoforming (colour bar indicates height). Top: $W_f = 3 \pm 0.3$ cm, bottom:$W_f = 14.5 \pm 0.3$ cm (only central portion near the scar is shown). The sheet rolls up, and twists at large W_f. **c,** 3D shape measures of the scarred sheet. Left: radius of curvature measured at the scar locus, R_{scar}, as a function of free edge width W_f. Right: angle between groove direction and rolling axis. Colours (legend) indicate whether sample was prepared with bias toward left- or right-twisting. **d,** 2D photography of a sheet with a single scar, thickness $t = 75\ \mu\mathrm{m}$, and $N = 10$ shallow grooves, fabricated with dynamic thermoforming. Scale bar: 5 cm. **e,** 2D shape measures of the scarred sheet. Left: scar radius of curvature R_{scar} for varying free edge width W_f. Right: angle between groove direction and rolling axis.

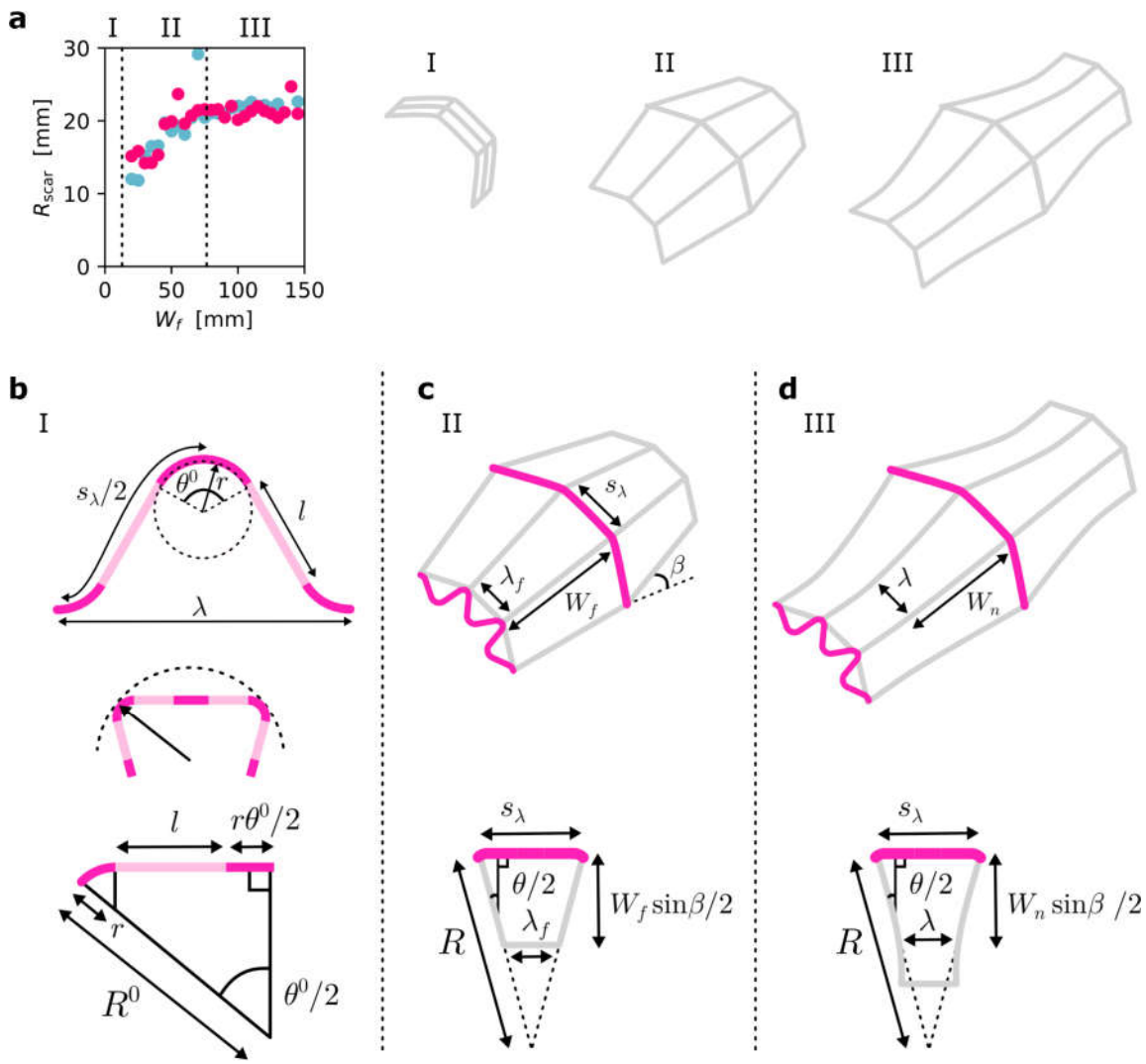

Fig. 5.41.: Variation of scar line curvature R with sheet edge width W_f. a, b, Top to bottom: A single groove has facet length l, radius of curvature r, and angle θ^0. Grooves have a resulting wavelength λ and arc length s_λ. A narrow strip near a scar line is deformed: the groove's valleys are flattened, while mountains retain heir original shape. The strip takes on a rolled shape with outer radius of curvature R^0. R^0 can be calculated from the flattened geometry (Eq. 5.33). **c,** Top: geometry of a rolled sheet at intermediate W_f, following the model in Fig. 5.39. Grooves between two mountain folds are flattened at the scar line to length s_λ, and relax over sheet width W_f to length λ_f. Straight grooves meet at the scar line at a small angle β. Bottom: the scar's radius of curvature, R, is calculated using the groove angle θ; under certain assumptions, R increases linearly with W_f (Eq. 5.34). **d,** In sheets with large W_f, grooves bend and relax to their initial wavelength λ over a fixed neutral width W_n. Increase in W_f does not lead to an increasing rolling radius R.

edge width in Fig. 5.41a. Our experiments show that the sheet's rolling radius R_{scar} has finite value at zero sheet width (regime I); initially increases linearly with W_f (regime II); and then plateaus (regime III). The behaviour in these three regimes can be understood, based on geometric considerations.

We start with regime I, where the rolling radius is finite as W_f goes to zero. In Fig. 5.41b, we consider a small strip of material around the scar line. The scar line consists of a chain of defects, created in the valleys of the grooves. Near the scar line, the defects are observed to flatten the valley folds. Assuming the mountains of the grooves remain undeformed, we can make an estimate of the rolling radius, disregarding the influence of the rest of the sheet. The groove is characterized by its arc length s_λ, radius of curvature r, and opening angle θ. Assuming that the folds are alternately flattened and at rest, we can define an outer rolling radius R^0:

$$R^0 = r + \frac{s_\lambda}{2\sin\theta/2} \ . \tag{5.33}$$

For our sheets, we estimate $R^0 \approx 13$ mm and 8.5 mm for the deep- and shallow-grooved sheets, respectively, in fair agreement with our measurements (Fig. 5.40c,e).

In regime II, the increase of the rolling radius R with sheet edge width W_f can be understood via the geometric model presented earlier in Fig. 5.39, where the grooves of a sheet are modelled as trapezoidal folds. As we illustrate in Fig. 5.41c, we assume that valley folds are flattened near the scar to length s_λ, and that the angle β at which grooves meet at the scar remains constant as W_f is increased. Finally, assuming that the folds relax to their equilibrium configuration at the sheet's edges to a typical length λ, we find a geometric expression for the outer rolling radius as a function of W_f:

$$R(W_f) \approx \frac{s_\lambda}{s_\lambda - \lambda} \sin\frac{\beta}{2} W_f \ , \tag{5.34}$$

which shows that the rolling radius should increase approximately linearly with W_f. Estimating $\beta \approx 0.1$ rad, the slope of R as a function of W_f should lie between 0.2 and 0.3, which is in fair agreement with the experimentally observed slope 0.15 ± 0.5 in this intermediate regime. Finally, we suggest in Fig. 5.41d that the roll radius' plateau value at large W_f can be understood by assuming that at large widths, the folds relax to their equilibrium state at a fixed neutral axis $W_n < W_f$, resulting in a constant value for R. Thus, while the details of the roll radius' variation with W_f depend on the sheet's shape parameters, the initial value of R, its increase, and its plateau can be understood geometrically.

Finally, we explore why wide scarred sheets twist, while narrow sheets do not. We attribute the twisting transition to an energetic competition between elastic deformations at the scar line and in the sheet's wings. This idea is based on a simple elastic model, formulated in detail in appendix A.12, in which a twisting transition is observed for scarred sheets with a large width. The main results, in the form of equilibrium scarred sheet shapes and their corresponding shape parameters, are shown in Fig. 5.42. Though no saturation of the rolling radius is observed (which we attribute to the absence of groove bending deformations in our simple model), we see an otherwise fair agreement between the modelled and experimental shape measures: the order of magnitude for the rolling radius, groove angle, and twisting transition width correspond reasonably well (compare

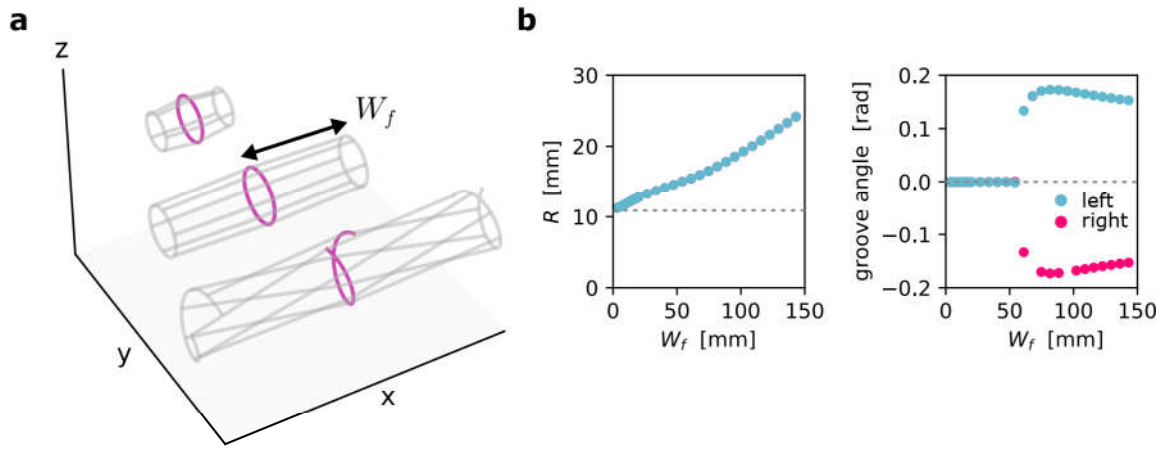

Fig. 5.42.: Twisting transition in a simple elastic model. a, Equilibrium configurations of the model at increasing edge width W_f. Scar line (pink) is either circular or helicoidal; grooves (grey lines) point away from the scar line at a small angle. See appendix A.12 for details. **b,** The scar rolling radius R increases from its initial value R_+ (Eq. 5.33, dashed line) with W_f. Initially, the sheet does not twist; at a critical value of W_f, a bifurcation to finite values of the groove angle is observed.

Fig. 5.40f).

In summary: sheets with single scar lines roll up into a cylindrical shape. The rolling can be understood by considering the geometry of a single groove. The rolled shape's details are set by an interplay of elastic bending and twisting energies. While the exact interplay is challenging to model exactly, experiments show three facts: first, the roll's radius of curvature is finite even for narrow sheets, and increases with sheet width before saturating to a plateau value; second, beyond a critical width, a symmetry-breaking transition causes the sheet's grooves to twist around the cylinder axis; and third, the critical twisting width depends on the groove geometry, with shallower grooves twisting at smaller sheet widths.

5.7.2. Combining scars

Above, we studied the shaping effect of a single scar line- but sheets can support more than one scar. Just a few scar lines can produce complex shapes, as we saw in Fig. 5.38. Can we connect single-scar reshaping to the much more complex multi-scar picture? We propose a simple framework, in which we limit ourselves to a small class of scar line configurations.

We consider only scar lines that are perpendicular to a sheet's grooves. These scar lines can be placed in *series* aligned in a chain, or in *parallel*, side by side. Recall that scar lines also have a parity: they can be made on the crests or in the valleys of grooves, and the two types of scar line yield line curvatures of opposite sign. Given these two options for our scar lines—series or parallel, positive or negative curvature—we can have four basic scar line configurations, which we explore in Fig. 5.43.

Recall the impact of a single scar line, shown in Fig. 5.43a: if made in the groove's valleys, the scar rolls up the sheet into a positive-curvature cylinder section. Fig. 5.43b

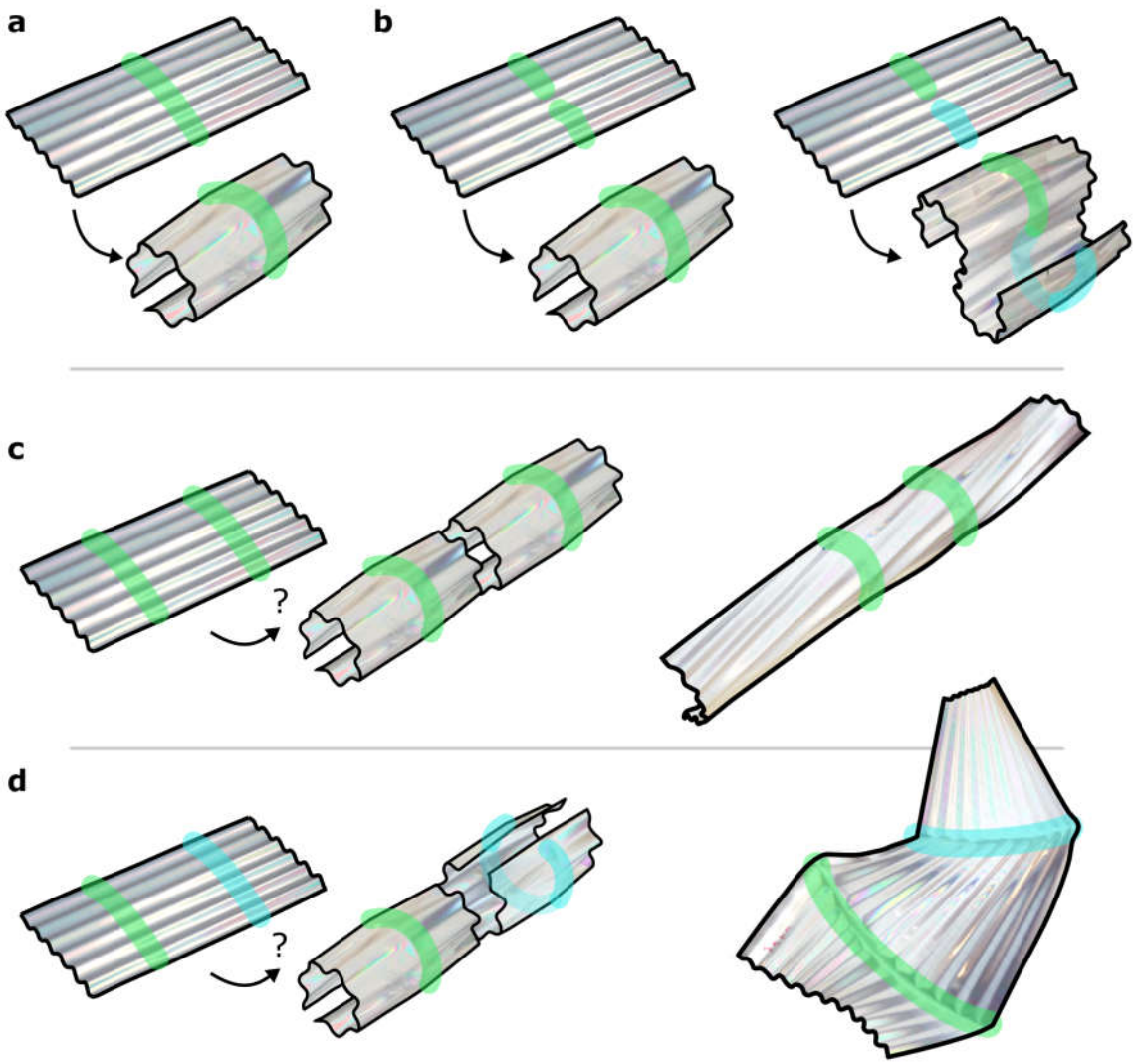

Fig. 5.43.: Combining scar lines. a, A scar line introduced in the crests of a groovy sheet (green line, top) produces a rolled shape (bottom). Groovy sheets shown are cropped and outlined photographs of real samples, viewed between crossed polarisers. **b,** Tiling scar lines in series. Two scar lines of equal parity (green lines) is geometrically equivalent to a single scar line: the sheet rolls up. Two scar lines of opposite parity, one in the sheet's crests (green) and one in the valleys (blue), lead to two rolls of opposite curvature, connected by a flat half-groove at their interface. **d,** Parallel scar lines form complex shapes. Two isolated equal-parity scar lines (green lines, left) form two rolls (middle). When connected, the sheet forms a rolled cylinder, its grooves always twisting around the cylinder's axis (right). **e,** Isolated opposite-parity scar lines (green and blue lines) form two rolls of opposite curvature. There is no simple geometric solution to connect the two rolls at their edges. Experimentally, the sheet section demarcated by the scar lines forms a helicoid; the free 'wings' twist and curve.

shows what happens when scar lines are placed in series. Evidently, two equal-parity scar lines are equivalent to a single scar line, and the sheet rolls up into a positive-curvature cylinder as before. Two opposite-parity scar lines in series (one scar in the grooves' crests, the other scar in their valleys) changes the sheet shape in an intuitive way. The two scar lines produce two cylinder sections, with opposite curvature, that must meet at their long edges. In practise, the two rolls are indeed connected together by a single (minimally-deformed) half-groove, into an S-shape. Thus, a purely geometric picture suffices to capture the shaping effect of scar lines in series: they produce sheets rolled into snake-like cylinder segments, whose sections have alternately positive or negative curvature, consistent with the scar parity. In short: scar lines in series form a stable route to complex shapes with a rolled geometry.

By contrast, geometry alone cannot tell us how scar lines in parallel reshape a sheet. This is illustrated in Fig. 5.43c, where two equal-parity scar lines are created side by side. Based on our simple geometric picture, the sheet should deform into two rolled sections, which must be connected at their lateral edges. It is not possible to create this connection without distorting the sheet: geometric frustration must arise. In practise, while the sheet does roll into a cylindrical shape, its grooves simultaneously twist around the rolling axis. Intriguingly, this twisting behaviour is universally observed across sheet sizes, groove shapes, and thicknesses. Here, both elasticity and geometry govern the sheet shape.

Opposite-parity scar lines in parallel, shown in Fig. 5.43d, are an even more egregious example of the importance of geometric frustration and resulting elastic deformation. The two scar lines now form two rolled sections that must be stitched together along edges with *opposite* curvature. A real sheet tackles this problem by forming a helicoidal surface, twisted around a straight central axis, allowing the scar lines to bend into helices of opposite curvature. While the geometric details vary, the helicoidal shape is present across a diversity of groovy sheets.

In conclusion: sheet shapes are geometrically predictable for scar lines that run in series. However, when scars lines are placed in parallel, elasticity and deformation play a crucial role. We explore this interplay between elasticity and geometry below.

5.7.3. Parallel scars

In this section, we investigate sheets with parallel scar lines. As illustrated previously in Fig. 5.43d-e, parallel scar lines produce complex sheet shapes that depend on the scars' parity. Below, we experimentally study sheet shapes for equal-parity and opposite-parity scars. As for single scars (section 5.7.1), we investigate the effect of the groove geometry on the final sheet shape by performing our experiments on two sheet types, with deep and with shallow grooves respectively (see Fig. 5.44). In addition, we quantify how sheet width and scar positioning affects the final shape. We present the shaping effect of two equal-parity scars in Fig. 5.45, and show there that sheets with two equal-parity parallel scar lines universally form cylindrical, slightly twisted rolls. By contrast, we show in Fig. 5.46 that sheets with opposite-parity scar lines form helicoid-like shapes. Our results show that parallel scar lines produce intricate but consistent rolling and helixing shapes, whose general attributes can be captured by simple shape measures across groove shapes, sheet widths, and scar positions.

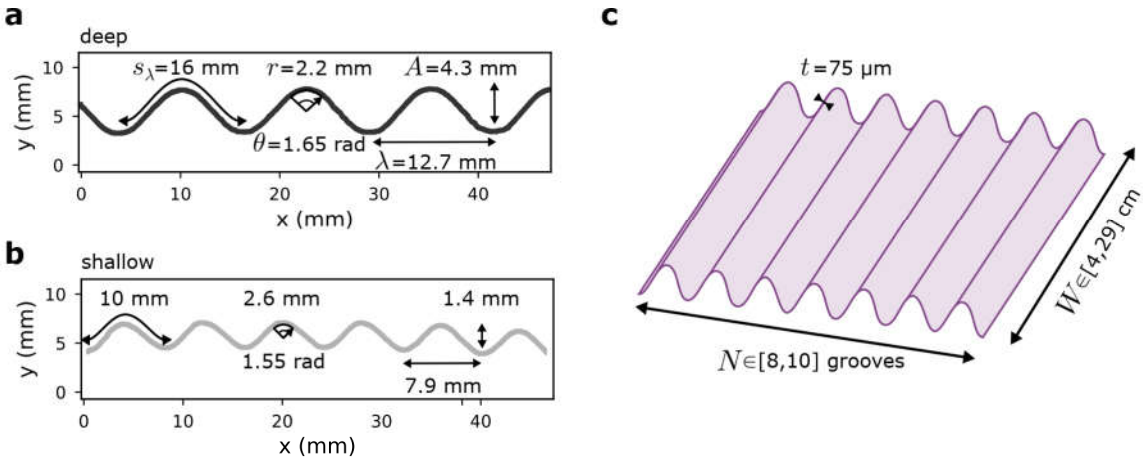

Fig. 5.44.: Geometry of sheets with deep and shallow grooves. a, Photography-derived profile of a sheet with deep grooves. Groove arc length s_λ, radius of curvature r, fold angle θ, wavelength λ and amplitude A are indicated; see section 5.7.1 for estimated errors. **b,** Profile of a shallow-grooved sheet with shape measures indicated as in **a. c,** Overall sheet size. We investigate sheets with fixed thickness $t = 75$ µm, variable width $W \in [4, 29]$ cm, and large number of grooves $N \in [8, 10]$.

Equal-parity scars

We start in Fig. 5.45 by experimentally measuring the shape of sheets with two equal-parity scar lines. As illustrated in Fig. 5.45a, the sheets have a fixed thickness $t = 75$ µm, $N = 10$ or 8 grooves, and a variable width W. The scar lines are placed symmetrically at a mutual distance D, each scar line at a distance $W_f = (W - D)/2$ to the nearest sheet edge (Fig. 5.45a). As first noted in Fig. 5.43c, we observe that sheets deform into cylindrical rolls, where the sheet's grooves consistently show a small amount of twisting around the rolling axis.

We first investigate the shape of a sheet with $N = 10$ deep grooves in Fig. 5.45b, where we show a typical example of a 3D-scanned, scarred sheet. Its cylindrical shape can be quantified via the roll's radius of curvature, which is maximal at the scar lines and decreases to R_{centre} in between the two scars. We use the central rolling radius, R_{centre}, to quantify rolling. The sheet's grooves consistently show a finite twisting around the rolling axis, which we quantify using the groove angle as before for single scar lines (recall Fig. 5.40b).

The rolling and twisting shape of deep-grooved sheets is measured for a variety of sheet widths $W \in [17, 29]$ cm and scar spacings $D \in [9, 21]$ cm. Note that the two scar lines are not stable if either $D \lesssim 7$ cm or $W_f \lesssim 3$ cm: in order not to unpop, the scar lines must be a sufficient distance away from each other and from the sheet's edge. The two shape measures—the central rolling radius and groove angle—are shown in Fig. 5.45c. We consider the rolling radius R_{centre} as a function of sheet width W. As for single scars, the rolling radius increases approximately linearly with the sheet width. Extrapolating this trend to small widths W, a finite rolling radius is expected even at vanishing sheet width. Generally, the order of magnitude of the rolling radius is comparable to the typical groove arc length s_λ. Both the finite (extrapolated) magnitude of R_{centre} at vanishing

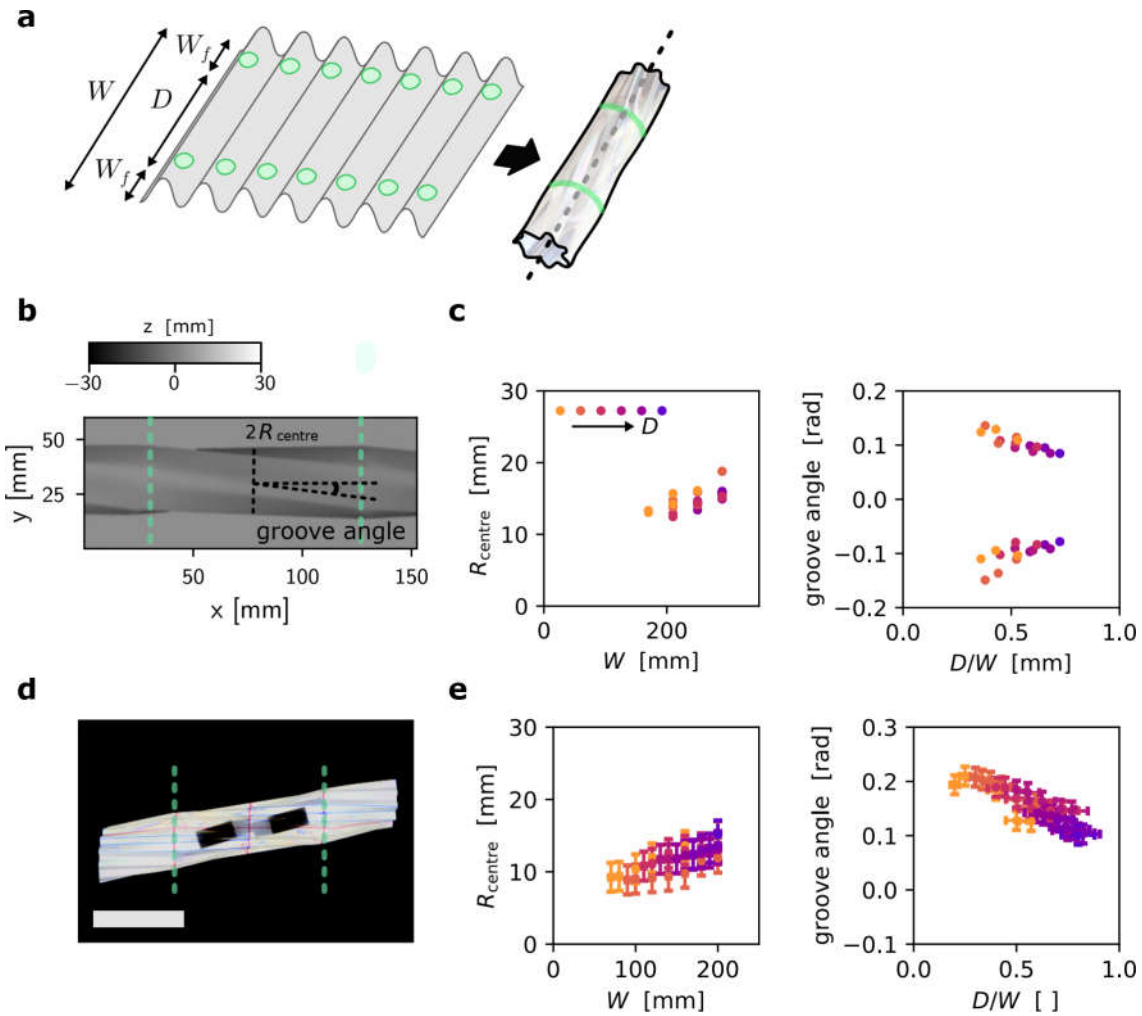

Fig. 5.45.: Shaping effect of equal-parity scar lines. a, Left: two parallel scar lines (green dots) are popped in a groovy sheet of width W at a mutual distance D. Each scar lies at distance W_f to its nearest free edge. Right: as a result, the sheet rolls up and twists around a straight axis (dashed line). **b,** 3D scan of a double-scarred sheet ($N = 10$ deep grooves), fabricated with static thermoforming. Here, $W_f = 4 \pm 0.5$ cm and $D = 9 \pm 0.5$ cm. The sheet's edges lie out of frame. Scar lines are indicated with green dashed lines. **c,** 3D shape measures of a scarred sheet. Left: radius of curvature measured at the middle of the sheet, R_{centre}, as a function of total length W. Right: angle between groove direction and rolling axis as a function of scar distance over total length D/W. Colours indicate constant value of D as a guide to the eye (inset). **d,** 2D photography of a shallow-grooved sheet of total width $W = 16 \pm 0.5$ cm with scars at mutual distance $D = 8 \pm 0.5$ cm and $N = 8$ grooves, fabricated with dynamic thermoforming. Dark rectangles are opaque supports; red marks on the sheet were used for alignment. Scale bar: 5 cm. **e,** 2D shape measures of a scarred sheet. Left: central radius of curvature R_{centre} for varying sheet width W, right: angle between groove direction and rolling axis.

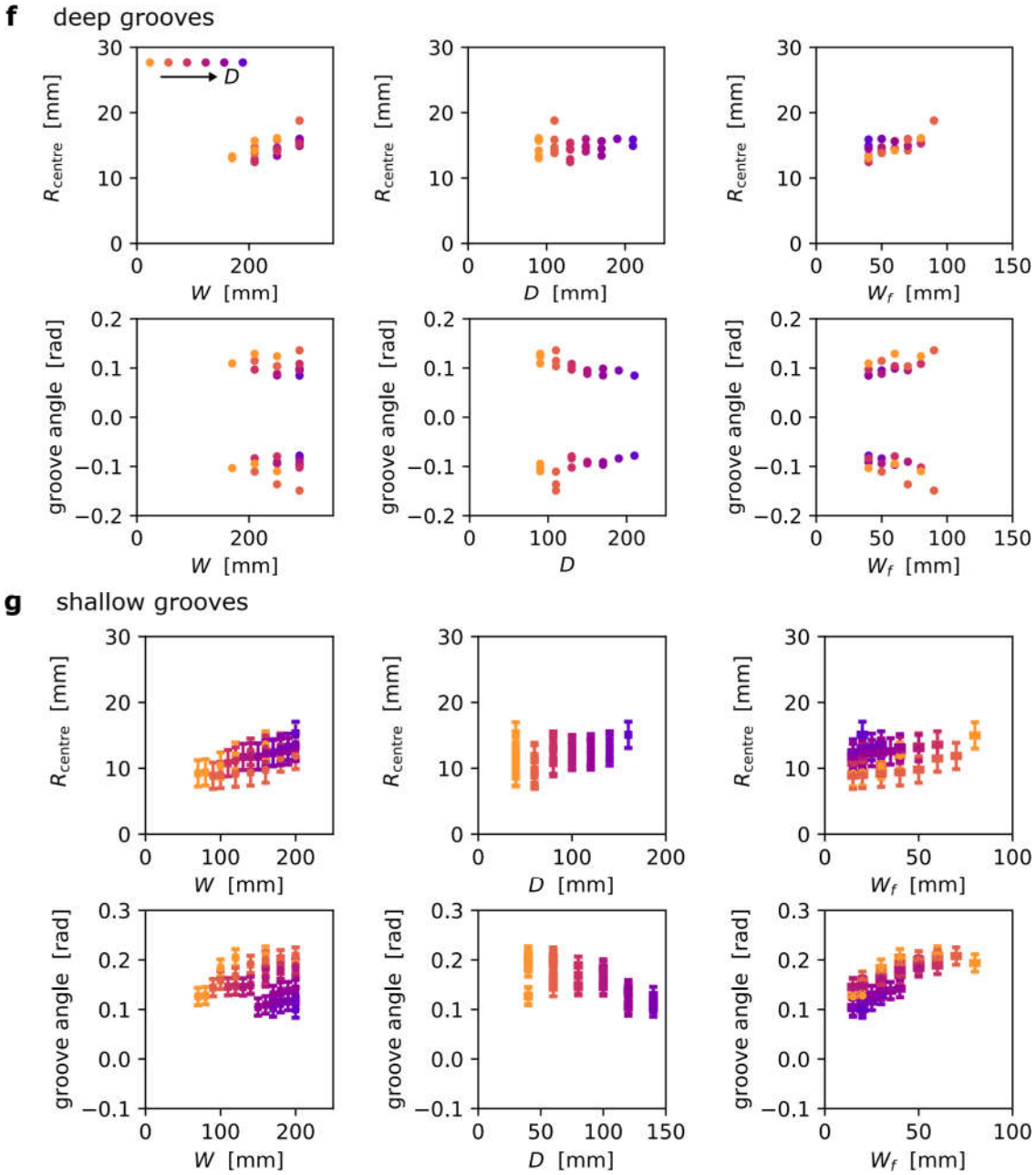

Fig. 5.45.: (continued) Shaping effect of equal-parity scar lines. f, Extended overview of the shape of sheets with deep grooves, corresponding to panels **b-c**. We show the central curvature radius R_{centre} and groove angle (rows) as a function of sheet size and scar positioning, quantified by sheet width W, scar line spacing D, and edge width W_f (columns). Colours correspond to the magnitude of D. **g,** Shape of sheets with shallow grooves, as in **d-e**. Rolling radius R_{centre} and groove angle (rows) are shown versus sheet width W, scar line spacing D, and edge width W_f (columns).

sheet width, as well as its linear increase, are consistent with the behaviour for a single scar explored in section 5.7.1. By contrast, the double-scarred sheet's twisting behaviour deviates from that of a single-scarred sheet. Fig. 5.45c reports the sheet's twist using the groove angle, which is shown as a function of scar separation relative to sheet width, D/W. The groove angle lies around 0.1 rad, similar to the groove angle for a single scar (recall Fig. 5.40c). The groove angle declines linearly as the ratio between scar spacing and sheet width grows; however, no twisting bifurcation is observed. That is, double-scarred sheets *always* twist.

Secondly, we explore the effect of groove geometry. We investigate the shape of scarred sheets with $N = 8$ shallow grooves, using 2D photography; a typical example is shown in Fig. 5.45d. The sheet's rolling and twisting shape measures, extracted using a custom Python script, are reported in Fig. 5.45e. Note that for these shallow-grooved sheets, scar lines must be more than $D \gtrsim 3$ cm away from each other, and $W_f \gtrsim 1.5$ cm away from the sheet edges; while the halving of these critical distances compared to those for deep-grooved sheets above is suggestive, we do not explore it further here. As before, the rolling radius R_{centre} is shown for shallow-grooved sheets in Fig. 5.45e (left) as a function of sheet width W. Consistent with previous results, the rolling radius is of the same order of magnitude as the typical groove arc length; it is, by extrapolation, finite at vanishing sheet width; and increases linearly with W. The sheet's groove angle is always finite, and lies near 0.2 rad for all probed ratios of scar spacing to sheet width, D/W. Note that the twisting angle for shallow grooves is about twice as large as the twist angle for deep grooves. While it is not clear where this difference in twisting magnitudes comes from, it is consistent with the twisting magnitude in the presence of a single scar line (recall Fig. 5.40c,e), which is twice larger for shallow grooves than for deep grooves.

For completeness, we show the rolling radius and the groove angle as a function of scar distance D, sheet width W, and edge width W_f for both deep- and shallow-grooved sheets in Fig. 5.45f–g. We observe the following two general trends. The rolling radius R_{centre} increases with W, but does not show a clear correlation with either D or W_f. In addition, the groove angle decreases with D, but shows an increase with W and W_f. Thus, while both shape measures vary to some degree with the scar and sheet widths, we propose that the sheet width W shows a good correlation with R_{centre}, while the scar-to-sheet-width ratio D/W (which metric unifies the groove angle's dependence on D and W) is a strong predictor for the groove angle.

In summary: sheets with two equal-parity scars always roll and twist. While the exact rolling and twisting magnitude depend on the groove geometry, the scar separation D, and the sheet width W, the typical twisted cylindrical shape is observed throughout.

Opposite-parity scars

We now move on to explore the shape of sheets with two *opposite*-parity scar lines in Fig. 5.46. Fig. 5.46a shows how we create two opposite-parity scar lines at mutual distance D in a sheet with width W; the scar lines are located at edge width $W_f = (W - D)/2$ to their nearest boundary. How the scarred sheet deforms is illustrated in Fig. 5.46a (right): the central portion of the sheet, between the scar lines, twists into a helicoidal shape (recall Fig. 5.43d). The sheet's central axis (around which the helicoid twists) remains straight, while the sheet's side lobes curve freely. Our experiments show that

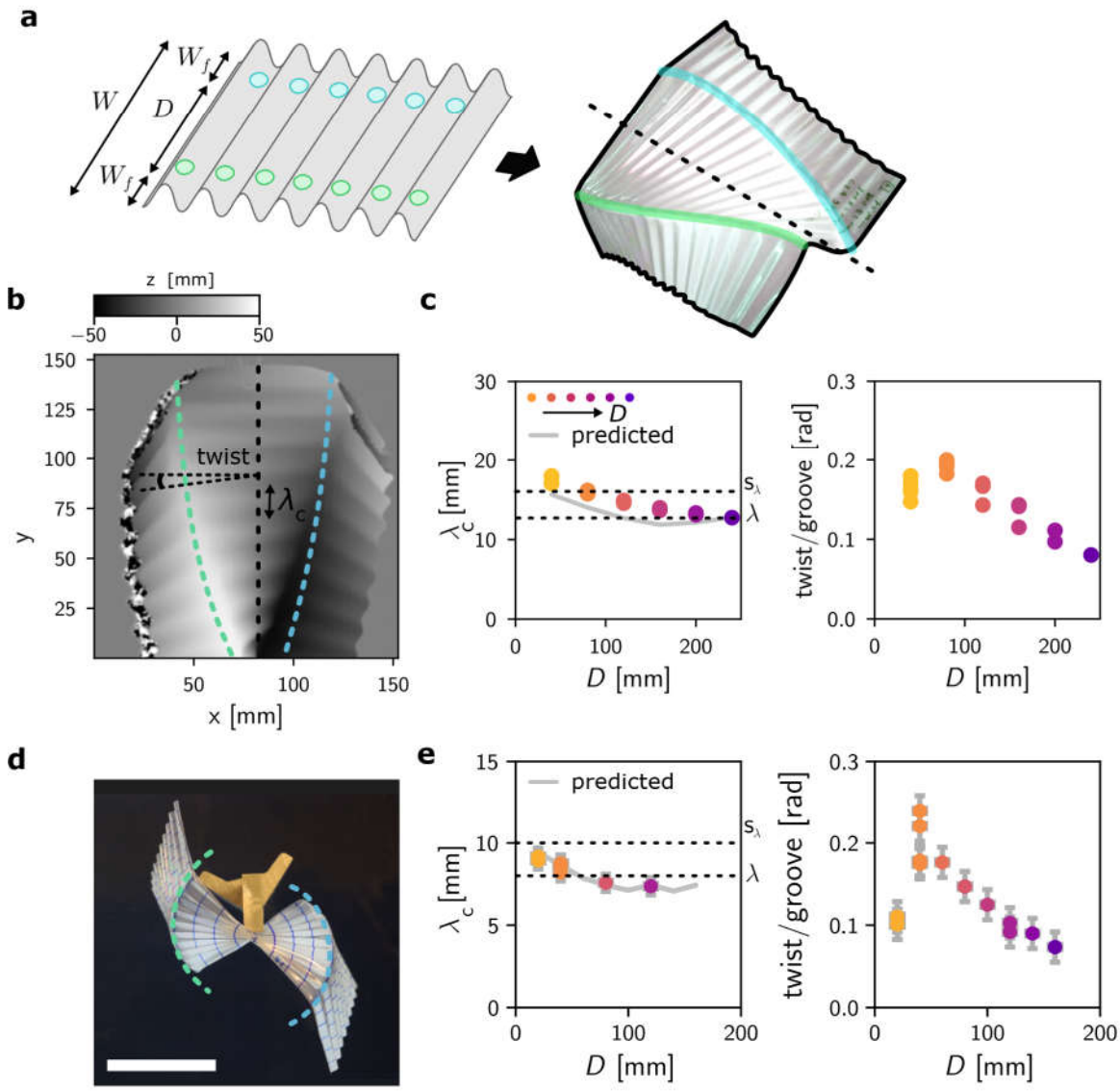

Fig. 5.46.: Shaping effect of opposite-parity scar lines. **a,** Left: two parallel, opposite-parity scar lines are popped into the top (green dots) and bottom(blue dots) of a groovy sheet of width W at a mutual distance D. Each scar lies at distance W_f to its nearest free edge. Right: the sheet's centre forms into a helicoidal shape, with curving side wings. The helicoid's central axis is shown (dashed line). **b,** 3D scan of a deep-grooved, double-scarred sheet ($N = 10$ grooves), fabricated with static thermoforming. Here, $W_f = 4.5 \pm 0.5$ cm and $D = 8 \pm 0.5$ cm. Twisting of the central sheet portion is quantified by the twisting angle per traversed groove; stretching of the axis is measured via the central groove wavelength λ_c, as indicated. **c,** 3D shape measures of a scarred sheet. Left: groove wavelength λ_c measured at sheet's central axis as a function of scar separation D, where dashed lines indicate the approximate resting and maximal wavelengths λ and s_λ. Average predicted values are shown (grey line, Eq.5.35). Right: twist angle per groove as a function of scar distance D. Colours correspond to constant values of D as a guide to the eye. **d,** Top-view photograph of a shallow-grooved sheet of total width $W = 14 \pm 0.5$ cm and $N = 9.5$ grooves with scars at mutual distance $D = 8 \pm 0.5$ cm. Dashed lines indicate scars. Orange block functions as sample support; markings on the sheet are used for alignment and calibration. Scale bar: 5 cm. **e,** 2D shape measures of a scarred sheet. Left: central axis wavelength for varying scar distance D (dashed lines are extremal wavelengths, solid line as in Eq.5.35), right: average twisting of grooves.

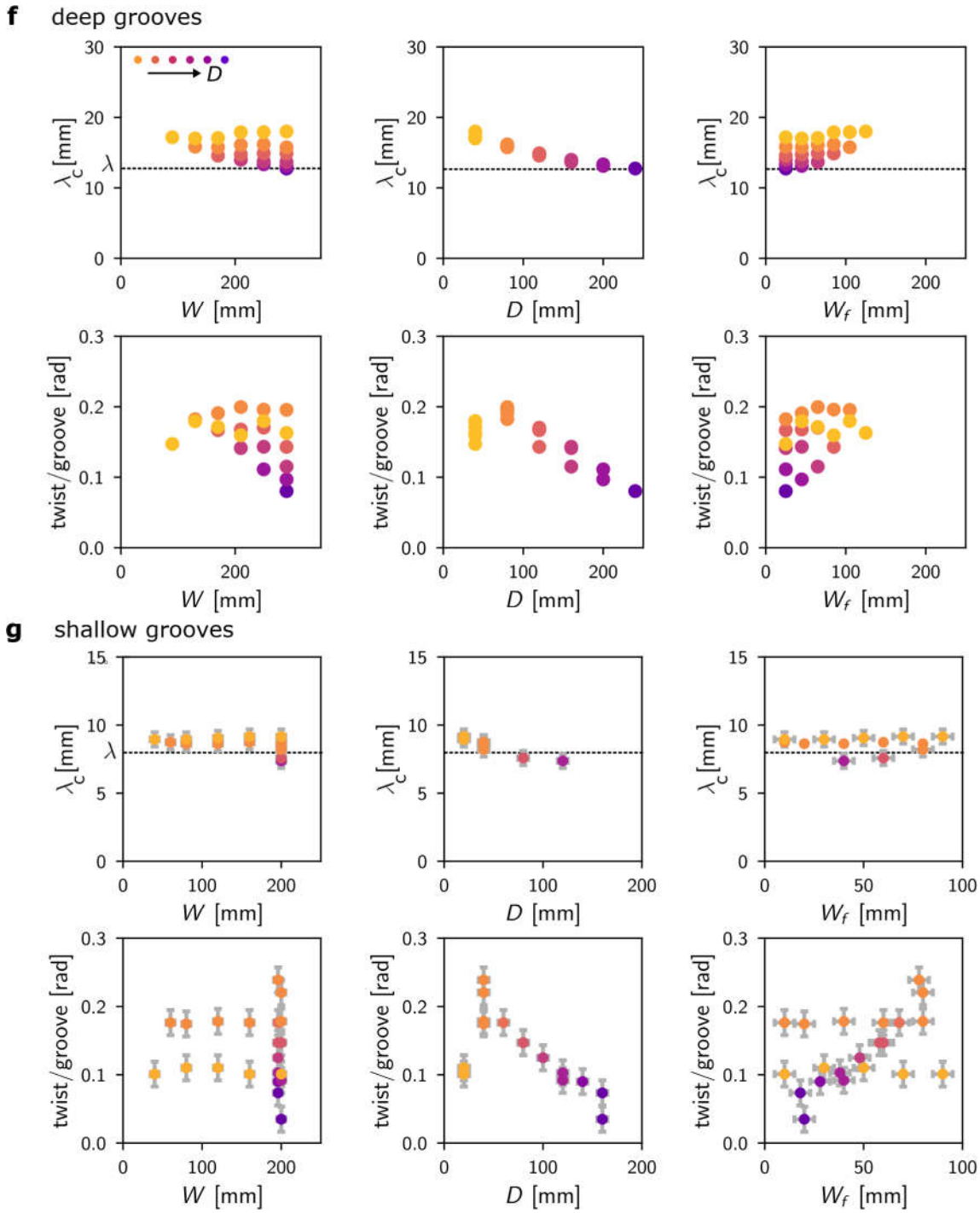

Fig. 5.46.: (continued) Shaping effect of opposite-parity scar lines. f, Extended overview of the shape of sheets with deep grooves, corresponding to panels **b-c**. We show the central axis' groove wavelength λ_c and twist angle per groove (rows) as a function of sheet size and scar positioning, quantified by sheet width W, scar line spacing D, and edge width W_f (columns). Colours correspond to the magnitude of D. Dashed lines correspond to the resting value of groove wavelength λ throughout. **g,** Shape of sheets with shallow grooves, as in **d-e**. Axial wavelength λ and twist per groove (rows) are shown versus sheet width W, scar line spacing D, and edge width W_f (columns).

the sheet between the two scar lines is well-approximated by a helicoid, as we will argue below.

Sheets with deep grooves are first studied via 3D scans (Fig. 5.46b). We study sheets with $N = 10$ grooves, variable width $W \in [9, 29]$ cm, and variable groove distance $D \in [4, 24]$ cm. Opposing scar lines are observed to be unstable if their mutual separation D is smaller than 3 cm, or when their edge distance W_f is smaller than about 2 cm. Opposite-parity scar lines thus have a larger range of stability than their equal-parity counterparts, which become unstable for $D \lesssim 7$ and $W_f \lesssim 3$ cm. Notably, the sheets show a consistent shape across the parameter space. Between the two scar lines, the sheet's folds remain approximately straight, but twist with respect to each other around the sheet's central axis to form a helicoidal surface (that is, the plane spanned by a double helix). Two shape measures characterize the helicoid: the average angular twist between two subsequent grooves, and the groove wavelength λ_c along the central axis.

Fig. 5.46c shows the central wavelength and the twisting per groove of the deformed sheet's helicoidal section. We first show the central wavelength as a function of scar line distance D. Note that the central wavelength may be longer or shorter than the resting length λ due to axial extension or compression of the sheet; it should not be larger than s_λ, which is the full arc length of a flattened groove. As shown in Fig. 5.46c (left), the central wavelength is maximal at small scar line separations. λ_c appears to lie above its maximal value of s_λ, which we tentatively attribute to image warping in our 3D-scanning procedure. As the scar lines are moved farther apart, λ_c decreases smoothly to approximately its equilibrium value λ. The measured data (21 data points) collapse with good accuracy to a single curve. Our data suggest that the sheet's central axis is nearly fully stretched at small scar separations, but relaxes to around its preferred length at large separations. Second, the average twisting angle per groove is shown in Fig. 5.46c (right) as a function of scar spacing D. We observe two regimes that cross over around $D \approx 8$ cm: the twisting angle initially grows when the scars are close together, but subsequently decreases as the scars are brought farther apart. The twisting angle lies around 0.1]radian, and is similar in magnitude to the groove angle reported for sheets with one or two equal-parity scars (Figs. 5.40c,e and 5.45c,e).

We now argue that the experimental data support that the sheet's central section is helicoidal. Bolstered by the success of our helix-based model in section 5.7.1, we assume that the two opposite-parity scar lines are helical. The two scars spiral around a cylinder of radius $D/2$. At the cylinder's axis, each groove has central wavelength λ_c; at the scar, a groove is stretched out to its maximal arc length s_λ. The relation between helix arc length and corresponding axis length is given by wavelength is given by $s_\lambda = \lambda_c\sqrt{1 + (\frac{D\zeta}{2\lambda_c})^2}$ for helices. Thus, if the sheet is helicoidal, the central wavelength λ_c may be calculated via the known scar separation D, average twist angle per groove ζ, and groove arc length s_λ via

$$\lambda_c = \sqrt{s_\lambda^2 - (\frac{D}{2}\zeta)^2)} \ . \tag{5.35}$$

The predicted central wavelength, based on the experimentally measured average twist per groove, is plotted in Fig. 5.46c. The prediction shows a reasonable quantitative agreement with experiments. Most importantly, the qualitative behaviour of the central

wavelength with varying D is reproduced: its initial maximal value s_λ at $D = 0$ decreases to a plateau value, around λ, for large scar separations. Thus, the sheet's central section is well-approximated by a helicoidal plane.

Secondly, we investigate the effect of groove shape in Fig. 5.46d, where the helicoidal shape of sheets with $N = 9.5$ shallow grooves is studied via photography. The sheet width and scar separation are varied between $W \in [4, 20]$ cm and scar separation $D \in [2, 16]$ cm. For these shallow-grooved sheets, opposite-parity scar lines are not stable if the scar separation or edge distance is too small: $D \lesssim 2$ cm or $D \lesssim 1$ cm, respectively. The sheet's total central length and total twisting angle are extracted manually from the photographs via graphical angle- and distance-measurement tools, and divided by the number of grooves to obtain the central wavelength λ_c and the average twisting angle per groove. The results are shown in Fig. 5.46e. First and foremost, we note that the trends in axial stretch and groove twist observed for deep-grooved sheets are reproduced here. Specifically, consider the sheet's central wavelength λ_c as a function of scar separation D. The central wavelength lies near its maximal value of s_λ at small D, and decreases to a plateau value around λ as the scars are moved farther apart. In addition, the average twist angle per groove is small for scars that are close together; however, the twisting increases to a peak value around $D \approx 4$cm, and subsequently decreases with D. The magnitude of the twisting per groove, around 0.1]radian, appears to be similar for both deep- and shallow-grooved sheets. Finally, the central wavelength predicted using the helicoid model in Eq. 5.35 is shown in Fig. 5.46e (left). The predicted and experimental values match both qualitatively and quantitatively. In conclusion: for shallow-grooved sheets, the sheet shape between the two scar lines is helicoidal.

Finally, we show the sheets' helicoidal shape parameters (centre wavelength λ_c and twisting per groove) as a function of scar distance D, sheet width W, and edge width W_f for both deep- and shallow-grooved sheets in Fig. 5.46f–g. Intriguingly, the scar spacing D is correlated most strongly with variations of the shape parameters. By contrast, neither the central wavelength nor the twisting appear to be significantly affected by either W or W_f. Thus, the scar spacing D is the strongest predictor for variations of the sheet shape.

Our findings above show that parallel scar lines produce distinct shapes, depending on their parity. Equal-parity scar lines consistently produce twisted, cylindrical rolls, while opposite-parity scar lines yield helicoidal sheet sections flanked by curving wings. The exact shape details—the amount of rolling, twisting, and helixing—depends on the sheet's size, the scar separation, and the groove geometry. However, the general shape of double-scarred sheets (a twisted roll; a helicoid) is retained throughout. We therefore envision a geometrical model, in which sheet sections flanked by scar lines can be seen as puzzle pieces. These puzzle pieces may be tiled and connected in series or in parallel as first illustrated in Fig. 5.43, based on rules of geometric compatibility and elastic deformation. Such a model could form a solid basis for future complex shape design of scarred groovy sheets.

5.7.4. Understanding sheet shapes: outlook

The experiments of the previous sections demonstrated that sheets with scar lines orthogonal to their grooves can roll, twist, and helix. Phenomenologically, the overall shape of the sheet depends mostly on its internal configuration of scar lines rather than its geometric details such as size and groove shape. This leads us to the question: *is there a way to model sheet shapes geometrically*?

We argue that there is. Our experiments show three important features of sheets with scars orthogonal to their grooves. First, their grooves are approximately straight, except very close to scar lines; second, scar lines have circular or helical shapes; and third, grooves appear to lie orthogonal to scar lines. There is a geometrical model for sheets with these properties: *ruled surfaces*. We previously used ruled surfaces to build an elastic model of sheets with a single scar line (recall section 5.7.1); here, we briefly review the basics of ruled surface geometry, and show that we can construct simple ruled surfaces whose shape closely mimics that of real groovy sheets.

Ruled surfaces are a subclass of geometrical surfaces that can be created as follows. The process starts with a base curve (or directrix) in 3D space, $\boldsymbol{g}$. The directrix has a local coordinate frame[108], the Serret-Frénet frame $(\hat{\boldsymbol{t}}, \hat{\boldsymbol{n}}, \hat{\boldsymbol{b}})$ (defined via the derivatives of $\boldsymbol{g}$) that describes how the curve bends and twists in space. Moving along the curve's arc length, straight lines (or rules) are drawn, starting from the curve and radiating out in space. Each rule can be described by its components along the local coordinate frame. Together, the directrix and rules form a surface in space.

Based on our observations, we propose to model our sheets as ruled surfaces under the following constraints. First, we assume that the scar line can be described as a helical directrix. Recall that we used the same assumption for our simple energetic model for single-scarred sheets in section 5.7.1. The helical scar line, g, is then given by

$$\boldsymbol{g}(t) = (R\cos s, R\sin s, Tt) \ , \tag{5.36}$$

where R is the helix' radius of curvature, and $2\pi T$ is the pitch along coordinate t over which the helix repeats itself. Note that the directrix is a simple circle if the pitch is zero. The directrix' coordinate frame is then given by:

$$\hat{\boldsymbol{t}} = \frac{1}{\sqrt{R^2+T^2}}(-R\sin t, R\cos t, T) \tag{5.37}$$

$$\hat{\boldsymbol{n}} = (-\cos t, -\sin t, 0) \tag{5.38}$$

$$\hat{\boldsymbol{b}} = \frac{1}{\sqrt{R^2+T^2}}(T\sin t, -T\cos t, R) \tag{5.39}$$

Secondly, we assume that groove facets can be modelled with straight rules. They lie orthogonal to the scar line: rules are linear combinations $\hat{\boldsymbol{r}} = \cos\beta\hat{\boldsymbol{b}} + \sin\beta\hat{\boldsymbol{n}}$ of the directrix' normal and binormal vectors. Lastly, given the periodicity of our sheets, we only consider rules that have fixed components along $\hat{\boldsymbol{n}}$ and $\hat{\boldsymbol{b}}$ across the entire directrix.

We illustrate in Fig. 5.47 how to use this constrained ruled-surface model to mimic sheet shapes with one or two scar lines. Fig. 5.47a shows a sheet with one central scar line with small width W, without any groove twisting. The scar line is modelled by

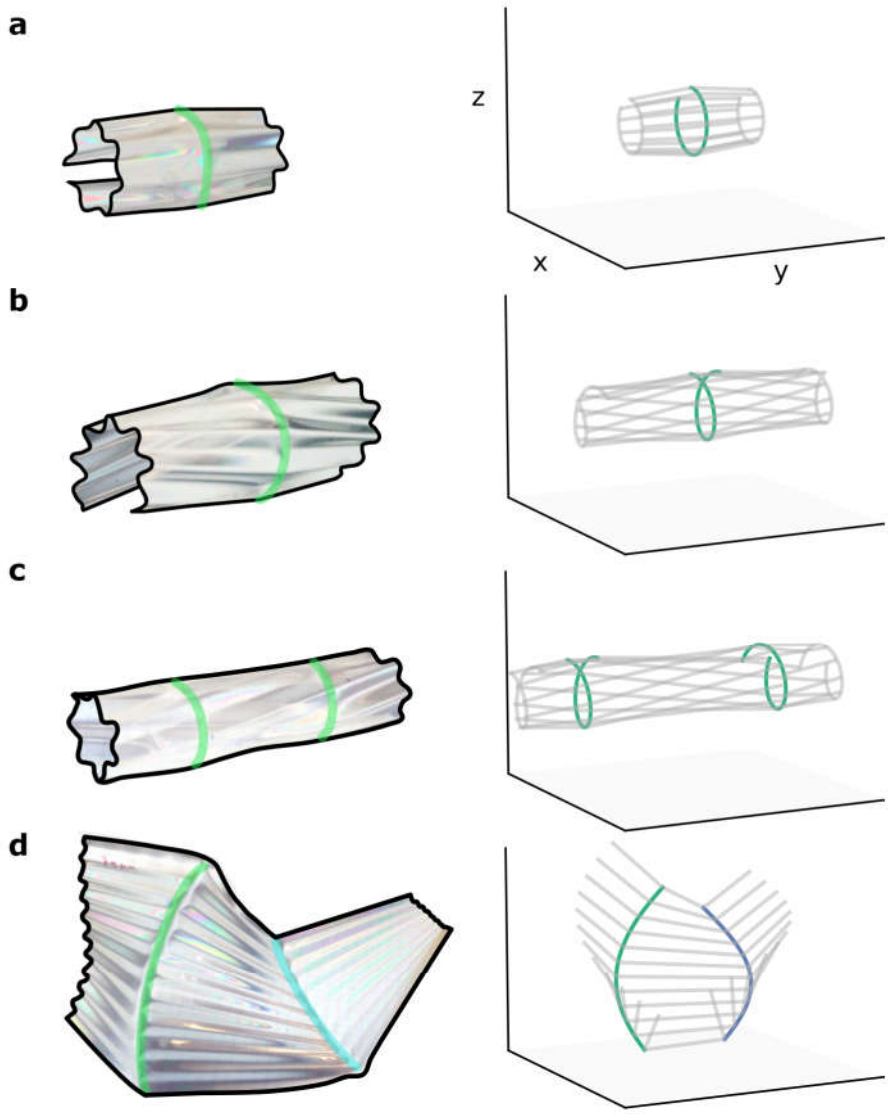

Fig. 5.47.: Groovy sheets look like ruled surfaces. a, A small sheet with a single central scar (left) is approximated by the ruled surface (right). The directrix (green) and rules (grey) corresponding to the scar line and groove facets are shown. The directrix is a circle with constant radius of curvature. Rules lie along a linear combination $\hat{\boldsymbol{r}} = \cos\beta\hat{\boldsymbol{b}} + \sin\beta\hat{\boldsymbol{n}}$ of the directrix' normal and binormal vectors $\hat{\boldsymbol{n}}, \hat{\boldsymbol{b}}$ at small $\beta = 0.1$. **b,** A wide sheet with a central scar rolls as well as twists. The scar line is modelled by a helical directrix with $T/R = 0.15$, while rules lie along the directrix' normal and binormal vector at a fixed ratio with $\beta = 0.1$. **c,** Rolling, twisting sheet with two equal-parity scar lines. Scar lines are helical ($T/R = 0.15$); rules lie along a fixed angle in the directrix' normal-binormal plane with $\beta = 0.1$ **d,** Helicoidal sheet with two opposite-parity scar lines (green, blue curves). Scar lines are helical (T/R=1) with a large pitch-to-curvature ratio. Rules between the scar lines are oriented along the directrix' normal vector; wing rules are chosen in the normal-binormal plane with $\beta = 0.5$

a circular directrix with zero twist T, while the groove facets are approximated with rules $\hat{\boldsymbol{r}} = \cos\beta\hat{\boldsymbol{b}} + \sin\beta\hat{\boldsymbol{n}}$ at a fixed normal-binormal ratio set by small values of β (see Fig. 5.47 for the values chosen to generate the illustrated surfaces). The resulting surface shape looks like two truncated cones, their bases aligned, similar to the real rolled sheet. Fig. 5.47b shows a sheet with larger width W that twists as well as rolls. We therefore model the scar line as a helical directrix with a small twist, $T/R \ll 1$. The rules can be

modelled, as before, to lie mostly along the local binormal with a small normal component. The model surface matches the real sheet's overall shape well. To show that our model can work for parallel scar lines, too, we consider a sheet with two equal-parity scar lines in Fig. 5.47c. Notably, the directrices and rules corresponding to the two scar lines and their connecting grooves can be modelled identically to those for a single scar line; the two scar lines do have a small phase offset due to their finite twist. As in the real sheet, the model surface has a rolled and twisted shape, where the radius of curvature of the roll decreases away from the scar lines. Finally, a sheet with two opposite-parity scars is illustrated in Fig. 5.47d. Here, the two directrices are identical helices with a twist comparable to the radius of curvature: $T/R \approx 1$. The directrices form a double helix, differing by a phase π, so that their mutual distance is constant at $2R$. The helices circle around the $\hat{\boldsymbol{z}}$-axis, while the rules that connect them lie perpendicular to $\hat{\boldsymbol{z}}$: the rules are oriented fully along the normal vector $\hat{\boldsymbol{n}}$. Rules in the surface's wings, that extend away from the central helicoidal surface, are chosen here to lie in the normal-binormal plane. The model surface's helicoidal section compares favourably to the real sheet.

Thus, groovy sheet shapes can be approximated as ruled surfaces. Specifically, we hypothesize that sheets with one or more scar lines may be modelled by surfaces generated from helicoidal base scars, where rules that mimic grooves point perpendicularly away from the scars. We envision an energetic extension to this purely geometric model that may be used to model groovy sheets more precisely, analogous to the simple model discussed in section 5.7.1. For example, it costs energy to open, close, and twist grooves in real sheets. This can be modelled by associating an energetic cost to deviations from parallelity of the surface's rules. In addition, scar lines appear to carry an intrinsic, constant curvature, which may be included in the surface model by penalizing deviations from this value. In short: we propose decorating our geometric model with elastic properties that mimic the mechanics of a real sheet. This strategy provides a clear avenue for predicting and designing the shapes of real groovy sheets.

5.8. Conclusions and outlook

In the preceding chapter, we showcased the unique shape-morphing capacities of groovy sheets. Several sheet fabrication methods were presented, including thermoforming plastic and spin-coating rubber, to create groovy sheets at the centimetre scale. We showed that elastic instabilities lie at the heart of groovy sheet's shape-shifting: each groove can support snap-through defects that locally change the structure's shape. We saw that snap-through defects are stable in sheets whose size lie in a goldilocks zone: they must be neither too narrow, nor too wide. Adjacent defects were shown to interact and attract at short range, resulting in their alignment into scar lines of contiguous defects. We explored and modelled the reshaping effect of individual scar lines, and argued that sheet shapes can be classified systematically according to their internal configuration of scar lines. Finally, we presented a novel approach for modelling groovy sheets with ruled surfaces- a strategy that proved successful for sheets with single scar lines.

Several avenues for deeper research present themselves now, and we discuss them briefly. First, the stability and interaction of defects in groovy sheets depends on the grooves' geometry. Preliminary experimental evidence shows that defect attraction is decreased in sheets with shallow grooves, which precludes the creation of stable scar lines. In such systems, staggered defect patterns rather than contiguous chains are observed. In short: tuning the interactions between defects could give rise to a host of new defect configurations besides scar lines, and corresponding exotic new shapes. Exploring the relation between geometry and defect interactions could thus provide a rich vein of new sheet shapes. Secondly, we have shown that the shape of scarred sheets can be captured successfully with ruled surfaces. Such ruled surfaces provide a convenient way to summarize sheet shape in a few parameters. However, quantitative models for sheets with multiple scars has yet to be developed; we envision that decorating ruled surfaces with energetic constraints, as we have done for sheets with single scars, will provide the means to predict and design complex sheet shapes.

What makes groovy sheets unique is their geometry-driven shape-morphing. In extant work, a variety of structural morphing strategies has been proposed: flat sheets can transform into complex 3D target shapes using patterns of folds, cuts, or regions that swell under mechanical forcing, heat or light. However, these strategies have their drawbacks. The resulting structures are only stable under sustained forcing, morph slowly or irreversibly, or need a distinct design for each desired target shape. By contrast, groovy sheets morph fast, via snap-through instabilities that occur on the order of the speed of sound in the underlying material. Groovy sheets morph elastically, since they are thin enough not to exceed plastic strains even under large deformations. And finally, groovy sheets morph into many different shapes with minimal programming. We propose that groovy sheets are one realization of a conceptual class of shape-morphing materials, whose reshaping properties come from their geometry, not their underlying material or size. We expect that our geometric approach can be extended to thin materials with different surface patterns, thus establishing a new paradigm for fast and reversibly shape-morphing sheets, with applications from stretchable electronics[167,168] to soft robotics[61–63].

Acknowledgements

This work is a testament to the importance of invention through play. Many thanks to Anika Jensenius, Oskar Jensenius, and Leonie Bisiot, for their discovery of the strange reshaping behaviour of groovy sheets during an errant craft project. Their findings brought forth this research.

We would like to thank Hadrien Bense, Lucie Domino, Théo Jules, Evgueni Filipov, Matthieu Labousse, Bas Overvelde and Albert Schenning for insightful discussions. We thank Klara Knupfer for seminal work on quantifying defect stability, and Daan van Velzen for developing a spin-coating method for corrugated rubber sheets. We are grateful to the precision manufacturing departments at AMOLF and Leiden University's Institute of Physics, especially Idsart Attema, Jan Verlinden, Marnix Verweij, and Mark Willemse, for developing and manufacturing the means to controllably thermoform plastic sheet material. We thank Dion Ursem and Jeroen Mesman-Vergeer for their ongoing technical support.

A. Appendices

A.1. Floppy motion of a triangular building block

The specific geometry of the triangular building block introduced in chapter 2, as shown in Fig. 2.1 and in Fig. A.1a, gives rise to a local floppy mode: the block can change its internal shape without deforming any of the rigid bonds. During this deformation, bonds pivot around the freely hinging nodes that connect them (Fig. A.1b).

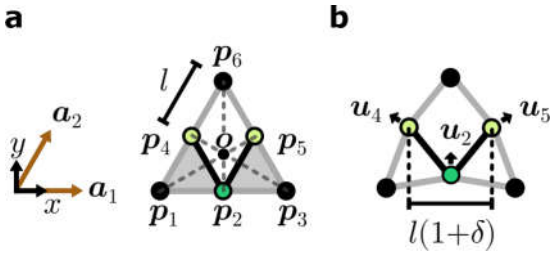

Fig. A.1.: Floppy motion of a building block. **a**, Anisotropic building block consisting of edge bonds (grey), internal bonds (black), corner nodes (black), majority edge-nodes (light green), and a minority edge-node (dark green). Node positions $\boldsymbol{p}$ are indicated in the xy-plane: the nodes are positioned at multiples of the lattice basis vectors $\boldsymbol{a}_1, \boldsymbol{a}_2$ with lattice constant l. **b**, Deformed building block in fat, expanded state. In the linear regime of small deformations, the edge-nodes move by a deflection $\boldsymbol{u}_i$. The two majority edge-nodes are separated by a length $l(1+\delta)$, where δ is a measure of block strain: it is positive for expansion (fat state) and negative for contraction (skinny state) of the block.

The positions $\{\boldsymbol{p}_i\}_{i=1}^6$ of the block's six nodes during the floppy deformation can be found via trigonometry. The deformation is prescribed by a single control parameter, the *block strain* $\delta \in [-1, 1]$ such that $l(1+\delta)$ encodes the distance between the two majority edge-nodes. The dimensionless quantity δ can be seen as a strain measure: positive δ indicate expansion of the block to a "fat" shape, associated with a positive block spin, while negative values signify contraction to a "thin" configuration with a negative block spin.

We calculate all node positions in units of the block's bond lengths l, which is set by the triangular basis vectors $\boldsymbol{a}_1 = l(1, 0)$ and $\boldsymbol{a}_2 = l(1/2, \sqrt{3}/2)$; the block's nodes are positioned at integer multiples of these vectors. The node positions as indicated in Fig. 2.1a are then given by the expressions below.

$$
\begin{aligned}
\boldsymbol{p}_1 &= \begin{pmatrix} -\frac{1}{2}\cos\theta - \frac{\sqrt{3}}{2}\sin\theta \\ \frac{\sqrt{3}}{2} - \frac{\sqrt{3}}{2}\cos\theta - \frac{1}{2}\sin\theta \end{pmatrix} & \boldsymbol{p}_2 &= \begin{pmatrix} 0 \\ \frac{\sqrt{3}}{2} - 2\sin\theta \end{pmatrix} \\
\boldsymbol{p}_3 &= \begin{pmatrix} \frac{1}{2}\cos\theta + \frac{\sqrt{3}}{2}\sin\theta \\ \frac{\sqrt{3}}{2} - \frac{\sqrt{3}}{2}\cos\theta - \frac{1}{2}\sin\theta \end{pmatrix} & \boldsymbol{p}_4 &= \begin{pmatrix} -\cos\theta \\ \frac{\sqrt{3}}{2} - \sin\theta \end{pmatrix} \\
\boldsymbol{p}_5 &= \begin{pmatrix} \cos\theta \\ \frac{\sqrt{3}}{2} - \sin\theta \end{pmatrix} & \boldsymbol{p}_6 &= \begin{pmatrix} 0 \\ \frac{\sqrt{3}}{2} \end{pmatrix},
\end{aligned}
\tag{A.1}
$$

where the equality $\delta = 2\cos\theta - 1$ has been used for legibility. Here, the origin of the xy-plane is chosen to lie at the centroid of the triangular block (see Fig. A.1a). In the linear regime of small shape changes such that $\delta << 1$, the node displacements $\{\boldsymbol{u}_i\}_{i=1}^6$, again

in units of bond length l, are determined up to rigid-body translations and rotations by:

$$\begin{aligned} \boldsymbol{u}_1 &= \begin{pmatrix} 0 \\ 0 \end{pmatrix} & \boldsymbol{u}_2 &= \begin{pmatrix} 0 \\ \frac{\delta}{\sqrt{3}} \end{pmatrix} \\ \boldsymbol{u}_3 &= \begin{pmatrix} 0 \\ 0 \end{pmatrix} & \boldsymbol{u}_4 &= \begin{pmatrix} -\frac{1}{2}\delta \\ \frac{1}{2\sqrt{3}}\delta \end{pmatrix} \\ \boldsymbol{u}_5 &= \begin{pmatrix} \frac{1}{2}\delta \\ \frac{1}{2\sqrt{3}}\delta \end{pmatrix} & \boldsymbol{u}_6 &= \begin{pmatrix} 0 \\ 0 \end{pmatrix}. \end{aligned} \tag{A.2}$$

In short, during the floppy deformation, the block's edge nodes move radially outward or inward from the triangle's centroid over a distance $\frac{\delta}{\sqrt{3}}$ during expansion or contraction.

A.2. Constructing delocalized SS-states

We show how to construct the $H_o - 1$ delocalized SS-states for any H-superhexagon metamaterial with $H_o > 1$ odd local loops. We consider the schematic shown in Fig. A.2, which illustrates how delocalized SS-states can be constructed iteratively. The network shown contains $H_o = 5$ odd local loops (numbered 1-5) that contains $H_o - 1 = 4$ delocalized SS-states (Fig. A.2a).

We first show how to create a delocalized SS-state running between a pair of two odd local loops (numbered 1, 2). We start by identifying a small subsection of the network to construct the SS-state in, consisting of the two incompatible superhexagons containing the odd local loops, and an arbitrary string of compatible superhexagons that connects the pair (Fig. A.2a, orange infill). We then transform this metamaterial strip into a compatible structure—in which all SS-states are known exactly—via a series of supertriangle rotations (Fig. A.2b, yellow triangles, arrows) that sequentially flip the parity of the local loops. We are left with a compatible structure in which all loop and radial SS-states are found by inspection (Fig. A.2c, radial SS-states not shown for clarity). As explained in Fig. 4.5e-g, these loop SS-states may then be recombined via sequential application of Eq. (4.4) under inversion of the applied supertriangle rotations, analogous to the construction discussed in Sec. 4.6.1. The linear combination of loop SS-states thus produces a delocalized SS-state of the metamaterial strip with the two odd local loops 1 and 2 (Fig. A.2d, arrows).

In a metamaterial with H_o odd loops, we can find $H_o - 1$ independent delocalized states using the above procedure. Independence is ensured by selecting $H_o - 1$ independent pairs of incompatible superhexagons (such that each is selected at least once), with strings of compatible superhexagons running between them. Figure A.2e demonstrates the three remaining delocalized SS-states found between defect pairs $(2, 3)$, $(3, 4)$, and $(4, 5)$ in our example.

It should be noted that the delocalized states are not unique: their shape depends on the path between each defect pair, and the choice of supertriangle rotations. However, the space spanned by the resulting basis of SS-states does not depend on the path choice. In particular, this procedure renders an independent, non-orthogonal set of $H_o - 1$ delocalized SS-states. Together with the known radial and loop SS-states, which are identified by inspection, a complete and independent basis of SS-space can be found for our metamaterials with any defect configuration.

A.3. Evolution of LB-spaces under architectural transformations

In Sec. 4.6, we discussed the evolution of a metamaterial's stress space (consisting of the SS- and complementary LB-space) under architectural transformations. We demonstrated that the evolution of the SS-space is limited to one, two, or no changing SS-states for distinct types of supertriangle rotations, denoted process I, process II, and process III, respectively. Here, we derive the concomitant evolution of the metamaterial's LB-space for all three processes.

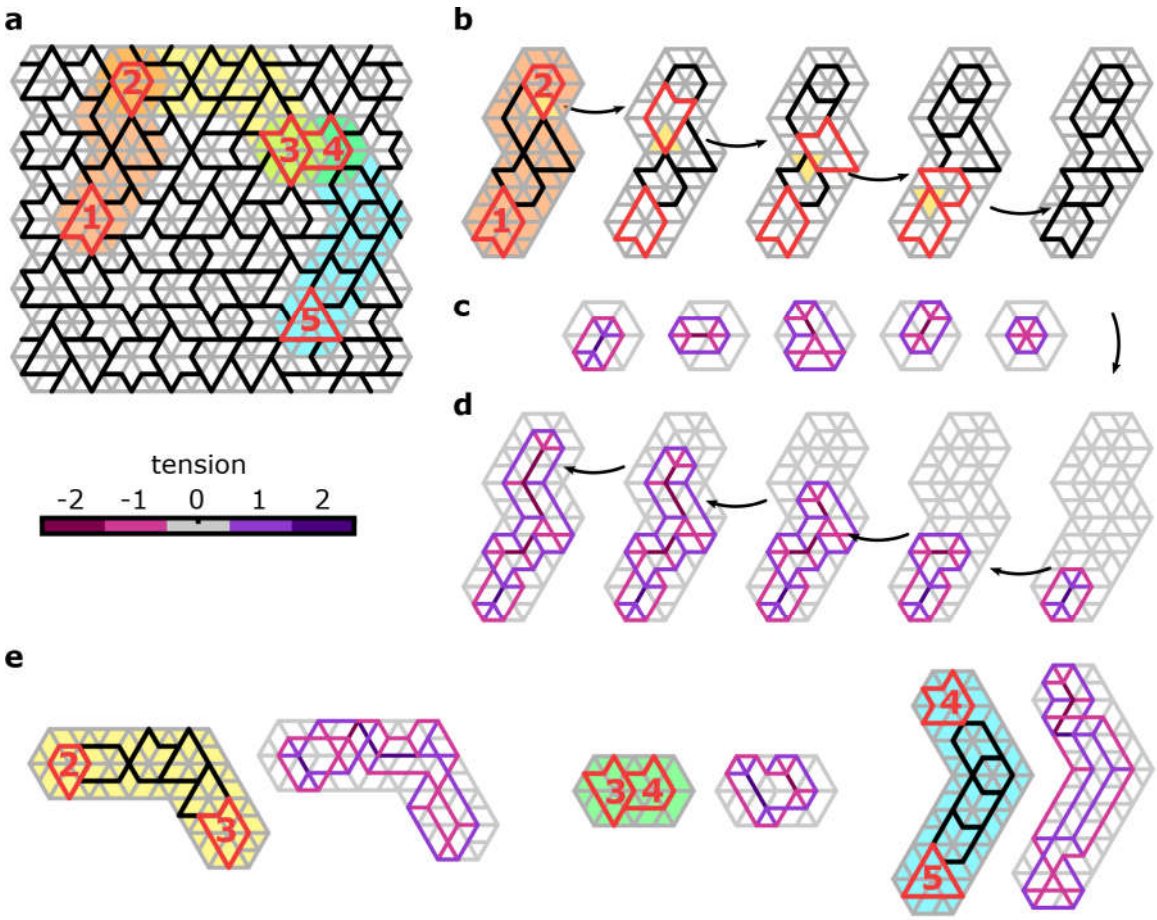

Fig. A.2.: **a**, An incompatible metamaterial architecture containing $H_o = 5$ odd local loops (numbers 1-5, red bold lines) and $H - H_0 = 72$ even ones (black bold lines). The metamaterial contains $H_o - 1 = 4$ delocalized SS-states, which are constructed on metamaterial paths connecting four independent pairs of incompatible hexagons (infills in orange, 1-2; yellow, 2-3; green, 3-4; and blue, 4-5). **b**, The incompatible metamaterial strip between superhexagons 1,2 is made compatible by sequential supertriangle rotations (yellow triangles, arrows) that change the parity of local loops. **c**, The compatible metamaterial's SS-states are spanned by radial (not shown) and loop SS-states (colour bar). **d**, The loop SS-states are recombined into a delocalized SS-state of the incompatible metamaterial strip using Eq. (4.4) (arrows), yielding a delocalized SS-state between the incompatible superhexagons 1 and 2. **e**, With the procedure demonstrated in b—d, the other three delocalized SS-states are constructed between the remaining pairs of odd local loops.

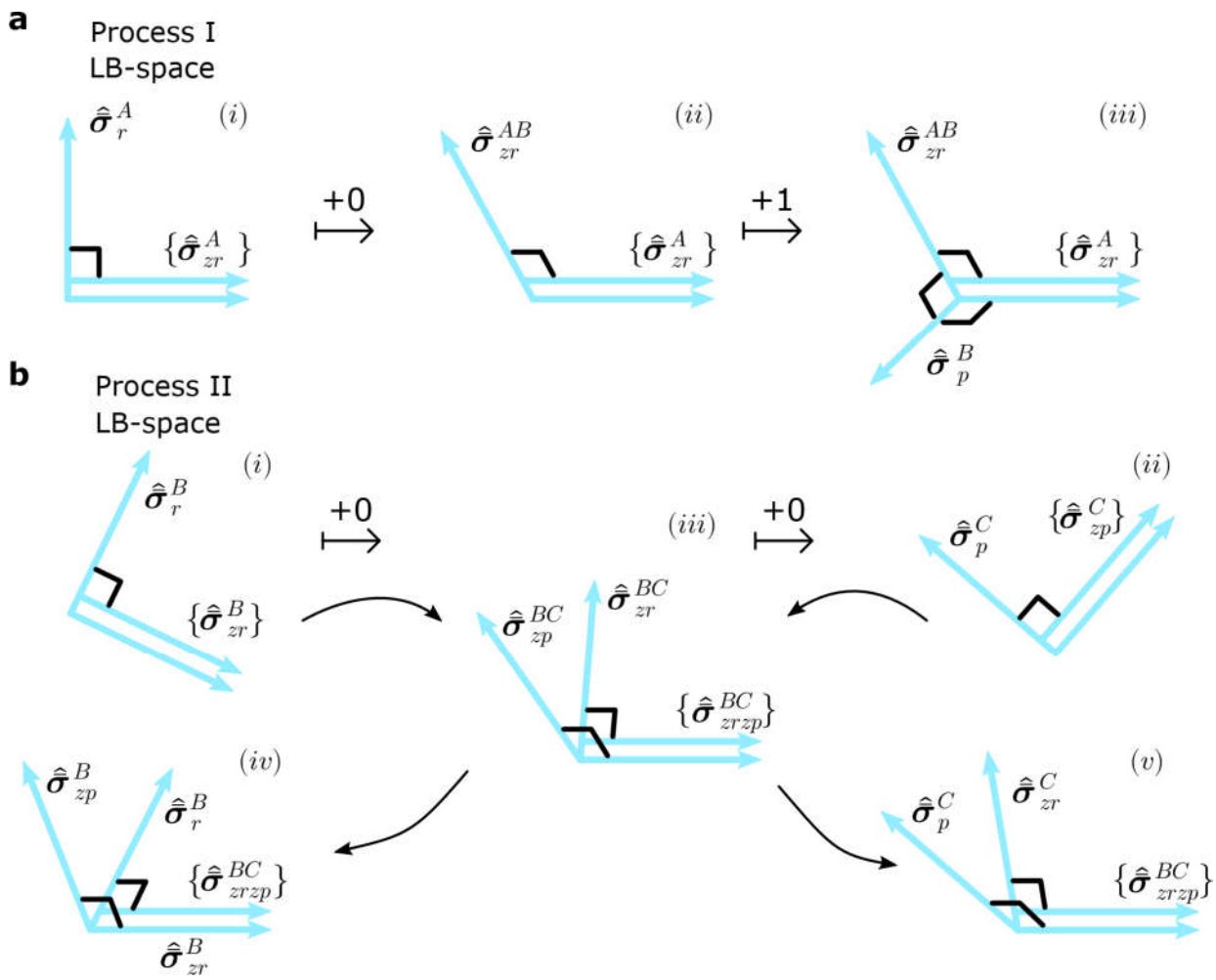

Fig. A.3.: Evolution of the LB-space under a supertriangle rotation according to processes I and II. **a**, Process I: a compatible network A is transformed to an incompatible network B via an intermediate network AB, by first removing bond r and then adding bond p (see Fig. 4.7). For network A, we construct an orthogonal basis for the LB-space that contains those states $\{\hat{\bar{\boldsymbol{\sigma}}}^{A}_{zr}\}$ that remain in network AB as well as B. The full bases of networks A and B additionally contain a state that is added ($\hat{\bar{\boldsymbol{\sigma}}}^{B}_{p}$) and a state that is modified ($\hat{\bar{\boldsymbol{\sigma}}}^{A}_{r}$ to $\hat{\bar{\boldsymbol{\sigma}}}^{AB}_{zr}$) during the architectural transformation; for details on the execution of steps *(i)-(iii)*, see text. **b**,Process II: an incompatible network B is transformed to an incompatible network C via an intermediate network BC, by first removing bond r and then adding bond p (see Fig. 4.8). For network B (P), we construct an orthogonal basis for the LB-space that contains states $\{\hat{\bar{\boldsymbol{\sigma}}}^{B}_{zr}\}$ ($\{\hat{\bar{\boldsymbol{\sigma}}}^{C}_{zp}\}$) without stress on r (p), and $\hat{\bar{\boldsymbol{\sigma}}}^{B}_{r}$ ($\hat{\bar{\boldsymbol{\sigma}}}^{C}_{p}$) with finite stress there. We construct a suitable basis of LB-space for the intermediate network BC (with no stress on p or r) via an orthogonalization procedure, which produces LB-states $\{\hat{\bar{\boldsymbol{\sigma}}}^{BC}_{zrzp}\}$ that are shared with networks B and C, and states $\hat{\bar{\boldsymbol{\sigma}}}^{BC}_{zp}$, $\hat{\bar{\boldsymbol{\sigma}}}^{BC}_{zr}$ that are modified to states $\hat{\bar{\boldsymbol{\sigma}}}^{B}_{zp}$ and $\hat{\bar{\boldsymbol{\sigma}}}^{C}_{zr}$ in networks B and C respectively. For details on the execution of steps *(i)-(v)*, see text. Black squares signify orthogonality, and arrows with numbers indicate changes in the dimensions of the LB-space.

A.3.1. Process I: compatible to incompatible metamaterial

We describe the evolution of the LB-space when a compatible network A is transformed into an incompatible network B; this evolution is shown schematically in Fig. A.3a. The architectural transformation occurs via a supertriangle rotation that removes a bond r and adds a bond p (see Fig. 4.7a). The LB-space evolution is closely related to the evolution of the SS-space discussed in Sec. 4.6.2 (see Fig. 4.7b), and involves three separate calculations *(i)-(iii)* below.

(i) We aim to construct a basis for the LB-space of network A that consists of one LB-state, $\hat{\bar{\boldsymbol{\sigma}}}_r^A$, that has a finite stress on bond r, and a remaining set of orthogonal vectors $\{\hat{\bar{\boldsymbol{\sigma}}}_{zr}^A\}$ that have zero stress om bond r (Fig. 4.7c, left). Under removal of bond r, only the LB-state $\hat{\bar{\boldsymbol{\sigma}}}_r^A$ will be modified. Since the set $\{\hat{\bar{\boldsymbol{\sigma}}}_{zr}^A\}$ is unaffected by removing r and adding p, we do not need to construct it explicitly, and focus on identifying $\hat{\bar{\boldsymbol{\sigma}}}_r^A$ instead. To construct this unique LB-state with nonzero stress on bond r, note that the stress state $\hat{\boldsymbol{r}}$ must be a linear combination of the SS-state $\hat{\bar{\boldsymbol{\tau}}}_r^A$ (see Sec. 4.6.2) and $\hat{\bar{\boldsymbol{\sigma}}}_r^A$—the only two stress states with nonzero stress on r—and since $\hat{\bar{\boldsymbol{\tau}}}_r^A$ and $\hat{\bar{\boldsymbol{\sigma}}}_r^A$ are perpendicular, we find

$$\hat{\bar{\boldsymbol{\sigma}}}_r^A \propto \mathrm{Rej}(\hat{\boldsymbol{r}}, \hat{\bar{\boldsymbol{\tau}}}_r^A) \ , \tag{A.3}$$

as shown in Fig. A.3a, left. Here, we define the vector rejection Rej( ) to be the complement of vector projection: $\mathrm{Proj}(\boldsymbol{u}, \boldsymbol{v}) = \frac{\boldsymbol{u}\cdot\boldsymbol{v}}{\boldsymbol{v}\cdot\boldsymbol{v}}\boldsymbol{v}$ and $\boldsymbol{u} = \mathrm{Proj}(\boldsymbol{u}, \boldsymbol{v}) + \mathrm{Rej}(\boldsymbol{u}, \boldsymbol{v})$, so that $\mathrm{Rej}(\boldsymbol{u}, \boldsymbol{v}) := \boldsymbol{u} - \frac{\boldsymbol{u}\cdot\boldsymbol{v}}{\boldsymbol{v}\cdot\boldsymbol{v}}\boldsymbol{v}$.

(ii) When bond r is removed from network A, the LB-state $\hat{\bar{\boldsymbol{\sigma}}}_r^A$ must disappear; the LB-states $\{\hat{\bar{\boldsymbol{\sigma}}}_{zr}^A\}$ remain. However, as the number of LB-states in AB is the same as in network A (see above), the intermediate network AB must contain a new LB-state, $\hat{\bar{\boldsymbol{\sigma}}}_{zr}^{AB}$, with zero stress on bond r. This state must be perpendicular to the SS-space spanned by $\{\hat{\bar{\boldsymbol{\tau}}}_{zr}^A\}$, and to the LB-states $\{\hat{\bar{\boldsymbol{\sigma}}}_{zr}^A\}$. However, $\hat{\bar{\boldsymbol{\sigma}}}_{zr}^{AB}$ does not need to be perpendicular to the state $\hat{\bar{\boldsymbol{\tau}}}_r^A$, so that we can construct $\hat{\bar{\boldsymbol{\sigma}}}_{zr}^{AB}$ from the states $\hat{\bar{\boldsymbol{\tau}}}_r^A$ and $\hat{\boldsymbol{r}}$:

$$\hat{\bar{\boldsymbol{\sigma}}}_{zr}^{AB} \propto Rej(\hat{\bar{\boldsymbol{\tau}}}_r^A, \hat{\boldsymbol{r}}) \ , \tag{A.4}$$

as shown in Fig. A.3a, middle.

(iii) Finally, when network AB evolves to network B by adding bond p, a new LB-state $\hat{\bar{\boldsymbol{\sigma}}}_p^B$ must appear. The new LB-state is perpendicular to both the SS-space spanned by $\{\hat{\bar{\boldsymbol{\tau}}}_{zr}^A\}$ as well as the LB-space spanned by $\{\{\hat{\bar{\boldsymbol{\sigma}}}_{zr}^A\}, \hat{\bar{\boldsymbol{\sigma}}}_{zr}^{AB}\}$, and has a finite stress on bond p. It is easy to check that the stress state $\hat{\boldsymbol{p}}$ uniquely satisfies these criteria: $\hat{\bar{\boldsymbol{\sigma}}}_p^B = \hat{\boldsymbol{p}}$ (Fig. A.3a, right).

In summary, as we illustrate in Fig. A.3a and Fig. 4.7, the stress spaces of architecturally related networks A and B are identical up to the following four independent vectors: the SS-state $\hat{\bar{\boldsymbol{\tau}}}_r^A$, present in network A, but not in B; the LB-state $\hat{\boldsymbol{p}}$, present in B but not in A; and the LB-state $\hat{\bar{\boldsymbol{\sigma}}}_r^A$ in network A that changes to the LB-state $\hat{\bar{\boldsymbol{\sigma}}}_{zr}^{AB}$ in network B. These four independent vectors are spanned by the set $\{\hat{\bar{\boldsymbol{\tau}}}_r^A, \hat{\boldsymbol{r}}, \hat{\boldsymbol{p}}\}$ consisting of the mutated SS-state and the pure stress vectors on bonds p and r.

A.3.2. Process II: incompatible to incompatible metamaterial

We now describe the evolution of the LB-space when an incompatible network B is transformed into a distinct incompatible network C as shown in Fig. A.3b, via a supertriangle rotation that removes a bond r and adds a bond p (see Fig. 4.8a). This evolution is closely related to the evolution of the SS-space discussed in Sec. 4.6.3 (see Fig. 4.8b), and involves five separate calculations *(i)*-*(v)* below.

We can construct the LB-spaces of networks B and C, analogous to step *(ii)* in process I. This readily yields bases *(i)* $\{\{\hat{\bar{\boldsymbol{\sigma}}}^B_{zr}\}, \hat{\bar{\boldsymbol{\sigma}}}^B_r\}$ and *(ii)* $\{\{\hat{\bar{\boldsymbol{\sigma}}}^C_{zp}\}, \hat{\bar{\boldsymbol{\sigma}}}^C_p\}$ (Fig. A.3b, left and right). However, as the sets $\{\hat{\bar{\boldsymbol{\sigma}}}^B_{zr}\}$ and $\{\hat{\bar{\boldsymbol{\sigma}}}^C_{zp}\}$ are not the same, the bases are not suitable to compare the LB-spaces.

(iii) We now construct an appropriate basis for the LB-space of network BC, which contains a set $\{\hat{\bar{\boldsymbol{\sigma}}}^{BC}_{zrzp}\}$ that is shared with the LB-spaces of network B and C (Fig. A.3b, middle). First, we can start from the LB-basis *(i)*, remove bond r, and analogous to step *(ii)* of process I, obtain a basis $\{\{\hat{\bar{\boldsymbol{\sigma}}}^B_{zr}\}, \hat{\bar{\boldsymbol{\sigma}}}^{BC}_{zr}\}$. Second, starting from the LB-basis *(ii)* and removing bond p we obtain a basis $\{\{\hat{\bar{\boldsymbol{\sigma}}}^C_{zp}\}, \hat{\bar{\boldsymbol{\sigma}}}^{BC}_{zp}\}$. These two bases both span the LB-space of network BC. We now use this to construct the appropriate basis of the LB-space, $\{\hat{\bar{\boldsymbol{\sigma}}}^{BC}_{zp}, \hat{\bar{\boldsymbol{\sigma}}}^{BC}_{zr}, \{\hat{\bar{\boldsymbol{\sigma}}}^{BC}_{zpzr}\}\}$, so that the set $\{\hat{\bar{\boldsymbol{\sigma}}}^{BC}_{zpzr}\}$ is shared with the LB-spaces of network B and C. We first perform a Gram-Schmidt process on the ordered set $\{\hat{\bar{\boldsymbol{\sigma}}}^{BC}_{zp}, \hat{\bar{\boldsymbol{\sigma}}}^{BC}_{zr}, \{\hat{\bar{\boldsymbol{\sigma}}}^B_{zr}\}\}$, and then define $\{\hat{\bar{\boldsymbol{\sigma}}}^{BC}_{zpzr}\}$ as the last $N_b - 2H - 1$ vectors of the resulting orthonormal basis. To facilitate comparison with networks B and C, we obtain a full LB-space basis of network BC by adding the vectors $\hat{\bar{\boldsymbol{\sigma}}}^{BC}_{zp}$ and $\hat{\bar{\boldsymbol{\sigma}}}^{BC}_{zr}$, so that all but the first two basis vectors are orthogonal.

We now obtain appropriate bases for the LB-spaces of networks B and C as follows (see Fig. A.3b, left and right).

(iv) We construct a basis for the LB-space of network B by ensuring the orthogonality of the LB-space basis of network BC, $\{\hat{\bar{\boldsymbol{\sigma}}}^{BC}_{zp}, \hat{\bar{\boldsymbol{\sigma}}}^{BC}_{zr}, \{\hat{\bar{\boldsymbol{\sigma}}}^{BC}_{zpzr}\}\}$, with the SS-space of network B. We do this by rejecting each vector on the SS-state $\hat{\bar{\boldsymbol{\tau}}}^B_r$, that is present in network B but not in BC. This rejection procedure results in an LB-space basis of network B: $\{\hat{\bar{\boldsymbol{\sigma}}}^B_{zp}, \hat{\bar{\boldsymbol{\sigma}}}^B_r, \{\hat{\bar{\boldsymbol{\sigma}}}^{BC}_{zpzr}\}\}$.

(v) A similar procedure results in an analogous LB-space basis for network C: $\{\hat{\bar{\boldsymbol{\sigma}}}^C_{zr}, \hat{\bar{\boldsymbol{\sigma}}}^C_p, \{\hat{\bar{\boldsymbol{\sigma}}}^{BC}_{zpzr}\}\}$.

In summary, as shown in Fig. A.3b and Fig. 4.8, the stress spaces of architecturally related networks B and C are identical up to the following vectors: the SS-state $\hat{\bar{\boldsymbol{\tau}}}^B_r$, present in network B, but not in C; the SS-state $\hat{\bar{\boldsymbol{\tau}}}^C_p$, present in network C, but not in B (see Sec. 4.6.3); the LB-state $\hat{\bar{\boldsymbol{\sigma}}}^B_r$ in network B that changes to the LB-state $\hat{\bar{\boldsymbol{\sigma}}}^C_{zr}$ in network C; and the LB-state $\hat{\bar{\boldsymbol{\sigma}}}^C_p$ in network C that changes to the LB-state $\hat{\bar{\boldsymbol{\sigma}}}^B_{zp}$ in network B. These four independent vectors are spanned by the set $\{\hat{\bar{\boldsymbol{\tau}}}^B_r, \hat{\bar{\boldsymbol{\tau}}}^C_p, \hat{\boldsymbol{r}}, \hat{\boldsymbol{p}}\}$ consisting of the mutated SS-states and the pure stress vectors on bonds p and r.

A.3.3. Process III: compatible to compatible metamaterial

A compatible network A may be transformed to a distinct compatible network A' by some supertriangle rotations that remove a bond r and add a bond p. Only supertriangle rotations at the system's edge that do not change the parity of any local loops (see Sec. 4.5) can generate such a network pair. By construction, these special architectural transformations do not change the shape of any local loops, and thus do not affect the SS-space (see Sec. 4.6.1). As a consequence, under an externally applied load that is supported by both networks A and A', the stress response of both networks must be identical. Since only the bonds r and p differ between the two networks, the stress spaces of networks A and A' are identical up to the following vectors: the LB-state $\hat{\bar{\boldsymbol{\sigma}}}_r^A = \hat{\boldsymbol{r}}$, present in network A but not in A', and the LB-state $\hat{\bar{\boldsymbol{\sigma}}}_p^{A'} = \hat{\boldsymbol{p}}$, present in A' but not in A. Since the stress response to external loading that is supported by both networks must be identical, the LB-states $\hat{\boldsymbol{r}}$ and $\hat{\boldsymbol{p}}$ will therefore not contribute to the network's mutual supported stress responses: the bonds r and p remain unstressed.

A.4. Mechanical interpretation of evolving LB-states

Having discussed the evolution of LB-space under supertriangle rotations in Appendix A.3, we now present the mechanical interpretation of the mutated LB-states. We show here that the few stress states that are added, removed, or modified in processes I and II (Secs. 4.6.2 and 4.6.3) correspond to the metamaterials' stress response to well-defined external nodal loads. In particular, we show below that all mutated LB-states correspond to nodal load dipoles along the two bonds r, p that are mutually exclusive between the post- and pre-transformation networks. A nodal load dipole generates equal and opposite forces at two nodes, and is oriented along the connecting line between the two nodes. The mutating LB-states either generate a large stress on a single bond and a diffuse field around it, or an extended stress field around a missing bond, as illustrated in Fig. A.4.

We first consider the stress response evolution of process I, when a compatible material A is transformed into an incompatible material B (Fig. A.4a). During this transformation, the LB-state $\bar{\boldsymbol{\sigma}}_r^A$ of network A changes. The physical interpretation of this stress state is as follows. The state $\bar{\boldsymbol{\sigma}}_r^A$ is a linear combination of the SS-state $\hat{\bar{\boldsymbol{\tau}}}_r^A$ and the unit bond stress $\hat{\boldsymbol{r}}$, such that the final LB-state is orthogonal to the SS-state (Eq. (A.3)). The unit bond stress corresponds via Hooke's law to a nodal load dipole $\sqrt{2}\hat{\boldsymbol{f}}_r$: that is, the two nodes connected by bond r undergo an equal and opposite force, extending the bond (here, the prefactor $\sqrt{2}$ is a consequence of normalization). The SS-state, by definition, generates no nodal loads. Thus, the stress state $\bar{\boldsymbol{\sigma}}_r^A$ in network A must map to the nodal load state $\sqrt{2}\hat{\boldsymbol{f}}_r$:

$$\bar{\boldsymbol{\sigma}}_r^A = \hat{\boldsymbol{r}} - (\hat{\boldsymbol{r}} \cdot \hat{\bar{\boldsymbol{\tau}}}_r^A)\hat{\bar{\boldsymbol{\tau}}}_r^A \leftrightarrow \sqrt{2}\hat{\boldsymbol{f}}_r \tag{A.5}$$

In network B, the LB-state $\bar{\boldsymbol{\sigma}}_r^A$ is replaced by a new LB-state $\bar{\boldsymbol{\sigma}}_{zr}^{AB}$. It is a linear combination of the SS-state $\hat{\bar{\boldsymbol{\tau}}}_r^A$ and the unit bond stress $\hat{\boldsymbol{r}}$ such that any stress on r is cancelled out (see Eq. (A.4)). Here, again, the unit bond stress $\hat{\boldsymbol{r}}$ maps to the nodal load $\sqrt{2}\hat{\boldsymbol{f}}_r$, while the SS-state $\hat{\bar{\boldsymbol{\tau}}}_r^A$ generates no load. Hence, in network B,

$$\bar{\boldsymbol{\sigma}}_{zr}^{AB} = \hat{\boldsymbol{r}} - \frac{1}{\hat{\boldsymbol{r}} \cdot \hat{\bar{\boldsymbol{\tau}}}_r^A}\hat{\bar{\boldsymbol{\tau}}}_r^A \leftrightarrow \sqrt{2}\hat{\boldsymbol{f}}_r \ . \tag{A.6}$$

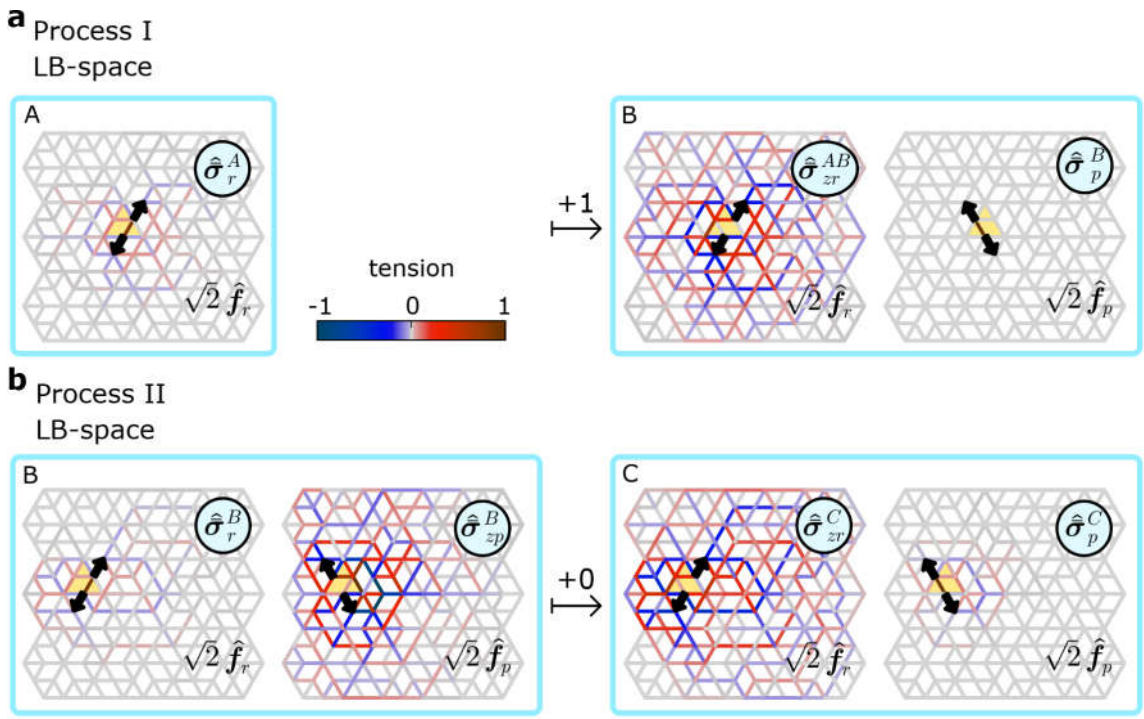

Fig. A.4.: Mechanical interpretation of the LB-states that change under a supertriangle rotation for processes I and II. **a**, A compatible network A transforms into an incompatible network B according to process I. One LB-state $\hat{\bar{\boldsymbol{\sigma}}}_r^A$ (colour bar) changes to $\hat{\bar{\boldsymbol{\sigma}}}_{zr}^{AB}$ under the transformation; both LB-states map to the same nodal load dipole $\sqrt{2}\hat{\boldsymbol{f}}_r$ along bond r (arrows). One LB-state $\hat{\bar{\boldsymbol{\sigma}}}_p^B$ is added in network B: it maps to the nodal load dipole $\sqrt{2}\hat{\boldsymbol{f}}_p$ along bond p, which load is not supported in network A. **b**, An incompatible network B transforms into an incompatible network C according to process II. The LB-state $\hat{\bar{\boldsymbol{\sigma}}}_r^B$ in network B changes to $\hat{\bar{\boldsymbol{\sigma}}}_{zr}^C$ in network C. Both LB-states map to the same nodal load dipole $\sqrt{2}\hat{\boldsymbol{f}}_r$ along bond r (arrows). In addition, the LB-state $\hat{\bar{\boldsymbol{\sigma}}}_p^C$ in network C changes to $\hat{\bar{\boldsymbol{\sigma}}}_{zp}^B$ in network B. Both LB-states map to the same nodal load dipole $\sqrt{2}\hat{\boldsymbol{f}}_p$ along bond p (arrows).

Lastly, process I introduces a new LB-state $\hat{\bar{\boldsymbol{\sigma}}}_p^B = \hat{\boldsymbol{p}}$ in network B. Using the same arguments as above, we find that the new LB-state corresponds to a load dipole $\sqrt{2}\hat{\boldsymbol{f}}_p$ along bond p:

$$\bar{\boldsymbol{\sigma}}_p^B = \hat{\boldsymbol{p}} \leftrightarrow \sqrt{2}\hat{\boldsymbol{f}}_p \ . \tag{A.7}$$

This LB-state has no counterpart in network A: there, the nodal load $\sqrt{2}\hat{\boldsymbol{f}}_p$ activates the compatible material's floppy mode, and is not supported. The remaining LB-states $\{\hat{\bar{\boldsymbol{\sigma}}}_{zr}^A\}$, that are shared between networks A and B, are unchanged; they map to identical loads in both networks. An overview of the mutated LB-states, and the nodal loads corresponding to the latter, is shown in Fig. A.4a.

Secondly, we treat the stress response evolution of process II, where an incompatible material B is mutated into an incompatible material C (Fig. A.4b). There are two LB-states that are modified during this transformation: $\hat{\bar{\boldsymbol{\sigma}}}_r^B$ and $\hat{\tilde{\bar{\boldsymbol{\sigma}}}}_{zp}^{BC}$ in network B are changed into $\hat{\bar{\boldsymbol{\sigma}}}_p^C$ and $\hat{\tilde{\bar{\boldsymbol{\sigma}}}}_{zr}^{BC}$ in network C. Using an analogous argument as for process I, the LB-state $\hat{\bar{\boldsymbol{\sigma}}}_r^B$ in network B maps to the nodal load $\sqrt{2}\hat{\boldsymbol{f}}_r$:

$$\bar{\boldsymbol{\sigma}}_r^B = \hat{\boldsymbol{r}} - (\hat{\boldsymbol{r}} \cdot \hat{\bar{\boldsymbol{\tau}}}_r^B)\hat{\bar{\boldsymbol{\tau}}}_r^B \leftrightarrow \sqrt{2}\hat{\boldsymbol{f}}_r \tag{A.8}$$

In intermediate network BC:

$$\bar{\boldsymbol{\sigma}}_{zr}^{BC} = \hat{\boldsymbol{r}} - \frac{1}{\hat{\boldsymbol{r}} \cdot \hat{\bar{\boldsymbol{\tau}}}_r^B}\hat{\bar{\boldsymbol{\tau}}}_r^B \leftrightarrow \sqrt{2}\hat{\boldsymbol{f}}_r \tag{A.9}$$

and finally in network C:

$$\bar{\boldsymbol{\sigma}}_{zr}^C = \mathrm{Rej}(\bar{\boldsymbol{\sigma}}_{zr}^{BC}, \hat{\bar{\boldsymbol{\tau}}}_p^C) = \hat{\boldsymbol{r}} - \frac{\hat{\bar{\boldsymbol{\tau}}}_r^B - (\hat{\bar{\boldsymbol{\tau}}}_r^B \cdot \hat{\bar{\boldsymbol{\tau}}}_p^C)\hat{\bar{\boldsymbol{\tau}}}_p^C}{\hat{\boldsymbol{r}} \cdot \hat{\bar{\boldsymbol{\tau}}}_r^B} \leftrightarrow \sqrt{2}\hat{\boldsymbol{f}}_r \tag{A.10}$$

Similarly, the LB-state $\hat{\bar{\boldsymbol{\sigma}}}_p^C$ maps to the nodal load $\sqrt{2}\hat{\boldsymbol{f}}_p$ in network C:

$$\bar{\boldsymbol{\sigma}}_p^C = \hat{\boldsymbol{p}} - (\hat{\boldsymbol{p}} \cdot \hat{\bar{\boldsymbol{\tau}}}_p^C)\hat{\bar{\boldsymbol{\tau}}}_p^C \leftrightarrow \sqrt{2}\hat{\boldsymbol{f}}_p \tag{A.11}$$

In intermediate network BC:

$$\bar{\boldsymbol{\sigma}}_{zp}^{BC} = \hat{\boldsymbol{p}} - \frac{1}{\hat{\boldsymbol{p}} \cdot \hat{\bar{\boldsymbol{\tau}}}_p^C}\hat{\bar{\boldsymbol{\tau}}}_p^C \leftrightarrow \sqrt{2}\hat{\boldsymbol{f}}_p \tag{A.12}$$

and finally in network B:

$$\bar{\boldsymbol{\sigma}}_{zp}^B = \mathrm{Rej}(\bar{\boldsymbol{\sigma}}_{zp}^{BC}, \hat{\bar{\boldsymbol{\tau}}}_r^B) = \hat{\boldsymbol{p}} - \frac{\hat{\bar{\boldsymbol{\tau}}}_p^C - (\hat{\bar{\boldsymbol{\tau}}}_p^C \cdot \hat{\bar{\boldsymbol{\tau}}}_r^B)\hat{\bar{\boldsymbol{\tau}}}_r^B}{\hat{\boldsymbol{p}} \cdot \hat{\bar{\boldsymbol{\tau}}}_p^C} \leftrightarrow \sqrt{2}\hat{\boldsymbol{f}}_p \tag{A.13}$$

The remaining LB-states $\{\hat{\bar{\boldsymbol{\sigma}}}_{zrzp}^{BC}\}$ are unmodified and map to the same nodal loads in both networks. The mutated LB-states are illustrated in Fig. A.4b.

Lastly, we discuss the stress response evolution for process III, where a compatible material A transforms to a distinct compatible material A'There are two LB-states that are modified during this transformation: $\hat{\boldsymbol{r}}$ and $\hat{\boldsymbol{p}}$ are mutually exclusive LB-states of networks A and A' respectively. Using similar arguments as above, the LB-state $\hat{\boldsymbol{r}}$ in

network A maps to the nodal load dipole $\sqrt{2}\hat{\boldsymbol{f}}_r$:

$$\hat{\boldsymbol{r}} \leftrightarrow \sqrt{2}\hat{\boldsymbol{f}}_r \tag{A.14}$$

This load dipole is not supported in network A'—it activates the global floppy mode of the system—and there is no counterpart to the LB-state $\hat{\boldsymbol{r}}$ in network A'. Analogously, in network A',

$$\hat{\boldsymbol{p}} \leftrightarrow \sqrt{2}\hat{\boldsymbol{f}}_p \ , \tag{A.15}$$

and this LB-state in network A', being unsupported by network A, has no counterpart in the LB-space of A.

A.5. Derivation of stress response differences

With our description of the stress space evolution and its physical interpretation in Appendices A.3 and A.4, we are now in a position to derive exactly how a metamaterial's stress response under external loading changes when its architecture is changed by rotating a supertriangle. In particular, we found that the SS-space of two networks related by a single supertriangle rotation are identical up to at most two mutually exclusive SS-states. Comparing two networks, related by a supertriangle rotation, by calculating their stress response difference $\Delta\boldsymbol{\sigma}$ under identical supported loads, we will now show that $\Delta\boldsymbol{\sigma}$ is a linear combination of only those SS-states that have been changed by the network's architectural transformation.

In any network, the stress response $\boldsymbol{\sigma}$ to an arbitrary supported load $\boldsymbol{f}$ can be written as a unique linear combination of LB-states: $\boldsymbol{\sigma} = \sum_{i=1} (C_i\boldsymbol{\sigma}_i)$, where the set $\{\boldsymbol{\sigma}_i\}$ is any linearly independent basis of stress vectors spanning the LB-space, and the coefficients C_i depend on the applied load, the material's geometry, and the choice of basis. The exact coefficients can be calculated using the matrix formalism discussed in Sec. 4.2. We use this representation to find an expression for the stress response difference between two networks, related via process I, II, or III, under identical supported loads.

We first consider networks A and B, related via process I. When structure A is subjected to a supported load $\boldsymbol{f}$—that is, a load that does not excite the FM of network A—the stress response $\boldsymbol{\sigma}^A$ is written in a straightforward way:

$$\boldsymbol{\sigma}^A = \sum_{i=1}^{N_b-2H-1} \left(C_i\hat{\bar{\boldsymbol{\sigma}}}^A_{zr,i}\right) + C_r\bar{\boldsymbol{\sigma}}^A_r \ , \tag{A.16}$$

where we have chosen a basis of LB-space such that the LB-states $\{\hat{\bar{\boldsymbol{\sigma}}}^A_{zr}\}$ are shared between the two networks, and the LB-state $\bar{\boldsymbol{\sigma}}^A_r$ is unique to network A (see Appendix A.3). As discussed in Appendix A.4, when a supertriangle is rotated in network A to produce network B, the nodal load dipole generated by the stress state $\bar{\boldsymbol{\sigma}}^A_r$ in network A is supported instead by the stress state $\bar{\boldsymbol{\sigma}}^{AB}_{zr}$ in network B; in addition, the basis of LB-space now contains an extra LB-state $\hat{\boldsymbol{p}}$ that maps to a load dipole along bond p. For network B, the stress response to the same external loading $\boldsymbol{f}$ is then written as:

$$\boldsymbol{\sigma}^B = \sum_{i=1}^{N_b-2H-1} \left(C_i\hat{\bar{\boldsymbol{\sigma}}}^A_{zr,i}\right) + C_r\bar{\boldsymbol{\sigma}}^{AB}_{zr} + C_p\hat{\boldsymbol{p}} \ . \tag{A.17}$$

Comparing Eqs. (A.16) and (A.17), we note that the LB-states $\{\hat{\bar{\boldsymbol{\sigma}}}^{A}_{zr,i}\}$ are shared between networks A and B, and map to identical loads, so that the coefficients C_i are equal. Furthermore, $C_a = 0$ by necessity, since the load dipole along bond p excites the FM of network A and cannot be part of our load $\boldsymbol{f}$, which must be supported by both networks. Lastly, the stress field $\bar{\boldsymbol{\sigma}}^{AB}_{zr}$ corresponds to the stress field $\bar{\boldsymbol{\sigma}}^{A}_{r}$—both mapping to the load dipole $\sqrt{2}\hat{\boldsymbol{f}}_r$—so that the coefficient C_r in both equations is equal. Using Eqs. (A.5-A.6) and Eqs. (A.16-A.17), we find the following expression for the stress response difference between networks A and B:

$$\Delta\boldsymbol{\sigma} = \boldsymbol{\sigma}^B - \boldsymbol{\sigma}^A = C_r \frac{-1 + (\hat{\boldsymbol{r}} \cdot \hat{\bar{\boldsymbol{\tau}}}^{A}_{r})^2}{\hat{\boldsymbol{r}} \cdot \hat{\bar{\boldsymbol{\tau}}}^{A}_{r}} \hat{\bar{\boldsymbol{\tau}}}^{A}_{r} \in \mathrm{Sp}(\hat{\bar{\boldsymbol{\tau}}}^{A}_{1}) \ . \tag{A.18}$$

Eq. (A.18) shows that the stress response difference between the two networks is parallel to the single mutated SS-state $\hat{\bar{\boldsymbol{\tau}}}^{A}_{r}$. We confirm this finding via numerical calculations: the stress response difference between network A with no defect and network B with a structural defect, illustrated in Fig. 4.1a (right) corresponds exactly to the lost state of self stress shown in Fig. 4.9b (top), resulting in a differential stress response that is localized near the defect.

A similar procedure allows us to find the stress response difference between two distinct incompatible networks B and C, related via process II. The stress response of network B may be written as:

$$\boldsymbol{\sigma}^B = \sum_{i=1}^{N_b-2H-1} \left(C_i \hat{\bar{\boldsymbol{\sigma}}}^{BC}_{zpzr,i} \right) + C_r \bar{\boldsymbol{\sigma}}^{B}_{r} + C_p \bar{\boldsymbol{\sigma}}^{B}_{zp} \ , \tag{A.19}$$

while the stress response of network C is given by:

$$\boldsymbol{\sigma}^B = \sum_{i=1}^{N_b-2H-1} \left(C_i \hat{\bar{\boldsymbol{\sigma}}}^{BC}_{zpzr,i} \right) + C_r \bar{\boldsymbol{\sigma}}^{C}_{zr} + C_p \bar{\boldsymbol{\sigma}}^{C}_{p} \ . \tag{A.20}$$

Here, the LB-states $\{\hat{\bar{\boldsymbol{\sigma}}}^{BC}_{zpzr}\}$ are shared between networks B and C, while the LB-states $\bar{\boldsymbol{\sigma}}^{B}_{r}$ and $\bar{\boldsymbol{\sigma}}^{B}_{zp}$, that map to load dipoles $\sqrt{2}\hat{\boldsymbol{f}}_r$ and $\sqrt{2}\hat{\boldsymbol{f}}_p$ in network B, are replaced by their commensurate counterparts $\bar{\boldsymbol{\sigma}}^{C}_{zr}$ and $\bar{\boldsymbol{\sigma}}^{C}_{p}$ in network C, consistent with Appendix A.4. Using Eqs. (A.19-A.20) and Eqs. (A.8-A.13), the stress response difference between the two structures then reduces to the following equation:

$$\begin{aligned}
\Delta\boldsymbol{\sigma} &= \boldsymbol{\sigma}^C - \boldsymbol{\sigma}^B \\
&= \hat{\bar{\boldsymbol{\tau}}}^{B}_{r} \left[C_r \left(\frac{-1 + (\hat{\boldsymbol{r}} \cdot \hat{\bar{\boldsymbol{\tau}}}^{B}_{r})^2}{\hat{\boldsymbol{r}} \cdot \hat{\bar{\boldsymbol{\tau}}}^{B}_{r}} \right) + C_p \left(\frac{-\hat{\bar{\boldsymbol{\tau}}}^{B}_{r} \cdot \hat{\bar{\boldsymbol{\tau}}}^{C}_{p}}{\hat{\boldsymbol{p}} \cdot \hat{\bar{\boldsymbol{\tau}}}^{C}_{p}} \right) \right] \\
&+ \hat{\bar{\boldsymbol{\tau}}}^{C}_{p} \left[C_p \left(\frac{1 - (\hat{\boldsymbol{p}} \cdot \hat{\bar{\boldsymbol{\tau}}}^{C}_{p})^2}{\hat{\boldsymbol{p}} \cdot \hat{\bar{\boldsymbol{\tau}}}^{C}_{p}} \right) + C_r \left(\frac{\hat{\bar{\boldsymbol{\tau}}}^{B}_{r} \cdot \hat{\bar{\boldsymbol{\tau}}}^{C}_{p}}{\hat{\boldsymbol{r}} \cdot \hat{\bar{\boldsymbol{\tau}}}^{B}_{r}} \right) \right] \\
&\in \mathrm{Sp}(\hat{\bar{\boldsymbol{\tau}}}^{B}_{r}, \hat{\bar{\boldsymbol{\tau}}}^{C}_{p}).
\end{aligned} \tag{A.21}$$

Once again, the two networks' stress response difference is contained in the space spanned by their two mutually exclusive SS-states, $\hat{\bar{\boldsymbol{\tau}}}^{B}_{r}$ and $\hat{\bar{\boldsymbol{\tau}}}^{C}_{p}$. Note that the stress response difference of Eq. (A.18) (process I) is a special case of the general expression in Eq. (A.21)

for process II.

Consider finally the two compatible networks A and A', related via process III. With the same procedure as for processes I and II, we can write:

$$\boldsymbol{\sigma}^{A} = \sum_{i=1}^{N_b-2H-1} \left(C_i \hat{\bar{\boldsymbol{\sigma}}}^{A}_{zr,i} \right) + C_r \hat{\boldsymbol{r}} \ , \tag{A.22}$$

while the stress response of network C is given by:

$$\boldsymbol{\sigma}^{A'} = \sum_{i=1}^{N_b-2H-1} \left(C_i \hat{\bar{\boldsymbol{\sigma}}}^{A}_{zr,i} \right) + C_p \hat{\boldsymbol{p}} \tag{A.23}$$

By definition, under a load that is supported in both networks, the coefficients C_r and C_p must be zero (see Appendix A.4); and hence, there is no stress response difference between the two structures A and A' under identical, supported loads. Again, the stress response difference for process III is a special case of Eq. (A.21) for process II.

In conclusion: the stress response difference between two networks (related by a single supertriangle rotation) under identical, supported loading is contained in the span of the structures' mutually exclusive SS-states. There may be zero, one, or two such states, corresponding to processes III, I, and II respectively. The precise magnitude of the stress response difference can be found using Eqs. (A.18) (process I) and (A.21) (process II); the stress response difference for process III is trivially zero.

A.6. BoPET film properties

To create multistable groovy sheets, their base material must be stiff under gravity; deformable with minimal permanent damage; and readily formable into a grooved geometry (section 5.2). Here, we discuss to what extent polymer film meets these criteria.

PET is a thermoplastic polymer resin in the polyester family[169], whose molecular chain contains ester functional groups. BoPET film is typically formed by extruding molten, amorphous resin in two orthogonal directions, and then partially crystallizing the extruded film by heating it above the glass transition temperature under tension[169]. BoPET film is widely used and produced; we use 'Mylar-A' films produced by Dupont Teijin[150]. The mechanical properties of PET film are consistent under a wide range of environmental conditions, and it is therefore used for applications that range from insulation to food packaging. Here, we use the consistency of commercially produced BoPET film to ensure that our experimental findings show a minimal dependence on material variations.

To confirm the reported[150] Young's modulus and yield point at room temperature of Mylar-A BoPET, we perform a series of tensile tests on the material following ASTM-D882[170]. These tensile tests produce stress-strain curves in the material's elastic regime (governed by the Young's modulus) and the plastic regime (determined by the yield point). A schematic of the experimental setup used is shown in Fig. A.5a. Mylar strips of width $W = 20 \pm 1$ mm, total length 150 ± 1 mm, and thickness $t = 23$ µm are mounted manually in clamps connected to an Instron 3360 model universal testing machine (UMT) outfitted with an Instron 2530 series static load cell with a capacity of 100 N[171,172]. The strip's length from clamp to clamp is $L = 100 \pm 1$ mm. The initial configuration is chosen such that the sample is slack in the testing machine, exerting only a gravitational force on the load cell. The UMT's translation stage extends the strip back and forth three times over a range of 1.5 mm at a typical rate of 0.1 mm/s. The translation stage's position and the force exerted on the load cell by the extended sample are recorded at a typical frequency of 5 Hz. Typical extensions u and forces $\langle F \rangle$, averaged over the extension cycles, are shown in Fig. A.5b). Force and extension are converted to engineering stress and strain, σ and ϵ, via:

$$\sigma = \frac{F - F_0}{Wt} \tag{A.24}$$

$$\epsilon = \frac{u - u_0}{L} \ , \tag{A.25}$$

where F_0 and u_0 are the estimates force and extension at the onset of sample stretching. We fit the relation between stress and strain with a Hookean model, $\sigma = E\epsilon$, over a strain range of nearly 0.01 (Fig. A.5c) to obtain an estimate of the Young's modulus E (Fig. A.5d). We estimate the yield point as the stress and strain σ_y and ϵ_y at which the curve deviates significantly from its initial linear trend, obtained from fracture tests on three distinct samples at cycle speeds of 0.1 mm/s (Fig. A.5e-f).

Notably, for large strain rates and sudden extension reversals, the recorded force curves exhibits unusual behaviour. The area under the force-displacement curve measures the energy dissipated during a test cycle. Normally, this area has a positive magnitude, corresponding to hysteretic energy loss: the recorded force under extension is larger than the force under compression. However, at large strain rates, this behaviour reverses due

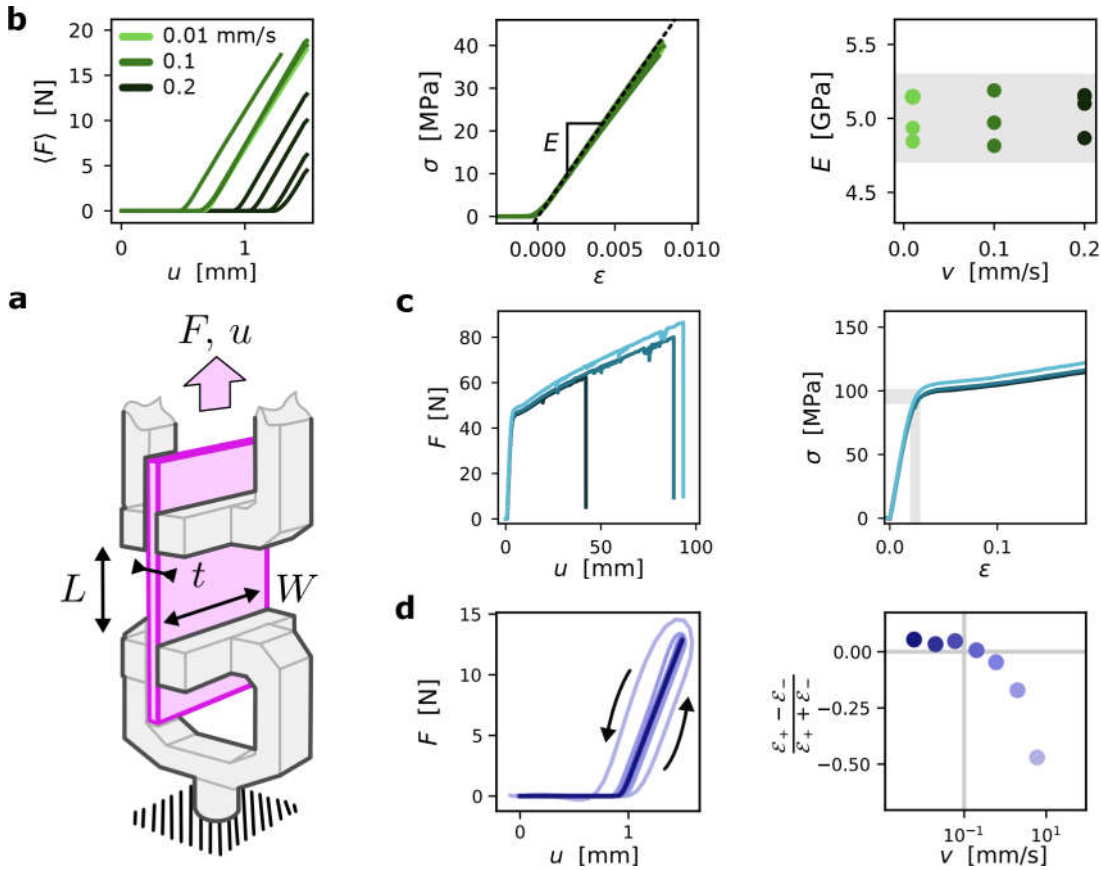

Fig. A.5.: Measuring material properties. **a**, A thin sheet of width $W = 20$ mm and thickness $t = 23$ µm (pink) is fastened between two clamps (grey) to obtain a gauge length $L = 100$ mm. The clamps are mounted in an Instron UTM. Displacement u of the upper clamp produces a force F, measured by a load cell mounted in the UTM. Forces and displacements are converted to engineering stress and strain (main text). **b**, Left to right: typical curves of force $\langle F \rangle$ versus displacement u averaged over three test cycles at variable extension speed v (legend). The corresponding engineering stress and strain σ and ϵ are linearly related via Young's modulus E. The fitted Young's modulus and standard error (grey area, main text) show no significant dependence on speed. **c**, Force-displacement curves until fracture for three samples at speed $v = 0.1$ mm/s (left). In the corresponding stress-strain curves (right), the material's yield point (grey area) is found where the curves deviate from linear behaviour. **d**, Left: high-speed tests produce unphysical results. The extensile force is smaller than the contractile force (arrows; light blue curve) rather than the reverse (normal hysteresis). Right: The normalized work performed by the setup (main text) is measured as a function of test speed. Negative values above 0.2 mm/s are unphysical.

to inertia of the static load cell's response: the compressive force is larger than the extensile force (Fig. A.5g) indicating a testing issue unrelated to the sample's properties. To quantify this behaviour, we compare the energy input and output $\mathcal{E}_+$ and $\mathcal{E}_-$ (that is, the area under the force-displacement curve during extension and retraction) using a normalized metric $\frac{\mathcal{E}_+ - \mathcal{E}_-}{\mathcal{E}_+ + \mathcal{E}_-}$. Fig. A.5h shows that this measure is negative and unphysical at cycle speeds over 0.2 mm/s positive. To ensure the measured material properties are not affected by this issue, we choose a typical cycle speed of 0.1 mm/s.

The standard error on the Young's modulus due to errors in length measurements is estimated at (assuming uncorrelated errors and insignificant errors in force, thickness,

and extension measurements):

$$\Delta E \approx \sqrt{(\frac{\Delta W}{W})^2 + (\frac{\Delta L}{L})^2 + (\frac{\Delta u_0}{u - u_0})^2} E \approx 0.06E \approx 0.3 \text{ GPa} , \tag{A.26}$$

where ΔW and ΔL are estimated at 1 mm and Δu_0 at 0.1 mm.

The resulting experimental estimates of the Young's modulus and yield stress are $E = 5 \pm 0.3$ GPa, averaged over 7 distinct samples; all measurements fall within the error margin. Additionally, we find a yield stress and strain $\sigma_y = 96 \pm 5$ MPa and $\epsilon_y = 0.025 \pm 0.007$, estimated from fracture tests on 3 samples. Our findings are consistent with the reported material properties.

A.7. Spring-back, yielding, and groove design

We would like to understand the effect that our thermoforming methods have on thin BoPET films (section 5.2). Here, we relate the post-forming shape of groovy sheets to the geometry imposed during thermoforming, via a simple model for plastic deformation[173]. In this model, applying a moment to a flat sheet produces an internal stress and strain field. If the stress exceeds a certain limit, the sheet deforms plastically. When the external moment is removed, a residual strain remains and sets the final shape of the sheet. Below, we quantify the difference between the imposed and final groove shape in terms of spring-back.

We assume a bilinear constitutive model for the material's stress-strain curve at room temperature (Fig. A.6a). The model is given by the following relation between stress σ and strain ϵ:

$$\sigma = \begin{cases} E\epsilon & : \epsilon \leq \epsilon_y \\ E\epsilon_y & : \epsilon > \epsilon_y \end{cases} \tag{A.27}$$

This constitutive model has an elastic regime, set by the Young's modulus E (the slope of the stress-strain curve in the elastic regime) and a plastic regime, set by the yield point (at a stress $\sigma_y = E\epsilon_y$ and strain ϵ_y, beyond which the stress is independent of the applied strain).

With the above model, we now make a prediction for the residual stresses, strains, and final shape of a thin sheet section of length $R\theta$ and width W (Fig. A.6b) that is forced to curve into a radius R over a subtended angle θ by applying a bending moment M (Fig. A.6c). The bending moment leads to a through-thickness strain ϵ. Since the sheet's thickness is small compared to other relevant length scales, there are no strains in any other directions. We calculate ϵ along the local coordinate ζ, which runs from the sheet's neutral axis along the surface normal. All (virtual) lines in the sheet parallel to the neutral axis undergo a length change from $R\theta$ to $(R+\zeta)\theta$. Thus, the engineering strain through the sheet's thickness is given by

$$\epsilon(\zeta) = \frac{(R+\zeta)\theta - R\theta}{R\theta} = \frac{\zeta}{R} \ . \tag{A.28}$$

When the sheet is curved strongly, the yield point is exceeded at the outer layers of the sheet, at a yield thickness $\zeta > \zeta^* = R\epsilon_y$. The corresponding engineering stress profile, $\sigma(\zeta)$, is then

$$\sigma(\zeta) = \begin{cases} E\frac{\zeta}{R} & : \zeta \leq \zeta^* \\ E\epsilon_y & : \zeta > \zeta^* \end{cases} \tag{A.29}$$

The moment M that must be exerted on the sheet to obtain the curvature R is then given by:

$$M = W\int_{t/2}^{t/2} \sigma(\zeta)\zeta \mathrm{d}\zeta = \frac{WE\epsilon_y}{12}\left(3t^2 - 4\zeta^{*2}\right) \tag{A.30}$$

When this external moment is removed, the sheet relaxes into a new configuration, with a residual strain $\epsilon'(\zeta)$ and stress $\sigma'(\zeta)$ that respect moment balance $M' = 0$ and the

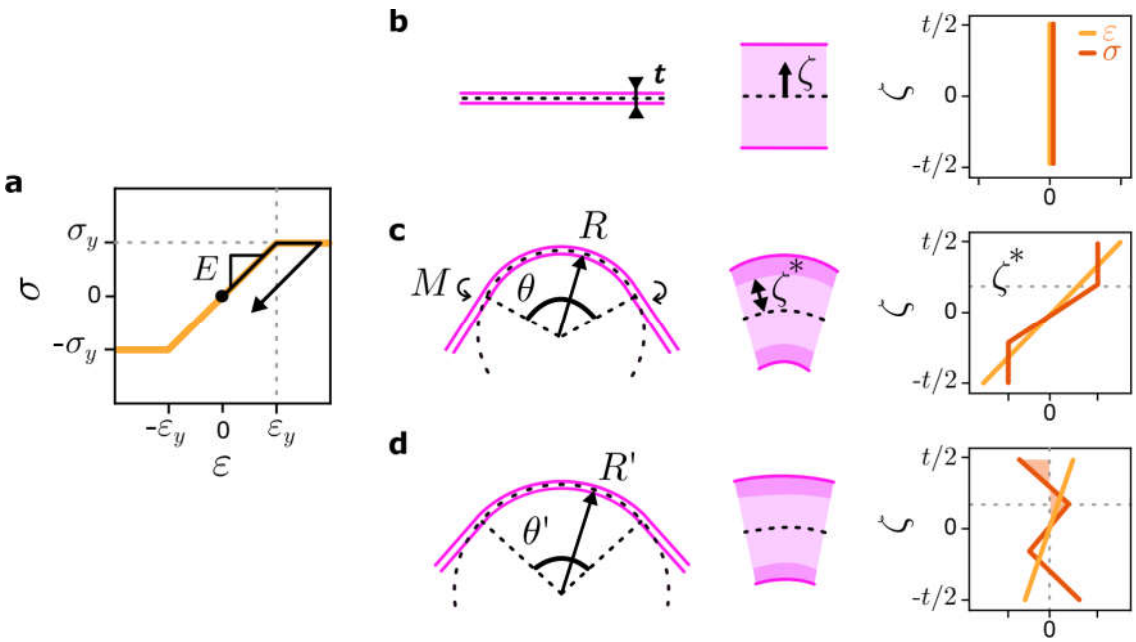

Fig. A.6.: Modelling plastic deformations of a thin film. **a**, A stress-strain relation $\sigma(\epsilon)$ (yellow line) to model plastic deformations. Small strains induce reversible stress proportional to the Young's modulus E. Above yield stress σ_y, achieved at strain ϵ_y, deformations are irreversible and the stress is constant. The stress-strain trajectory (black line) of a material under (partially) plastic deformation is illustrated. **b**, A thin flat sheet of thickness t (left) with zero initial stress or strain along the sheet's normal direction ζ, measured from the sheet's centre (middle, right). **c**, Bending the sheet to a curvature R over a length θR by applying a moment M (left) induces plastic deformations up to a thickness ζ^* (middle), above which the yield stress is exceeded (right). **d**, Removing the moment (left, middle) relaxes the sheet to a curvature R' over length $R'\theta'$. The relaxed curvature is due to residual stresses and strains in the material (right).

constitutive equations, $\sigma'(\zeta) = \sigma(\zeta) - E(\epsilon - \epsilon')$ (Fig. A.6d). Thus, we find

$$M' = W \int_{t/2}^{t/2} \sigma'(\zeta)\zeta \mathrm{d}\zeta = \frac{EW}{12}\epsilon_y \left(3t^2 - 4\zeta^{*2}\right) + \frac{EW}{12}t^3(\frac{1}{R'} - \frac{1}{R}) = 0 \ , \tag{A.31}$$

from which we obtain an expression for the spring-back in terms of the difference between imposed and relaxed curvatures $\kappa' = \frac{1}{R'}$ and $\kappa - \frac{1}{R}$:

$$\kappa' - \kappa = \frac{\epsilon_y}{t}\left(4(\frac{R\epsilon_y}{t})^2 - 3\right) \ . \tag{A.32}$$

From this equation, we see that the relaxed curvature κ' is (of course) always smaller than the imposed curvature κ: there is always some spring-back that flattens the sheet out after deformation. Note that the amount of spring-back is maximal when the yield thickness lies outside the sheet, $\zeta^* > t/2$, in which case $\kappa' - \kappa = -\kappa$: the sheet does not deform plastically. Conversely, when the yield thickness is much smaller than the sheet thickness, the spring-back decreases proportionally: $\kappa' - \kappa = -3\epsilon_y/t$.

As an aside, note that the opening angle θ and radius of curvature R before and after forming are related, since the neutral axis' length remains constant:

$$R\theta = R'\theta' \ . \tag{A.33}$$

As a back-of-the-envelope check, observations show that a visible permanent deformation is left in thin sheets of thicknesses $15, 23, 50$, and 100 µm at the following radii of curvature: $0.2, 0.5, 1$, and 2 mm. At these radii, the plasticity-free region inside the sheet has a thickness of $2\epsilon_y R$, or approximately (assuming $\epsilon_y = 0.02$) $8, 20, 40$, and 80 µm respectively. These qualitative results support the validity of our simple model.

We use the model presented above to estimate which groove geometries do not give rise to significant plastic deformation after the initial forming stage. During typical experiments, the material's yield stress may not be exceeded; in practise, this means that the groove's radius of curvature R must be much larger than the sheet's thickness t. Here, we estimate a lower bound for the ratio between R and t, above which we expect minimal yielding of the sheets during our experiments.

Consider a sheet section where an applied moment produces a positive radius of curvature R: this is the initial forming stage. A subsequent opposite moment changes the radius of curvature to zero, flattening the sheet, which models subsequent probing of the sheet. We now estimate the maximal initial radius of curvature that may be flattened without inducing extra plasticity. The initially applied strain and stress profiles are, as before,

$$\epsilon(\zeta) = \frac{\zeta}{R} \tag{A.34}$$

$$\sigma(\zeta) = \begin{cases} E\frac{\zeta}{R} & : \zeta \leq \zeta^* \\ \sigma_y & : \zeta > \zeta^* \end{cases} \ , \tag{A.35}$$

where $\zeta^* = R\sigma_y/E$ is the groove's yield thickness. Applying a flattening strain $\Delta\epsilon = -\frac{\zeta}{R}$ will lead to no yielding at the sheet surface under the following condition:

$$\frac{R}{t} > \frac{E}{4\sigma_y} \ , \tag{A.36}$$

that is, the ratio between the initial radius of curvature and sheet thickness must be larger than a quarter of the ratio between Young's modulus and yield stress. Equivalently, the yield thickness ζ^* must be larger than a quarter of the sheet thickness t.

Note that the above result is derived from a model with no temperature increase during the initial plastic deformation. If such a temperature increase is incorporated, the corresponding stress relaxation inside the sheet allows for a stronger initial curvature without plastic deformations under flattening. Therefore, our result above forms a sensible lower limit for the ratio between the forming radius and sheet thickness.

Mylar-A BoPET has a reported Young's modulus $E = 4$ GPa and a yield stress 71 MPa. Thus, we find a safe shape limit as

$$\frac{R}{t} \approx 14 \ .$$

We use BoPET sheets with thicknesses between 23 and 100 µm. The corresponding minimal radius of forming curvature to prevent plastic deformations under flattening then lies between 0.3 and 1.4 mm. Thus, we aim for groove shapes with radii of curvature above this size range.

A.8. Elasticity of groovy sheets: accordion model

We present the mathematical analysis of the accordion model discussed in section 5.4.4 here. The accordion mimics the in-plane stretching response of a groovy sheet. The accordion consists of $2N$ bars of length s^0 and stiffness k_t connected by torsional springs of stiffness k_s and rest angle ϕ^0, forming a structure with N grooves. Extension by a force F produces an elongation u; the system's Lagrangian $\mathcal{L}$ is given by

$$\mathcal{L} = -2N\frac{1}{2}k_t(\phi-\phi_0)^2 - 2N\frac{1}{2}k_s(s-s^0)^2 + F\left(u - 2N(s\cos\frac{\phi}{2} - s^0\cos\frac{\phi^0}{2})\right) , \tag{A.37}$$

where the first term on the right hand side corresponds to opening of the grooves, the second to stretching of the bars, and the third to a length constraint enforced by the Lagrange multiplier F. Minimization of the Lagrangian with respect to the fold angle ϕ, bar length s, and force F produce a system of coupled governing equations,

$$k_s(s-s^0) = -F\cos\frac{\phi}{2} \tag{A.38}$$

$$k_t(\phi-\phi^0) = F\frac{s}{2}\sin\frac{\phi}{2} \tag{A.39}$$

$$u_x = 2N(s\cos\frac{\phi}{2} - s^0\cos\frac{\phi^0}{2}) . \tag{A.40}$$

There are analytic solutions for F in terms of the extension u only in the limits of small or large displacements, as we show now.

We first consider where a crossover from small to large values of the extension takes place, by considering when the bar length changes significantly so that $\Delta s = s - s^0$ becomes large compared to s^0. With the equilibrium equations above, we express the bar length as a function of fold angle:

$$s = \frac{s^0}{2}\left(1 + \sqrt{1 - 8\frac{k_t}{(s^0)^2 k_s}\frac{\phi-\phi^0}{\tan\frac{\phi}{2}}}\right) \tag{A.41}$$

$$\frac{\Delta s}{s^0} = \frac{1}{2}\left(\sqrt{1 - 8\frac{k_t}{(s^0)^2 k_s}\frac{\phi-\phi^0}{\tan\frac{\phi}{2}}} - 1\right) . \tag{A.42}$$

Evidently, bar stretching is important if the (positive) quantity $-8\frac{k_t}{l_0^2 k_s}\frac{\phi-\phi^0}{\tan\frac{\phi}{2}}$ becomes significant compared to unity. If we consider a value of $8C$, where C is some small constant below e.g. 0.01, we find a crossover inequality:

$$\frac{\phi-\phi^0}{\tan\frac{\phi}{2}} > C\frac{(s^0)^2 k_s}{k_t} . \tag{A.43}$$

This transcendental inequality can be evaluated numerically for an accordion model of fixed stiffness and geometry. From numerical investigations, we find that the quantities ϕ and $\frac{(s^0)^2 k_s}{k_t}$ are typically of the same order of magnitude around the crossover region. Assuming that realistic estimates for the bars and hinges' stiffness scale with the real sheet's thickness $t \lesssim \mathcal{O}\left(10^{-4}\right)$ m to first and third order respectively, and that the bar

length lies around $s^0 \gtrsim \mathcal{O}\left(10^{-3}\right)$ m, we find $\frac{(s^0)^2 k_s}{k_t} \lesssim \mathcal{O}\left(10^{-2}\right)$. This in turn implies that the accordion must flatten out almost completely, $\phi \lesssim \mathcal{O}\left(10^{-2}\right)$, for bar stretching to become significant.

Secondly, we consider the below-crossover regime, where the accordion has not flattened out and bar stretching is not significant. In that case, from Eq. A.39, we find

$$\lim_{s \to s^0} u = 2Ns^0(\cos\frac{\phi}{2} - \cos\frac{\phi^0}{2}) \tag{A.44}$$

$$\lim_{s \to s^0} F = 2\kappa \frac{\phi - \phi^0}{s^0 \sin\frac{\phi}{2}} \approx -\frac{8Nk_t}{(2Ns^0 sin\frac{\phi^0}{2})^2} u + \mathcal{O}\left(u^2\right) \tag{A.45}$$

which corresponds to a rigid-bar model with infinitely large stretching stiffness. Note here that the relation between force and displacement $F(u)$ is linear for small values of u only.

Thirdly, we study the above-crossover regime, where the accordion is fully flattened and bar stretching dominates the response. With the governing equations A.38- A.40, we find

$$\lim_{\phi \to 0} u = 2N(s - s^0 \cos\frac{\phi^0}{2}) \tag{A.46}$$

$$\lim_{\phi \to 0} F = \lim_{\phi \to 0} k_s(s - s^0)/\cos\frac{\phi}{2} = k_s\left(\frac{u}{2N} - s^0(1 - \cos\frac{\phi^0}{2})\right) \tag{A.47}$$

As expected, the force increase in this regime is purely due to bar stretching.

In short, when the accordion is stretched, fold opening dominates at first. If the stiffness ratio $\frac{(s^0)^2 k_s}{k_t}$ is small, the model's response crosses over to bar stretching after the accordion is almost fully flattened.

A.9. 3D numerical sheet model

We construct a simple numerical model that mimics the behaviour of groovy sheets.

A simulated groovy sheet is shown in Fig. A.7a. The structure consists of squares of Hookean springs with unit length $l = 1$ and unit stiffness $k_s = 1$, cross-braced by diagonal springs (length $\sqrt{2}l$ and stiffness k_{sd}). The springs are connected at their corners by nodes with a torsional stiffness k_t. The square cells are arranged in an accordion-like pattern at a fold angle ϕ^0 to copy the geometry of a real groovy sheet.

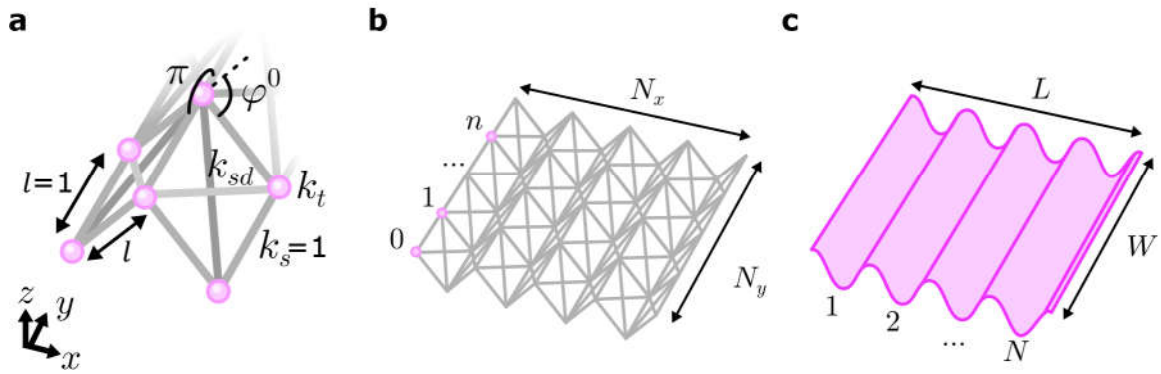

Fig. A.7.: Computational model of a groovy sheet. a, Zoom-in of the model: a square lattice (grey bars) of Hookean edge springs (length l, stiffness k_s) cross-braced by diagonal springs (length $\sqrt{2}l$, stiffness k_{sd}) and connected by nodes (pink circles) with torsional hinges (stiffness k_t, and resting angle ϕ^0 along $\hat{\boldsymbol{x}}$ and π along $\hat{\boldsymbol{y}}$). **b,** A model sheet of N_x by N_y nodes; indices n are indicated to show node numbering convention. **c,** The discrete structure aims to model to a groovy sheet with N grooves, width W, and length L.

A.9.1. Parameters

In order to mimic a groovy sheet's elastic properties, the model is assigned the following parameters. First, we rescale all lengths and stiffnesses by the square cell size and the edge spring stiffness, $l = 1$ and $k_s = 1$. Lengths are thus measured in terms of the cell size l, and energies are measured in units $k_s l^2$. One unit of energy then corresponds to the work needed to stretch an edge spring to twice its length. To ensure an isotropic in-plane response, the diagonal springs must have a stiffness $0.5k_s$. However, this value overestimates the bending energy of the facets, and we choose a slightly lower value of $k_{\mathrm{sd}} = 0.1k_s$ instead. In addition, we expect the facet bending The torsional stiffness is set to $k_t = 1 \cdot 10^{-4}$, which is the same order of magnitude as the ratio between torsional and stretching stiffness in a real sheet (see section 5.4.5). Finally, the fold angle is set to $\phi^0 = 2\mathrm{rad}$, which yields an amplitude-to-groove size ratio $A/s_\lambda \approx 0.3$, similar to that of real grooves (section 5.2.2).

A.9.2. Algorithm

The simulated sheet's mechanics are probed as follows. While all springs in the structure are initially at rest at time $t = 0$, with the nodes at position vector $\boldsymbol{Q}^{t=0}$, the springs

can be deformed by displacing selected nodes to new positions $\boldsymbol{Q}^{t=1}$. To find the sheet's final shape under the applied displacement, it is slowly relaxed to a mechanical equilibrium (that is, a minimal energy $\mathcal{E}(\boldsymbol{Q})$) via a two-step gradient descent algorithm. First, the restoring force $\nabla_Q \mathcal{E}$ on each node is calculated from the deformed sheet geometry. Second, each node is displaced in the direction of its restoring force, modified by a multiplicative *gradient descent parameter* α. These two steps are iterated: the restoring force is calculated and corresponding node displacements are applied as follows:

$$\boldsymbol{Q}^{t+1} = \boldsymbol{Q}^t - \alpha \nabla_Q \mathcal{E}(\boldsymbol{Q}^t) \ , \tag{A.48}$$

until either the system's geometrical change $|\Delta \boldsymbol{Q}|$ becomes insignificant compared to machine precision, or until a computationally reasonable maximal number of iterations (here, we choose $t_{\max} = 10^6$) is reached. We choose a gradient descent parameter $\alpha = 0.25$, maximal loops $t_{\max} = 10^6$, and cutoff geometric change $|\Delta \boldsymbol{Q}| = 10^{-15}$. After this optimization procedure, the sheet's equilibrium configuration under the imposed constraints is reached with good accuracy: the geometric change shows a steady, logarithmic decrease below $|\Delta \boldsymbol{Q}| < 10^{-6}$ (a reasonable size compared to the length and stiffness scales used) by the end of all simulations presented here.

A.9.3. Energy and forces

We briefly summarize the mathematical implementation of the sheet model and its gradient descent algorithm below. The model's configuration is fully described by the node positions $q_{i,n}$, collected in the position vector

$$\boldsymbol{Q} = (q_{x,0}, q_{y,0}, q_{z,0}, ..., q_{x,N_{\text{tot}}-1}, q_{y,N_{\text{tot}}-1}, q_{z,N_{\text{tot}}-1}) \ , \tag{A.49}$$

where n indexes the network's N_{tot} nodes and i indexes the coordinates x,y and z. A sheet with N grooves, width W and wavelength λ is thus modelled by a network of $N_x = 2N + 1$ by $N_y = \lceil W/\lambda \rceil$ nodes, totalling $N_{\text{tot}} = N_x N_y$. We adopt a standard numbering convention using indices $n_x \in [0, N_x - 1], n_y \in [0, N_y - 1]$, so that $n = n_x N_x + n_y$. With this convention, the initial position $\boldsymbol{q}_n$ of node n is given by

$$\boldsymbol{q}_n = l(n_x \cos\frac{\phi}{2}, n_y, (-1)^{n_x+1}\frac{1}{2}\sin\frac{\phi}{2}) \ . \tag{A.50}$$

Each node is connected via harmonic springs to *i)* nearest neighbours (NN) by a Hookean edge spring of length l and stiffness k_t; *ii)* next-nearest neighbours (NNN) by a diagonal Hookean spring of length $\sqrt{2}l$ and stiffness k_{td}; and *iii)* next-next-nearest neighbour (NNNN) pairs by a torsional spring of stiffness k_t with rest angle $\theta = \pi - \phi$ along $\hat{\boldsymbol{x}}$, and with rest angle π along $\hat{\boldsymbol{y}}$. Deformation of these springs costs elastic energy, which is calculated from the node positions $\boldsymbol{Q}$ as follows:

$$\mathcal{E}(Q) = \frac{1}{2}\sum_{\text{NN}} k_s (l'_{rs} - l_{rs})^2 + \frac{1}{2}\sum_{\text{NNN}} k_{sd}(l'_{rs} - l_{rs})^2 \tag{A.51}$$

$$+\frac{1}{2}\sum_{\text{NNNN}} k_t (\theta'_{rst} - \theta_{rst})^2 \ , \tag{A.52}$$

where superscripts signify deformed spring lengths and angles. Spring lengths and angles are calculated via

$$l_{rs} = |\boldsymbol{q}_r - \boldsymbol{q}_s| \tag{A.53}$$

$$\theta_{rst} = \arccos\left(\frac{(\boldsymbol{q}_r - \boldsymbol{q}_s)\cdot(\boldsymbol{q}_t - \boldsymbol{q}_s)}{l_{rs}l_{st}}\right) . \tag{A.54}$$

The force experienced by the network nodes, $\nabla_Q \mathcal{E}(Q)$, is calculated by taking the derivative of the total energy $\mathcal{E}(Q)$ with respect to each node's position $\boldsymbol{q}_n$:

$$\begin{aligned}
\frac{\partial \mathcal{E}}{\partial \boldsymbol{q}_n} = & \sum_{n\in\mathrm{NN}} k_s \left(1 - \frac{l_{ns}}{|\boldsymbol{q}_n - \boldsymbol{q}_s|}\right)(\boldsymbol{q}_n - \boldsymbol{q}_s) \\
& + \sum_{n\in\mathrm{NNN}} k_{sd} \left(1 - \frac{l_{ns}}{|\boldsymbol{q}_n - \boldsymbol{q}_s|}\right)(\boldsymbol{q}_n - \boldsymbol{q}_s) \\
& + \sum_{\mathrm{NNNN}\ nst} -k_t(\theta'_{nst} - \theta_{nst})\frac{1}{l'_{ns}}\frac{\mathrm{Rej}(\hat{\boldsymbol{u}}_{st}, \hat{\boldsymbol{u}}_{sn})}{|\mathrm{Rej}(\hat{\boldsymbol{u}}_{st}, \hat{\boldsymbol{u}}_{sn})|} \\
& + \sum_{\mathrm{NNNN}\ rnt} k_t(\theta'_{rnt} - \theta_{rnt})\left(\frac{1}{l'_{rn}}\frac{\mathrm{Rej}(\hat{\boldsymbol{u}}_{nt}, \hat{\boldsymbol{u}}_{nr})}{|\mathrm{Rej}(\hat{\boldsymbol{u}}_{nt}, \hat{\boldsymbol{u}}_{nr})|} + \frac{1}{l'_{tn}}\frac{\mathrm{Rej}(\hat{\boldsymbol{u}}_{nr}, \hat{\boldsymbol{u}}_{nt})}{|\mathrm{Rej}(\hat{\boldsymbol{u}}_{nr}, \hat{\boldsymbol{u}}_{nt})|}\right) .
\end{aligned}$$

Here, $\mathrm{Rej}(\boldsymbol{u}, \boldsymbol{v})$ indicates the vector rejection $\boldsymbol{u} - (\boldsymbol{u}\cdot\hat{\boldsymbol{v}})\hat{\boldsymbol{v}}$ of $\boldsymbol{u}$ on $\boldsymbol{v}$. Indices (r, s, t) refer to an ordered triad of next-next-nearest neighbour nodes at positions $\boldsymbol{q}_r$,$\boldsymbol{q}_s$ and $\boldsymbol{q}_t$ connected by a torsional spring with rest angle θ_{rst}. The line connecting centre node s to node r is described by $\hat{\boldsymbol{u}}_{sr} = \frac{\boldsymbol{q}_s - \boldsymbol{q}_r}{l_{rs}}$. Physically, forcible opening of the triad's rest angle results in restoring forces that bring nodes r and t away from (and node s toward) the triad's centre of mass, which produces in a fold-closing motion during gradient descent optimization. To account for orientation during the angle calculation, we check the orientation of the outer product of $\hat{\boldsymbol{u}}_{st}$ and $\hat{\boldsymbol{u}}_{sr}$ with respect to the locations of nearest neighbour nodes; a switch in alignment of this vector compared to the configuration at rest means that the complement angle to the numerical value $\arccos\cos\theta_{rst}$ must be used instead. The energy and restoring force are calculated at each time step by querying all nodes, which results in an algorithm with complexity $\mathcal{O}(N_{\mathrm{tot}})$.

A.10. Defect energetics in a 3D numerical sheet model

In section 5.6.2, Fig. 5.34, the elastic energy of an equal- and opposite-parity defect pair was calculated with the computational model outlined in section 5.4.5. Reference curves were shown that correspond to the energy needed to create the pair's two defects individually. The reference curves were obtained by calculating the energy of isolated defects, as follows.

Fig. A.8a shows the network model consisting of square cells of Hookean springs (stiffness $k_s = 1$ for cell edges and $0.1k_s$ for diagonal braces), connected by torsional springs (stiffness $k_t = 1 \cdot 10^{-4}$). The model is discrete: the smallest length scale is the cell size, $l = 1$. Fig. A.8b shows a positive (negative) defect, created at a distance w from the sheet centre, at energy cost $\mathcal{E}_+$ ($\mathcal{E}_-$). The defect's energy varies with its position, as shown in Fig. A.8c.

Defects can only be made along a groove at integer multiples of l. To ensure defect *pairs* are as symmetrically spaced as possible at a mutual distance d, the first defect is created at $w = \lceil \frac{d}{2} \rceil$; the second at $w = \lfloor \frac{d}{2} \rfloor$, where brackets $\lceil\ \rceil$ and $\lfloor\ \rfloor$ refer to rounding to the nearest larger and smaller integer, respectively. Thus, the pair energy $\mathcal{E}_{++}(d)$ should be compared to the sum of individual energies

$$\sum \mathcal{E}_+(d) = \mathcal{E}_+(\lceil \frac{d}{2} \rceil) + \mathcal{E}_+(\lfloor \frac{d}{2} \rfloor) \ , \tag{A.55}$$

and similarly, pair energy $\mathcal{E}_{+-}(d)$ must be contrasted to the sum of individual energies

$$\sum \mathcal{E}_\pm(d) = \mathcal{E}_-(\lceil \frac{d}{2} \rceil) + \mathcal{E}_+(\lfloor \frac{d}{2} \rfloor) \ . \tag{A.56}$$

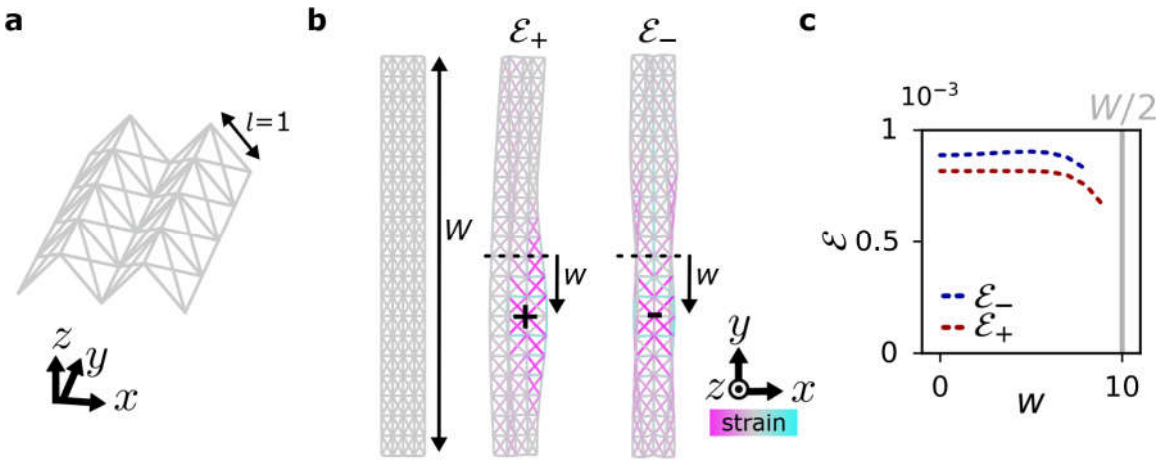

Fig. A.8.: Modelling defect energy. **a,** Zoom-in of network model consisting of Hookean springs connected by torsional hinges. Lengths are measured in terms of cell size $l = 1$. **b,** Model sheet with $N = 2$ grooves and width $W = 20$ (left). A defect is made at distance w from the sheet centre, either in a mountain fold at energy cost $\mathcal{E}_+$ (middle), or in a valley fold at energy cost $\mathcal{E}_-$ (right). Spring strain indicated for clarity (colour bar). **c,** Energies $\mathcal{E}_+$ ($\mathcal{E}_-$) as a function of w.

A.11. Calculating surface curvature

We briefly review how we compute the curvature of a groovy sheet from its three-dimensional profile, obtained via the 3D-scanning method described in section 5.3.2.

3D-scanned height profiles z on a square grid in the x, y-plane form our starting point. The height profile's discrete derivatives, $\frac{\partial z}{\partial x}$ and $\frac{\partial z}{\partial y}$, must be calculated to obtain surface curvatures. Making use of the fact that our measurements produce height profiles with a regular grid spacing, we use the following formula to calculate a five-point discrete derivative at each grid site (x_i, y_i)[174]:

$$\frac{\partial z}{\partial x}|_{x_i,y_i} \approx \frac{8(z(x_{i+1}, y_i) - z(x_{i-1}, y_i)) - (z(x_{i+2}, y_i) - z(x_{i-2}, y_i))}{6(x_{i+1} - x_{i-1})} \tag{A.57}$$

Finally, we calculate the mean and Gaussian curvatures K_m and K_g from the discrete derivatives as follows[108]:

$$K_m = \frac{(1 + (\frac{\partial z}{\partial x})^2)\frac{\partial^2 z}{\partial y^2} + (1 + (\frac{\partial z}{\partial y})^2)\frac{\partial^2 z}{\partial x^2} - 2\frac{\partial z}{\partial x}\frac{\partial z}{\partial y}\frac{\partial z}{\partial x \partial y}\frac{\partial z}{\partial y \partial x}}{2(1 + \frac{\partial z}{\partial x}^2 + \frac{\partial z}{\partial y}^2)^{3/2}} \tag{A.58}$$

$$K_g = \frac{\frac{\partial^2 z}{\partial x^2}\frac{\partial^2 z}{\partial y^2} - \frac{\partial z}{\partial x \partial y}\frac{\partial z}{\partial y \partial x}}{(1 + \frac{\partial z}{\partial x}^2 + \frac{\partial z}{\partial y}^2)^2} \tag{A.59}$$

The principal curvatures, K_1 and K_2, can be obtained via:

$$K_1 = K_m - \sqrt{K_m^2 - K_g} \tag{A.60}$$

$$K_2 = K_m + \sqrt{K_m^2 - K_g}\ . \tag{A.61}$$

The principal curvatures are the minimal and maximal values of the local 2D curvature field. As an example, Fig. A.9 shows the principal curvatures of groovy sheets with various defects and defect pairs. The presented data correspond directly to the mean and Gaussian curvatures illustrated in Fig. 5.37.

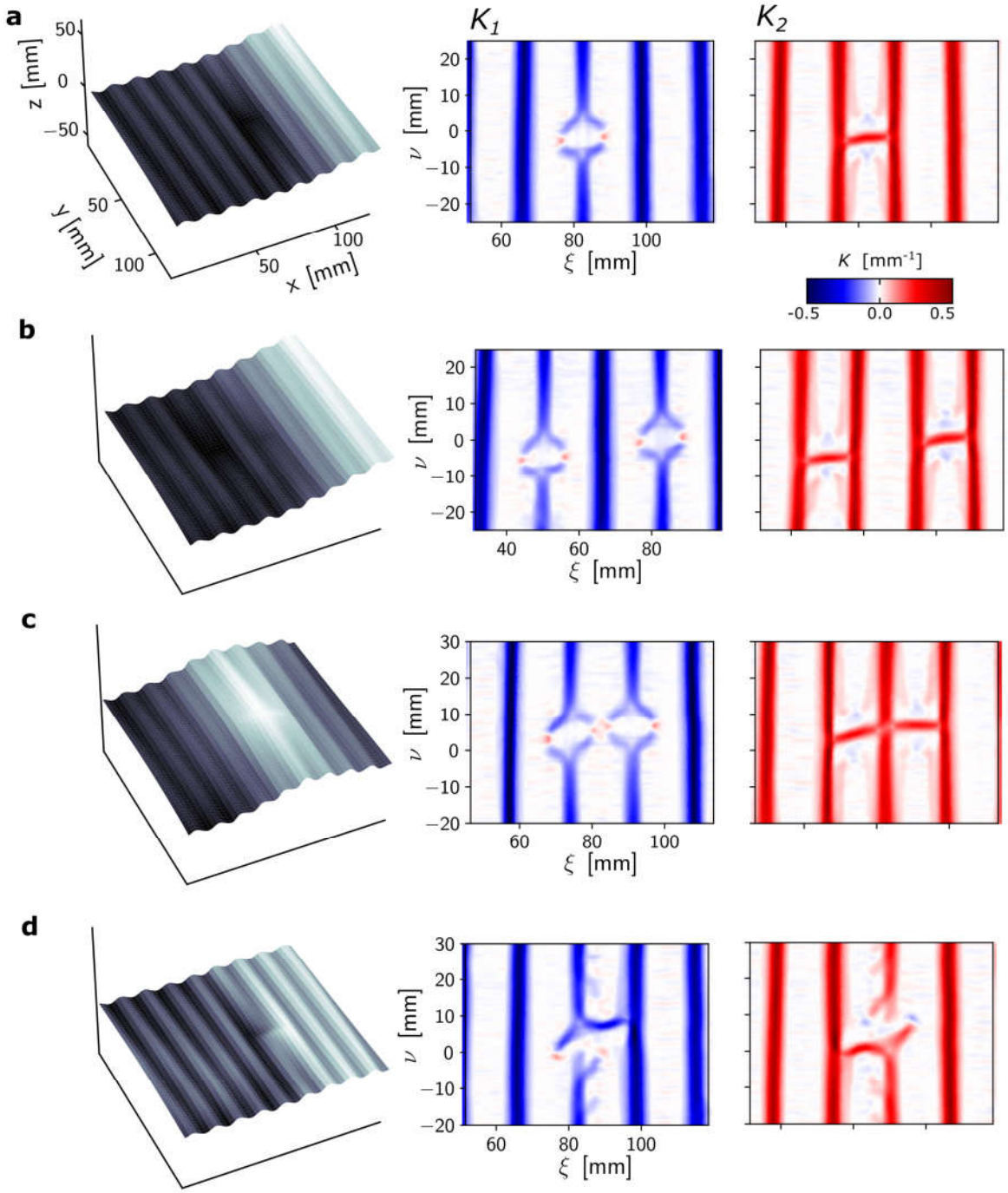

Fig. A.9.: Principal curvatures in the presence of defects. a, Principal curvatures K_1 and K_2 (right, colour bar) in a groovy sheet with one defect. The sheet has thickness $75\ \mu\mathrm{m}$, width $W = 13\ \mathrm{cm}$, and $N = 10$ grooves (left; greyscale matches height z) **b,** Curvatures for an adjacent, equal-parity defect pair at a distance of $0\ \mathrm{cm}$ along ν (and two grooves core separation along ξ). **c,** Results for an adjacent equal-parity defect pair at a core separation of one groove. **d,** Adjacent opposite-parity defect pair at half a groove core separation.

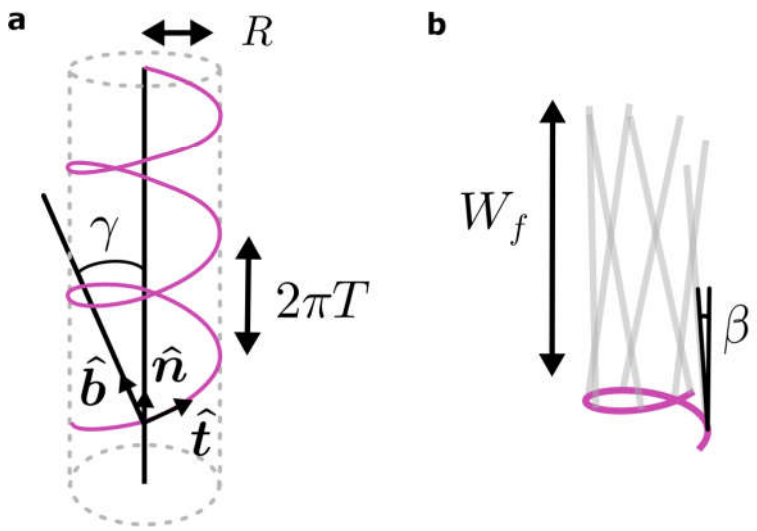

Fig. A.10.: A helix and a corresponding ruled surface. a, A helical curve (pink line) with radius R and wavelength $2\pi T$ has local coordinate frame $(\hat{\boldsymbol{t}}, \hat{\boldsymbol{n}}, \hat{\boldsymbol{b}})$. Binormal vector $\hat{\boldsymbol{b}}$ has angle $\gamma = \arctan T/R$ with respect to the cylinder axis. **b,** Ruled surface generated by drawing straight lines (grey lines) of length W_f that point away from the helical curve at a small angle β; local rule direction is given by $\cos\beta\hat{\boldsymbol{b}} + \sin\beta\hat{\boldsymbol{n}}$.

A.12. Elastic model of groovy sheets with a single scar line

Groovy sheets with a single central scar line orthogonal to their grooves roll up. If the scar's distance to the sheet edge, W_f, is large, the sheet undergoes a transition to a twisted shape (see e.g. Fig. 5.40). Here, we construct an energetic model to investigate the origin of this twisting bifurcation. Our findings suggest that this bifurcation arises from an energetic competition between deformations of the scar line and deformations in the rest of the sheet.

Intuitively, the twisting bifurcation takes place to relieve compressive strain between neighbouring grooves. Consider a rolled sheet with a single curved scar line, where grooves point away from the scar line at a small angle. The grooves form a conical cage: they are far apart at the scar line, but converge away from the scar line. At large sheet widths, the grooves must intersect to maintain the rolled sheet shape, indicating that grooves are highly compressed. In order to relieve this compression, the scar line may twist, which allows the grooves to spread (similar to a hyperboloid of one sheet, as seen in wicker chairs). We capture this intuition in a simplified model, as follows.

We assume that rolled sheets can be described as ruled surfaces, as illustrated in Fig. A.10: the scar line forms a generating curve, and grooves are modelled as straight lines that point away from the base curve. We approximate the scar line as a helical base curve $h(t)$ with constant radius R and constant wavelength $2\pi T$, which is described by the parametrization

$$\boldsymbol{h}(t) = (R\cos s, R\sin s, Tt) \ , \tag{A.62}$$

as shown in Fig. A.10a. The base curve has a local coordinate frame (the Serret-Frénet frame), which is given by the tangent, normal, and binormal vectors:

$$\hat{\boldsymbol{t}} = \frac{1}{\sqrt{R^2+T^2}}(-R\sin t, R\cos t, T) \tag{A.63}$$

$$\hat{\boldsymbol{n}} = (-\cos t, -\sin t, 0) \tag{A.64}$$

$$\hat{\boldsymbol{b}} = \frac{1}{\sqrt{R^2+T^2}}(T\sin t, -T\cos t, R)\ . \tag{A.65}$$

The angle between the binormal vector and the cylinder axis is set by $\gamma = \arctan T/R$. The helix' curvature k and torsion g are constants, calculated to be $k = |\frac{\partial t}{\partial s}| = \frac{|R|}{T^2+R^2}$ and $g = \hat{\boldsymbol{b}} \cdot |\frac{\partial n}{\partial s}| = \frac{T}{T^2+R^2}$, where $s = \sqrt{T^2+R^2}t$ is the arc length along the helix. Fig. A.10b illustrates how grooves are modelled as straight lines of length W_f, that point away from the scar line along vectors $\cos\beta\hat{\boldsymbol{b}} + \sin\beta\hat{\boldsymbol{n}}$, where β is a constant, small angle. Thus, the scar line and grooves, via radius R and twist T, and angle β and groove length W_f respectively, set the shape of the modelled sheet; we assume that these shape parameters are constant along the entirety of the sheet.

In order to mimic the elastic properties of a real sheet, we now model the energy costs for deformations of the scar line, and for distortions of the grooves.

We first consider the elasticity of the scar line. We assume that the scar line has a preferred curvature $k^0 = \frac{1}{R^0}$ and torsion $g^0 = 0$. We estimate the resting radius $R^0 \approx \frac{s_\lambda}{2\sin\theta/2} = \mathcal{O}\,(10\text{ mm})$, based on the experiments illustrated in Fig. 5.40 and the geometric argument shown in Fig. 5.41. Note that we assume here, as before, that grooves are flattened completely at the scar line to their full arc length s_λ. Deviations from the scar's resting curvature and torsion for a scar line section of length s_λ, between two grooves, are then penalized via:

$$\mathcal{E}_k \sim (k-k^0)^2 s_\lambda\ , \tag{A.66}$$

$$\mathcal{E}_g \sim (g-g^0)^2 s_\lambda\ . \tag{A.67}$$

Secondly, we assume that grooves point orthogonally away from the scar line at small preferred folding angle β^0. We estimate $\beta^0 \approx 0.2$ based on experiments (Fig. 5.40). We assume that the folding of grooves around the scar line takes place over a characteristic width comparable to the groove wavelength λ. The energy cost for deviations of the folding angle β over a scar line section of length s_λ is then modelled as

$$\mathcal{E}_\beta \sim \left(\frac{\beta-\beta^0}{\lambda}\right)^2 s_\lambda\ . \tag{A.68}$$

Lastly, we attribute an energy cost to sheet deformations away from the scar line. The sheet prefers to remain flat, its grooves parallel; thus, rolling and splaying (either in- or out-of-plane) of the grooves is penalized. We first consider how much the sheet rolls. Specifically, if the scar line has a finite radius of curvature R, the sheet's local curvature at a distance w from the scar line is given by $k(w) = \frac{R(w)}{R(w)^2+T^2}$, where $R(w) = \sqrt{(R-w\sin\beta)^2 + (w\sin\gamma\cos\beta)^2}$. The energy cost to deviate from the flat state, $k(w) =$

0, is then given by

$$\mathcal{E}_{\mathsf{roll}} \sim \int_0^{W_f} k(w)^2 \mathrm{d}w \ . \tag{A.69}$$

Finally, we assign an energy cost to splaying of the grooves. Neighbouring grooves have a preferred constant distance λ. When attached to a helical scar line, their distance d varies with the length w away from the scar line. Defining a splay strain as $\epsilon(w) = \frac{d(w)-\lambda}{\lambda}$, we find a splay energy

$$\mathcal{E}_{\mathsf{splay}} \sim \frac{1}{\lambda^2} \int_0^{W_f} \epsilon(w)^2 \mathrm{d}w \ . \tag{A.70}$$

$$\tag{A.71}$$

Here, we assume that deformations that produce splaying take place over distances of order λ. For completeness, the distance $d(w)$ between neighbouring grooves attached to a scar line with radius of curvature R and pitch $2\pi T$ is given by

$$d^2(w) = T^2 t^2 + 2(1-\cos t)(R^2 - w^2(1 - \frac{R^2}{R^2+T^2}\cos^2\beta)) - 2Rw\sin\beta \tag{A.72}$$

where t is defined via ${s_\lambda}^2 = T^2t^2 + 2R^2(1-\cos t)$. While this expression is complex, we hypothesize that the exact mathematical form of the splay strain is not crucial, as long as non-zero splay is penalized.

Thus, the total energy is given by:

$$\mathcal{E}_{\mathsf{tot}} = \mathcal{E}_k + \mathcal{E}_g + \mathcal{E}_\beta + K(\mathcal{E}_{\mathsf{splay}} + \mathcal{E}_{\mathsf{roll}}) \ , \tag{A.73}$$

where $K = 0.1$ is a factor that we choose heuristically. Experience suggests that the scar line is stiffer against deformations than the remainder of the sheet, which we take into account via K, by penalizing sheet deformations less than scar line deformations.

In short: we have defined energetic terms corresponding to deformations of the scar line and groovy sheet. We may now calculate the minimal-energy configurations of such a sheet, given the equilibrium parameters k^0, λ, s_λ, and β^0 for the scar curvature, groove wavelength, groove arc length, and scar folding angle estimated above, using the degree of freedom K to tune the relative cost of scar line versus sheet deformations.

We calculate equilibrium sheet shapes with a custom Python script, which numerically finds a local energetic minimum in the sheet shape parameter space. The resulting shapes are illustrated in Fig. A.11b for short, intermediate, and long widths. Sheet shapes match experimental observations well: narrow sheets roll, while wide sheets twist. Fig. A.11c shows how the sheet shape parameters vary with the sheet width W_f. The shape parameters show qualitative agreement with experimentally observed shapes (Fig. 5.40). First, the rolling radius R starts at an initial, nonzero value at $W_f = 0$, and subsequently increases with W_f. Experiments show that the rolling radius reaches a plateau; this feature is not reproduced by our model, which we attribute to the absence of groove bending in our theory. Secondly, the scar folding angle β lies near its equilibrium value. Lastly, the twisting parameter T undergoes a bifurcation at some critical value of W_f. The energy of the corresponding configurations increases monotonically with W_f.

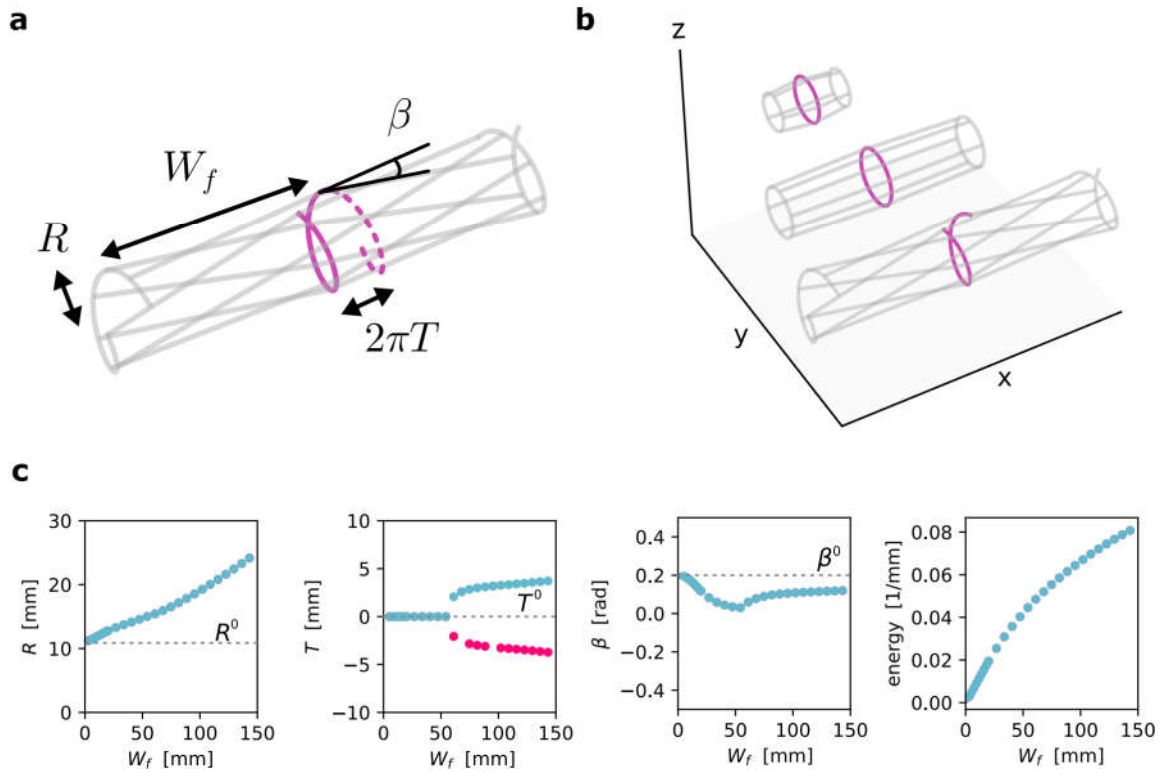

Fig. A.11.: Twisting transition in a simple elastic model. a, Sheets are modelled as ruled surfaces. The scar line forms a helical directrix (pink line) with radius of curvature R and wavelength $2\pi T$. Grooves (grey lines) are approximated as straight lines of length W_f, pointing orthogonally away from the scar line at a small angle β. **b,** Equilibrium configurations of the model at increasing edge width W_f (see text for details). Scar lines are either circular or helicoidal; grooves point away from the scar line at a small angle and exhibit twisting at large W_f. **c,** Equilibrium shape parameters and energy are shown as a function of W_f. The scar rolling radius R increases from its initial value R^0 (Eq. 5.33) with W_f. Initially, the sheet does not twist; at a critical value of W_f, a bifurcation to finite twisting is observed. The angle β at which grooves point away from the scars initially decreases with W_f, but approaches its initial value once more as W_f increases. The total equilibrium energy per sheet section increases monotonically. Initial values R^0, T^0, and β^0 are indicated by dashed grey lines throughout.

In conclusion: despite the need for manual tuning of the relative stiffnesses of scar and sheet, our model suggests that an energetic competition (between twisting deformations of the scar and splaying in the sheet) yields a twisting bifurcation at finite sheet width, consistent with experimental observations.

Bibliography

[1] J. T. B. Overvelde, T. Kloek, J. J. A. D'haen, and K. Bertoldi. "Amplifying the response of soft actuators by harnessing snap-through instabilities". In: *Proceedings of the National Academy of Sciences* 112.35 (2015), pp. 10863–10868.

[2] X. Shang, L. Liu, A. Rafsanjani, and D. Pasini. "Durable bistable auxetics made of rigid solids". In: *Journal of Materials Research* 33.3 (2018), pp. 300–308.

[3] F. Ilievski et al. "Soft Robotics for Chemists". In: *Angewandte Chemie International Edition* 50.8 (2011), pp. 1890–1895.

[4] M. Marder, R. D. Deegan, and E. Sharon. "Crumpling, buckling, and crackling: Elasticity of thin sheets". In: *Physics Today* 60.2 (2007), pp. 33–38.

[5] M. Pezzulla, G. P. Smith, P. Nardinocchi, and D. P. Holmes. "Geometry and mechanics of thin growing bilayers". In: *Soft Matter* 12.19 (2016), pp. 4435–4442.

[6] M. Pezzulla et al. "Curvature-Induced Instabilities of Shells". In: *Physical Review Letters* 120.4 (2018), p. 048002.

[7] C. Coulais et al. "Combinatorial design of textured mechanical metamaterials". In: *Nature* 535.7613 (2016), pp. 529–532.

[8] L. H. Dudte, E. Vouga, T. Tachi, and L. Mahadevan. "Programming curvature using origami tessellations". In: *Nature Materials* 15.5 (2016), pp. 583–588.

[9] C. Coulais, A. Sabbadini, F. Vink, and M. van Hecke. "Multi-step self-guided pathways for shape-changing metamaterials". In: *Nature* 561.7724 (2018), pp. 512–515.

[10] T. Frenzel, M. Kadic, and M. Wegener. "Three-dimensional mechanical metamaterials with a twist". In: *Science* 358.6366 (2017), pp. 1072–1074.

[11] F. G. Broeren, W. W. van de Sande, V. van der Wijk, and J. L. Herder. "A general method for the creation of dilational surfaces". In: *Nature Communications* 10.1 (2019).

[12] N. P. Bende et al. "Overcurvature induced multistability of linked conical frusta: how a 'bendy straw' holds its shape". In: *Soft Matter* 14.42 (2018), pp. 8636–8642.

[13] A. S. Meeussen, E. C. Oğuz, Y. Shokef, and M. L. van Hecke. "Topological defects produce exotic mechanics in complex metamaterials". In: *Nature Physics* 16.3 (2020), pp. 307–311.

[14] A. S. Meeussen, E. C. Oğuz, M. L. van Hecke, and Y. Shokef. "Response evolution of mechanical metamaterials under architectural transformations". In: *New Journal of Physics* 22.2 (2020), p. 23030.

[15] T. Mullin, S. Deschanel, K. Bertoldi, and M. C. Boyce. "Pattern transformation triggered by deformation". In: *Physical Review Letters* 99.8 (2007), pp. 1–4.

[16] B. G.-g. Chen et al. "Topological Mechanics of Origami and Kirigami". In: *Physical Review Letters* 116.13 (2016), pp. 1–5.

[17] J. Paulose, B. G.-g. Chen, and V. Vitelli. "Topological modes bound to dislocations in mechanical metamaterials". In: *Nat. Phys.* 11.2 (2015), pp. 153–156.

[18] J. Paulose, A. S. Meeussen, and V. Vitelli. "Selective buckling via states of self-stress in topological metamaterials". In: *Proceedings of the National Academy of Sciences* 112.25 (2015), pp. 7639–7644.

[19] M. Serra-Garcia et al. "Observation of a phononic quadrupole topological insulator". In: *Nature* 555.7696 (2018), pp. 342–345.

[20] B. Florijn, C. Coulais, and M. van Hecke. "Programmable Mechanical Metamaterials". In: *Physical Review Letters* 113.17 (2014), p. 175503.

[21] K. Bertoldi, V. Vitelli, J. Christensen, and M. van Hecke. "Flexible mechanical metamaterials". In: *Nature Reviews Materials* 2.11 (2017), p. 17066.

[22] S. H. Kang et al. "Complex ordered patterns in mechanical instability induced geometrically frustrated triangular cellular structures". In: *Physical Review Letters* 112.9 (2014), pp. 1–5.

[23] C. Nisoli, R. Moessner, and P. Schiffer. "Colloquium: Artificial spin ice: Designing and imaging magnetic frustration". In: *Rev. Mod. Phys.* 85.4 (2013), pp. 1473–1490.

[24] R. F. Wang et al. "Artificial 'spin ice' in a geometrically frustrated lattice of nanoscale ferromagnetic islands". In: *Nature* 439.7074 (2006), pp. 303–306.

[25] C. Castelnovo, R. Moessner, and S. L. Sondhi. "Magnetic monopoles in spin ice". In: *Nature* 451.7174 (2008), pp. 42–45.

[26] N. D. Mermin. "The topological theory of defects in ordered media". In: *Rev. Mod. Phys.* 51.3 (1979), pp. 591–648.

[27] G. P. Alexander, B. G.-g. Chen, E. A. Matsumoto, and R. D. Kamien. "Colloquium: Disclination loops, point defects, and all that in nematic liquid crystals". In: *Rev. Mod. Phys.* 84.2 (2012), pp. 497–514.

[28] J. N. Grima, A Alderson, and K. E. Evans. "Auxetic behaviour from rotating rigid units". In: *Phys. Status Solidi B* 242.3 (2005), pp. 561–575.

[29] C. Coulais, C. Kettenis, and M. Van Hecke. "A characteristic length scale causes anomalous size effects and boundary programmability in mechanical metamaterials". In: *Nature Physics* 14.1 (2018), pp. 40–44.

[30] R. M. A. Zandbergen. "On the Number of Configurations of Triangular Mechanisms". Bachelor's Thesis. Leiden University, 2016.

[31] M. J. Morrison, T. R. Nelson, and C. Nisoli. "Unhappy vertices in artificial spin ice: new degeneracies from vertex frustration". In: *New Journal of Physics* 15.4 (2013), p. 045009.

[32] I. Syôzi. "Statistics of Kagomé Lattice". In: *Prog. Theor. Phys.* 6.3 (1951), pp. 306–308.

[33] K. Kano and S. Naya. "Antiferromagnetism. The Kagomé Ising net". In: *Prog. Theor. Phys.* 10.2 (1953), pp. 158–172.

[34] K. Bertoldi, P. M. Reis, S. Willshaw, and T. Mullin. "Negative poisson's ratio behavior induced by an elastic instability". In: *Advanced Materials* 22.3 (2010), pp. 361–366.

[35] G.-W. Chern and O. Tchernyshyov. "Magnetic charge and ordering in kagome spin ice". In: *Philosophical Transactions of the Royal Society A: Mathematical, Physical and Engineering Sciences* 370.1981 (2012), pp. 5718–5737.

[36] M. O. Blunt et al. "Random Tiling and Topological Defects in a Two-Dimensional Molecular Network". In: *Science* 322.5904 (2008), pp. 1077–1081.

[37] P. A. MacMahon. *Combinatory Analysis.* Vol. 2. London: Cambridge University Press, 1916.

[38] N. J. A. Sloane. *The On-Line Encyclopedia of Integer Sequences.* 1996. URL: `https://oeis.org/A008793`.

[39] E. T. Filipov, T. Tachi, and G. H. Paulino. "Origami tubes assembled into stiff, yet reconfigurable structures and metamaterials". In: *Proceedings of the National Academy of Sciences* 112.40 (2015), pp. 12321–12326.

[40] S. Gaitanaros, S. Kyriakides, and A. M. Kraynik. "On the crushing response of random open-cell foams". In: *International Journal of Solids and Structures* 49.19-20 (2012), pp. 2733–2743.

[41] G. Toulouse. "Theory of the frustration effect in spin glasses: I". In: *Commun. Phys.* 2 (1977), pp. 115–119.

[42] A. Ortiz-Ambriz and P. Tierno. "Engineering of frustration in colloidal artificial ices realized on microfeatured grooved lattices". In: *Nature Communications* 7.1 (2016), p. 10575.

[43] C. Nisoli, V. Kapaklis, and P. Schiffer. "Deliberate exotic magnetism via frustration and topology". In: *Nature Physics* 13.3 (2017), pp. 200–203.

[44] C. L. Kane and T. C. Lubensky. "Topological boundary modes in isostatic lattices". In: *Nature Physics* 10.1 (2013), pp. 39–45.

[45] Y. Lao et al. "Classical topological order in the kinetics of artificial spin ice". In: *Nature Physics* 14.July (2018), pp. 723–728.

[46] R. J. Lang. *Origami In Action: Paper Toys That Fly, Flag, Gobble and Inflate!* St. Martin's Publishing Group, 1997.

[47] M. A. Bessa, P. Glowacki, and M. Houlder. "Bayesian Machine Learning in Metamaterial Design: Fragile Becomes Supercompressible". In: *Advanced Materials* 31.48 (2019), p. 1904845.

[48] M. P. Bendsøe and O. Sigmund. *Topology optimization: theory, methods, and applications.* New York: Springer, 2004.

[49] N. Singh and M. van Hecke. "Design of pseudo-mechanisms and multistable units for mechanical metamaterials". 2020. URL: `http://arxiv.org/abs/2003.11239`.

[50] C. Schumacher et al. "Microstructures to control elasticity in 3D printing". In: *ACM Transactions on Graphics* 34.4 (2015), 136:1–136:13.

[51] M. Kadic, T. Bückmann, R. Schittny, and M. Wegener. "Metamaterials beyond electromagnetism". In: *Reports on Progress in Physics* 76.12 (2013), p. 126501.

[52] S. sp. z o.o. *Sinterit LISA product specification.* 2014. URL: `https://www.sinterit.com/wp-content/uploads/2014/05/LISA_Specification.pdf`.

[53] S. sp. z o.o. *Sinterit Flexa Black specification.* 2014. URL: `https://www.sinterit.com/wp-content/uploads/2014/05/Flexa-Black-Specification.pdf`.

[54] S. Pellegrino and C. Calladine. "Matrix analysis of statically and kinematically indeterminate frameworks". In: *International Journal of Solids and Structures* 22.4 (1986), pp. 409–428.

[55] S. Pellegrino. "Structural computations with the singular value decomposition of the equilibrium matrix". In: *International Journal of Solids and Structures* 30.21 (1993), pp. 3025–3035.

[56] B. Audoly and Y. Pomeau. *Elasticity and Geometry.* New York: Oxford University Press, 2010.

[57] ISO. *ISO 37:2017 Rubber, vulcanized or thermoplastic — Determination of tensile stress-strain properties.* 2017.

[58] D. Mousanezhad et al. "Hierarchical honeycomb auxetic metamaterials". In: *Scientific Reports* 5 (2015), p. 18306.

[59] B. Liu et al. "Topological kinematics of origami metamaterials". In: *Nat. Phys.* 14.August (2018), pp. 1–5.

[60] X. Ning et al. "Assembly of advanced materials into 3D functional structures by methods inspired by origami and kirigami: A review". In: *Adv. Mater. Interfaces* 5.13 (2018), pp. 1–13.

[61] M. A. McEvoy and N Correll. "Materials that couple sensing, actuation, computation, and communication". In: *Science* 347.6228 (2015), p. 1261689.

[62] P. M. Reis, H. M. Jaeger, and M. Van Hecke. "Designer matter: A perspective". In: *Extreme Mech. Lett.* 5 (2015), pp. 25–29.

[63] M. Wehner et al. "An integrated design and fabrication strategy for entirely soft, autonomous robots". In: *Nature* 536.7617 (2016), pp. 451–455.

[64] J. T. Overvelde et al. "A three-dimensional actuated origami-inspired transformable metamaterial with multiple degrees of freedom". In: *Nature Communications* 7 (2016), pp. 1–8.

[65] J. L. Silverberg et al. "Using origami design principles to fold reprogrammable mechanical metamaterials". In: *Science* 345.6197 (2014), pp. 647–650.

[66] P. Celli et al. "Shape-morphing architected sheets with non-periodic cut patterns". In: *Soft Matter* 14.48 (2018), pp. 9744–9749.

[67] N. W. Bartlett et al. "A 3D-printed, functionally graded soft robot powered by combustion". In: *Science* 349.6244 (2015), pp. 161–165.

[68] R. S. Lakes. "Foam structures with a negative Poisson's ratio". In: *Science* 235 (1987), pp. 1038–1040.

[69] M. Kadic et al. "On the practicability of pentamode mechanical metamaterials". In: *Applied Physics Letters* 100.19 (2012), p. 191901.

[70] A. Libál, C. Reichhardt, and C. J. O. Reichhardt. "Realizing Colloidal Artificial Ice on Arrays of Optical Traps". In: *Physical Review Letters* 97.22 (2006), p. 228302.

[71] Y. Han et al. "Geometric frustration in buckled colloidal monolayers". In: *Nature* 456.7224 (2008), pp. 898–903.

[72] Y. Shokef, A. Souslov, and T. C. Lubensky. "Order by disorder in the antiferromagnetic Ising model on an elastic triangular lattice". In: *Proceedings of the National Academy of Sciences* 108.29 (2011), pp. 11804–11809.

[73] F. Leoni and Y. Shokef. "Attraction Controls the Inversion of Order by Disorder in Buckled Colloidal Monolayers". In: *Physical Review Letters* 118.21 (2017), p. 218002.

[74] J. N. Grima and K. E. Evans. "Auxetic behavior from rotating squares". In: *Journal of Materials Science Letters* 19.17 (2000), pp. 1563–1565.

[75] W. G. Ellenbroek, Z. Zeravcic, W. van Saarloos, and M. van Hecke. "Non-affine response: Jammed packings vs. spring networks". In: *EPL (Europhysics Letters)* 87.3 (2009), p. 34004.

[76] W. G. Ellenbroek et al. "Rigidity Loss in Disordered Systems: Three Scenarios". In: *Physical Review Letters* 114.13 (2015), p. 135501.

[77] C. P. Goodrich, A. J. Liu, and S. R. Nagel. "The Principle of Independent Bond-Level Response: Tuning by Pruning to Exploit Disorder for Global Behavior". In: *Physical Review Letters* 114.22 (2015), p. 225501.

[78] J. W. Rocks et al. "Designing allostery-inspired response in mechanical networks". In: *Proceedings of the National Academy of Sciences* 114.10 (2017), pp. 2520–2525.

[79] D. M. Sussman, C. P. Goodrich, and A. J. Liu. "Spatial structure of states of self stress in jammed systems". In: *Soft Matter* 12.17 (2016), pp. 3982–3990.

[80] D. Hexner, A. J. Liu, and S. R. Nagel. "Linking microscopic and macroscopic response in disordered solids". In: *Physical Review E* 97.6 (2018), p. 063001.

[81] D. Hexner, A. J. Liu, and S. R. Nagel. "Role of local response in manipulating the elastic properties of disordered solids by bond removal". In: *Soft Matter* 14.2 (2018), pp. 312–318.

[82] D. S. Bassett et al. "Extraction of force-chain network architecture in granular materials using community detection". In: *Soft Matter* 11.14 (2015), pp. 2731–2744.

[83] S. D. Guest and J. W. Hutchinson. "On the determinacy of repetitive structures". In: *Journal of the Mechanics and Physics of Solids* 51.3 (2003), pp. 383–391.

[84] J. C. Maxwell. "On the calculation of the equilibrium and stiffness of frames". In: *The London, Edinburgh, and Dublin Philosophical Magazine and Journal of Science* 27.182 (1864), pp. 294–299.

[85] C. R. Calladine. "Buckminster Fuller's "Tensegrity" structures and Clerk Maxwell's rules for the construction of stiff frames". In: *International Journal of Solids and Structures* 14.2 (1978), pp. 161–172.

[86] R. Connelly. "Rigidity and energy". In: *Inventiones Mathematicae* 66.1 (1982), pp. 11–33.

[87] T. C. Lubensky et al. "Phonons and elasticity in critically coordinated lattices". In: *Reports on Progress in Physics* 78.7 (2015), pp. 1–38.

[88] G. H. Wannier. "Antiferromagnetism. The Triangular Ising Net". In: *Physical Review* 79.2 (1950), pp. 357–364.

[89] E. Lerner. "Quasilocalized states of self stress in packing-derived networks". In: *European Physical Journal E* 41.8 (2018), pp. 1–8.

[90] F. S. Nascimento, L. A. Mól, W. A. Moura-Melo, and A. R. Pereira. "From confinement to deconfinement of magnetic monopoles in artificial rectangular spin ices". In: *New Journal of Physics* 14 (2012).

[91] D. Z. Rocklin et al. "Mechanical Weyl Modes in Topological Maxwell Lattices". In: *Physical Review Letters* 116.13 (2016), pp. 1–5.

[92] S. D. Guest and P. W. Fowler. "A symmetry-extended mobility rule". In: *Mechanism and Machine Theory* 40.9 (2005), pp. 1002–1014.

[93] W. Ji et al. "Theory for the density of interacting quasilocalized modes in amorphous solids". In: *Physical Review E* 99.2 (2019), pp. 1–8.

[94] S. Wijtmans and M. Lisa Manning. "Disentangling defects and sound modes in disordered solids". In: *Soft Matter* 13.34 (2017), pp. 5649–5655.

[95] J. H. Snoeijer, T. J. H. Vlugt, M. van Hecke, and W. van Saarloos. "Force Network Ensemble: A New Approach to Static Granular Matter". In: *Physical Review Letters* 92.5 (2004), p. 054302.

[96] K. Ramola and B. Chakraborty. "Stress Response of Granular Systems". In: *Journal of Statistical Physics* 169.1 (2017), pp. 1–17.

[97] G. Lois et al. "Stress correlations in granular materials: An entropic formulation". In: *Physical Review E - Statistical, Nonlinear, and Soft Matter Physics* 80.6 (2009), pp. 1–4.

[98] E. Cerda and L. Mahadevan. "Conical Surfaces and Crescent Singularities in Crumpled Sheets". In: *Physical Review Letters* 80.11 (1998), pp. 2358–2361.

[99] T. A. Witten. "Stress focusing in elastic sheets". In: *Reviews of Modern Physics* 79.2 (2007), pp. 643–675.

[100] S. Conti and F. Maggi. "Confining thin elastic sheets and folding paper". In: *Archive for Rational Mechanics and Analysis* 187.1 (2008), pp. 1–48.

[101] E. Cerda, S. Chaieb, F. Melo, and L. Mahadevan. "Conical dislocations in crumpling". In: *Nature* 401.6748 (1999), pp. 46–49.

[102] T. Jules, F. Lechenault, and M. Adda-Bedia. "Local mechanical description of an elastic fold". In: *Soft Matter* 15.7 (2019), pp. 1619–1626.

[103] H. Kobayashi, B. Kresling, and J. F. V. Vincent. "The geometry of unfolding tree leaves". In: *Proceedings of the Royal Society of London. Series B: Biological Sciences* 265.1391 (1998), pp. 147–154.

[104] E. Couturier, S. Courrech du Pont, and S. Douady. "A Global Regulation Inducing the Shape of Growing Folded Leaves". In: *PLoS ONE* 4.11 (2009). Ed. by S. Humphries, e7968.

[105] K. A. Seffen. "Compliant shell mechanisms". In: *Philosophical Transactions of the Royal Society A: Mathematical, Physical and Engineering Sciences* 370.1965 (2012), pp. 2010–2026.

[106] V. Brunck, F. Lechenault, A. Reid, and M. Adda-Bedia. "Elastic theory of origami-based metamaterials". In: *Physical Review E - Statistical, Nonlinear, and Soft Matter Physics* 93.3 (2016), pp. 1–14.

[107] A. Norman, K. Seffen, and S. Guest. "Morphing of curved corrugated shells". In: *International Journal of Solids and Structures* 46.7-8 (2009), pp. 1624–1633.

[108] B. Audoly and Y. Pomeau. *Elasticity and Geometry.* New York: Oxford University Press, 2010.

[109] K. F. Gauss. *General Investigations of Curved Surfaces.* Ed. by P. Pesic. Princeton: Princeton University Library, 1992.

[110] V Pini et al. "How two-dimensional bending can extraordinarily stiffen thin sheets". In: *Scientific Reports* 6.1 (2016), p. 29627.

[111] E. Kebadze, S. D. Guest, and S. Pellegrino. "Bistable prestressed shell structures". In: *International Journal of Solids and Structures* 41.11-12 (2004), pp. 2801–2820.

[112] M. Pignataro, N. Rizzi, and A. Luongo. *Stability, bifurcation and postcritical behaviour of elastic structures.* Amsterdam: Elsevier Science Publishers B.V., 1991.

[113] N. Oppenheimer and T. A. Witten. "Shapeable sheet without plastic deformation". In: *Physical Review E - Statistical, Nonlinear, and Soft Matter Physics* 92.5 (2015), pp. 1–14.

[114] J. L. Silverberg et al. "Origami structures with a critical transition to bistability arising from hidden degrees of freedom." In: *Nat. Mater.* 14.4 (2015), pp. 389–393.

[115] S. Waitukaitis, R. Menaut, B. G.-g. Chen, and M. van Hecke. "Origami Multistability: From Single Vertices to Metasheets". In: *Physical Review Letters* 114.5 (2015), p. 055503.

[116] A. Pandey, D. E. Moulton, D. Vella, and D. P. Holmes. "Dynamics of snapping beams and jumping poppers". In: *EPL (Europhysics Letters)* 105.2 (2014), p. 24001.

[117] K. Seffen, B Wang, and S. Guest. "Folded orthotropic tape-springs". In: *Journal of the Mechanics and Physics of Solids* 123 (2019), pp. 138–148.

[118] A. Norman, K. Seffen, and S. Guest. "Multistable corrugated shells". In: *Proceedings of the Royal Society A: Mathematical, Physical and Engineering Sciences* 464.2095 (2008), pp. 1653–1672.

[119] M. G. Walker. "Mechanics of generically creased disks". In: *Physical Review E* 101.4 (2020), p. 43001.

[120] Y. Forterre, J. M. Skotheim, J. Dumals, and L. Mahadevan. "How the Venus flytrap snaps". In: *Nature* 433.7024 (2005), pp. 421–425.

[121] T. Savin et al. "On the growth and form of the gut". In: *Nature* 476.7358 (2011), pp. 57–62.

[122] H. Liang and L. Mahadevan. "Growth, geometry, and mechanics of a blooming lily". In: *Proceedings of the National Academy of Sciences* 108.14 (2011), pp. 5516–5521.

[123] A. Vaziri. "Mechanics of highly deformed elastic shells". In: *Thin-Walled Structures* 47.6-7 (2009), pp. 692–700.

[124] A. Nasto et al. "Localization of deformation in thin shells under indentation". In: *Soft Matter* 9.29 (2013), p. 6796.

[125] M. Das, A. Vaziri, A. Kudrolli, and L. Mahadevan. "Curvature Condensation and Bifurcation in an Elastic Shell". In: *Physical Review Letters* 98.1 (2007), p. 014301.

[126] L. Walsh, R. Meza, and E. Hamm. "Weakening of a thin shell structure by annihilating singularities". In: *Journal of Physics D: Applied Physics* 44.23 (2011), p. 232002.

[127] N. P. Bende et al. "Geometrically controlled snapping transitions in shells with curved creases". In: *Proceedings of the National Academy of Sciences of the United States of America* 112.36 (2015), pp. 11175–11180.

[128] J. P. Udani and A. F. Arrieta. "Programmable mechanical metastructures from locally bistable domes". In: *Extreme Mechanics Letters* (2020), p. 101081.

[129] T. Tallinen, J. Ojajärvi, J. A. Åström, and J. Timonen. "Scaling Behavior in Non-Hookean Compression of Thin-Walled Structures". In: *Physical Review Letters* 105.6 (2010), p. 066102.

[130] E. Efrati, E. Sharon, and R. Kupferman. "Elastic theory of unconstrained non-Euclidean plates". In: *Journal of the Mechanics and Physics of Solids* 57.4 (2009), pp. 762–775.

[131] M. Lewicka, L. Mahadevan, and M. R. Pakzad. "The Föppl-von Kármán equations for plates with incompatible strains". In: *Proceedings of the Royal Society A: Mathematical, Physical and Engineering Sciences* 467.2126 (2011), pp. 402–426.

[132] T. J. Healey, Q. Li, and R.-B. Cheng. "Wrinkling Behavior of Highly Stretched Rectangular Elastic Films via Parametric Global Bifurcation". In: *Journal of Nonlinear Science* 23.5 (2013), pp. 777–805.

[133] M. A. Dias and B. Audoly. ""Wunderlich, Meet Kirchhoff": A General and Unified Description of Elastic Ribbons and Thin Rods". In: *Journal of Elasticity* 119.1-2 (2015), pp. 49–66.

[134] A. P. Korte, E. L. Starostin, and G. H. M. van der Heijden. "Triangular buckling patterns of twisted inextensible strips". In: *Proceedings of the Royal Society A: Mathematical, Physical and Engineering Sciences* 467.2125 (2011), pp. 285–303.

[135] E. Fried. *The Mechanics of Ribbons and Möbius Bands.* Ed. by R. Fosdick and E. Fried. Dordrecht: Springer Netherlands, 2016, pp. 35–48.

[136] M. A. Dias and B. Audoly. "A non-linear rod model for folded elastic strips". In: *Journal of the Mechanics and Physics of Solids* 62.1 (2014), pp. 57–80.

[137] H. Olbermann. "The shape of low energy configurations of a thin elastic sheet with a single disclination". In: *Analysis & PDE* 11.5 (2018), pp. 1285–1302.

[138] K. A. Seffen. "Fundamental conical defects: The d-cone, its e-cone, and its p-cone". In: *Physical Review E* 94.1 (2016), p. 013002.

[139] J. Genzer and J. Groenewold. "Soft matter with hard skin: From skin wrinkles to templating and material characterization". In: *Soft Matter* 2.4 (2006), p. 310.

[140] H. Vandeparre et al. "Wrinkling hierarchy in constrained thin sheets from suspended graphene to curtains". In: *Physical Review Letters* 106.22 (2011), pp. 2–5.

[141] J. Hure, B. Roman, and J. Bico. "Stamping and Wrinkling of Elastic Plates". In: *Physical Review Letters* 109.5 (2012), p. 054302.

[142] B. Li, Y.-P. Cao, X.-Q. Feng, and H. Gao. "Mechanics of morphological instabilities and surface wrinkling in soft materials: a review". In: *Soft Matter* 8.21 (2012), p. 5728.

[143] E. Sharon, B. Roman, and H. L. Swinney. "Geometrically driven wrinkling observed in free plastic sheets and leaves". In: *Physical Review E - Statistical, Nonlinear, and Soft Matter Physics* 75.4 (2007), pp. 1–7.

[144] H. Liang and L Mahadevan. "The shape of a long leaf". In: *Proceedings of the National Academy of Sciences* 106.52 (2009), pp. 22049–22054.

[145] W. H. Frey. "Modeling buckled developable surfaces by triangulation". In: *Computer-Aided Design* 36.4 (2004), pp. 299–313.

[146] Z. Y. Wei et al. "Geometric Mechanics of Periodic Pleated Origami". In: *Physical Review Letters* 110.21 (2013), p. 215501.

[147] B. L. Wardle. "Impact and Quasi-Static Response of Cylindrical Composite Shells". In: (1992).

[148] K. A. Seffen. "On the Behavior of Folded Tape-Springs". In: *Journal of Applied Mechanics* 68.3 (2001), pp. 369–375.

[149] M. G. Walker and K. A. Seffen. "On the shape of bistable creased strips". In: *Thin-Walled Structures* 124 (2018), pp. 538–545.

[150] DuPont Teijin Films. *Mylar ® polyester film: physical-thermal properties.* 2003.

[151] S. P. Timoshenko. *History of strength of materials.* New York: Dover Publications, Inc., 1983.

[152] Zhermack S.p.A. *Elite Double vinylpolysiloxane (addition silicone) duplicating material.* 2016.

[153] A. N. Gent. "On the Relation between Indentation Hardness and Young's Modulus". In: *Rubber Chemistry and Technology* 31.4 (1958), pp. 896–906.

[154] D. G. Van Velzen. "Elastic Moduli of Smooth and Corrugated Thin Silicone Rubber". MSc thesis. Leiden University, 2017.

[155] S. Van der Jeught, J. A. M. Soons, and J. J. J. Dirckx. "Real-time microscopic phase-shifting profilometry". In: *Applied Optics* 54.15 (2015), p. 4953.

[156] S. Wildeman. "Real-time quantitative Schlieren imaging by fast Fourier demodulation of a checkered backdrop". In: *Experiments in Fluids* 59.6 (2018), p. 97.

[157] P. S. Huang. "Novel method for structured light system calibration". In: *Optical Engineering* 45.8 (2006), p. 083601.

[158] J. E. Gordon. *Structures , or Why Things Don't Fall Down.* Cambridge: Da Capo Press, 2003.

[159] T. G. Hicks. *Civil Engineering Formulas.* 2nd ed. New York: McGraw-Hill, 2010.

[160] F. Lechenault, B. Thiria, and M. Adda-Bedia. "Mechanical Response of a Creased Sheet". In: *Physical Review Letters* 112.24 (2014), p. 244301.

[161] Wolfram Research Inc. *Mathematica, version 11.2.* Champaign, IL, 2020.

[162] C. D. Santangelo. "Nambu–Goldstone modes and diffuse deformations in elastic shells". In: *Soft Matter* 9.34 (2013), p. 8246.

[163] A. Vaziri and L Mahadevan. "Localized and extended deformations of elastic shells". In: *Proceedings of the National Academy of Sciences* 105.23 (2008), pp. 7913–7918.

[164] R. D. Schroll, E. Katifori, and B. Davidovitch. "Elastic Building Blocks for Confined Sheets". In: *Physical Review Letters* 106.7 (2011), p. 074301.

[165] B. Roman and A. Pocheau. "Stress Defocusing in Anisotropic Compaction of Thin Sheets". In: *Physical Review Letters* 108.7 (2012), p. 074301.

[166] T. Barois, L. Tadrist, C. Quilliet, and Y. Forterre. "How a Curved Elastic Strip Opens". In: *Physical Review Letters* 113.21 (2014), p. 214301.

[167] C. Keplinger et al. "Stretchable, transparent, ionic conductors". In: *Science* 341.6149 (2013), pp. 984–987.

[168] J.-Y. Sun et al. "Highly stretchable and tough hydrogels". In: *Nature* 489.7414 (2012), pp. 133–136.

[169] DuPont Teijin Films. *Mylar ® polyester film: introduction.* 2003.

[170] ASTM. "D 882: Standard Test Method for Tensile Properties of Thin Plastic Sheeting". In: *Astm* 14 (2002), pp. 1–10.

[171] Instron. *Instron 3360 Series.* 2015.

[172] Instron. *Instron 2530 Series Static Load Cells.* 2016.

[173] University of Cambridge. *DoITPoMS: bending and torsion of beams.* 2008. URL: `https://www.doitpoms.ac.uk/tlplib/beam_bending/index.php`.

[174] B. Fornberg. "Generation of finite difference formulas on arbitrarily spaced grids". In: *Mathematics of Computation* 51.184 (1988), pp. 699–699.

Summary

The research presented in this dissertation spans several years of work that I've done at AMOLF and Leiden University, where I've been active in the field of material design. Collectively, our community works to design mechanical structures. These structures have a mechanical function, just like mattress foam or door hinges do. We invent special architectures and fabricate prototypes with various techniques, from casting rubber in 3D-printed moulds, to laser-cutting foam and thermoforming plastic. The goal is to create novel materials that function differently than traditional ones do: concrete, wood, solid rubber. The unusual behaviour of the structures we design comes from their internal geometry, rather than from the basic stuff they are made of. This idea is certainly not new: knitted fabric is definitely different from a skein of yarn, which is why we wrap ourselves in scarves instead of thread. The underlying idea, then, is that novel structural designs can be made out of whatever material is on hand; it just needs to be cast into the right shape.

But inventing a material that does a specific job (and does it well) is not easy. A huge number of design strategies exist. Many designs (brick-laying, knitting, and weaving patterns, for example) have been invented centuries or even millennia ago, and continue to be passed on through the years. But (historically) recently, our quickly industrializing world has seen enormous developments in materials science, engineering, rapid prototyping and computation. And along with this has come an explosion of new material design methods: biology-inspired approaches, genetic algorithms, topology optimization, and other mouthfuls. Each technique has its own benefits and drawbacks. There is no unified approach to material design. What we have instead is a rich and growing variety of tactics available to those of us who want to design functional structures.

In this dissertation, I present material design strategies that revolve around defects. Errors, flaws and imperfections in mechanical structures are usually better avoided. But from one (perhaps rather dry) point of view, we can reframe flaws: they are manifestations of underlying physical principles. In and of themselves, they are neither good nor bad: they are. Understanding their origins helps us avoid mechanical failure, from broken windows to buckled grain silos. But it also allows us to *use* flaws, on purpose, to create new materials with novel and useful behaviour.

I use two kinds of mechanical flaws to create materials with new properties: topological defects, and snap-through instabilities.

Chapters 2 to 4 of this dissertation deal with the first design strategy, using topological defects. In Chapter 2, we start by designing the basic structure: a flat material, made out of slender rods connected by flexible hinges. At first, the structure is soft and deforms easily when squeezed. But then, by switching the positions of a few rods, we introduce a topological error. Topology, here, refers to how the structure's rods are interconnected: the right way (which produces a soft material) or the wrong way (which gets us a topological defect). It turns out that this topological error leads to new behaviour, which we

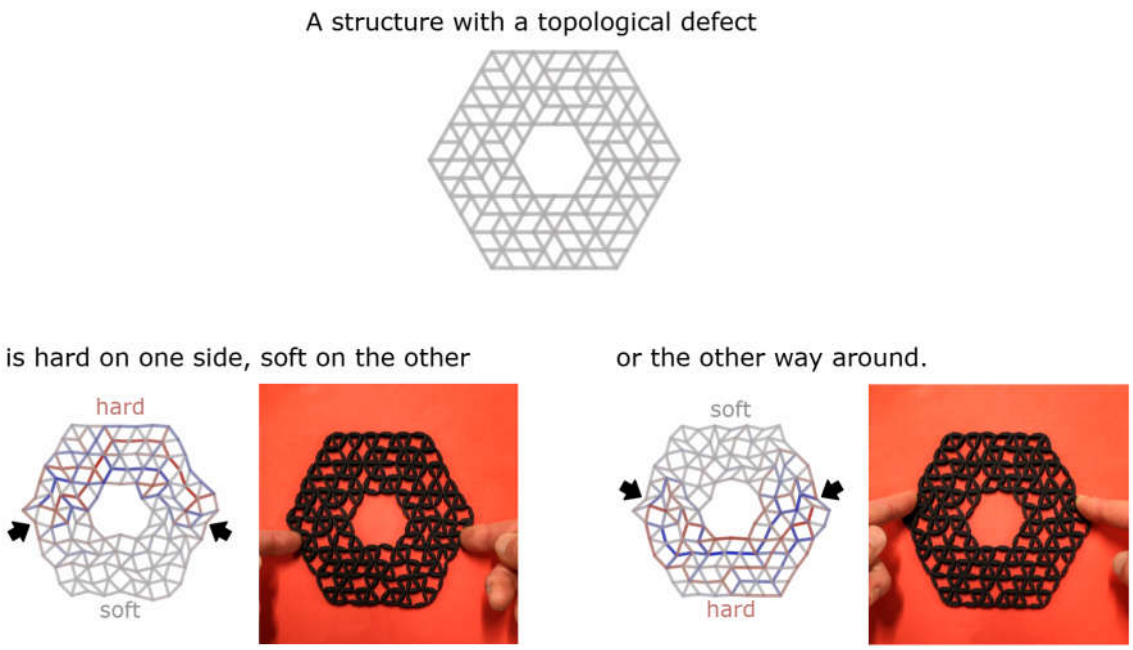

Fig. S1.: Topological defects control where a material is hard or soft, depending on how it is pushed.

explore in Chapter 3. There, we show that materials with a topological error have adaptive regions that are soft or stiff; where these regions are depends on how the structure is squeezed. In Chapter 4, we dive into the mathematical nitty-gritty, and describe what exactly happens mechanically when we switch those few rods. Figure S1 summarizes the overall result: topological flaws allow us to design material that can be both soft and hard, depending on where it is pushed.

Finally, Chapter 5 introduces a material that shape-shifts via snap-through defects. The basic idea behind this shape-morphing behaviour is illustrated in Figure S2. Everything starts with a thin sheet with parallel grooves, like miniature corrugated roofing: a groovy sheet. The curved shape of the grooves is important here: because of its shape, each groove can be snapped through with a pop. This effect is also seen in very long tape measures, which can click into a folded shape. Crucially (and unlike tape measures) the grooves in large sheets *stay* snapped, bending and curving into a new, three-dimensional shape. What shape the sheet takes on depends on where the grooves are popped through: different popping patterns lead to different shapes. Intuitively, all this snapping action might break up the material, but as long as the sheet is thin enough, it stays intact. That means that groovy sheets are true shape-shifters: because they can handle these snap-through defects, groovy sheets can be popped, unpopped, and re-popped at will.

In short: the research reported in this dissertation shows how imperfections can be used to create functional mechanical structures. I hope that this work will find its place in the ever-growing field of material design.

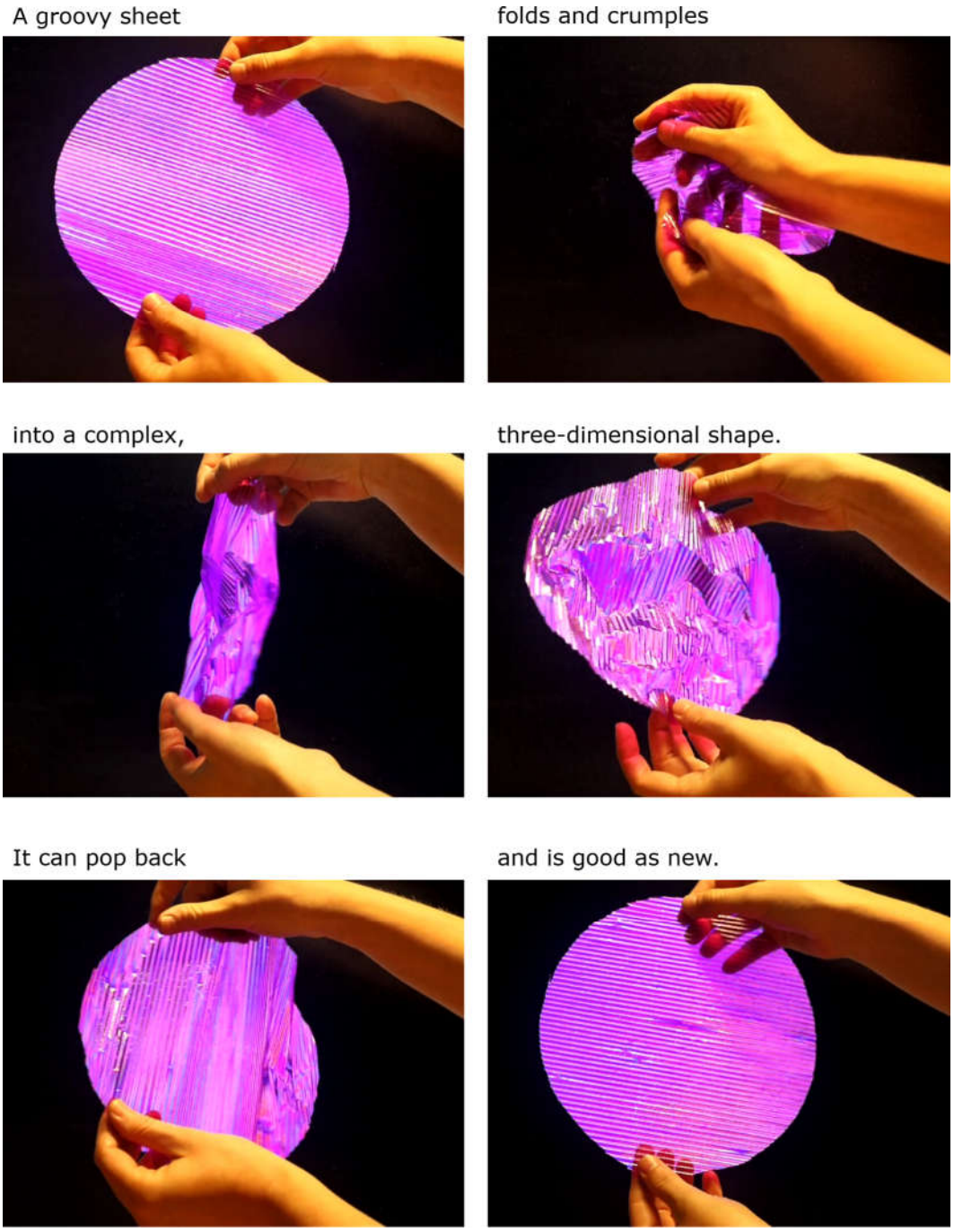

Fig. S2.: Flat groovy sheets snap back and forth into complex three-dimensional shapes.

Samenvatting

Het onderzoek dat in deze dissertatie beschreven staat is het resultaat van enkele jaren werk bij AMOLF en de Universiteit Leiden, waar ik met het ontwerpen van nieuwe materialen bezig ben geweest. Onze onderzoeksgemeenschap werkt met elkaar aan het ontwerpen van mechanische structuren. Zulke structuren hebben een mechanische functie, net als matrasschuim en deurscharnieren dat hebben. We vinden speciale vormen en architecturen uit, en maken daar prototypes van met allerlei technieken: rubber gieten in 3D-geprinte vormen, schuim lasersnijden en thermovormen met plastic. Het doel is om nieuwe materialen te maken, die zich anders gedragen dan de traditionele varianten: beton, hout, rubber.

De reden dat onze structuren anders zijn dan anders is hun interne constructie, niet de grondstof waar ze van gemaakt zijn. Dit is geen nieuw idee: gebreide stof, bijvoorbeeld, is nogal anders dan een bolletje garen (daarom dragen we ook sjaals in plaats van strengen draad). Het onderliggende idee is dus dat nieuwe materiaal-ontwerpen gemaakt kunnen worden van een willekeurige grondstof- op voorwaarde dat ze in de juiste vorm worden gegoten.

Maar het is niet gemakkelijk om een nieuw materiaal uit te vinden dat een specifieke functie vervult (en dat ook goed doet). Er zijn massa's aan strategieën. Door de eeuwen en zelfs millenia heen zijn er talloze ontwerpen bedacht—bijvoorbeeld metselverbanden of brei- en weefpatronen—die nog steeds van generatie tot generatie worden overgedragen. Daarnaast hebben er relatief kort geleden enorme ontwikkelingen plaatsgevonden in de materiaalkunde, vormgevingstechniek, en informatica. En met deze opmars kwam een explosie aan ontwerpmethodes: tactieken gebaseerd op de natuur, genetische algoritmes, topologie-optimalisering, en nog meer van zulke dure woorden. Elke methode heeft zijn eigen voor- en nadelen. Er is geen standaard aanpak voor het ontwerpen van structuren. Wat we wél hebben is een rijke keuze aan tactieken voor wie een nuttig materiaal wil ontwerpen.

In deze dissertatie laat ik een nieuw soort ontwerptactiek zien, die draait om imperfecties. Afwijkingen, defecten, en onvolkomenheden in mechanische structuren kun je normaal gesproken beter vermijden. Maar we kunnen imperfecties ook vanuit een ander (wel wat formeel) perspectief bekijken: ze zijn maar verschijnselen die voortkomen uit onderliggende natuurkundige principes. Van zichzelf zijn ze niet goed of slecht: ze zijn. Als we begrijpen waar ze precies vandaan komen, kunnen we mechanische schade vermijden, van gebroken ruiten tot ingestortte graansilo's. Maar met dat begrip kunnen we afwijkingen ook *gebruiken*, expres, om nieuwe materialen te maken met buitengewoon en nuttig gedrag.

Ik gebruik in deze dissertatie twee soorten mechanische imperfecties om materialen te maken met nieuwe eigenschappen: topologische imperfecties, en doorknik-instabiliteiten.

Hoodstuk 2 tot en met 4 van dit proefschrift gaan over de eerste ontwerptactiek, met

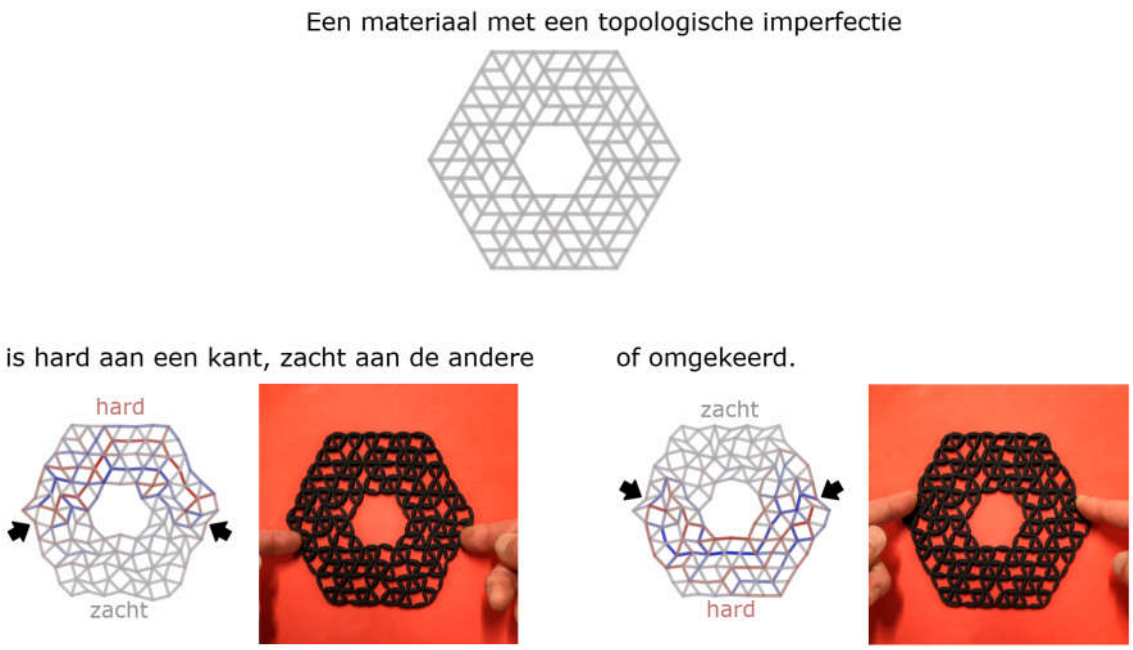

Fig. S3.: Topologische imperfecties maken een materiaal plaatselijk zacht of hard. Waar de zachte en harde plekken zitten hang af van hoe de structuur wordt ingeduwd.

topologische imperfecties. We beginnen in hoofdstuk 2 met het ontwerpen van een basisstructuur: een vlak materiaal, gemaakt van dunne staafjes die aan elkaar zitten met flexibele scharnieren. Die basisstructuur is zacht, en vervormt makkelijk als hij ingeknepen wordt. Maar dan, door het verplaatsen van een paar staafjes, maken we een *topologische imperfectie*. Topologie verwijst hier naar hoe de staafjes in het materiaal aan elkaar zitten: op de goede manier (dat leidt tot een zacht materiaal), of de verkeerde manier (dat zorgt voor een topologische imperfectie). Uit ons onderzoek blijkt dat deze topologische afwijking nieuw mechanisch gedrag veroorzaakt, en dat onderzoeken we in hoofdstuk 3. Daar laten we zien dat materialen met zo'n afwijking adaptieve harde en zachte zones vertonen. Waar die stevige en zachte plekken precies zitten kan je manipuleren; dat hangt namelijk af van hoe het materiaal ingeduwd wordt. In hoofdstuk 4 duiken we de wiskunde in, om te beschrijven wat er precies gebeurt op mechanisch niveau, als die paar staafjes verplaatst worden. Figuur S3 vat de uitkomst samen: met topologische imperfecties kunnen we materialen ontwerpen die hard én zacht zijn, afhankelijk van waar je ze induwt.

Tot slot presenteren we in hoofdstuk 5 een nieuw soort structuur, die van vorm verandert door door te knikken. Het idee achter dit metamorfose-gedrag staat in figuur S4 uitgelegd. Het begint allemaal met een dun stuk gegolfd plastic, een soort miniatuurversie van golfplaat: een ribbelvel. De ronde vorm van de ribbels is hier belangrijk, want door die vorm kan elke ribbel doorgeknikt worden door erop te duwen. Lange rolmaten doen iets soortgelijks: ze klikken om tot een gevouwen vorm. Maar, anders dan in een rolmaat, *blijven* de ribbels in grote stukken ribbelvel doorgeknikt, en vouwen en rollen ze op tot een nieuwe, driedimensionale vorm. Welke vorm dat precies is, hangt af van waar de ribbels zijn doorgeknikt: met verschillende knikpatronen krijg je verschillende vormen. Instinctief zou je verwachten dat het plastic breekt door al dat geknik; maar zolang het vel dun genoeg is, blijft het heel. Dat betekent dat ribbelvellen echte vormbare

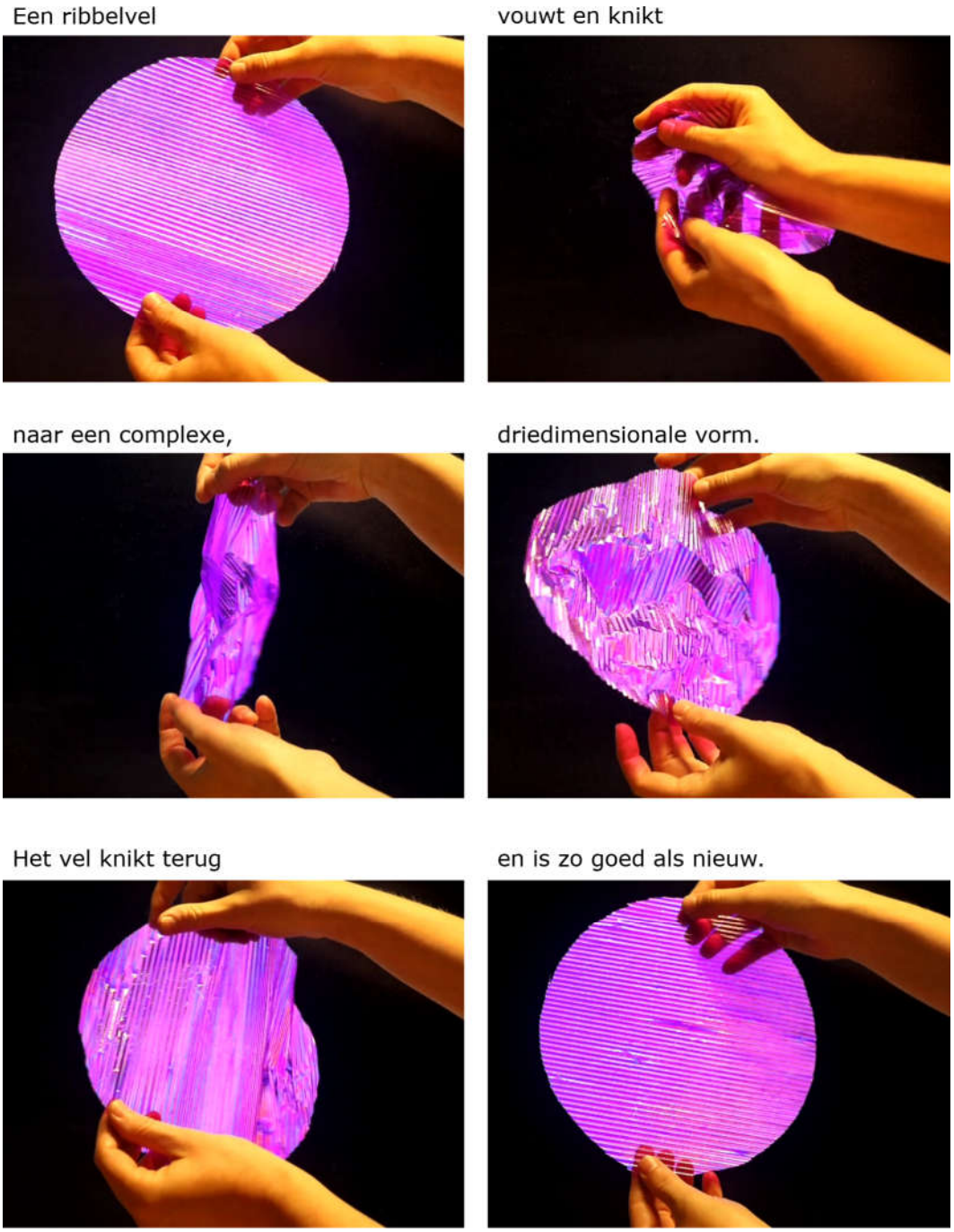

Fig. S4.: Vlakke ribbelvellen knikken door, en vormen zich zo om tot ingewikkelde, driedimensionale vormen.

materialen zijn: omdat ze om kunnen gaan met al dat doorknikken, kunnen ribbelvellen steeds weer om-, terug-, en hergevormd worden.

Kortom: in deze dissertatie laten we zien hoe imperfecties gebruikt kunnen worden om nuttige mechanische structuren te ontwerpen. Ik hoop dat dit werk zijn plek vindt in het zich steeds verder ontwikkelende veld van de materiaalkunde.

Publications

Publications treated in this dissertation

A.S. Meeussen and M. van Hecke. "Reversible shape-morphing sheets via snap-through instabilities". Manuscript in preparation (2021).

A.S. Meeussen, E.C.O. Oğuz, M. van Hecke, and Y. Shokef. "Response evolution of mechanical metamaterials under architectural transformations". In: *New Journal of Physics* 22 (2020), p. 023030.

A.S. Meeussen, E.C.O. Oğuz, Y. Shokef, and M. van Hecke ."Topological defects produce exotic mechanics in complex metamaterials". In: *Nature Physics* 2 (2020), pp. 1745-2481.

Other

A.S. Meeussen, J. Paulose, and V. Vitelli. "Geared topological metamaterials with tunable mechanical stability". In: *Phys Rev. X* 6 (2016), p. 041029.

J. Paulose, A.S. Meeussen, and V. Vitelli. "Selective buckling via states of self-stress in topological metamaterials". In: *Proc. Natl. Acad. Sci. USA* 112 (2015), pp. 7639-7644.

F. van Beijnum, A.S. Meeussen, C. Rétif, and M.P. van Exter. "Rayleigh scattering of surface plasmons by sub-wavelength holes". In: *Opt. Express 22* (2014), pp. 10317-10331 .

Curriculum Vitae

About

name	Anne Sophia Meeussen
born	12 August 1990, Rotterdam, The Netherlands
contact	a.meeussen@gmail.com +31613994495
orcID	orcid.org/0000-0003-1243-0318

Career

2021-	Postdoctoral researcher of Materials Design, Harvard University (Cambridge, USA) Supervision: Prof. dr. Katia Bertoldi.
2016-2021	PhD Experimental Physics, Leiden University and AMOLF (Leiden and Amsterdam, Netherlands) Thesis: design of reshapeable and topological mechanical metamaterials. Supervision: Prof. dr. Martin van Hecke.

Education

2013-2016	MSc Research in Theoretical Physics, Leiden University (cum laude) Thesis: developing topological design principles for mechanical metamaterials. Supervision: Prof. dr. Vincenzo Vitelli and Dr. Jayson Paulose.
2009-2013	BSc Physics, Leiden University (cum laude) Thesis: investigating the behavior of surface plasmon polaritons in randomly porous dielectric media. Supervision: Prof. dr. Martin van Exter and MSc Frerik van Beijnum.
2002-2008	Gymnasium, Krimpenerwaard College Krimpen aan den IJssel Focus: natural sciences, engineering and health.

Thank you

My gratitude goes to AMOLF and Leiden University, for providing the means to perform the work presented in this dissertation. A special thanks goes out to all supporting personnel at these institutions, without whose valuable work our research would not have been possible. In particular, many thanks to Danielle Duijn and Wouter Harmsen for administrative and to Dion Ursem and Jeroen Mesman-Vergeer for technical support.

A heartfelt thanks to Martin van Hecke for his guidance and mentorship. Your kindness, intelligence, and perseverance are an inspiration.

A toast to the many people I've had the privilege to count among my colleagues: to Corentin Coulais, Scott Waitukaitis, Song-Chuan Zhao, Matthieu Labousse, and Hadrien Bense, my seniors, for their postdoc guidance. To Peter Dieleman, Nitin Singh, Luuk Lubbers; Amitesh Singh, Jiangnan Ding, Ryan van Mastrigt, Jingran Liu, and Lennard Kwakernaak, my dear colleagues, for their team spirit. To Daan van Velzen, Margherita Botto, Rivka Zandbergen, and Klara Knupfer, for being my patient students. And to Yair Shokef and Erdal Oğuz, my fond collaborators.

My gratitude to Victor, Emma, Nikki, Bas, and Ben for their unconditional support and encouragement.

And to all others who, in ways big and small, helped bring this work into the world: making headway is done best with the support of a warm community. It takes a village–thank you for being mine.

Casimir PhD series, Delft-Leiden 2021-03
ISBN 978-90-8593-469-1
MMXXI